Numerical modelling of tunnelling in sand using a state parameter constitutive model

By

Bowen Yang

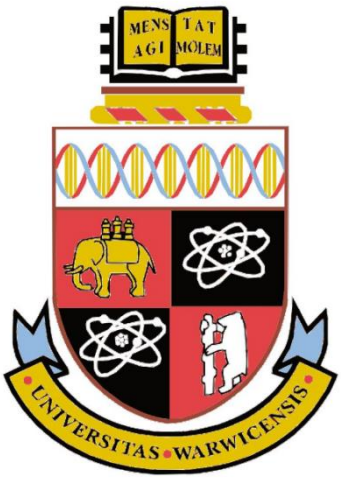

A thesis submitted for the degree of Doctor of Philosophy at the
The University of Warwick

School of Engineering

Supervised by

Alan Bloodworth *and* ***Benoit Jones***

January 2018

Table of contents

TABLE OF CONTENTS I

ACKNOWLEDGEMENTS VI

ABSTRACT VII

DECLARATION VIII

LIST OF FIGURES IX

LIST OF TABLES XVII

NOTATION XVIII

CHAPTER 1. INTRODUCTION 1

1.1 MOTIVATION 1

1.2 SCOPE OF THE RESEARCH 2

1.3 OUTLINE OF THE THESIS 2

CHAPTER 2. LITERATURE REVIEW 4

2.1 INTRODUCTION 4

2.2 GROUND MOVEMENTS INDUCED BY TUNNELLING 4

2.2.1 Transverse troughs 5

2.2.1.1 Deformations around the profile 5

2.2.1.2 The Gaussian curve 6

2.2.1.3 The trough width 8

2.2.1.4 Volume loss 9

2.2.1.5 Subsurface settlement troughs 12

2.2.1.6 Horizontal movements 15

2.2.2 Longitudinal troughs 17

2.3 PREDICTION OF GROUND DEFORMATIONS 18

2.3.1 Empirical methods 19

2.3.2 Analytical methods 19

2.4 GROUND LOADING ON THE TUNNEL LINING 26

2.4.1 Lining in clay 27

2.4.2 Lining in sands. 28

2.5 CRITICAL STATE OF SAND 29

2.5.1 The definition of critical state *29*
2.5.2 Critical state models *30*
2.5.2.1 Cam Clay 31
2.5.2.2 Modified Cam Clay 33
2.5.3 State parameter sand models *34*
2.5.3.1 Norsand (Jefferies 1993) 35
2.5.3.2 A state parameter model for clay and sand (Yu 1998) 36
2.5.3.3 A two surfaces model for sand (Manzari & Dafalias 1997) 37
2.5.3.4 Summary 38
2.6 FINITE ELEMENT MODELLING OF TUNNEL CONSTRUCTION 39
2.6.1 Two dimensional finite element analysis *39*
2.6.2 Three dimensional finite element analysis *41*
2.6.2.1 Tunnel heading 42
2.6.2.2 Around the shield 43
2.6.2.3 The tail void 44
2.6.3 Boundary conditions *44*
2.6.4 Stress coefficient K_0 ..... *45*

CHAPTER 3. FORMULATION AND APPLICATION OF THE NORSAND MODEL 47

3.1 INTRODUCTION 47
3.2 THE STATE PARAMETER MODEL – NORSAND 47
3.2.1 The critical state *48*
3.2.2 The state parameter *52*
3.2.3 Infinity of NCL *53*
3.2.4 Stress dilatancy *55*
3.2.5 Yield surface *57*
3.2.6 A case of shearing *61*
3.2.7 Internal cap *63*
3.2.8 Image parameters *65*
3.2.9 Hardening and softening law *67*
3.2.10 Elasticity *70*
3.3 DETERMINATION OF INPUT PARAMETERS 70
3.3.1 The critical state line (CSL) *71*
3.3.2 The critical stress ratio M_{tc} *78*
3.3.3 State-dilatancy χ_{tc} *79*
3.3.4 The plastic hardening modulus H *81*
3.3.5 Shear modulus G *81*
3.3.6 Summary *82*

3.4 APPLICATIONS 85
3.4.1 Drained compression tests *85*
3.4.2 Undrained compression tests *90*
3.5 SUMMARY 93

CHAPTER 4. A PROPOSED SAND MODEL 94

4.1 INTRODUCTION 94
4.2 ELASTICITY IN THE PROPOSED MODEL 94
4.2.1 The small strain elastic modulus *95*
4.2.2 The non-linear elastic shear stiffness *97*
4.2.3 The non-linear elastic bulk stiffness *100*
4.2.4 Change of stress path direction *107*
4.2.5 Summary *107*
4.3 NUMERICAL IMPLEMENTATION OF THE PROPOSED MODEL 109
4.3.1 Stress increment *109*
4.3.2 Consistency condition during hardening *110*
4.3.3 Consistency condition during softening *112*
4.3.4 Calculation flow in FEM *115*
4.4 COMPARISON BETWEEN THE PROPOSED MODEL AND THE NORSAND 117
4.5 EFFECT OF NONLINEAR ELASTICITY AND MODEL PARAMETERS 123
4.5.1 Influence of initial state *123*
4.5.2 Influence of elasticity properties *124*
4.5.3 Influence of plasticity properties *124*
4.6 SUMMARY 129

CHAPTER 5. FEM ANALYSIS OF A CENTRIFUGE TUNNELLING PROTOTYPE IN SAND 130

5.1 INTRODUCTION 130
5.2 THE CENTRIFUGE TUNNEL PROTOTYPE 130
5.2.1 The geometry and boundary conditions *131*
5.2.2 Characters of the ground material *132*
5.2.3 Details of volume loss control *132*
5.3 THE FEM MODEL 133
5.3.1 Model geometry *133*
5.3.2 Element type and meshing *134*
5.3.3 Boundary conditions *136*
5.3.4 Modelling the volume loss *136*
5.3.4.1 The volume loss control process 136
5.3.4.2 The flexible tunnel periphery 139

5.3.5 The applied constitutive models and input parameters *140*
5.3.5.1 The Hardening Soil model 140
5.3.5.2 The proposed model 142
5.3.6 The monitoring points *144*
5.4 PARAMETRIC STUDY OF THE INITIAL STATE PARAMETER ψ_0 145
5.4.1 Vertical settlement troughs *146*
5.4.2 Horizontal ground displacement *151*
5.4.3 Effect on stresses *157*
5.4.3.1 Stress paths around tunnel 157
5.4.3.2 Stress distribution above tunnel crown 160
5.4.4 Effect on strains *161*
5.4.5 Summary *163*
5.5 EFFECT OF K_0 164
5.5.1 Effect on ground displacements *164*
5.5.2 Effect on stresses *167*
5.6 COMPARISON OF THE PROPOSED MODEL AND HARDENING SOIL 168
5.6.1 Deformation of the tunnel profile *168*
5.6.2 Vertical ground displacements *169*
5.6.2.1 Vertical settlement patterns 169
5.6.2.2 Vertical settlement troughs 170
5.6.3 Horizontal ground displacements *175*
5.6.4 Stresses *177*
5.6.4.1 Stress paths 179
5.6.4.2 Stress above tunnel 179
5.6.4.3 Shear bands 181
5.6.5 Strain developments *182*
5.6.6 Dilation and contraction *184*
5.7 EVALUATION OF GROUND DEFORMATION PREDICTION METHODS 189
5.7.1 Surface settlement troughs *189*
5.7.2 Subsurface settlement troughs *192*
5.8 CHAPTER SUMMARY 194

CHAPTER 6. CONCLUSIONS 196

6.1 THE PROPOSED CONSTITUTIVE SAND MODEL 196
6.2 FE MODELLING OF TUNNEL VOLUME LOSS INDUCED GROUND RESPONSE 196
6.3 FURTHER RESEARCH 198

REFERENCES 200

APPENDIX A. TRIAXIAL TESTS INVOLVED IN DETERMINATION OF INPUT MODEL PARAMETERS 210

A.1 The critical state locus 210

A.2 M_{tc} and N 212

A.3 χ_{tc} 214

APPENDIX B. DISPLACEMENTS OF THE FE TUNNEL PERIPHERY 215

APPENDIX C. GROUND RESPONSE CALCULATED BY USING THE PROPOSED MODEL WITH Ψ_0 = 0.1 218

C.1 Settlement troughs 218

C.2 Horizontal displacement 221

APPENDIX D. EFFECT OF K_0 223

D.1 Effect on horizontal displacement 223

D.2 Effect on stress path 224

APPENDIX E. FORTRAN CODE OF THE PROPOSED SAND MODEL 226

Acknowledgements

I would like to present my sincere thanks to my supervisors Doctor Benoit Jones and Doctor Alan Bloodworth. They have provided me loads of academic support and unbelievable patience throughout the four years. Without their efforts the completion of my PhD work would be almost impossible.

I also would like to give my gratitude to all the academic staff that have helped me during my period of study. Particularly, I am very appritiate of the academic and financial support from Professor Stefano Utili who have given me plenty of valuable suggestions on my research and the opportunity of secondment in Tongji University.

I am also grateful to my friends and colleagues at the University of Warwick including Dr. Guannan Hu, Dr. Zhaohui Wang, Dr. Vishwajeet Ahuja and Dr. Chen Chen. Those sparkling conversations, unforgettable trips, inspiring basketball times and countless meals in the School of Engineering have made my PhD life unbelievably colourful and enjoyable.

Lastly, I give my sincere thanks to my parents. This PhD is a wonderful new beganing of my career. I hope I made you proud. Thanks for the love.

Abstract

During urbanisation, tunnelling in soft ground is an inevitable issue. In the last hundred years, the tunnelling techniques have been developed considerably so that the excavation speed has considerably increased; the tunnel diameter becomes so large that a single tunnel is able to contain dual direction traffic; the settlement influence induced by tunnelling has been reduced by magnitudes. On the other hand, our understanding of soft ground has improved less relative to the improvements of tunnelling techniques, due to complexity of the ground formation and difficulty of obtaining detailed data of the ground.

Tunnelling in sand has drawn less research interest in recent decades compared to tunnelling in clay. However tunnelling is ubiquitous in many cities that don't have regular stiff clay ground. This thesis focuses on numerical predictions of ground response induced by tunnelling in sand. Two main topics of research are covered in this study, namely constitutive behaviour of sand and numerical modelling of tunnel volume loss induced ground response.

An existing constitutive sand model - Norsand is used as the base theory of the new developed sand model. Small strain stiffness, non-linear elasticity during unloading and the flow rule during softening are either improved or added in the proposed sand model compared to Norsand. Laboratory data of drained and undrained triaxial compression tests on different types of sands are used for validation of the proposed model. Numerical simulation of triaxial testing demonstrates good agreement with the test data in both small and large strain situations.

The proposed model is implemented into the commercial finite element geotechnical analysis software Plaxis 3D for numerical modelling of a centrifuge tunnelling prototype carried out in sand. A standard constitutive soil model - Hardening Soil is also applied in the numerical modelling for comparison. Numerical ground movement results from both soil models illustrate good agreement with the centrifuge test result around small – medium tunnel deformation level. However the dilation – contraction behaviour of sand in all deformation levels is clearly demonstrated in the results calculated by the proposed model while the Hardening Soil model hardly models this feature.

This research proposed a new developed sand model that can describe the dilation-contraction behaviour and the small strain stiffness of sand, and demonstrated the capability of predicting the ground response induced by tunnelling in sand using this model.

Declaration

This thesis is submitted to the University of Warwick in support of my application for the degree of Doctor of Philosophy. It has been composed by myself and has not been submitted in any previous application for any degree. The work presented (including data generated and data analysis) was carried out by the author except in the cases outlined below:

(1) The raw triaxial test data used in Chapter 3 and Chapter 4 from the Golder Associates.
(2) The centrifuge data used in Chapter 5 from Marshall (2009).

Bowen Yang
December 2017

List of figures

Figure 2.1 Green field ground movement induced by tunnelling (Attewell et al. 1986)..... 5

Figure 2.2 Deformation around the tunnel profile (after Gonzalez and Sagaseta, 2001) 6

Figure 2.3 Settlement mechanism based on centrifuge tests (Mair, 1979; Chambon and Corté, 1994)..... 8

Figure 2.4 Influence of α on modified Gaussian curve 8

Figure 2.5 Tunnel volumes loss induced by shield tunnelling 11

Figure 2.6 Variation of trough width parameter K with depth..... 13

Figure 2.7 Soil volume loss versus tunnel volumes loss in sand..... 14

Figure 2.8 Surface horizontal movement 16

Figure 2.9 Longitudinal settlement curve..... 18

Figure 2.10 Three steps of the approximate solution (Sagaseta 1987)..... 22

Figure 2.11 The gap parameter g (Lee et al. 1992) 26

Figure 2.12 Load on the lining after lining installation. a). Beneath Regent's Park (Barratt et al. 1994); b). Beneath St James's Park (Dimmock 2003)..... 27

Figure 2.13 The critical state locus of soil (Bolton 1979). 30

Figure 2.14 Cam Clay and Modified Cam Clay yield surface in the stress (p'-q) plane..... 34

Figure 2.15 Norsand yield surface (Jefferies 1993). 36

Figure 2.16 The scheme of the two surfaces model (Manzari & Dafalias 1997). 38

Figure2.17 The settlement profiles given by the gap parameter (bottom fixed) method and the free convergence method (centre fixed)(Borst et al. 1996). 41

Figure. 2.18 Advancement of the TBM using excavation elements (Komiya et al. 1999) 43

Figure 3.1 Critical states of Erksak 330/0.7 sand reached in undrained triaxial compression tests ($p' \leqslant$ 1000 kPa). 49

Figure 3.2 Critical states with stress axis plotted on a logarithmic scale (full range of p')..... 49

Figure 3.3 Critical states and the initial states of Toyoura sand in v-p plane (Verdugo & Ishihara 1996)..... 51

Figure 3.4 Critical states of Erksak 330/0.7 sand with fitting of the power law relationship. 52

Figure 3.5 The state parameter in *e*-ln*p'* plane. 53

Figure 3.6 The compression line and the critical state line in *v*(vertical axis)-ln*p'*(horizontal axis) plane (linear CSL). (a) Unique NCL (b) Infinite NCL. 54

Figure 3.7 Shear of two sand layers. 55

Figure 3.8 The pattern of plastic potential (integration of D^p). 57

Figure 3.9 The normalised yield locus and vectors of plastic strain increment (Graham & Houlsby 1983). 58

Figure 3.10 Norsand yield surface and internal cap for dense sand. *The internal cap will be discussed in section 3.2.7. 60

Figure 3.11 Norsand yield surface and internal cap for loose sand. 60

Figure 3.12 Hardening and softening of the yield surface during shearing. 62

Figure 3.13 Approaching the critical state of dense sand in shear. 64

Figure 3.14 Undrained triaxial tests for determining the critical state. 73

Figure 3.15Undrained triaxial tests for determining the critical state 74

Figure 3.16 Drained triaxial tests selected for determining the critical state. 75

Figure 3.17 Determination of the critical state line in the *e-p'* plane. 76

Figure 3.18 The critical state locus in *e*-ln*p'* plane. 76

Figure 3.19 Relationship between peak stress ratio and peak dilatancy of Toyoura sand in triaxial compression. 79

Figure 3.20 Derivation of the input parameter χ_{tc} for Toyoura sand. 80

Figure 3.21 Triaxial compression test CID_3 88

Figure 3.22 Triaxial compression test CID_2A 88

Figure 3.23 Triaxial compression test CID_G460 89

Figure 3.24 Triaxial compression test CID_G462 89

Figure 3.25 Undrained triaxial test GIU_G919 91

Figure 3.26 Undrained triaxial test GIU_G908 91

Figure 3.27 Undrained triaxial test GIU_G911 92

Figure 4.1 Very small strain shear modulus against stress level 97

Figure 4.2 Shear modulus against stress level (Oztoprak & Bolton 2012); (a) ε_1=0.0001%; (b) ε_1=0.001% 98

Figure 4.3 Shear modulus versus strain level data. (Oztoprak & Bolton 2012) 99

Figure 4.4 The hyperbolic description of small strain shear modulus. 100

Figure 4.5 Isotropic consolidation and unloading of Esksak 330/0.7 sand. Data from Jefferies and Been (2000) 102

Figure 4.6 The unloading reloading line starting from p' = 500 kPa predicted by Equation [4.12] with stress reversal points at e=0.4 and 0.5 respectively. 102

Figure 4.7 URLs experimental data and predictions of non-linear elasticity of sand using Equation [4.13]; m=0.55. Test data from Jefferies and Been (2000) 105

Figure 4.8 The relationship between r and void ratio e. 106

Figure 4.9 The dependence of D_s on stress level and void ratio 106

Figure 4.10 The flow rule of Erlsak sand during loading and unloading. (A.E.Dabeet 2008) 112

Figure 4.11 The calculation flow of the proposed model in FEM 116

Figure 4.12 Numerical modelling with and without small strain & non-linear elasticity - Triaxial compression test CID_2A 119

Figure 4.13 Numerical modelling with and without small strain & non-linear elasticity - Triaxial compression test CID_3 119

Figure 4.14 Numerical modelling with and without small strain & non-linear elasticity - Triaxial compression test CID_G462 120

Figure 4.15 Numerical modelling with and without small strain & non-linear elasticity - Triaxial compression test CID_G460 120

Figure 4.16 Numerical modelling with and without small strain & non-linear elasticity - Triaxial compression test CIU_G919 121

Figure 4.17 Numerical modelling with and without small strain & non-linear elasticity - Triaxial compression test CIU_G908 121

Figure 4.18 Numerical modelling with and without small strain & non-linear elasticity - Triaxial compression test CIU_G911 122

Figure 4.19 Effect of critical state slope λ 125

Figure 4.20 Effect of critical state altitude Γ 125

Figure 4.21 Effect of initial state parameter ψ_0 126

Figure 4.22 Effect of shear modulus index C_i 126

Figure 4.23 Effect of the elasticity threshold parameter ε_e 127

Figure 4.24 Effect of the elasticity reference strain parameter ε_r 127

Figure 4.25 Effect of the hardening parameter H_h 128

Figure 4.26 Effect of the critical stress ratio M_{tc} 128

Figure 5.1 The centrifuge tunnel prototype package (Marshall 2009). 131

Figure 5.2 The tunnel prototype (Marshall & Mair 2009). 133

Figure 5.3 Geometry of FEM model (all dimensions in millimetres) 134

Figure 5.4 The tetrahedral soil element with three local coordinates and its numbering of the nodes 134

Figure 5.5 The triangle plate element with two local coordinates, six nodes and three integration points (×). 135

Figure 5.6 The FEM model in Plaxis 3D. 135

Figure 5.7 Displacement boundary conditions of the FEM model. 136

Figure 5.8 Points used for calculating the tunnel cross section area. 138

Figure 5.9 Volume loss control process in FEM 139

Figure 5.10 Input material parameters of the plate elements on cylinder 2. 139

Figure 5.11 The basic idea of the Hardening Soil model in a triaxial compression version (Brinkgreve et al. 2013) 141

Figure 5.12 Input parameters of the proposed Norsand based model in Plaxis 3D 143

Figure 5.13 Sections for ground displacement analysis. 145

Figure 5.14 Points for stress development examination (dimensions in mm). 145

Figure 5.15 Vertical settlement troughs at three depths (surface, -70mm and -120mm) calculated by the proposed model with $V_{l,t}$=0.5%. 147

Figure 5.16 Vertical settlement troughs at three depths (surface, -70mm and -120mm) calculated by the proposed model with $V_{l,t}$=1.0%. 148

Figure 5.17 Vertical settlement troughs at three depths (surface, -70mm and -120mm) calculated by the proposed model with $V_{l,t}$=2.5%. 149

Figure 5.18 Vertical settlement troughs at three depths (surface, -70mm and -120mm) calculated by the proposed model with $V_{l,t}$=5.0%. 150

Figure 5.19 Horizontal ground displacements 15mm away from the tunnel periphery calculated by the proposed model. 153

Figure 5.20 Horizontal ground displacements 30mm away from the tunnel periphery calculated by the proposed model. 154

Figure 5.21 Horizontal ground displacements 45mm away from the tunnel periphery calculated by the proposed model. 155

Figure 5.22 Horizontal ground displacements 60mm away from the tunnel periphery calculated by the proposed model. 156

Figure 5.23 Stress paths at point A calculated by the proposed model. 157

Figure 5.24 Stress paths at point B calculated by the proposed model. 158

Figure 5.25 Stress paths at point C calculated by the proposed model. 159

Figure 5.26 Stress paths at point D calculated by the proposed model. 159

Figure 5.27Stress paths at point E calculated by the proposed model..... 159

Figure 5.28 Mean effective stress above tunnel crown calculated by the proposed model... 160

Figure 5.29 Volumetric behaviour of point A. 161

Figure 5.30 Volumetric behaviour of point B. 161

Figure 5.31 Volumetric behaviour of point C. 162

Figure 5.32 Volumetric behaviour of point D. 162

Figure 5.33 Volumetric behaviour of point E..... 163

Figure 5.34 Evaluation of K_0 of the Leighton Buzzard Fraction E sand under normal consolidation state (Gao et al. 2014). 164

Figure 5.35 Effect of K_0 on vertical ground displacement. 165

Figure 5.36 Effect of K_0 on horizontal ground displacement 15mm from tunnel periphery. 166

Figure 5.37 Effect of K_0 on stress path at point A. 167

Figure 5.38 Effect of K_0 on stress path at point C. 167

Figure 5.39 Original and deformed tunnel periphery in the FE model (undeformed tunnel plotted using black line). 169

Figure 5.40 Vertical displacement contours of (a) FE model calculated by the proposed model, (b) centrifuge test (Marshall 2009). 170

Figure 5.41 Vertical displacement contours of (a) FE model calculated by the Hardening Soil model, (b) centrifuge test (Marshall 2009). 170

Figure 5.42 Surface settlement troughs. 171

Figure 5.43 Settlement troughs at -70mm. 172

Figure 5.44 Settlement troughs at -120mm. 173

Figure 5.45 Horizontal displacement contours of (a) FE model calculated by the Hardening Soil model, (b) centrifuge test (Marshall 2009) 175

Figure 5.46 Horizontal displacement contours of (a) FE model calculated by the proposed model (note that legend should contrarily apply to numerical results in this figure due to setting issues in Plaxis3D), (b) centrifuge test (Marshall 2009)..... 175

Figure 5.47 Horizontal ground displacements predicted by the FE model. 176

Figure 5.48 Calculated stress paths above tunnel. 177

Figure 5.49 Calculated stress paths at side of tunnel. 178

Figure 5.50 Calculated mean stress above tunnel crown. 180

Figure 5.51 Shear bands in (a) FE model calculated by the proposed model; (b) FE model calculated by Hardening Soil; (c) the centrifuge model. 181

Figure 5.52 Calculated strain developments above tunnel. 182

Figure 5.53 Calculated strain developments at side of tunnel. 183

Figure 5.54 Contour plots of volumetric strain at $V_{l,t}$ = 2.0% (compression positive). 185

Figure 5.55 Contour plots of volumetric strain at $V_{l,t}$ = 5.0% (compression positive) 186

Figure 5.56 Ground volume loss induced by tunnel volume loss. 187

Figure 5.57 Normalised ground volume loss induced by tunnel volume loss. 188

Figure 5.58 The predicted surface settlement troughs at 1% tunnel volume loss using (a) analytical methods with adjusted parameters; (b) all applied approaches. 190

Figure 5.59 The predicted -70mm settlement troughs at 1% tunnel volume loss using (a) analytical methods with adjusted parameters; (b) all applied approaches. 192

Figure 5.60 The predicted -120mm settlement troughs at 1% tunnel volume loss using (a) analytical methods with adjusted parameters; (b) all applied approaches. 193

Figure A.1 Drained triaxial compression tests used for deducing the CSL 210

Figure A.2 Undrained triaxial compression tests used for deducing the CSL 211

Figure A.3 Drained triaxial compression used for deducing M_{tc} and N. 212

Figure A.4 Drained triaxial compression used for deducing M_{tc} and N. 213

Figure A.5 Undrained triaxial compression test used for deducing M_{tc}. 213

Figure B.1 Nine points used for tunnel volume loss calculation. 215

Figure C.1 Settlement troughs with $V_{l,t}$=0.5%.Table B.2 Cylinder movement calculated by Hardening Soil 215

Figure C.2 Settlement troughs with $V_{l,t}$=0.5% 218

Figure C.3 Settlement troughs with $V_{l,t}$=1.0% 219

Figure C.4 Settlement troughs with $V_{l,t}$=2.5% 220

Figure C.5 Settlement troughs with $V_{l,t}$=5.0% 220

Figure C.6 Horizontal ground displacement (a) 15mm and (b) 30mm away from tunnel periphery 221

Figure C.7 Horizontal ground displacement (a) 45mm and (b) 60mm away from tunnel periphery. 222

Figure D.1 Effect of K_0 on horizontal ground displacement 30mm from tunnel periphery. . 223

Figure D.2 Effect of K_0 on horizontal ground displacement 45mm from tunnel periphery. . 223

Figure D.3 Effect of K_0 on horizontal ground displacement 60mm from tunnel periphery. . 224

Figure D.4 Effect of K_0 on stress path at point B. 224

Figure D.5 Effect of K_0 on stress path at point D. 225

Figure D.6 Effect of K_0 on stress path at point E. 225

List of tables

Table 3.1 The drained and undrained tests of Toyoura sand used for determination of the critical states (Data from Golder Associates). 77

Table 3.2 Drained tests for determination of χ_{tc} (data from Golder Associates). 83

Table 3.3 Input parameters of Norsand 84

Table 3.4 Input initial conditions for numerical modelling of triaxial compression 86

Table 3.5 Input initial conditions for numerical modelling of undrained triaxial tests 90

Table 4.6 Typical values of the very small strain stiffness $G_0$with C_i = 5640..... 98

Table 4.7 Input parameters for small strain and nonlinear elasticity..... 117

Table 4.8 Base parameters applied for the analysis of the effect from input parameters..... 123

Table 5.9 Input parameters of the Hardening Soil model..... 142

Table A.1 Determination of χ_{tc} using linear and curved CSL. 214

Table B.1 Cylinder movement calculated by Hardening Soil. 215

Table B.2 Cylinder movement calculated by the proposed model with ψ_0 = 0.1..... 216

Table B.3 Cylinder movement calculated by the proposed model with ψ_0 = 0..... 216

Table B.4 Cylinder movement calculated by the proposed model with ψ_0 = -0.1 217

Table B.5 Cylinder movement calculated by the proposed model with ψ_0 = -0.2 217

Notation

A_t	the cross section area of the tunnel
C	distance from surface to tunnel crown
C_i	model parameter affects shear modulus
c	cohesion
D	diameter
D^{e}	elastic stiffness matrix
D^p	plastic dilation rate
D_m	mined diameter
D_l	lined diameter
$D^p_{\min}$	minimum ratio of dilation
E	effective Young's modulus
E_i	initial stiffness
E_{ur}	unloading reloading elastic stiffness
e	void ratio
e_c	critical void ratio
e_n	normal consolidated void ratio
G	elastic shear modulus
G_0	initial shear modulus
g	gap parameter
g	plastic potential surface
H	hardening parameter
H_u	softening parameter
i	horizontal distance from the tunnel centreline to the inflexion point
i	subscript i stands for image point
K	trough width parameter
K	bulk modulus

K_0	coefficient of earth pressure at rest
M	stress ratio at the critical state
N	model parameter
p	superscript p stands for plasticity
p	mean stress
p_i	internal supporting pressure
p_i	stress level of current image point
p_w	pore pressure
p_c	mean stress at critical state
p_{ref}	reference pressure which is often set to 101 kPa
p'_{rev}	p' at the stress reversal point
q	deviatoric stress
q_0	initial deviatoric stress
R	tunnel radius
$S_{v,x}$	vertical settlement of ground with a horizontal distance of x from the tunnel central line
S_{max}	vertical settlement value at the tunnel centreline
$S_{,h}$	horizontal movement
$S_{h,x}$	horizontal movement of ground with a horizontal distance of x from the tunnel central line
T	shear force
tc	subscript tc stands for critical state determined under triaxial compression condition
u_x	horizontal deformation of soil
u_z	vertical deformation of soil
V_t	tunnel ground loss
V_s	ground loss
V_s	area of the settlement trough
$V_{l,t}$	tunnel volume loss
$V_{l,s}$	ground volume loss

v	specific volume (1+e)
W	work done by stress
x	the horizontal offset from the tunnel centreline
z	depth
z_0	tunnel axis level
χ	model parameter relating to stress dilatancy
ε	uniform convergence of tunnel
ε_1	principal strain (axial strain/vertical strain under triaxial compression conditions)
ε_e	model parameter affecting small strain stiffness
ε_q	volumetric strain
ε_q	deviatoric strain
ε_r	model parameter affects small strain stiffness
ε_v	volumetric strain
δ	ovalization of tunnel
τ	shear stress
Γ	the critical void ratio when p'=1kPa
κ	the slope of elastic unloading reloading lines
λ	the slope of critical state line
λ_h	plastic multiplier during hardening
λ_s	plastic multiplier during softening
ν	Poisson's ratio
ω_s	model parameter affects small strain stiffness
ψ	dilation angle
ψ	state parameter
ψ_0	initial state parameter
ψ_i	state parameter at the image point
ξ	parameter controlling the curvature of the critical state line
σ_v	vertical stress

η	stress ratio q/p'
η_{rev}	stress ratio q/p' at the stress reversal point
θ	lode angle
φ	friction angle
φ_c	the critical friction angle
$'$	stress with a prime stands for effective stress
$\dot{}$	a dot above a symbol means incremental quantity

Chapter 1. Introduction

1.1 Motivation

With the booming progress of urbanisation all around the world, the amount of underground construction has remained large in volume in recent decades. Tunnelling as an effective construction method, has been sufficiently developed and widely used for more than a hundred years due to its small impact on people's daily life on the ground surface.

Many major cities are in low-lying areas adjacent to coasts or large rivers where there are sedimentary deposits, therefore underground construction in these cities mainly encounters various types of soft ground. When studying ground response induced by tunnelling in soft ground, the ground can be roughly classified into two type of soil: drained soil and undrained soil (short term). During tunnelling in undrained soil like London Clay, the amount of settlement at a certain depth is always approximately consistent with the amount of inward ground movement from excavation periphery to the permanent support, this ground movement close to the tunnel is called the tunnel volume loss. The situation in drained soil like sand is much more complicated as the ground water is free to move through the voids, thus the volume of the ground is allowed to change during tunnelling. Consequently the amount of ground settlement is not directly related to the tunnel volume loss any more. In addition the developments of the stresses and strains in the ground are affected by the granular shape of the sand particles during ground deformation.

Numerical simulation as an effective prediction approach has been widely used in analysing ground response induced by tunnelling, and has been proven to be able to give meaningful predictions of short term ground response induced by tunnelling in undrained soil such as London Clay. By comparison, research of numerical prediction of tunnelling in drained soil such as sand is still insufficient mainly due to the lack of proper and easy-to-use constitutive sand models. It is fortunate that various published researches have tried to replicate and predict the constitutive behaviour of sand and have made certain achievements. The uncertainties remain about which aspects should be covered in a practical sand model? Which theories should be applied in the model? How well can the ground response induced by tunnelling in sand be theoretically explained? These questions generate the motivation of this

research - to bring the tunnelling industry a useful and practical constitutive sand model that can capture the key features of sand behaviour during tunnelling in sand.

1.2 Scope of the research

The aim of this thesis is to develop and validate a constitutive sand model that is practical to use for the tunnelling industry. The following specific works are carried out:

- Development of a constitutive sand model based on the existing Norsand model. This model considers the critical stress-strain state of sand, small strain stiffness and non-linear elasticity in unloading. Experimental data of drained and undrained triaxial compression tests on Toyoura sand are used for the validation of the new model in a Visual Basic Excel based subroutine. Two popular definitions of critical state line (CSL) – linear and curved CSL are both applied in the validations.

- Numerical implementation of the proposed sand model in Plaxis 3D using FORTRAN.

- Numerical simulation of a published green field centrifuge tunnelling prototype test in sand. A continuous surface contraction method is applied for simulating the tunnel volume loss control process in the centrifuge test.

- Parametric studies of K_0 and an important input model parameter ψ_0 of the proposed model. Understanding the influence of these parameters on ground stress development, stress strain relationships and ground displacements.

- Calculation of the surface and subsurface ground response using the Hardening Soil model for comparison with the published centrifuge data, the numerical result calculated by the proposed sand model and some widely used empirical and analytical methods of predicting green field tunnelling induced ground deformation.

- Evaluation and comparison of the calculated and measured results.

1.3 Outline of the thesis

Chapter 2 summarised current understanding of green field ground response induced by tunnelling in both sandy and cohesive ground. Several most widely used empirical and analytical predicting methods are discussed. The critical state mechanics based clay and sand constitutive models are also discussed, as a precursor to the base knowledge of Chapter 3.

Chapter 3 describes the critical state theory and the formulation of the Norsand model. Numerical validations of Norsand with curved and linear CSL are carried out using a Visual Basic subroutine in Excel.

Chapter 4 consists of the formulation and validations of the proposed sand model. Based on the Norsand model, improvements are made on the small strain stiffness, non-linear elasticity during unloading and softening flow rule during unloading. The numerical implementation of the proposed model is also outlined for a better understanding of how the softening flow rule works in the model.

Chapter 5 describes the methodology and modelling results of the numerical analysis. The numerical results calculated by the proposed model and the Hardening Soil model are compared with published centrifuge test data. The parametric studies of K_0 and ψ_0 are also described in this chapter. Prediction results calculated by the empirical and analytical approaches discussed in chapter 2 are also compared with the numerical results.

The main findings of this thesis and recommended further research works based on the topic of numerical modelling of tunnelling in sand are summarised in chapter 6.

Chapter 2. Literature Review

2.1 Introduction

This chapter presents a review of the literature that discuses ground movements induced by tunnelling in soft ground and, specifically, in sand. As the core technique in numerical modelling, constitutive modelling of sand is also discussed.

2.2 Ground movements induced by tunnelling

The time gap between excavation and installation of supporting measures causes changes of the stress distributions of the surrounding ground mass, thus ground losses and subsequent ground movements occur during tunnelling in soft ground. Mair and Taylor (1997) summarised five main components of the ground losses associated with shield tunnelling (excavation using closed-face techniques like tunnel boring machine/TBM), which can be simplified as follows:

(1) Relaxation of the ground towards excavation face;
(2) Radial ground movements toward the tunnel profile;
(3) Deflection of the tunnel lining due to ground loadings; and
(4) Ground consolidation caused by long term pore water pressure changes.

When using shield tunnelling methods, the first component of ground losses can be minimised into a negligible magnitude if the face pressure is carefully designed and controlled. However for open face tunnelling, especially in clay, component (1) can be of the major importance (Mair et al. 1993; Peck, 1969) due to stress relief ahead of the face. Component (2) is of more importance in shield tunnelling and is mainly due to the over cutting of the cutter head and the tail void created around the installed tunnel lining before grouting. Component (3) is generally small compared to the former two once the desired strength of the lining is reached. In most shield or open-face tunnelling cases, the majority of the short term ground losses occur due to the first three components (Lee et al. 2004). The subsequent ground movements associated with the ground losses in “green field” conditions, in which case no structure exists near the tunnel, are as shown in Figure 2.1. As the tunnel is advancing, the ground mass that is away from the excavation face tends to reach new

equilibrium condition (the long term consolidation of ground is ignored), thus the ground movements there can be simplified as a 2D problem in *x*-*z* plane from Figure 2.1. Correspondingly, the ground movement above the excavation area is a more complicated case that can be accomplished by incorporating both transverse and longitudinal (*y*-*z* plane from Figure 2.1) ground movements. The 3D tunnelling problem is then broken into two 2D problems: the transverse troughs and the longitudinal troughs.

2.2.1 Transverse troughs

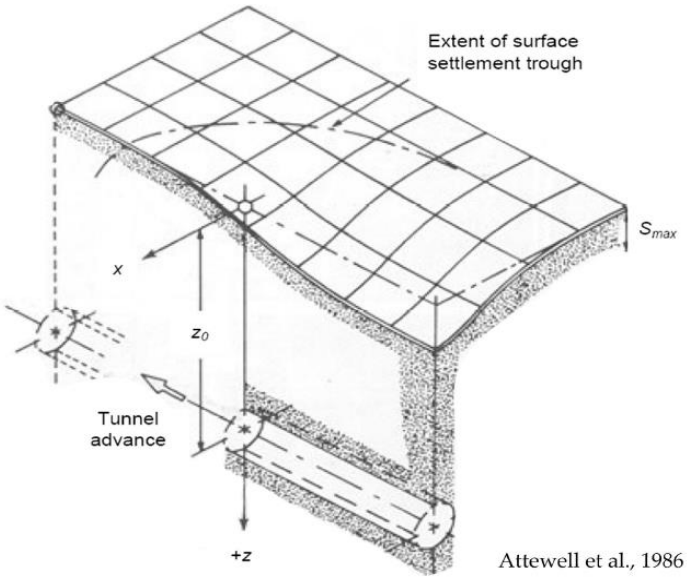

Figure 2.1 Green field ground movement induced by tunnelling (Attewell et al. 1986)

It can be seen that the form of the transverse troughs away from the excavation are only affected by components 2 and 3 discussed above. It is then necessary to make clear how the ground deforms around the tunnel profile, and how much consequent ground loss is generated.

2.2.1.1 Deformations around the profile

The construction method of tunnelling employed in soft ground usually consists of shield excavation followed by immediate installation of lining. For simplicity, the following discussion is mainly related to ground movements induced by shield tunnelling. Due to components 2 and 3, the final cut profile of the soil is larger than the lining profile. The deference between them in terms of volume per unit length of tunnel is referred to as tunnel ground loss (V_t), and can be simply calculated as:

$$V_t = \frac{\pi}{4}\left(D_m^2 - D_l^2\right) \qquad [2.1]$$

where D_m and D_l refer to the mined diameter and the lined diameter respectively. For simplicity, the area of ground loss can be generalised as a concentric circle compassing the mined area according to Equation [2.1], in other words, the mined tunnel uniformly converged after ground deformation (Sagaseta, 1987; Verruijt and Booker, 1996; Bobet, 2001). However, in most cases, the majority of the actual ground losses are concentrated around the tunnel crown and two sides; very little amount of ground deformation occurs at the tunnel invert (Potts, 1976; Loganathan and Poulos, 1998). This could be due to the lining tending to rest on the bottom boundary of the excavation, because of gravity, as the excavation face advances (Rowe & Kack 1983). Apart from the uniform radial displacement and the downward uniform movement of tunnel profile mentioned above, an ovalisation (distortion) of the tunnel without change of the area of the cross section (no ground loss) can be induced (Pinto & Whittle 2000). Therefore, considering the three components of displacement above, the final ground deformation forms an elliptical area as shown in Figure 2.2.

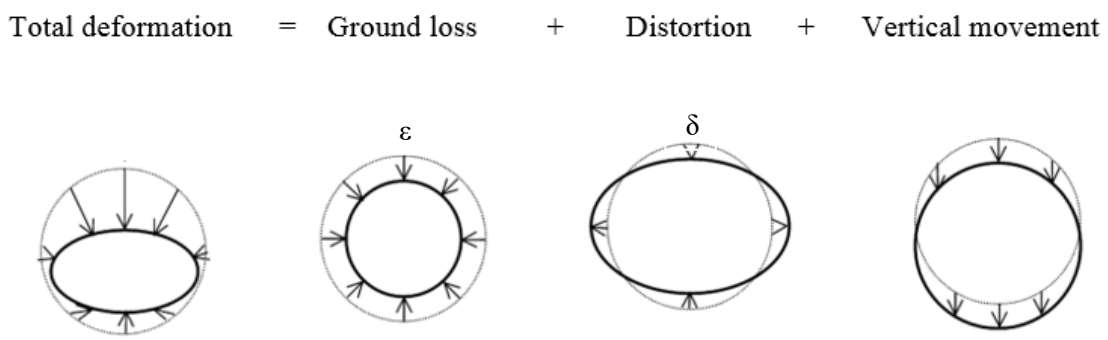

Figure 2.2 Deformation around the tunnel profile (after Gonzalez and Sagaseta, 2001)

2.2.1.2 The Gaussian curve

From the tunnel profile throughout the depth of the soil above the tunnel, the shape of the ground loss gradually evolve from an elliptical area into transverse settlement troughs in the *x*-*z* plane. The transverse trough in soft ground, on the surface level, can be simplified as a Gaussian curve (Peck 1969):

$$S_{v,x} = S_{\max} \exp\left(-x^2 / 2i^2\right) \qquad [2.2]$$

Where $S_{v,x}$ stands for vertical settlement, S_{max} is the vertical settlement value at the tunnel centreline, x is the horizontal offset from the tunnel centreline, and *i* is the horizontal distance from the tunnel centreline to the inflection point of the settlement trough where the curvature of the settlement trough is zero. By integrating Equation [2.2], the value of the maximum vertical settlement can be obtained as follows:

$$S_{\max} = \frac{V_s}{\sqrt{2\pi} \cdot i} \qquad [2.3]$$

Where V_s is the area of the settlement trough. It can be seen that V_s defines the size of the settlement while *i* controls the shape. The Gaussian curve has been proved to be able to give good fit to settlement data in undrained soil, like Clay (Peck, 1969; Clough and Schmidt, 1981; Mair et al., 1993). For drained soil like sands, however, the Gaussian curve does not always provide a reasonable fit (O'Reilly and New, 1983; Celestino et al., 2000). The surface settlement trough is found to be generally narrower than the Gaussian curve (Mair and Taylor, 1997; Jacobsz et al., 2004; Vorster et al., 2005). In addition, with larger S_{max}, settlement tends to cause narrower trough width due to the "chimney" mechanism in sand as shown in Figure 2.3. To obtain better fit to the settlement data in sand, Vorster et al., (2005) provided a modified Gaussian curve of the following form:

$$S_{v,x} = \frac{n \cdot S_{\max}}{(n-1) + \exp\left[\alpha \left(x/i\right)^2\right]} \qquad [2.4]$$

$$n = e^{\alpha} \cdot \frac{2\alpha - 1}{2\alpha + 1} + 1$$

where *n* is a function parameter which controls the width of the curve; and α is the parameter that ensures *i* remains the distance to the inflection point from the tunnel central line. Therefore *i* has the same definition as in Equation [2.4]. To obtain the value of S_{max}, integration of Equation [2.4] is needed, however this will lead to the use of the polylogarithm function. To avoid the use of the complicated function, by following the approach stated by Marshall, (2009), the maximum vertical settlement value can be calculated by the following method

$$S_{\max} = V_s / (T \cdot i) \qquad [2.5]$$

$$T \approx \exp\left(1.699 + 0.522\alpha - 1.472\sqrt{\alpha}\right)$$

where T is a function parameter. From Equation [2.4] it can be found that the vertical settlement value at the inflection point $S_{v,i} = \exp(-0.5)\ S_{max}$, thus, according to Equation [2.5], the vertical position of the inflection point is affected by α. On the other hand, the horizontal position of the inflection point is still controlled by i in Modified Gaussian curve. It should be noted that Modified Gaussian curve becomes Gaussian curve when n=1. The use of parameter α gives additional flexibilities to the Gaussian curve so it can fit different types of soil. Figure 2.4 shows the comparison between the original Gaussian curve (α=0.5) and Modified Gaussian curves with varying α. We can imagine that when the ground loss V_s is known in tunnelling, a smaller value of α gives a narrower settlement trough, thus can provide better description of the "chimney" mechanism of the settlement trough in sand.

Figure 2.3 Settlement mechanism based on centrifuge tests (Mair, 1979; Chambon and Corté, 1994)

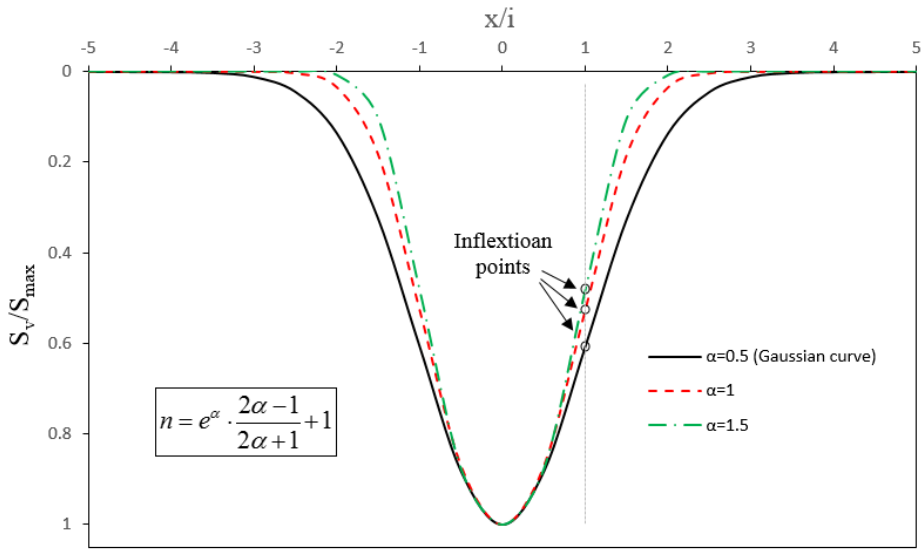

Figure 2.4 Influence of α on modified Gaussian curve

2.2.1.3 The trough width

Either using the original Gaussian curve or Modified Gaussian curve in describing the surface settlement trough, it is necessary to suggest the value of i in order to locate the position of the

inflection point. Some researchers (Peck, 1969; Clough and Schmidt, 1981) concluded that, for soft soil, the value of i is affected by the tunnel depth z_0 and the tunnel diameter D. Similar phenomenon has been validated by series of centrifuge tests of tunnelling in clays (Mair et al., 1981; Clough and Schmidt, 1981; Lee et al., 1999) and sands (Atkinson and Potts, 1977; Lee et al., 2004). In contrast, O'Reilly and New (1982) showed that for relative deep tunnels, where the cover above the tunnel C is larger than the Diameter (C/D>1), the relationship between z_0 and i is approximately linear, and i is not sensitive to the tunnel diameter:

$$i = K \cdot z_0 \qquad [2.6]$$

Where K is a trough width parameter. Based on a survey of UK tunnelling data, they recommended that the value of K could be taken as 0.5 for tunnels in clays and a lower value of 0.25 is suitable for tunnels in sands and gravels. The data from tunnels in clays showed the scatter in the data generally fall within $i = 0.4z_0$ and $i = 0.6z_0$. In soft or stiff clays, for practical purposes, taking K as 0.5 is reasonable in most cases no matter which construction method is used (Fujita 1981). The data for tunnels in sands illustrate more scatter than for tunnels in clays, the majority of the data fall within the range of $i = 0.25z_0$ and $i = 0.45z_0$, therefore a mean line of $i = 0.35z_0$ is suggested by Mair and Taylor (1997). For shallow tunnels, where the surface settlements are affected by the tunnel size, Equation [2.6] is not suitable to evaluate the surface settlement. (Clough & Schmidt 1981) suggested the following equation for the trough width i in soft ground:

$$i = \left(\frac{D}{2}\right)\left(\frac{z_0}{D}\right)^{0.8} \qquad [2.7]$$

Cording (1991) has noted that for tunnels in sand, the trough width i cannot be simply linearly deduced by an empirical parameter K, however, the trough width depends to some extent on the amount of the settlement (the volume of the lost ground). Larger ground losses tend to cause narrower settlement troughs. This reminds the importance of investigating the ground loss in defining the transverse settlement troughs.

2.2.1.4 Volume loss

It is convenient to express the volume of the ground loss around the tunnel (V_t) in terms of the proportion (present as percentage) to the cross section area of the tunnel profile:

$$V_{l,t} = \frac{V_t}{A_t} \cdot 100\% \qquad [2.8]$$

where A_t is the cross section area of the tunnel which can be deduced as $A_t = \pi D_l^2/4$. $V_{l,t}$ is referred as tunnel volume loss and is widely used in describing the effect of ground loss that is in immediate vicinity to the tunnel. The tunnel volume loss can be affected by a wide range of factors including construction methods; tunnel geometry; standards of workmanship and ground conditions (Mair & Taylor 1997). Many researchers have reviewed the tunnel volume loss from tunnelling projects and laboratory tests. Clough and Schmidt (1981); Attewell et al. (1986) and Sagaseta (1987) proposed relationships between stability ratio N and $V_{l,t}$ based on the site data. Mair et al. (1981) and Mair (1989) stated that $V_{l,t}$ should not only related to N but also the critical stability ratio N_c. This is validated by O'Reilly (1988) based on site data from six tunnelling projects in London Clay.

By reviewing 35 research papers associated with settlement induced by tunnelling, Mair and Taylor (1997) summarised the following conclusions on the magnitude of $V_{l,t}$in soft ground: the tunnel volume losses induced by open face tunnelling in stiff clays are generally between 1% and 2%; open face construction with sprayed concrete linings can effectively control the ground movements, $V_{l,t}$ in this case varies from 0.5% to 1.5%; when using closed face excavation methods (earth pressure balance machine or slurry machine), a better level of ground movement control can be achieved where $V_{l,t}$ can be as low as 0.5% in sands and between 1% and 2% in soft clays; for mixed face condition, generally larger $V_{l,t}$ values were obtained (2% - 4%).

Recent settlement data from 34 shield tunnelling projects in soft ground around the world were provided by Dindarloo and Siami-Irdemoosa (2015). These projects were constructed for metro or sewer applications in the urban area. The site data associated with the surface settlement is plotted in Figure 2.5 and the data agreed well with Mair and Taylor (1997)'s conclusions that in the majority of the projects, values of $V_{l,t}$ are within 2%.

When the values of $V_{l,t}$ are plotted against z_0S_{max}/D^2, the relationship between them is shown to be generally linear. As multiple types of soft ground including sands and clays are involved in the database, the values of α_1 and α_2 in Figure 2.5 provide best fit of general soft ground, and should be adjusted accordingly if applied in specific ground conditions. The meaning of the term z_0S_{max}/D^2 can be seen as the magnitude factor of the disturbed ground above the tunnel divided by the size factor of the tunnel. Figure 2.5 illustrates that although larger

tunnels usually give generally larger amount of lost ground, larger tunnel tends to have smaller tunnel volume loss (remember $V_{l,t}$ is the proportion to the tunnel size in terms of volume per unit length of the tunnel, but not the amount of the lost ground). The data from tunnels with diameter D less than 3m show a much higher level of scatter than the data from larger tunnels. The magnitude of the ground movement induced by larger diameter tunnels (D>5m) is relative small ($z_0S_{max}/D^2<2*10^{-4}$ in most cases) compared to the tunnel size.

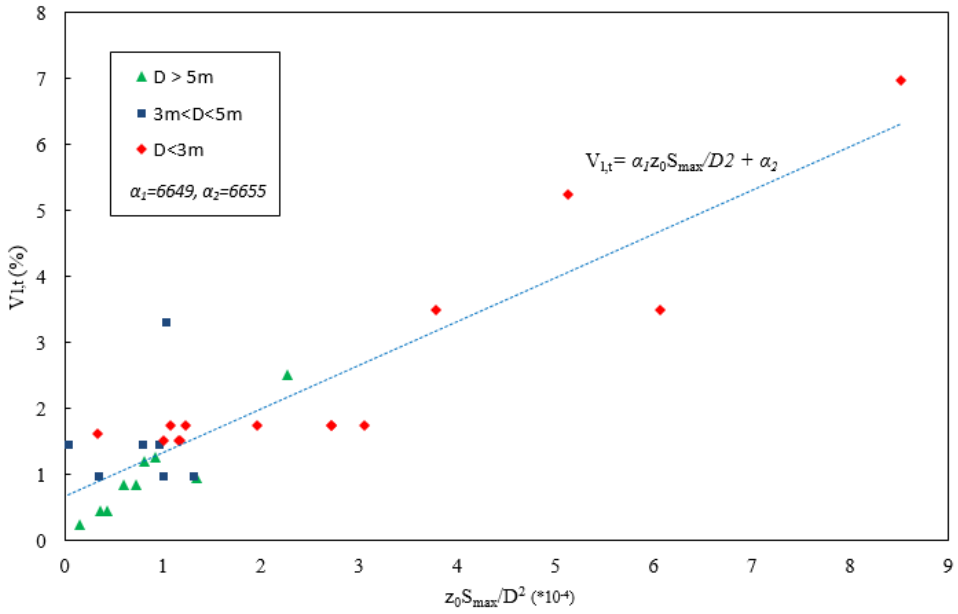

Figure 2.5 Tunnel volumes loss induced by shield tunnelling

As discussed in section 2.2.1.2, V_s defines the size of the settlement troughs. For consistency, V_s can be written in terms of percentage to the tunnel size:

$$V_{l,s} = \frac{V_s}{A_t} \cdot 100\% \qquad [2.9]$$

where $V_{l,s}$ is referred as soil volume loss. When tunnelling in cohesive soil, for example in London Clay, ground movement always occur under undrained conditions, where $V_{l,s} = V_{l,t}$, which means the maximum value of surface settlement can be directly deduced according to tunnel volume loss using the modified/original Gaussian curve. When tunnelling in sands, the ground behaves in a drained manner, for example in dense sand $V_{l,s}$ is always less than $V_{l,t}$, so the surface settlement trough is not directly related to $V_{l,t}$. Dindarloo and Siami-Irdemoosa (2015) analysed 7 variables associated with surface settlement including z_0, D, $V_{l,t}$, ground water level, soil property, tunnelling method and $V_{l,s}/V_{l,t}$ (normalised volume loss). Through a

correlation matrix, the variable $V_{l,s}/V_{l,t}$ gives the highest correlation with the surface settlement. The main reason causing the difference between $V_{l,s}$ and$V_{l,t}$ is the soil dilation in dense sands and contraction in relative loose sands during shearing (Rowe, 1962; Cording and Hansmire, 1975; Zhao, 2008).

2.2.1.5 Subsurface settlement troughs

Above discussion is about surface settlement and associated factors. The ground movements beneath the surface become important as well when existing underground structures are involved in the constructions of new tunnels. In addition, subsurface settlements can be seen as the direct causes of surface settlements, hence it is also important to understand how subsurface settlements developed and how they related to surface settlements.

In contrast to surface settlement data, few field subsurface ground movement data are available. It is often assumed that the subsurface settlement trough can also be described by the Gaussian curve (Mair et al. 1993) if z_0 is replaced by z_0-z in Equation[2.2], hence the subsurface trough width, by following Equation[2.6], is expressed as:

$$i = K \cdot (z_0 - z) \qquad [2.10]$$

where z is any soil depth. Mair et al. (1993) analysed several site data from tunnelling projects in the UK and series of centrifuge tests in soft clays, and concluded the empirical expression of K in clay:

$$K = \frac{0.175 + 0.325(1 - z/z_0)}{1 - z/z_0} \qquad [2.11]$$

The limitation of using Equation [2.10] and [2.11] is that as z/z_0 approaching unity, in other words, when the depth of interest is close to the tunnelling region, the trough width is overestimated (Grant & Taylor 2000), because dependency of the tunnel size is neglected. In order to introduce some degree of dependency of trough width i on tunnel size, by taking the tunnel diameter into consideration, following Equation [2.7], Moh et al. (1996) suggested:

$$i = \left(\frac{D}{2}\right)\left(\frac{z_0}{D}\right)^{0.8}\left(\frac{z_0 - z}{z_0}\right)^m \qquad [2.12]$$

where *m* is the "subsurface width parameter". It should be noticed that the values of *m* is dependent on the property of the ground and is not affected by the *i* values. *m* is suggested by the author to be taken as 0.4 for tunnels in silty sands and 0.8 for tunnels driven in silty clays. Figure 2.6 shows the relationships of Equation 2.11 and 2.12 (with m = 0.4 and 0.8 respectively).

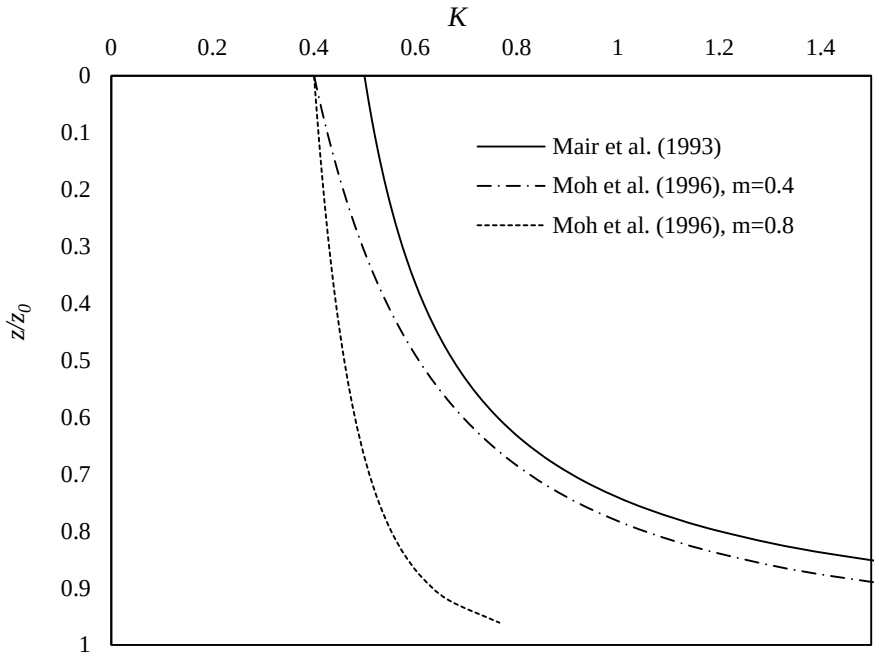

Figure 2.6 Variation of trough width parameter K with depth

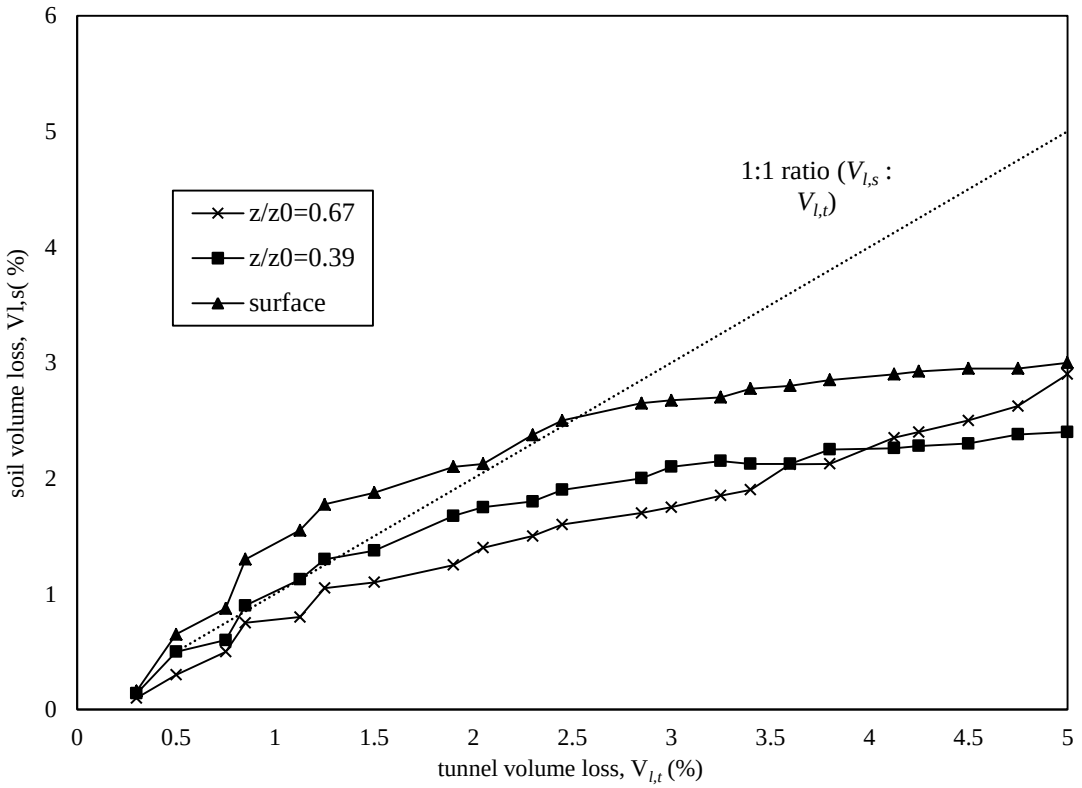

Figure 2.7 Soil volume loss versus tunnel volumes loss in sand

Unlike tunnelling in clay, where the volumetric change of the ground at depths always stay constant with the volumetric change of ground at the tunnel level, when tunnelling in sand, the ratio of $V_{l,s}/V_{l,t}$ varies with depth. This phenomenon has been proved by some centrifuge models of tunnelling in sandy ground (Jacobsz, 2002; Vorster et al., 2005; Marshall et al., 2012). Figure 2.7 plots the subsurface $V_{l,s}/V_{l,t}$ data (Marshall 2009) of a centrifuge tunnel model in sand, it can be seen that the values of $V_{l,s}/V_{l,t}$ are far away from the 1:1 line at different depths, which means the soil volume loss is not consistent with the tunnel volume loss at different depths. The scatter between the soil volume loss and the tunnel volumes loss is, of course, a result of soil volumetric strain development from the tunnelling level to the surface. The slope of tangent of the $V_{l,s}/V_{l,t}$ curve larger than one illustrates the soil is contracting while slope of tangent smaller than one means the ground is dilating. The $V_{l,s}/V_{l,t}$ ratios at different depths show a general decreasing trend as tunnel volume loss increasing. However, the data of z/z_0 at higher tunnel volume loss values deserve special notices. The ground here starts dilating as the slope becomes larger than one after the tunnel volumes loss reaches around 4.5%. Therefore the ground at depth of $z/z_0 = 0.67$ experiences contraction followed by dilation. The transfer from contraction to dilation of sand has been observed by

Zhao (2008) who concluded that for sand under confining pressure of around 200 kPa (the ground at $z/z_0 = 0.67$ in Marshall's test is under confining pressure of 144kPa), the sample shows a contraction tendency when shear strain is less than 0.3%, a dilation tendency when the shear strain is larger than 0.3%. Therefore, the ground from the surface to the tunnel level is experiencing complicated volumetric changes during tunnelling. As discussed in section 2.2.1.4, the maximum surface settlement is affected by the ratio of $V_{l,s}/V_{l,t}$, as the ratio of $V_{l,s}/V_{l,t}$ varies with depth in sand, it is not hard to conclude that the subsurface maximum settlement value varies with depth due to soil dilation and contraction. What's more, Jacobsz (2002) and Vorster et al. (2005) also state that there is a general decreasing trend of the width parameter K with soil volume loss which means Equation 2.11 cannot be simply directly apply for tunnelling in sand issue as the ratio of $V_{l,s}/V_{l,t}$ is now a factor that need to be considered.

2.2.1.6 Horizontal movements

Damage of buildings and underground structures can not only arise from vertical ground movement, but also from horizontal movements. However the horizontal movements are not measured as frequently as vertical ground movements (Mair & Taylor 1997). By assuming the ground movement vectors around the tunnel are pointed to the centre point of the tunnel profile, O'Reilly and New (1982) and Attewell (1978) proposed the relationship between the horizontal movements and vertical movements caused by tunnelling in cohesive soils as (at surface):

$$S_h = \frac{x}{z_0} S_v \qquad [2.13]$$

Therefore, according to the Gaussian distribution of Equation[2.2], the distribution of the surface (z=0) and subsurface horizontal movements can be simply expressed as:

$$S_{\mathrm{h},x} = \frac{x}{z_0 - z} S_{\max} \exp\left(-x^2/2i^2\right) \qquad [2.14]$$

where$S_{h,x}$is the horizontal movement of ground at the depth of z with a horizontal distance of x from the tunnel central line. According to Equation [2.13] and [2.14], as shown in Figure 2.8, the maximum horizontal movement at a certain depth is located at the point of inflection of

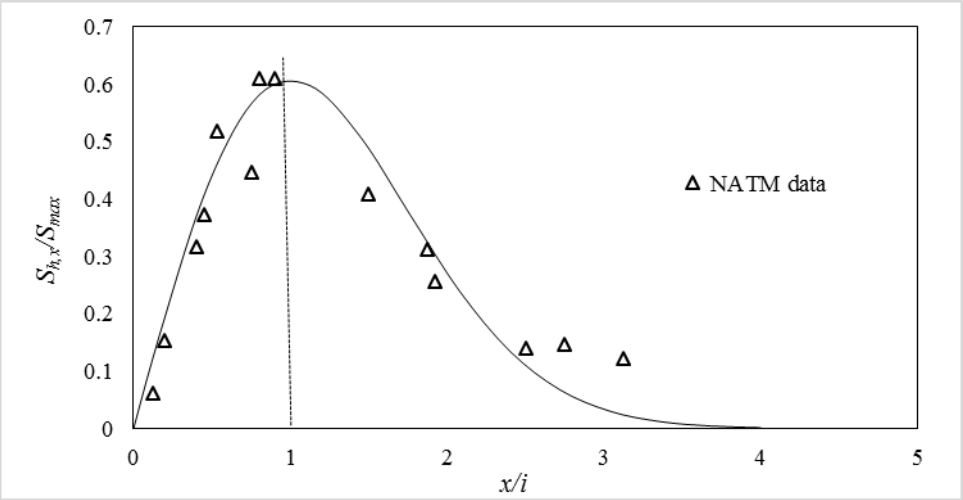

Figure 2.8 Surface horizontal movement

the transverse trough where $x = i$. At surface, the maximum horizontal movement is around $0.61KS_{max}$. The horizontal displacement becomes negligible when it is 4 times of inflection point away from the tunnel central line. When Equation [2.13] and [2.14] apply, the trough width parameter K is assumed to be constant with depth. The method above is known as *the point sink radial-flow* method. The displacement flow is pointed towards a "sink" which is located at the central point of the tunnel. When considering the variation of K following Equation [2.11], as shown in Figure 2.6, the "sink" should be located at a point below the tunnel axis level (Taylor 1995) where $z = (1+0.175/0.325)z_0$. This will give horizontal movements 35% less than those calculated by Equation[2.14]. By studying the field data form the Heathrow trail tunnel, New and Bowers (1994) concluded that the point sink method considering variation of K gives good agreement with the field data. Grant and Taylor (2000) also successfully validated the method provided by Taylor (1995) by means of centrifuge modelling in clay.

However the volumetric strain is assumed to be zero throughout the ground in all cases above, as soil volumes loss V_s is constant and is not changing with depth. This is only a condition for undrained soil such as clay. For tunnelling in sand, the surface horizontal movements are observed to be much larger than those induced by tunnelling in clay (Mair & Taylor 1997). Even by assuming the ground movements are directed towards the tunnel axis (the method predicting more horizontal movement), the horizontal movements at surface are still underestimated near the edge of the settlement trough (around $x/i = 4$) (Cording 1991). Similar conclusions have been found by Cording and Hansmire (1975) who stated that the horizontal movements around the edge of the settlement trough exceed the vertical ground

displacements. This phenomenon can be seen in Figure 2.8, where the data from a 10m diameter NATM (New Austrian Tunnelling Method) tunnel in sandy ground is presented (Hong & Bae 1995). From around *x/i*=2.5, the field data is been significantly underestimated by Equation [2.14].

2.2.2 Longitudinal troughs

Studying transverse settlement troughs is actually simplifying the tunnelling process as a two dimensional problem, as the length of the tunnel is much larger than its diameter, it is reasonable to make such an assumption when studying the cross section ground movement profile behind the excavation face where the ground is relative steady after large deformations. In urban area, there may be existing structures directly above the tunnel central line, in which case more damage can be induced by the progressive longitudinal settlement trough ahead of the advancing face than those caused by the transverse settlement trough. By reviewing numbers of tunnelling in clay cases, Attewell and Woodman (1982) stated that the longitudinal trough can be reasonably described a cumulative probability curve in the following form:

$$S_{v,y} = S_{\max} \frac{1}{i_y \sqrt{2\pi}} \int_{-\infty}^{y} e^{-t^2 / \left(2 i_y^2\right)} dt \qquad [2.15]$$

where, $S_{v,y}$ is the vertical ground movement on the longitudinal settlement trough, S_{max} is the maximum vetical settlement on the curve, y is the horizontal distance to the steady ground, i_y is the trough width parameter of the longitudinal settlement curve, and is the only parameter that controls the shape of the longitudinal curve. Nyren (1998) concluded that the width of the longitudinal settlement i_y can be related to the width of the transverse settlement i by $i_y = i_x/1.3$. It is not difficult to imagine that the value of S_{max} in Equation [2.2] and [2.15] is consistent, as S_{max} in each curve is always the steady value of the settlement above the tunnel axis.

After the shape of the longitudinal curve is difined, it is necessary to locate the position of the curve. For open-face tunnelling, Attewell et al. (1986) found that above the advancing face, the vertical settlement should be around 50% of the value of S_{max} as shown in Figure 2.9. For pressurised face shield tunnelling, the settlement ahead of the tunnelling face is significantly controlled, most of the settlement is induced by the tail void (component 2 in section 2.2), and very less ground relaxation towards the excavation face occurs (component 1) (Moh et al.

1996), therefore, for the shield tunnelling projects using EPB or slurry TBMs, the surface settlement directly above the advancing face is much less than 50% of S_{max} (Mair & Taylor 1997). This phenomenon has been proved by some shield tunnelling cases, including the project in Japan (Nomoto et al. 1995) using EPB and slurry machines in sands and the tunnel in Cairo (Ata A. 1996) using slurry shield in medium to dense sand overlain by clay. It is found that the vertical settlement directly above the advancing face is within the range of 25%~35% of S_{max}. It can be concluded that the shape of the longitudinal settlement trough in soft ground can be reasonably described by the cumulative probability curve. The vertical settlement value directly above the excavation face should be regarded as the parameters controlling the position of the longitudinal curve. The factor that significantly affect the position of the curve is the method of excavation (with or without face supporting).

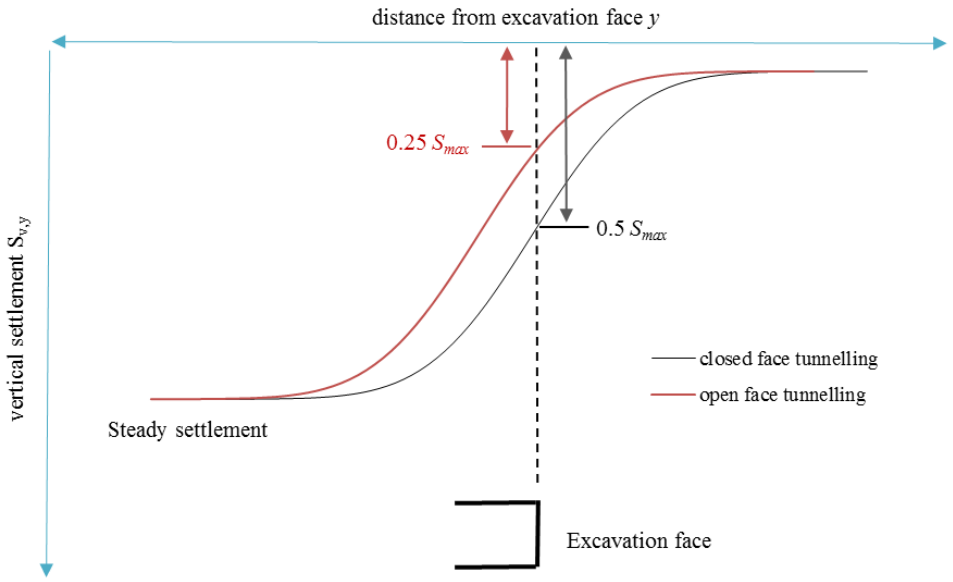

Figure 2.9 Longitudinal settlement curve

2.3 Prediction of ground deformations

Predicting methods for ground movement induced by tunnelling can be summarised as empirical methods, analytical methods and numerical modelling. Numerical modelling is strictly relevant to this research thus is presented in later sections.

2.3.1 Empirical methods

The empirical methods are concluded from site data and test data, thus should be treated as the reflection of reality. Therefore, these methods can give reasonable prediction results of ground movements. The most widely used empirical methods are based on the Gaussian curve as described by Equation [2.2](Peck 1969), and the cumulative probability curve as defined by Equation [2.15](Attewell & Woodman 1982). As discussed in section 2.2.1, later modifications of the Gaussian distribution are mainly focused on the trough width i (or the width parameter K) (Clough and Schmidt, 1981; O'Reilly and New, 1982; Cording, 1991; Mair et al., 1993; Moh et al., 1996) and the surface and subsurface trough in sandy ground considering volumetric strains (Jacobsz, 2002; Vorster et al., 2005; Marshall et al., 2012). The settlement value at the inflection point i is always 60% of the maximum settlement value according to Equation [2.2] which is not the case in reality. Celestino and Ruiz (1998) and Celestino et al., (2000) introduced the yield-density curve, which has three curve parameters, thus is more flexible than the Gaussian curve and is able to give better prediction of the vertical settlement value at the inflection point.

For each empirical method, the trough width and the magnitude of the settlement $V_{l,s}$ have to be assumed based on the past experience and site/lab data. When predicting the settlement using the empirical curves, the following limitations can be encountered (Mair & Taylor 1997):

- The empirical methods are generally only applicable to a single tunnel or multiple tunnels that have a certain distance in between so that the interaction can be ignored.
- Only short term ground deformations are considered, as the long term post construction ground movements are less amenable to empirical methods.
- The empirical curves are only describing the Greenfield conditions. Nearby surface and subsurface structures or any material of significant stiffness are not taken into account.

2.3.2 Analytical methods

Despite from the empirical methods based on experience and data, there are also a variety of solutions that have been produced for solving tunnelling problem theoretically. These methods make simplifying assumptions regarding the basic constitutive soil behaviour, thus provide more consistent and comprehensive interpretation of vertical and horizontal ground

movements than the empirical methods. In principle, the analytical methods need a small number of input parameters that can be easily obtained and calibrated according to site/lab data. They also provide an alternative reference for assessing the accuracy of numerical simulation apart from the empirical methods.

The theoretical prediction for ground movements induced by tunnelling can be traced back to Kirsch (1898), who produces a 2-D cross-section analytical solution for deep tunnelling in undrained soil by assuming the soil is isotropic and linear elastic. The deformations of the tunnel can be separated into two components - the uniform convergence ε induced by the volumetric total stress p_0 and the ovalization δ induced by the deviatoric total stress q_0. The horizontal and vertical deformations of the surrounding soil u_x and u_z can be calculated as follows:

$$\text{Convergence}\begin{cases} u_x(x,z) = \varepsilon \cdot \dfrac{x \cdot R}{x^2 + z^2} \\ u_z(x,z) = \varepsilon \cdot \dfrac{z \cdot R}{x^2 + z^2} \end{cases} \qquad [2.16]$$

$$\textit{Ovalization}\begin{cases} u_x(x,z) = \delta \cdot \dfrac{R}{3-4v} \cdot x \cdot \dfrac{(3-4v)\left(x^2+z^2\right)^2 - \left(3z^2 - x^2\right)\left(x^2+z^2-R^2\right)}{\left(x^2+z^2\right)^3} \\ u_z(x,z) = \delta \cdot \dfrac{R}{3-4v} \cdot z \cdot \dfrac{(3-4v)\left(x^2+z^2\right)^2 - \left(3x^2 - z^2\right)\left(x^2+z^2-R^2\right)}{\left(x^2+z^2\right)^3} \end{cases}$$

where R is the tunnel radius and v is the elastic Poisson's ratio. By tracking the movement of the tunnel cavity wall, ε and δ are considered as input parameters in Equation [2.16]. It is also useful to introduce the solution when the movement information of the cavity wall is unknown which is the real case most of the time. The maximum elastic deformations of the cavity wall are:

$$\begin{aligned} \varepsilon &= \frac{(p_0 - p_i) \cdot R}{2G} \\ \delta &= -\frac{q_0 \cdot R}{2G} \cdot (3-4v) \end{aligned} \qquad [2.17]$$

where G is the elastic shear modulus of the surrounding soil. p_i is the interior supporting pressure (e.g., pressure from grouting or compression from the tunnel lining). When considering tunnelling with no immediate supporting like the NATM method, p_i can then be

taken as zero in Equation [2.17]. The in situ total volumetric stress p_0 and deviatoric stress q_0 can be deduced from:

$$p_0 = \sigma_v' \cdot \frac{(1+K_0)}{2} + p_w$$
$$q_0 = \sigma_v' \cdot \frac{(1-K_0)}{2} \qquad [2.18]$$

where σ_v' stands for the initial vertical effective stress (compression positive), p_w is the pore pressure and K_0 the coefficient of earth pressure at rest. Although this method is an idealised case that corresponds to isotropy and linear elasticity, it provides a benchmark for predicting the ground movement using simple parameters σ_v', p_w, G, K_0, v and p_i which can be easily obtained from the site or simple conventional laboratory tests. However this stress-strain method is unable to predict the surface ground movement as the stresses at the surface can only be zero. For analysing shallow tunnel problems, two kinds of methods have been proposed. The first one can be called the approximate solution which only considers the effect induced by the excavation by ignoring the geometry of the actual tunnel. The second one is the 'exact' solution that considering both the effects and the geometry of the excavation.

Sagaseta (1987) produced an approximate approach for shallow tunnelling in undrained soil assuming linear elasticity. As shown in Figure 2.10, the volume change of the ground is simplified as a point sink located at the tunnel centreline. The radius of the point sink is defined as a, therefore the area of the sink πa^2 represents the tunnel volume loss $V_{l,t}$. The effect of the surface is neglected and the sink is assumed to be in an infinite isotropic elastic medium, this means the sink will produce strains on the surface level (step 1). The strains will then produce stresses on the surface which violate the stress-free requirement of the surface. The stresses on the surface can be eliminated by step 2 (one of the following two methods) and step 3:

i. Introduce a virtual source of soil which is a mirror image of the point sink with respect to the neglected surface (step 2a). The normal stresses σ_{z0} (from the sink) and σ_z (from the image soil) cancel each other out. The shear stress on the surface are doubled.
ii. As in method 1 but consider a new source of sink. This will produce doubled normal stress on the surface. The shear stresses τ_0 (form the original sink) and τ' (from the image virtual sink) cancel each other out.

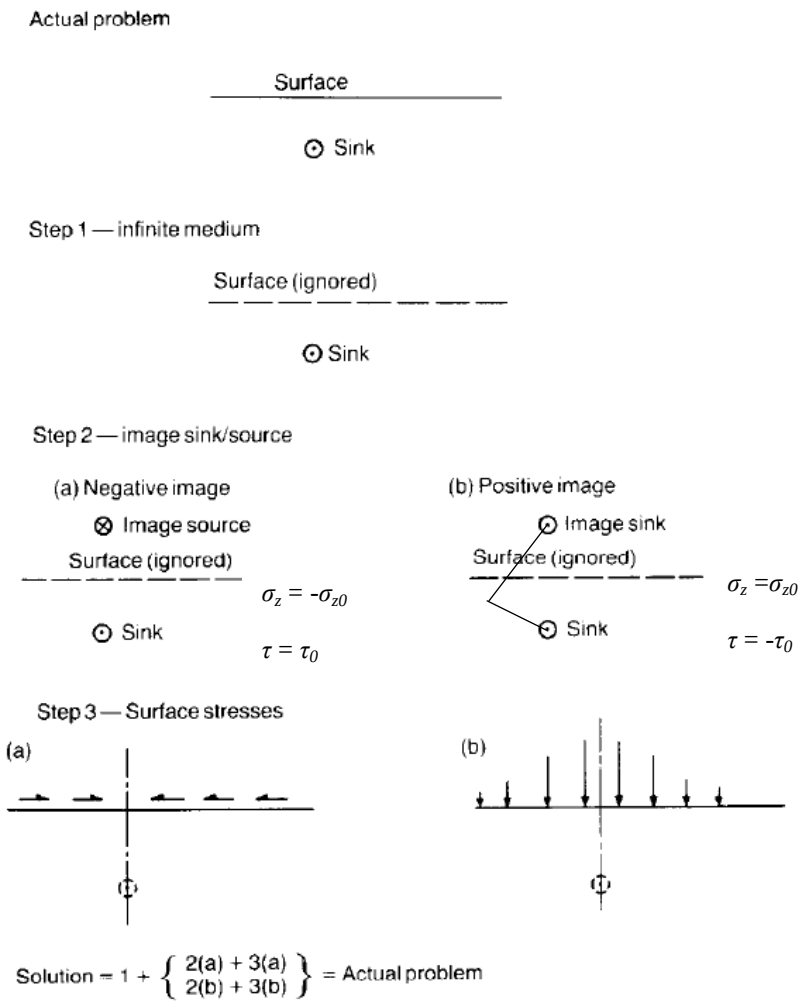

Figure 2.10 Three steps of the approximate solution (Sagaseta 1987).

Strep 3 is to remove the remaining shear or normal stresses from step 2. For method i, the vertical displacements induced by the point sink and the virtual soil are first calculated. As discussed above, the shear stresses on the surface level are doubled which violates with the free surface requirement. By introducing a system of forces acting on the surface equal and opposite to the doubled shear stresses in step 2, the shear stresses on the surface are removed. The horizontal movement can be obtained by integrating the horizontal forces on an elastic half space, referred as Cerruti's problem. In this situation the surface experience no vertical stress but is constrained in the horizontal direction. This is close to the reality where the ground surface is covered by flexible but inextensible membrane like pavement. Method i is a better choice compared to method ii, because the situation in method ii is far from reality as the surface is totally constrained in the vertical direction and is free to move horizontally.

The final ground movement is then given by considering the vertical displacements induced by the point sink and the virtual soil, and the horizontal displacements obtained from integrating the horizontal loads. The ground movement in the 2-D x-z plane is presented as:

$$u_x = -\frac{a^2}{2}\left(\frac{x}{r_1^2}-\frac{x}{r_2^2}\right)-a^2\frac{x}{r_2^2}\left[1-2\frac{z(z+h)}{r_2^2}\right]$$
$$u_z = -\frac{a^2}{2}\left[\frac{z-h}{r_1^2}-\frac{z+h}{r_2^2}\right]+a^2\frac{z}{r_2^2}\left(1-2\frac{x^2}{r_2^2}\right) \qquad [2.19]$$

where

$$r_1 = \left[x^2+(z-h)^2\right]^{1/2}$$
$$r_2 = \left[x^2+(z+h)^2\right]^{1/2}$$

r_1 and r_2 are the distances from the point of interest (x,z) to the point sink and the virtual point respectively. It should be noticed that in this solution, the material is assumed to be incompressible (the Poisson's ratio is 0.5), the vertical load produces no horizontal displacement (described as the inextensible paved surface) and the applied horizontal load produce no vertical displacement (the Cerruti's problem).

Verruijt & Booker (1996) extended the previous work by considering the ground as a compressible material so that Poisson's ratio can be varied. The effect of ovalization (Wood 1975) is also taken into consideration. According to the process in Figure 2.10 but not completely following Sagaseta (1987), the method used in step 2 is to add an image sink above the surface instead of an image of soil. The normal stresses on the surface are then doubled. These normal stresses need to be removed in order to satisfy the surface-free condition, therefore a system of normal stresses equal and opposite to the doubled normal stresses need to be added. After step 1 and 2, the displacements due to the virtual sink and the point sink can be derived as:

$$u_x = -\varepsilon R^2\left(\frac{x}{r_1^2}+\frac{x}{r_2^2}\right)+\delta R^2\left[\frac{x\left(x^2-kz_1^2\right)}{r_1^4}+\frac{x\left(x^2-kz_2^2\right)}{r_2^4}\right] \qquad (1)$$
$$u_z = -\varepsilon R^2\left(\frac{z_1}{r_1^2}+\frac{z_2}{r_2^2}\right)+\delta R^2\left[\frac{z_1\left(kx^2-z_1^2\right)}{r_1^4}+\frac{x\left(kx^2-z_2^2\right)}{r_2^4}\right] \qquad (2) \qquad [2.20]$$

where R is the radius of the tunnel, ε is the amount of the uniform convergence of the tunnel (radius of the uniform displacement ring in Figure 2.2) and δ is the amount of distortion as illustrated in Figure 2.2. According to Figure 2.10, $z_1 = z - h$, $z_2 = z + h$, r_1 and r_2 is as in Equation [2.19]. The vertical normal stresses σ_z at the surface level is doubled in this solution and the shear stresses are removed. Following the Fourier transforms proposed by Sneddon (1951) and to meet the boundary condition of: when z = 0, the normal stresses and the shear stresses are zero, the displacements induced by step 3 can be written as:

$$\begin{aligned} u_x &= \int_0^\infty C(1-maz)\exp(-az)\sin(ax)\,da \\ u_z &= -\int_0^\infty C(1+m+maz)\exp(-az)\cos(ax)\,da \end{aligned} \qquad [2.21]$$

where m is a variable related to the Poisson's ratio by m = 1/(1-2v), C is defined as:

$$C = -\frac{1}{m\pi G}\frac{1}{a}\int_0^\infty \sigma_z(x)\cos(ax)\,dx \qquad [2.22]$$

where G is the shear modulus of the material and the normal stress distribution $\sigma_z(x)$ at surface, which according to Verruijt and Booker (1996), is:

$$\sigma_z(x) = -4G\varepsilon R^2\frac{x^2-h^2}{\left(x^2+h^2\right)^2} - \frac{8Gm\delta R^2}{m+1}\frac{h^2\left(3x^2-h^2\right)}{\left(x^2+h^2\right)^3} \qquad [2.23]$$

Substitution of Equation [2.23] into [2.21], using the integrals of Erdélyi & Bateman (1954), the displacements induced by step 3 can be derived as:

$$\begin{aligned} u_x &= -\frac{2\varepsilon R2x}{m}\left(\frac{1}{r_2^2}-\frac{2mzz_2}{r_2^4}\right) - \frac{4\delta R^2 xh}{m+1}\left(\frac{z_2}{r_2^4}+\frac{mz\left(x2-3z_2^2\right)}{r_2^6}\right) \\ u_z &= \frac{2\varepsilon R^2}{m}\left[\frac{(m+1)z_2}{r_2^2}-\frac{mz\left(x^2-z_2^2\right)}{r_2^4}\right] - 2\delta R^2 h\left[\frac{x^2-z_2^2}{r_2^4}+\frac{m}{m+1}\frac{2zz_2\left(3x^2-z_2^2\right)}{r_2^6}\right] \end{aligned} \qquad [2.24]$$

After the 3 steps of analysis, the final displacements induced by tunnelling can be calculated by the sum of Equation [2.20] and [2.24]. However, this solution is found to overestimate the horizontal ground movement (Loganathan & Poulos 1998), thus the settlement troughs are wider than measured results, in addition, the maximum vertical settlements are underestimated. The reasons for the inaccuracy are 1) the real soil behaviour consists not only linear elasticity but also nonlinear behaviour sometimes plasticity; and 2) in reality the

majority of the ground movements around the tunnel occur at the tunnel crown, especially in TBM tunnels, while the ground movement next to the tunnel is assumed to be uniformly deployed around the tunnel in Sagaseta (1987) and Verruijt & Booker (1996)'s method.

In order to capture the real ground deformation character at the tunnel-soil interface, based on the solution of Verruijt & Booker (1996), Loganathan & Poulos (1998) proposed an analytical approach using the concept of 'gap parameter' introduced by Lo and Rowe (1982) and Rowe & Kack (1983). The gap parameter is defined as the addition of the two dimensional space formed around the tunnel, over cut by the TBM around the tunnel periphery and the physical gaps related to the tunnelling machine, shield and the tunnel lining geometry. Lee et al. (1992) theoretically developed an estimation of the gap parameter g based on the known TBM conditions and the soil parameters:

$$g = G_p + U_{3D} + w \qquad [2.25]$$

where G_p is the physical gap including the space between outer surface of the shield and the tunnel lining, and the thickness of the TBM tail element; U_{3D} is the elasto-plastic deformation from the excavation face; and w is a parameter that related to the quality of workmanship. In this method, only the short term uniform convergence of the tunnel wall ε is considered, the long term distortion of the tunnel wall is ignored. Following Equation [2.20] and [2.24], taking the gap parameter g into consideration, the total ground displacements are derived as:

$$\begin{aligned} u_x &= -R^2 x\left[\frac{1}{x^2+(z_0-z)^2}+\frac{3-4\nu}{x^2+(z_0+z)^2}-\frac{4z(z+z_0)}{x^2+(z_0+z)^2}\right] \\ &\quad \cdot\frac{4gR+g^2}{4R^2}\exp\left\{-\left[\frac{1.38x^2}{(z_0+R)^2}+\frac{0.69z^2}{{z_0}^2}\right]\right\} \\ u_z &= R^2\left\{-\frac{z-z_0}{x^2+(z-z_0)^2}+(3-4\nu)\frac{z+z_0}{x^2+(z+z_0)^2}-\frac{2z\left[x^2-(z+z_0)^2\right]}{\left[x^2+(z+z_0)^2\right]^2}\right\} \\ &\quad \cdot\frac{4Rg+g^2}{4R^2}\exp\left\{-\left[\frac{1.38x^2}{(z_0+R)^2}+\frac{0.69z^2}{{z_0}^2}\right]\right\} \end{aligned} \qquad [2.26]$$

where R is radius of the tunnel; z_0 is the vertical distance from the surface to the tunnel axis; and g is the gap parameter. This 2-D method indirectly considered the 3-D effect from the excavation face by using the parameter U_{3D}, and is proven to be generally useful in predicting vertical and horizontal ground movements by some tunnelling cases in clay such as the

Heathrow Express tunnel in London, the Thunder Bay tunnel in Ontario and the Green Park tunnel in London. However the predicted displacements show relatively poor agreements with the measured data when sandy ground is involved (Loganathan & Poulos 1998).

The above three solutions are ‘approximate’ approaches which not considering the infinite geometry of the tunnel. There is another category of solutions called the ‘exact’ solutions (Verruijt 1996; Verruijt 1997; Pinto 1999) that is able to describe the behaviour of the tunnel boundaries and assume the displacements vanish at infinity (Pinto 1999). These methods adopt complicated formulations of planar elasticity and is not directly related to this research, thus will not be further discussed.

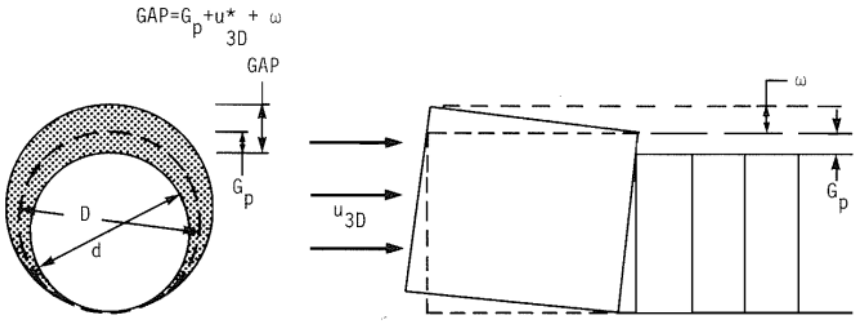

Figure 2.11 The gap parameter g (Lee et al. 1992)

2.4 Ground loading on the tunnel lining

Tunnels are often driven into soft ground which is not self-supporting. The function of the tunnel lining is to take the load from the surrounding ground that is required to reach a new equilibrium condition after excavation of the existing soil. In some rock tunnels, the tunnel lining may be employed for the purpose of water resistance. The knowledge of the ground loading is useful in estimating the deformation mechanism of the tunnel, as the deformation of the tunnel lining is directly related to the ground loading conditions on the tunnel periphery.

2.4.1 Lining in clay

According to the measurement of load in a cast iron tunnel lining driven in free air, Grove (1943) found that the load in the lining gradually reached the full overburden load within 14 days after the excavation. Peck (1969) reported that the short-term loading experienced by the lining, in some soft ground cases in clay, was inversely proportional to the displacements of the surrounding soil that have occurred prior to the installation of the tunnel lining. The loading in the lining built up rapidly after the excavation and gradually reach the full overburden within a few weeks to a year. Later measurement made by Barratt et al. (1994) in a 4m diameter 20m deep tunnel lined with expanded segmental lining in London Clay

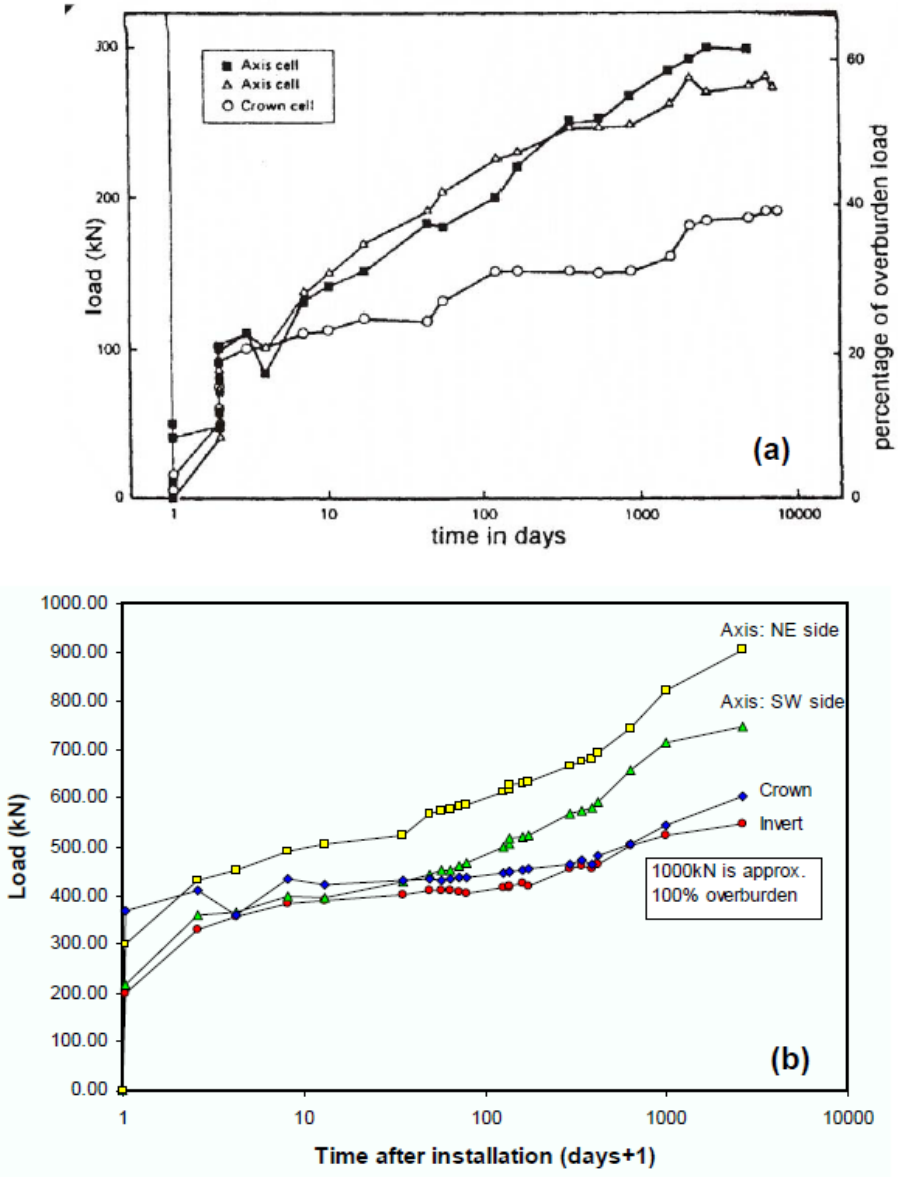

Figure 2.12 Load on the lining after lining installation. a). Beneath Regent's Park (Barratt et al. 1994); b). Beneath St James's Park (Dimmock 2003)

illustrates that the vertical load in the lining shortly after the excavation equivalent to 30% of the full overburden pressure, and then gradually builds up to 60% of the full overburden pressure where the load in the lining appear to stabilised. The measurement from Bowers and Redgers (1996) confirms Peck's point that the load in the lining is not subject to the original in situ ground conditions when the lining is installed into place. The ground displacements that occur prior to the installation of the lining have a major influence in reduction of the stabilised ground loading to certain values that are lower than the original in situ stresses.

As shown in Figure 2.12, the vertical load measured at the crown or invert of the tunnel is 70% of the horizontal load measured at axis levels. The larger vertical load on the lining compared to the horizontal load is often accompanied with squatting of the tunnel lining (Ward et al. 1965; Nyren 1998). The phenomenon of greater horizontal load values also applies in highly consolidated clay either in the short-term or long-term, where the horizontal to vertical stress ratio K_0 also considered as greater than 1 (Mair 1994).

It has been proven by Negro et al. (1996) that the short term lining loads are inversely related to the delay of the lining installation. Measurement data from some tunnel cases in Sao Paulo, Brazil clearly illustrate a trend of decreasing in lining loads with increasing of distance between the excavation face and the latest closed ring (where the lining is cast into place and the sprayed concrete invert is closed).

2.4.2 Lining in sands.

The situation in drained soil is a different picture, the lining loads in sandy ground and gravels are found to be relatively low compared to the tunnels in cohesive soil like London Clay (Peck 1969). From the work published by Ward and Pender (1982), the conclusion can be drawn that the measured loadings in dense sands and gravelly soils are much lower than in clays and silts. In deeper tunnels in sandy ground, the effective stresses on the tunnel lining are very low, the majority of the vertical pressure come from the pore pressure under the water table (Ohta et al. 1995). For long term loading, in sandy soil, as the excavation and installation of the lining is carried out in drained conditions thus little or no increase of the long term ground loading will happen (Peck 1969).

2.5 Critical state of sand

It is clear that the ground movements and stress developments induced by tunnelling in sand differs a lot from the ground response induced by tunnelling in clay. The source cause these differences are the unique stress – strain characters of sand, or in other words, the constitutive behaviour of sand. The constitutive modelling of cohesive soils has achieved certain success in past decades, however the modelling of sand behaviour remain great challenging due to its unique volumetric behaviour during stress changes (Dafalias and Herrmann 1982;Ling and Yang 2006; Li 2013). Nowadays, one of the most widely used type of constitutive sand models are the critical state based models, due to less number of input model parameters and simplicity of the theory.

2.5.1 The definition of critical state

Before the establishment of the critical state soil mechanics, Casagrande (1936) has conducted series of drained direct shear tests on sand and found that loose sand tend to decrease its volume while dense sand expand during shearing. In addition, it was found that regardless of the initial density of the sandy soil, all soil samples tended to reach same shear strength (under same confining stress) and a common void ratio. This ultimate void ratio was called the critical void ratio. Based on Casagrande's idea, Roscoe et al. (1958) defined the critical state of soil as "the state at which the soil continuous to deform at constant stress and constant void ratio". From these early studies on sand behaviour, it is clear that, after experienced large amount of shear strain, sand samples will finally reach a steady state in terms of void ratio and shear stress.

This steady state of sand was further studied by Castro（1969), who systematically achieved series of points of the steady state of sand in the void ratio – mean effective stress space (*v-p'* space), and concluded these locus as the critical state of sand. With more research work been carried out on studying the constitutive behaviour of sand, it becomes clear that the steady states of sand in laboratory tests tend to form a unique locus in *v-p'* space (in this thesis all stresses refer to effective stress as only drained condition is applied for numerical modelling of sand behaviour), in other words, for one type of sand, the critical state in *v-p'* space is unique regardless of the initial state of the sample and the experiment type.

A lot of discussion and laboratory work on studying the uniqueness of the critical state of sand has been published in recent decades. It is now commonly agreed that, for one type of

sand, the critical state (or the ultimate steady state) is unique, and the locus of the critical state can be directly related to stress *p'* and void ratio *e* or the specific volume *v* (1+*e*) (Poulos 1981;Alarcon-Guzman et al. 1988;Negussey and Islam 1994;Chu 1995). The concept of critical state is summarised by Wood (1990) as

"*A unique locus exists in q, p', e space such that soil can be deformed without limit at constant stress and constant void ratio; this locus is called the critical state locus (CSL).*"

In the above definition of critical state, the mean stress *p'* is described as a constant to avoid complicating the definition. However it should be noted that on the CSL, the critical void ratio does change with the mean stress *p'*. The locus of the critical state is usually simplified as a straight line in *v-p'* space as shown in Figure 2.13, where *e* is the void ratio of soil; e_c is the critical void ratio; Γ is the critical void ratio when *p'*=1kPa; λ is the slope of CSL; κ is the slope of elastic unloading reloading lines.

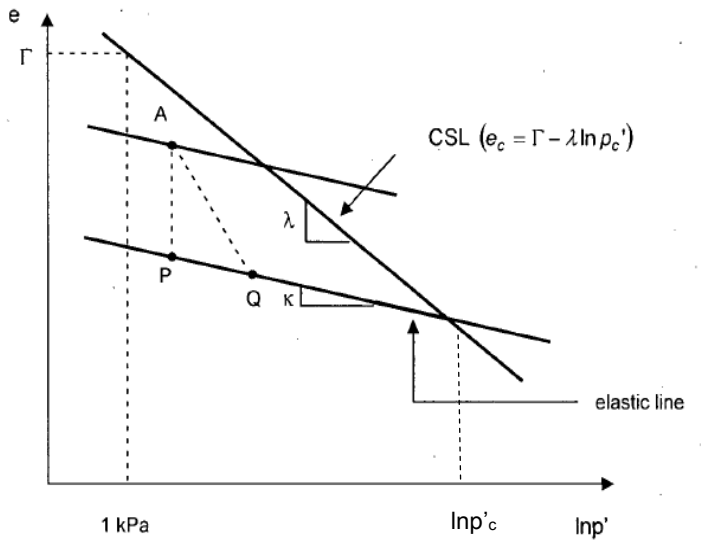

Figure 2.13 The critical state locus of soil (Bolton 1979).

2.5.2 Critical state models

The critical state soil mechanism has now been developed as a mutual theory (Wood 1990) and been successfully applied in different geotechnical aspects (Atkinson 1993) including constitutive modelling of sand (Been and Jefferies 1985,Manzari and Dafalias 1997,Li et al.

1999,Yu 1998 and Yao et al. 2004, among others). Although a large number of constitutive soil models and sand models have been developed based on the critical state soil mechanics framework, these models share common fundamental structures:

- Elastic properties
- A yield surface (sometimes multi yield surfaces) act as the boundary between elasticity and plasticity.
- Hardening rules determining the size of the yield surface according to strains
- Flow rules which determine the directions of the plastic strain increment vectors

2.5.2.1 Cam Clay

Thefirst widely used constitutive soil model developed based on the critical state soil mechanics is the Cambridge Clay model (Roscoe et al. 1963) (or Cam Clay for short), this model has been widely applied in modelling cohesive soil like London Clay. However it has been rarely used for modelling sand, in addition, it has been proven that the numerical results predicted by Cam Clay cannot be considered as valid for sandy soil (Nova & Wood 1979). Although Cam Clay si not suitable to be directly applied in modelling sand, many lately developed critical state sand models (Been and Jefferies 1985,Li et al. 1999 and Yao et al. 2008) are based on Cam Clay, thus it is useful to briefly understand the fundamental idea and the development of Cam Clay formulation.

The basic idea of Cam Clay is the work dissipation during shearing, which can be related to mean effective stress *p'* and deviatoric stress *q*:

$$p'\dot{\varepsilon}_p^p + q\dot{\varepsilon}_q^p = \dot{W} \qquad [2.27]$$

where $\dot{W}$ is the work increment done by stresses, $\dot{\varepsilon}_p$ and $\dot{\varepsilon}_q$ are the volumetric and deviatoric strain increments respectively. The superscript *p* stands for plasticity. In Equation [2.27] an assumption is made that the dissipated work is plastic part of work, all the elastic part of work is stored as strain energy. To make the above plastic work dissipation increment $\dot{W}$ dimensionless, the plastic dilation rate D^p (rate of volumetric strain increment over deviatoric strain increment) and the stress ratio η are introduced:

$$D^p = \dot{\varepsilon}_p^p / \dot{\varepsilon}_q^p ; \eta = q / p' \qquad [2.28]$$

Here another assumption in Cam Clay is made that the dimensionless plastic energy dissipation rate is constant and equals to an input parameter *M*. Combining Equation [2.27] and [2.28] gives:

$$D^p + \eta = \frac{\dot{W}}{p' \dot{\varepsilon}_q^p} = M \qquad [2.29]$$

This is the flow rule of Cam Clay that tells the directions of plastic strain increments. The flow rule also indicate that at critical state, under which situation the plastic dilation rate D^p is zero, the critical stress ratio η_c equals to *M*.

To deduce a yield surface, a possible way is to find the stress increment vectors which are along the tangent of the yield surface, thus the yield surface can be deduced by integrating the stress increment vectors. From Equation [2.28], the increment vector of deviatoric stress *q* is

$$\dot{q} = p' \dot{\eta} + \eta \dot{p}' \qquad [2.30]$$

By assuming normality (the plastic strain increment vector D^p is always perpendicular to the yield surface, thus perpendicular to the stress increment vector):

$$\frac{\dot{q}}{\dot{p}'} = -D^p \qquad [2.31]$$

Substituting Equation [2.30] in [2.31] gives

$$\frac{\dot{p}'}{p'} + \frac{\dot{\eta}}{D^p + \eta} = 0 \qquad [2.32]$$

By Substituting Equation [2.29] in [2.32], and integration, after certain rearrangements, the yield surface of Cam Clay is deduced as:

$$\frac{\eta}{M} = 1 - \left(\ln \frac{p'}{p_c'} \right) \qquad [2.33]$$

p_c is the stress level where the current unloading-reloading line meets the critical state line as shown in Figure 2.13. The above function defines the shape of Cam Clay yield surface; p'_c indicates current position of the elastic unloading line, thus defines the size of current yield surface (the size of the elasticity zone).

2.5.2.2 Modified Cam Clay

Although it is a simple and easy-to-use model, Cam Clay model remains certain defects in modelling soil behaviour. It over estimates the strain increments induced by stress changes around very small strain area; it generates shear strain under isotropic compression condition. To overcome these defects, Roscoe and Burland (1968) proposed the following energy dissipation function:

$$\dot{W} = p'\sqrt{\left(\dot{\varepsilon}_p^p\right)^2 + \left(M\dot{\varepsilon}_q^p\right)^2} \qquad [2.34]$$

This gives a flow rule as the following formation:

$$D^p = \frac{\dot{\varepsilon}_p^p}{\dot{\varepsilon}_p^q} = \frac{M^2 - \eta^2}{2\eta} \qquad [2.35]$$

The above flow rule ensures that during isotropic consolidation, only plastic volumetric strain is generated. On the other hand, at critical state, where M equals to η, the volumetric plastic strain is guaranteed as zero. By following the procedure used for deducing the Cam Clay yield surface, the yield surface of Modified Cam Clay is formulated as:

$$\frac{p'}{p_c} = \frac{M^2}{M^2 + \eta^2} \qquad [2.36]$$

The yield surfaces of Cam Clay and Modified Cam Clay are plotted together in Figure 2.14.

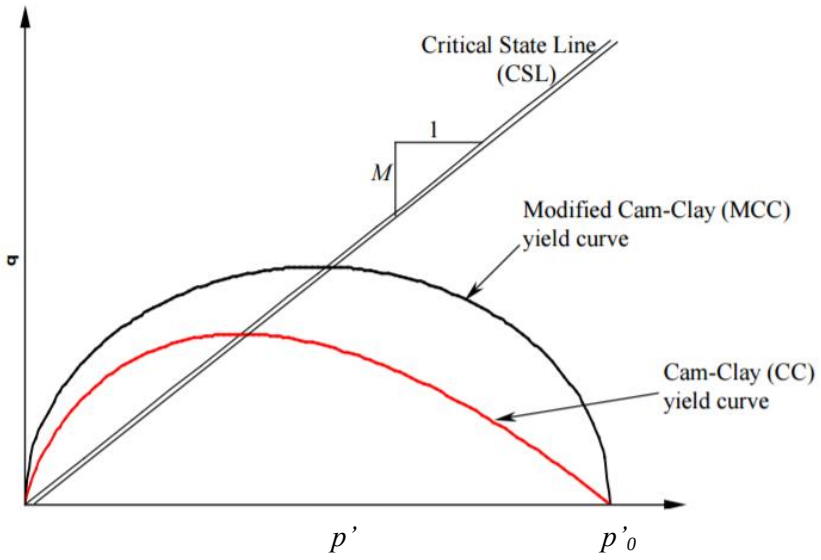

Figure 2.14 Cam Clay and Modified Cam Clay yield surface in the stress (*p'*-*q*) plane.

2.5.3 State parameter sand models

Dilation and compression of volume (change of density) due to the granular particle shape during shearing is a crucial part of sand behaviour. On the other hand, Cam Clay and Modified Cam Clay do not consider void ratio as a variable in the constitutive formulation, thus can hardly capture the volumetric behaviour of sandy soil. Been and Jefferies (1985) stated that density should be considered as a variable in constitutive modelling of sand, so that one type of sand with different initial densities can be considered as one material under different conditions. To theoretically describe the initial density of sand, the concept of state parameter is proposed:

$$\psi = e - e_c \qquad [2.37]$$

where ψ is the state parameter indicating current density of soil, e is current void ratio and e_c is the critical void ratio for current stress p'. Many lately developed advanced sand models are based on the critical state soil mechanics and the concept of state parameter. A specific character of sand is that during continuous shearing, dense sand will firstly expand and then decrease its volume; relative loose sand will decrease the volume and then expand. To capture this feature of sand, the critical state is used as the 'boundary' between dense and loose, the state parameter is employed as the measurement indicating how dense (or loose) the current soil is.

2.5.3.1 Norsand (Jefferies 1993)

During plastic deformation, unlike the situation in clay, the change of yield surface size of sand is not monotonic, a quasi-steady state (Alarcon-Guzman et al. 1988) indicating the switch from hardening to softening of the yield surface will be reached before arriving the final steady state (the critical state). The Norsand model uses a limitation value of the dilation ratio D^p to indicate this switch point (also called the image point):

$$D^p_{\min} = \chi\psi_i \qquad [2.38]$$

where $D^p_{\min}$ is the minimum ratio of dilation, χ is an empirical model parameter (further discussion in chapter 3),ψ_i is the state parameter at the image point for current yield surface and is deduced as

$$\psi_i = \psi_0 + \lambda \ln\left(\frac{p_i}{p}\right) \qquad [2.39]$$

whereψ_0 is the initial state parameter; p_i is the stress level of current image point. From above descriptions, it can be seen that the initial state parameter (the initial density) of the sand defines the switch point of hardening and softening. The derivation of the yield surface of Norsand follows the same approach used for deducing the Cam Clay yield surface, but appliesNova (1982)'s stress dilatancy rule

$$D^p = (M - \eta)/(1 - N) \qquad [2.40]$$

where N is coupling parameter, thus the yield surface of Norsand is

$$\begin{aligned} \eta &= \frac{M}{N}\left[1 + (N-1)\left(\frac{p}{p_i}\right)^{N(1-N)}\right] \quad \text{if } N \neq 0 \\ \eta &= M\left[1 + \ln\left(\frac{p_i}{p}\right)\right] \qquad\qquad \text{if } N = 0 \end{aligned} \qquad [2.41]$$

The Norsand yield surface in comparison with Modified Cam Clay yield surface is shown in Figure 2.15. It is useful to know that the Cam Clay yield surface is a special case (N = 0) of the Norsand yield surface. The Norsand model is proved to be an enlightening and reasonable representation of sand behaviour (Jefferies & Been 2006).

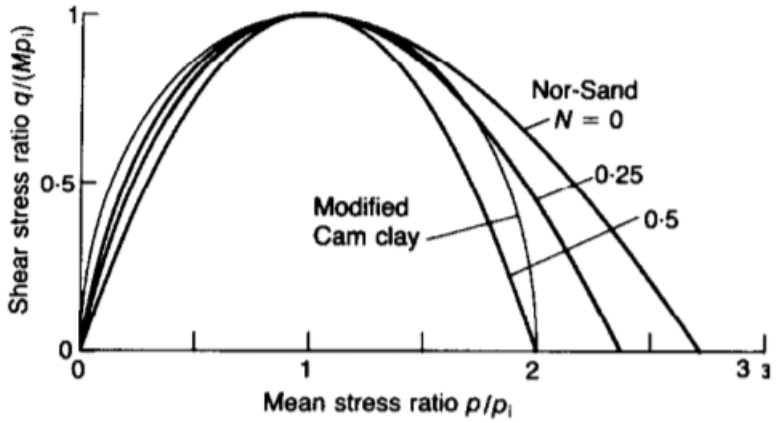

Figure 2.15 Norsand yield surface (Jefferies 1993).

2.5.3.2 A state parameter model for clay and sand (Yu 1998)

This unified model uses the Cam Clay yield surface but modified by a model parameter n:

$$\left(\frac{\eta}{M}\right)^n = 1 - \frac{\psi}{\psi_R} \qquad [2.42]$$

where ψ_R is the vertical distance between the normal consolidation line and the critical state line and is presented as

$$\psi_R = (\lambda - \kappa)\ln r \qquad [2.43]$$

where r is an input parameter. By using Equation [2.43], the normal consolidation line is assumed to be parallel with t critical state line as they share the same value of slope λ in v-ln$p$ plane. The flow rule applied in this model is the stress dilatancy relationship proposed by Rowe (1962):

$$D^p = \frac{9(M - \eta)}{9 + 3M - 2M\eta} \qquad [2.44]$$

Here arise a problem that the flow rule used for deducing the yield surface is not the flow rule applied in the model, thus normality no longer apply in this model (the plastic strain increment vectors are not perpendicular to the yield surface). Therefore, for deducing the hardening rule, a plastic potential surface (the surface that is perpendicular to the plastic strain increment vectors) is needed. Details of the plastic potential and the deducing of the

hardening rule can be seen in Yu (1998). The advantage of this model is that it applies the critical state soil mechanism thus is able to capture the ultimate strength of both clay and sand under drained and undrained conditions. However, when modelling sand, in small-medium strain range, certain deviation remains between test data and numerical predictions.

2.5.3.3 A two surfaces model for sand (Manzari & Dafalias 1997)

To simulate both monotonic and cyclic loading conditions, a two surfaces model is developed for sand. The yield surface is not the Cam Clay type of shape in the *p*-*q* space, as shown in Figure 2.16, the yielding criterion of this model is formed by two separate stress ratios, thus the elastic zone is located within these two linear lines (the grey zone in the figure). The yield surfaces are formulated as

$$f = \eta - \alpha \pm m \qquad [2.45]$$

where α is the bisector of the elastic zone, with 2m been the wedge 'opening', the cap and bottom of the elastic zone are Oc and Oe respectively.

As in the Norsand model, the state parameter controls the softening, which is the process between the peak strength and the critical state strength. The peak strength is named as the bounding surface, or bounding stress ratio (M_c^b). The critical state strength is the critical state stress ratio shown as M_c. The bounding surface is related to the current state parameter by

$$M_c^b = M_c + k_c^b \langle -\psi \rangle \qquad [2.46]$$

where k_c^b is a model parameter, the bracket $\langle \ \rangle$ defines the calculation $\langle -\psi \rangle = -\psi$ if $-\psi > 0$; $\langle -\psi \rangle = 0$ if $-\psi = 0$. The use of this bracket is to prevent the peak strength M_c^b from being smaller than the critical stress strength when $-\psi > 0$.

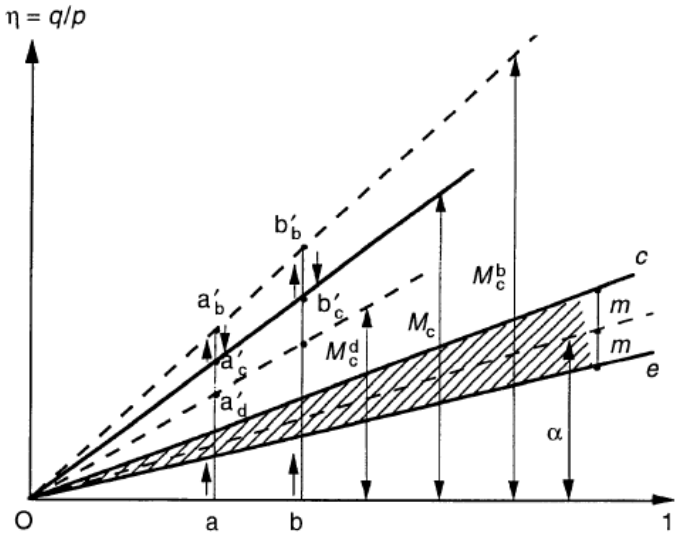

Figure 2.16 The scheme of the two surfaces model (Manzari & Dafalias 1997).

2.5.3.4 Summary

Similar to the models described above, many other models developed for modelling sand uses the concept of critical state and state parameter in past years (Li 1997,Li et al. 1999, Ling and Yang 2006 and Dafalias and Manzari 2004, among others). Basically the critical state defines the destination of the deformation and stress path while the state parameter indicates the current relative density and controls hardening and softening of the yield surface. It is unscientific to conclude which model is best for modelling sand behaviour, as they were developed for varies purposes and platforms of applications. For the consideration of the following aspects:

- Platform of this study – Plaxis, where state variables (indicating current position of yield surface) for each step of integration are automatically stored by the routine, thus use of hardening surface like Cam Clay type of surface is convenience.
- Numerical implementation – less number of input parameters is always preferred.
- The case – Ground response induced by tunnel volume loss, in which case cyclic loading maybe considered as unnecessary; small strain ground response is involved.

the Cam Clay based Norsand model is selected for further improvement and numerical implementation in this study.

2.6 Finite element modelling of tunnel construction

With the rapid development of computational power, numerical simulation becomes a popular method in predicting tunnelling induced ground movements. Compared to the empirical and analytical methods, numerical modelling appears to have the following advantages (Negro & Queiroz 1999): the ability to solve problems related to complicated structure - ground interactions; the flexibility of using different constitutive soil models according to the ground conditions; simulating the construction process including ground treatments (e.g. tail void grouting in TBM tunnel); considering both short term and long term ground movements and dealing with hydraulic ground conditions. The use of numerical techniques can be seen as a new type of testing which can investigate various types of cases without costing any testing material. According to the review published by Negro and Queiroz (1999), the finite element method (FEM) is currently the most widely used numerical technique. Among more than 65 reviewed papers about numerical modelling of tunnel projects, 96% of the cases are used FEM, and the remaining 4% used the finite different method (FDM) or others. Considerable progress on numerical analysis of NATM tunnelling has been made since the early 1980s, from then on, the more complex shield tunnelling models begin quickly developing start with 2D analyses (Kasper & Meschke 2004).

2.6.1 Two dimensional finite element analysis

The two dimensional FEM simulation of TBM tunnelling can be dated back to Clough et al. (1983), who analysed the first EPB project in the US. Although the tunnelling process is a three dimensional problem, the simulation of tunnelling starts from analysing 2D problems – the transverse cross section plane model and the longitudinal plane model. The longitudinal plane cuts along the axis of the tunnel and is able to concern the effects from around the excavation face which cannot be accounted to in the transverse cross section plane (Clough et al. 1983; Finno & Clough 1985). However, as the length of the tunnel is much larger than the diameter and the settlement recorded ahead of the excavation face is small, it is more useful to analyse the ground movements in the transverse plane.

In the transverse model, the source of the ground movements around the tunnel periphery in the FEM analysis can be introduced by prescribing certain amount of $V_{l,t}$ before the installation of the tunnel lining. The following four approximation methods of introducing $V_{l,t}$ are frequently used:

1. Convergence deconfinement

In this method the soil within the excavation is firstly removed. A sets of supporting stress which equilibrates the initial in situ stress distribution is then applied inside the tunnel periphery to support the ground. The tunnelling process can be simulated by gradually decreasing the stresses applied on the excavation periphery (Bernat & Cambou 1998; Bernat et al. 1999). The stress reducing factor λ affects the stress relaxation process by:

$$\sigma_r = (1-\lambda)\sigma_{r0} \qquad [2.47]$$

where σ_r is the applied stress on the excavation profile and σ_{r0} is the initial applied stress equilibrated with the initial in situ stress. The value of λ can be taken as 0~100%. In the case of λ equals 100%, it means all the supporting stress is cancelled and the ground is totally self-supported. The value of λ should be decided according to the tunnel volume loss. Typically λ can be taken as 30%~50% (Wongsaroj 2006).

2. Soil softening (Swoboda 1979)

This method was developed for simulating the NATM tunnelling. The stiffness of the soil inside the excavation is reduced by multiplying by the stiffness reduction factor β before the installation of the tunnel lining. The value of $V_{l,t}$ is then directly related to the value of β in the simulation.

3. Uniform convergence

In the transverse cross section, estimate and prescribe a value of $V_{l,t}$ according to the settlement data on the completion of the excavation. This method is the most widely used one in modelling transverse 2D tunnelling (Wongsaroj 2006), as the amount of tunnel deformation in the FEM model can be prescribed as the same as in the reality.

4. The gap parameter g

The gap parameter method was introduced by Lo & Rowe (1982). The definition of the gap parameter g is as Equation [2.25], discussed in Section 2.3.2. Before the installation of the lining, the allowed magnitude of the ground deformation is described by g. As the value of g is prescribed artificially according to the tunnelling machinery and construction experience, thus the accuracy of g will significantly affect the simulation results. The advantage of this method is that not only the amount of the convergence of the soil, but also the shape of the ground movement around the excavation is considered.

It can be seen that the first three methods will give similar ground movements as they gradually unload the ground until $V_{l,t}$ reaches the prescribed level without controlling the pattern of the ground convergence. The gap parameter method however let the majority of the ground convergence happen above the tunnel crown and along the two sides, the tunnel invert is fixed in both *x* and *y* directions. The difference between the simulation results given by the above two sorts of 2D convergence methods is found to be significant (Borst et al. 1996). The gap parameter method give deeper and narrower vertical displacement troughs and is more close to the measured data as shown in Figure2.17.

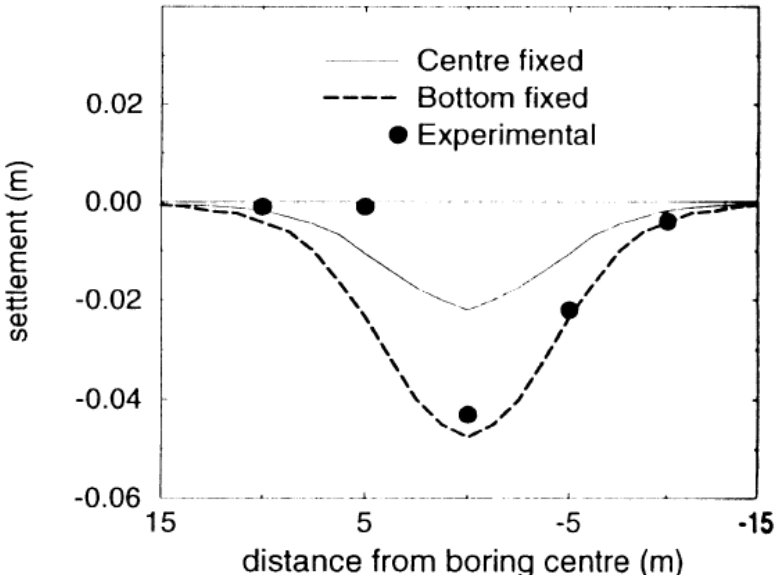

Figure2.17 The settlement profiles given by the gap parameter (bottom fixed) method and the free convergence method (centre fixed)(Borst et al. 1996).

2.6.2 Three dimensional finite element analysis

Although many of the current analyses are using 2D transverse cross section analysis, it should be noticed that the actual tunnelling process disturbs the in situ 3D stress strain distributions. The stress disturbance and the ground movement prior of the passage of the excavation face and ahead of the face are not considered in the 2D analysis (Farias et al. 2004). Panet and Guenot (1982) performed a 3D FEM simulation using an elastic soil model where 27% of the final ground displacements are due to the pre-convergence of the ground that occurred before the passage of the excavation face. Moraes Jr (1999) reported that up to

50% of the total ground movements measured on site are due to the pre-convergence in NATM tunnelling.

When modelling the NATM construction using 3D analysis, the excavation process can be simulated by using methods discussed in Section 2.6.1, but in a 3D space, and considering the excavation face as a source of ground movement, thus require more computational effort. The excavation process can be modelled by the removal of the soil elements.

The 3D FEM analysis for shield tunnelling is a more complicated process, as more factors should be taken into account such as installation of the segmental lining, grouting in the tail void, movement of the shield and the interactions between the shield and the surrounding ground. The first 3D FEM analysis for shield tunnelling was carried out by Lee and Rowe (1990; 1990a) simulating undrained ground conditions using a Mohr-Coulomb soil model. A relatively more comprehensive 3D simulation of TBM tunnelling was developed by Mansour (1996) in which case the ground movements related to the excavation face, the shield and the tail void were considered as separate ground movement sources. This concept was then become the most widely used method in 3D modelling of TBM tunnelling. The whole problem is then broken down into three: in front of the face, along the shield and the tail void.

2.6.2.1 Tunnel heading

The modelling of the exact excavation process of the cutter head is very difficult as the cutting of soil violates the continuum assumption made in FEM analysis. In conventional FEM modelling, the excavation of the soil is modelled by removing the soil elements ahead of the current excavation face and adding nodal forces (obtained from the hydraulic jack and the applied pressure from the cutterhead) on the new face. However the calculated ground displacements will dependent on the length of the removed soil elements; the movement of the advancing face may also not matching the movement of the shield. Instead of applying forces on the excavation face, later proposed FEM models (Komiya et al. 1999; Ezzeldine 1999) improved the former models by introducing the effects induced by the hydraulic jack that is pushing the excavation face, the segmental lining and the shield.

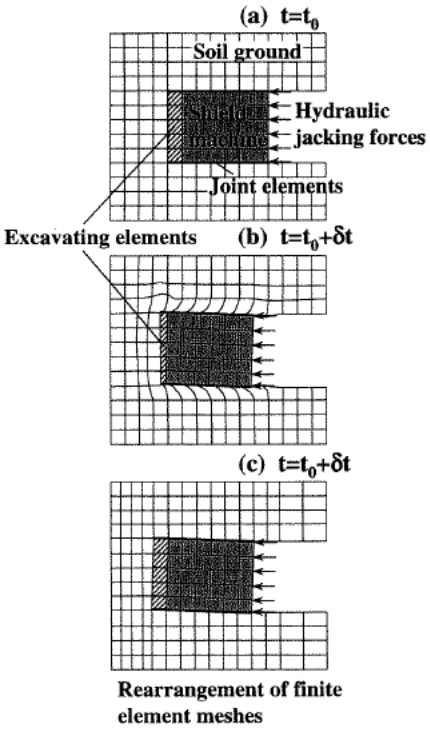

Figure. 2.18 Advancement of the TBM using excavation elements (Komiya et al. 1999)

Instead of removing the soil elements, an alternative method of simulating the excavation process can be done by introducing the excavating elements (Komiya et al. 1999). At the beginning of each advancing step $t=t_0$ in Figure. 2.18 (a), jacking forces are applied on the rear of the shield elements; the value of the forces can be decided according to the design. In the cases where face pressure is used (e.g. EPB and slurry TBMs), nodal forces that are equivalent to the average support pressure in the chamber can be applied in front of the shield elements. During the stage of $t = t_0 + \delta t$ (Figure. 2.18 b), the excavating element and the adjacent soil elements are deformed due to the jacking forces. With large stiffness, the shield itself will advance as a rigid body. After the time increment of δt, the model is remeshed to the same geometry as when $t=t_0$ but in the new location as shown in Figure. 2.18(c). The new excavating element is formed in front of the advance face before applying the jacking force. In this way, the advancing of the shield is simulated without removing any soil elements.

2.6.2.2 Around the shield

The sources of the ground movements around the shield in the FEM simulation can be summarised into two categories: the convergence of the surrounding soil towards the shield and the shearing between the shield and the soil.

The convergence of the surrounding soil can be obtained by:

1. Stress reduction, where the initial stress that is applied on the tunnel periphery is gradually reduced. The magnitude of the stress reduction is related to the size difference between the shield and the cutterhead. Mroueh and Shahrour (2002) adopted a stress reduction of 50% when simulating a TBM tunnel in sandy ground with the length of the ungrouted tunnel equal to the diameter of the tunnel.
2. Controlling $V_{l,t}$, where the ground is allowed to move inwards until the value of $V_{l,t}$ reaches a prescribed value. The tunnel lining (tunnel boundary) is then installed (Lee & Rowe 1991; De Borst et al. 1996).
3. Contracting the tunnel boundary. The tunnel boundary is not fixed but contracted until the contraction value is achieved (Komiya et al. 1999; Koelewijn and Verruijt 2006).

The interaction between the shield and the soil can be simulated by introducing the joint elements between the shield elements and the soil elements (Komiya et al. 1999). The stiffness of the joint elements is dependent on the friction between the shield and the soil.

2.6.2.3 The tail void

In some more detailed modelling, the ground movement at the rear of the shield are modelled. These movements are generated in the time gap between the passage of the shield and the grouting around the tunnel lining due to the closure of the void produced by the size difference between the installed segmental lining and the excavated profile. In tunnelling projects, material will be grouted into the void to control the closure. Simulation of the grouting in FEM analysis can be achieved by introducing grouting elements using saturated porous materials between the soil elements and the lining elements (Kasper & Meschke 2004). The pore pressure boundary conditions on the nodes of the grouting elements are updated to simulate the pore pressure generated by the grouting in undrained conditions. The time dependent stiffness of the grouting material due to hydration is modelled by the time-dependent Young's modulus (Meschke et al. 1996).

2.6.3 Boundary conditions

The boundary conditions in 2D or 3D FEM analysis are always set as: the vertical boundaries are fixed in horizontal directions but are free to move in vertical directions; the bottom boundary is fixed in both horizontal and vertical directions; the surface is free in all directions.

In reality, the surrounding soil can be approximated as infinite material while in FEM simulation, due to the limitation of time and computational power, the size of the FE model is constrained. However, the boundaries should be set in a way that they have negligible effects on the simulations results.

According to Figure 2.9, the settlement of the steady area is quite different from the settlement over the excavation face, thus the mesh should be long enough to allow the excavation face to advance until the measurement can be taken on the steady area. Ezzeldine (1999) produced a FEM model where the length of the mesh was 20 times of the tunnel diameter so the rear and front vertical boundaries are far enough from the excavation face. (van der Berg 1999) simulated an 8m diameter 17.2m deep tunnel and found that after advancing of 15m (2 diameters of the tunnel), the excavation face had no effect on the ground movements. Dias et al. (2000) modelled a 9.8m diameter 25m deep tunnel and concluded that the steady condition in the longitudinal plane was reached after the excavation face advanced for 45m into the mesh. Very little information is in the literature about how far should the vertical boundary been placed ahead of the excavation face.

In the transverse cross section plane, the width of the mesh in Ezzeldine (1999)'s model was selected as 10 diameters of the tunnel in this model. Van der Berg (1999) claimed that the lateral vertical boundary needed to be at least 143m (14 diameters of the tunnel) away from the tunnel centre line in order to reduce the settlement around the boundary to approximately zero.

2.6.4 Stress coefficient K_0

The coefficient of the earth pressure at rest K_0 (the ratio of the in situ horizontal stress / vertical stress) significantly affects the numerical simulation results in both 2D and 3D analyses (Guedes de Melo & Santos Pereira 2000; Addenbrooke et al. 1997). However, the consideration of K_0 does not necessarily improve the simulation results (Gunn 1993). According to the 2D modelling of the Jubilee Line Extension tunnel in London Clay, Addenbrooke et al. (1997) proposed the similar conclusion that modelling the effects of K_0, when using realistic soil parameters could not significantly improve the simulation results. The FE model made by Franzius et al. (2005) analysed the influences of the stress ratio K_0 on both 2D and 3D models. The value of K_0, varied from 0.5 to 1.5. A low value of K_0 tended to give over predicted maximum vertical settlement. The settlement troughs predicted by using

higher value of K_0 were too wide and too shallow compared to the field data. Again, the incorporation of the soil anisotropy does not ensure a better simulation results.

For tunnelling in overconsolidated clay, in contrast, Simpson et al. (1996) was able to give narrower vertical settlement troughs that better fit the ground movement data when considering the effects of K_0 in their 2D plane strain model.

Chapter 3. Formulation and application of the Norsand model

3.1 Introduction

The constitutive soil model in numerical modelling can be treated as a 'black box' between the stresses and the strains, and can transform the stresses into the strains, or vice versa. Therefore, the constitutive equations should be able to properly describe the soil stress – strain behaviour during variations of the stress distribution induced by change of loading conditions. There are several soil models developed for modelling general soft ground which have been used in modelling sand behaviour, and it has been proved to be possible to give reasonable simulation results of conventional laboratory tests. However, numerical modelling of tunnelling in sands, as discussed in the literature review, as a specific problem, requires a constitutive model that can reflect the unique characters of sand, such as critical state, stress dilatancy and localisation to give a valid prediction of ground movements.

The state parameter model – Norsand model originally developed by Been and Jefferies (1986) used the similar approach as in the famous critical state model Cam Clay (Schofield & Wroth 1968) to describe the critical mechanics of sand. The critical state (Casagrande 1936) is the end situation of sand during continuously deformation (ultimate shearing with zero volumetric strain). In addition, this model is able to describe the stress dilatancy of sand by using the concept of state parameter (Been & Jefferies 1985), which stands for the relative density of the sample. In this chapter, the theories and derivations of the Norsand formulations which are implemented in the later FEM analysis will be firstly discussed. The approach of determining the input model parameters will also be given followed by verification of the Norsand model using the determined soil properties of Toyoura sand – numerical simulation of conventional triaxial compression tests in both drained and undrained conditions.

3.2 The state parameter model – Norsand

One important principle about modelling soil behaviour is that a given type of soil under different conditions should not be treated as a different material with different properties. In other words, one kind of soil is a material that can exist in different states. Therefore, the constitutive equations should be able to describe the theoretical reasons causing the particular

behaviours under particular situations. The first idea of the Norsand model is using the relative density as the description of the current state of the sand, as sand is very likely to change its volume during loading and unloading (except at the critical state where there is no volumetric strain).

3.2.1 The critical state

Given the nature of any continuous material, it is not difficult to understand that soil cannot dilate or contract forever, in other words, the value of $\int d\varepsilon_v$ cannot be infinite during continuous deformation. For instance, concern about the termination of the soil dilation has been noticed by (Li 1997):

"The plastic volumetric strain will eventually become constant. This makes sense physically because otherwise, under a drained condition, the soil will explode since its volume would be able to increase indefinitely."

On the other hand, the soil mass will disappear if its volume was able to contract without termination. The termination of soil dilation and contraction draw the interest of research onto the critical state behaviour of sands. A constitutive model must be able to fundamentally explain and capture the end state of the soil - we must know where the calculation is heading to. The Norsand model, like many other widely used constitutive soil models, uses the critical state as the end state of soil.

To study the critical state of sand, Been et al., (1991) carried out 56 sets of drained and undrained triaxial tests on Erlsak 330/0.7 sand with three different approaches of reaching the critical state: strain controlled compression, load controlled compression and strain controlled extension. The tests were performed with the confining stress p' ranging from 6 kPa up to 3250 kPa, for geotechnical engineering purpose, the captured critical states with the mean effective stress p' rang from 6kPa to 1000kPa (representing a point roughly 50m deep in normal soft ground) are plotted in Figure 3.1. According to Figure 3.1, the critical states uniformly distributed around the critical state locus: $e = - 0.012\ln(p') + 0.81$; the distribution is apparently independent of the load controlling methods. This reminds us that the relationship between $\ln p'$ and void ratio is linear for Erlsak 330/0.7 sand.

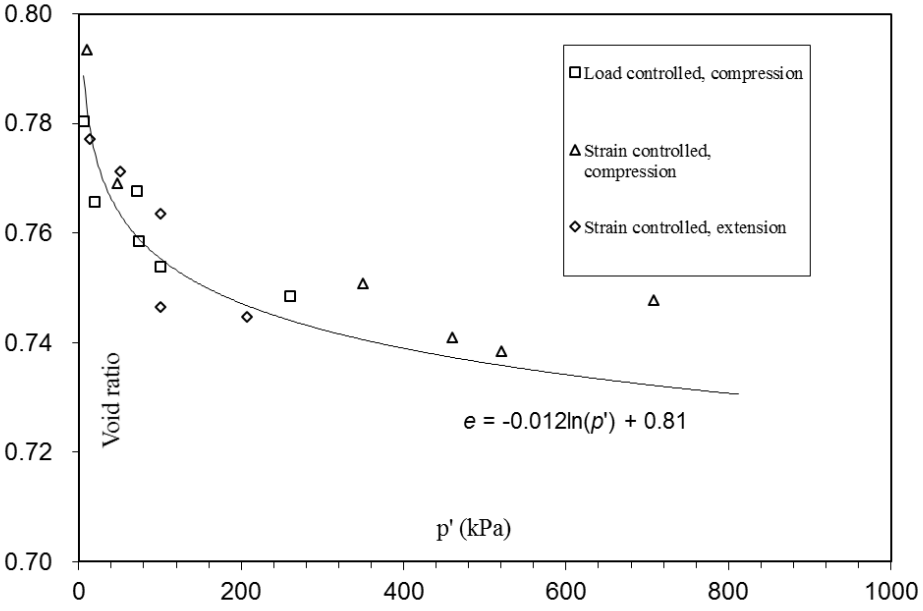

Figure 3.1 Critical states of Erksak 330/0.7 sand reached in undrained triaxial compression tests ($p' \leq$ 1000 kPa).

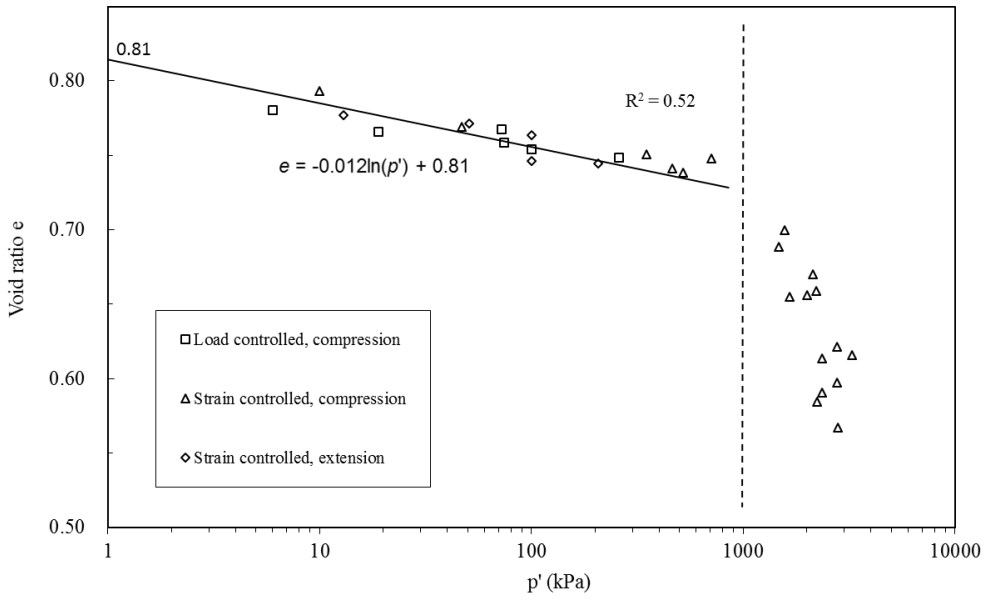

Figure 3.2 Critical states with stress axis plotted on a logarithmic scale (full range of p').

It has been empirically proved that for mean stress p' up to 1000 kPa, the CSL is approximately linear in the compression plane if the stress axis is plotted on a logarithmic scale for most types of soil. By using the data in Figure 3.1, replotting the critical states in the

v-ln*p* plane, the linear CSL can clearly be seen in Figure 3.2. The critical state locus (with stress level smaller than 1000 kPa) where the soil experiences infinite shear strain ε_q without change of volumetric strain ε_v, in the *v*-ln*p'* plane, can therefore be approximately expressed as

$$CSL: \mathrm{e} = \Gamma - \lambda \ln p', \qquad p' < 1000kPa \tag{3.1}$$

where λ is the slope of CSL in the *v*–ln*p'* (specific volume-mean stress) plane (referred as *v*-*p'* plane in the following texts for simplicity), Γ is the value of the specific volume on the CSL when the mean stress *p'*=1kPa (ln*p* is zero). From the Erlsak sand test data in Figure 3.2, it can be concluded that $\Gamma = 0.81$; $\lambda = -0.012$.

Although the critical state data within the stress level of 1000 kPa shows approximate linear distribution, when the stress level goes beyond 1000 kPa, as shown in Figure 3.2, the critical state distribution no longer follows the idealised linear locus. A similar conclusion can be drawn by plotting the 'quasi steady state' of the Toyoura sand (Figure 3.3) generated by series undrained monotonic compression tests (Verdugo & Ishihara 1996) with a wider range of the confining pressure (up to 3000 kPa). It can be clearly seen from Figure 3.3 that a linear distribution cannot approximate the critical state locus of sand any more when the confining stress *p'* goes to a relatively high value. In order to consider a wider range of confining stress level, Li (1997) produced the power law equation for the description of the critical state locus of sands:

$$CSL: \mathrm{e} = \Gamma - \lambda_c \left(\frac{p}{p_{ref}} \right)^{\xi} \tag{3.2}$$

where Γ stands for the same meaning as in Equation [3.1]; λ_c controls the curvature of the CSL instead of being the slope in Equation [3.1], the subscript indicates the curved critical state; p_{ref} is a reference pressure which is often set to 101 kPa (absolute atmospheric pressure) and ξ is a material constant that should be set based on laboratory test data. Now fit the data of full range of stress levels from Figure 3.2 with the power law equation, as shown in Figure 3.4. Equation [3.2] fits the data well from 1kPa up to 3500 kPa, and the coefficient of determination R^2 of the fitting is 0.91. However, in terms of geotechnical engineering interest (say from 20 kPa to 1000 kPa), the value of R^2 for the power law fitting reduces to 0.45 which is even lower than the R^2 (0.52) for the linear fitting in Figure 3.2. In other words, the power law relationship is a better description of the CSL when dealing with wider range of stress

levels of Erksak sand, while it sacrifices certain amount of accuracy compared to the linear description when studying the geotechnical range of stresses. However this does not mean that Equation [3.1] is a better description of CSL when the confining stress is smaller than 1000 kPa. For instance, the test data of Toyoura sand in Figure 3.3 illustrates that even with confining stress $p' < 1000$ kPa, the critical states perfectly fits the power law relationship. The linear description and the power law equation are both empirical approximation of the test data, thus there is no general conclusion telling which one is absolutely better. Which approximation to use depends completely on which equation fits the data better within the relevant range of confining stress level. For comparison purpose, both Equation [3.1] and Equation [3.2] will be used in later applications of Norsand in this chapter.

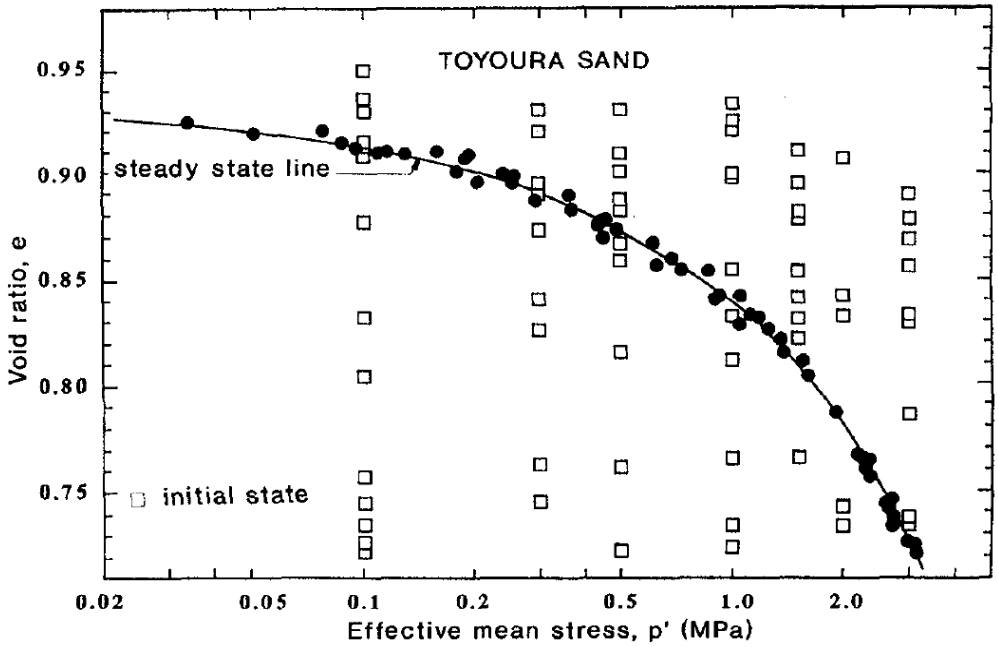

Figure 3.3 Critical states and the initial states of Toyoura sand in *v-p* plane (Verdugo & Ishihara 1996)

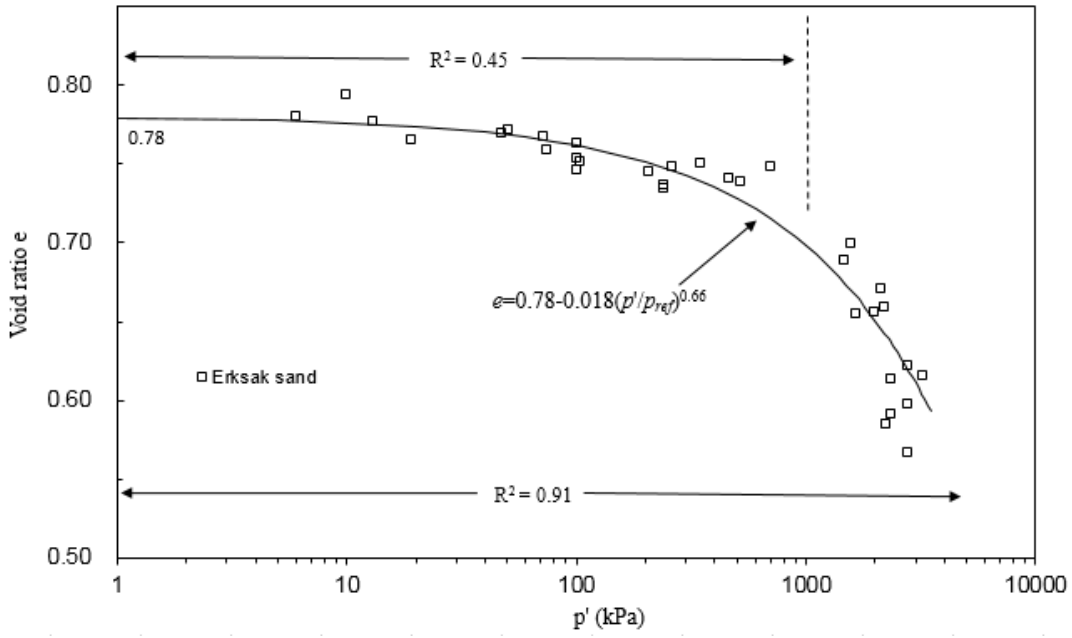

Figure 3.4 Critical states of Erksak 330/0.7 sand with fitting of the power law relationship.

3.2.2 The state parameter

The critical state defines the final destination of the volumetric strain, yet a parameter describing the current situation of the soil is needed. Schofield and Wroth (1968) theoretically developed the framework of critical state soil mechanics and pointed out that density (or void ratio) of soil should be captured as a state variable rather than a material property. In other words, sand is a material that can exist in different states (described by density or void ratio). The current state of the soil determines whether the sample will contract or dilate with further shearing. Cam Clay and the modified Cam Clay have explained why and how current density and stress level can affect soil behaviour (for example, the yield surface of the modified Cam Clay is related to the current void ratio e and the stress level p'). However, particularly for sands, samples at sufficiently different densities are usually treated as different materials (Been & Jefferies 1986), because sand is a material which has properties that are very sensitive to density and current confining stress level (not only density because same soils with same density but under different stress levels have different properties, for example, one sand sample will initially dilate during shearing under low stress level but will initially contract under very high stress level). In order to simulate sand samples with different densities under given stress level using consistent sets of constitutive equations, the relative density need to be introduced into the constitutive model as a state variable. Also, according

to engineering experiences, many soil properties and sand behaviours can be easily explained using simple functions of the density and stress level (Jefferies & Been 2006). Been and Jefferies (1985) then proposed such a state parameter as fundamental to the constitutive sand model:

$$\psi = e - e_c \qquad [3.3]$$

As shown in the above equation and Figure 3.5, the state parameter ψ is defined as the difference between the current void ratio e and the void ratio e_c on the critical state line CSL for current stress level p'. The relative density of the sand can be defined as the difference between the current void ratio e and a specific reference void ratio. The reason for using e_c as the reference density is that the CSL is an ultimate condition of the soil, thus is a proper reference status of the soil structure.

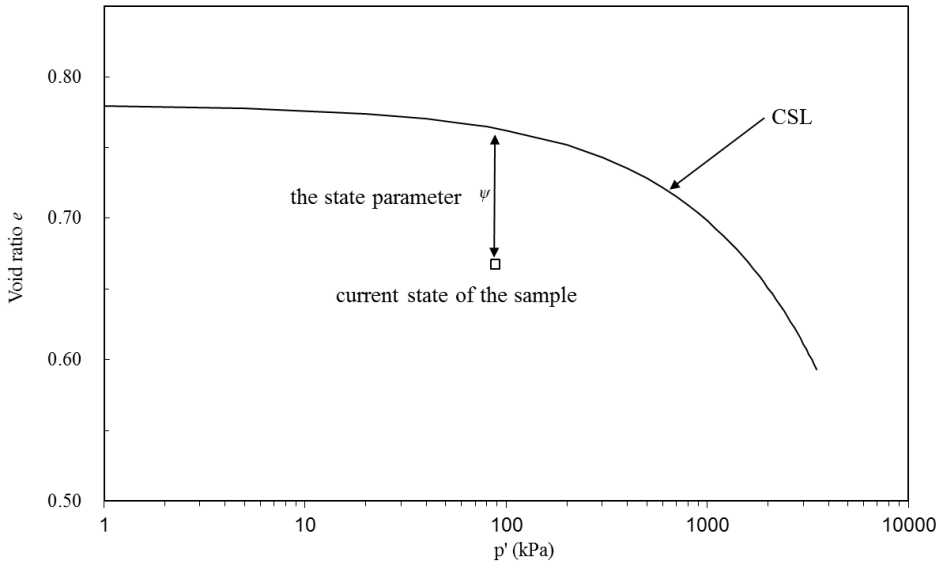

Figure 3.5 The state parameter in e-lnp' plane.

3.2.3 Infinity of NCL

In conventional critical elasto-plastic soil mechanics, there is a unique normal consolidation line (NCL also known as the one-dimensional compression line) in the v-p' plane. The normal consolidation line (NCL) is normally assumed to be parallel with the linear CSL (Wood 1990) as shown in Figure 3.6, and can be expressed as:

$$NCL : \mathrm{e_n} = N - \lambda \ln p' \qquad [3.4]$$

where e_n is the normal consolidated void ratio for current stress level; N is the void ratio when the confining stress is 1 kPa; and λ is the slope (or the curvature parameter if the power law equation is used for defining the CSL) of the NCL so that the NCL is parallel with the CSL. The URL in Figure 3.6 is the unloading – reloading line, thus any overconsolidated soil sample would be theoretically located on URLs. When applying loading on an overconsolidated sample, the state of the soil will move from the URL onto the NCL; the intersection point of URL and NCL is where elastic behaviour transfers to plastic behaviour. The overconsolidation ratio R is then p'_0/p'. The uniqueness of the NCL, if applied on sand, means that sand samples with different state parameters will have same elasto-plastic mechanical properties as they all necessarily follow the same route (the unique NCL) in the v-p' plane. This conflicts with reality. The Norsand model therefore applies the concept of infinity of the NCL (Drucker et al. 1957). The form of infinite NCLs is summarised in Figure 3.6 (b), which illustrates that each state parameter is generating one NCL. Although the NCL is not explicitly defined in the Norsand constitutive equations, applying infinite NCL means adopting infinity of the yield surface, as the NCL can been seen as the trace of the hardening yield surface in the v-p' plane. In this way, the yield surface is made to be state parameter dependent by using the concept of infinite NCL. The mechanism of how infinite NCLs relate to the infinite yield surfaces will be discussed in Section 3.2.6. An example of the infinity of NCL and can be seen in Figure 4.5.

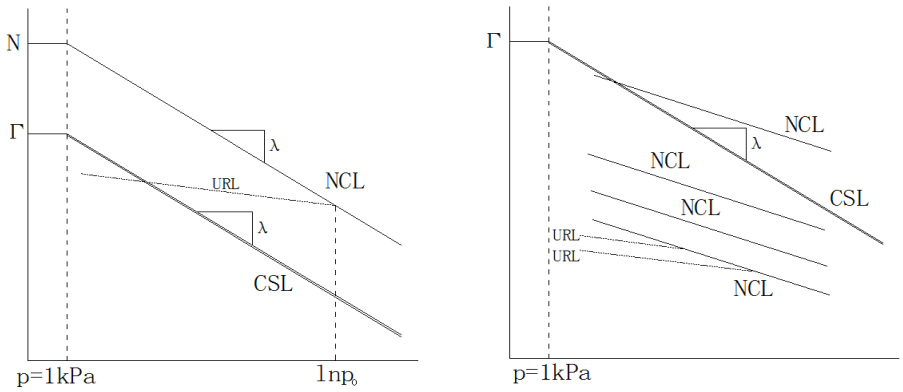

(a) (b)

Figure 3.6 The compression line and the critical state line in v(vertical axis)-lnp'(horizontal axis) plane (linear CSL). (a) Unique NCL (b) Infinite NCL.

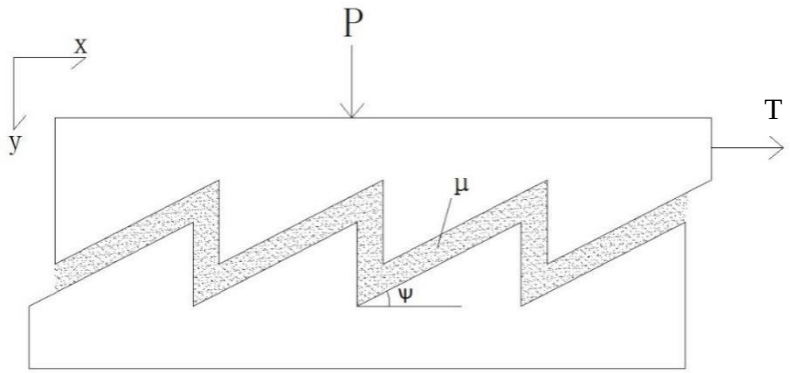

Figure 3.7 Shear of two sand layers.

3.2.4 Stress dilatancy

Unlike most artificial engineering materials, volumetric strain of soil is not negligible during loading and unloading, especially for drained soil, like sand. For instance, as air and water that filling the space among sand particles is free to move in and move out during loading and unloading, dense sand will increase in volume during shearing due to restructuring of the particles; on the other side, loose sand will initially contract during shearing, causing compacting of the sand particles. The so called 'dilatancy' is the trend of change in volume of soil, the critical state is then the destination of this trend, and can be seen as the ultimate steady state of the soil volume during shearing. By reaching this steady state, the shear stress becomes equal to the sum of the friction generated by contacting particles, and the reaction force caused by the angle of dilatancy (see Figure 3.7). This phenomenon can be summarised as: strength equals friction plus dilatancy. During shearing, it is reasonable to simplify two contacting sand layers as Figure 3.7, where P is the normal load; T is the shear force; μ is the friction coefficient between sand layers; ψ is the angle of dilation (dilation is the rate of increment of volumetric strain over increment of shear strain during shearing); x and y horizontal and vertical direction.

According to Figure 3.7, 'strength = friction + dilatancy' can be expressed as:

$$\mu = \frac{\tau}{P} + \frac{\dot{y}}{\dot{x}} \qquad [3.5]$$

where $\dot{x}$ and $\dot{y}$ is increment of horizontal (shear) and vertical (volume) movement respectively. This can be rewritten as the form of 'energy = shear work + volumetric work' as:

$$W = \tau \dot{x} + P\dot{y} \qquad [3.6]$$

where W is the input energy cost in the shearing. It is reasonable to assume that during shearing, the work W input by the shear stress and the normal load was all dissipated in friction (Taylor 1948), in other words no energy is stored in elastic strain. This energy function can then be expressed in the form of using mean effective stress *p'* and the deviatoric stress *q*:

$$W = q'\dot{\varepsilon}_q^p + p'\dot{\varepsilon}_p^p \qquad [3.7][2.27]$$

where $\dot{\varepsilon}_p^p$ is the increment of plastic volumetric strain $\dot{\varepsilon}_q^p$ is the plastic deviatoric strain increment. The superscript p stands for plasticity, the subscripts *p* and *q* means the strain is induced by the means stress *p'* and the deviatoric stress q respectively. Assuming that the energy dissipation rate $\frac{W}{p'\varepsilon_q^p}$ is a constant *M*, Equation [3.7] can be rewritten as:

$$M = D^p + \eta \qquad [3.8][2.29]$$

where D^p is the dilatancy ratio ($D^p = \dot{\varepsilon}_p^p / \dot{\varepsilon}_q^p$); η is the stress ratio *q*/*p'*; note that *M* is the stress ratio η at the critical state when D^p is zero. Equation [3.8] is the stress dilatancy relationship used in Cam Clay. The Norsand model applies M_i (the stress ratio at the image point where $\varepsilon_p^p = 0$, see Figure 3.10. the value of M_i is dependent on the state parameter and other input model parameters, the value of M_i will be discussed in Section 3.2.8) instead of *M*, thus the stress dilatancy applied in Norsand becomes:

$$M_i = D^p + \eta \qquad [3.9]$$

The image point is where contraction transits to dilation for initially loose sand; or dilation transfers to contraction for initially dense sand. As the fundamental of the Norsand is the state parameter, therefore one of the advantages of using M_i is that the yield surface deduced from Equation [3.9] can be directly related to the state parameter. This stress dilatancy relationship is the flow rule of the constitutive model that indicate the direction (ratio of $\dot{\varepsilon}_p^p / \dot{\varepsilon}_q^p$) of the plastic strain development in the $\varepsilon_p^p - \varepsilon_q^p$ plane.

3.2.5 Yield surface

As the stress dilatancy relationship indicates the direction of plastic strain increment, D^p can be seen as a vector which is the sum of the plastic strain increment components $\dot{\varepsilon}_p^p$ and $\dot{\varepsilon}_q^p$ in the strain plane. Accepting that the plastic volumetric strain and the plastic deviatoric strain start from a yield point with axes parallel to p' and q respectively to form the increment vector D^p, then $\dot{\varepsilon}_p^p$ / $\dot{\varepsilon}_q^p$ and p'/q can be drawn in the same coordinate system. Therefore the starting point of vector D^p becomes the yield point in the p'- q plane. If we draw a very short line, in the p'-q plane, orthogonal to D^p at the yield point, according to sufficient amount of data, a family of these short lines will form a curve which is orthogonal to all pairs of $\dot{\varepsilon}_p^p$ and $\dot{\varepsilon}_q^p$ as shown in Figure 3.8. This curve is therefore the potential of the plastic strains and, in the p'-q space, can be deduced by integration of stress increments. In deducing the yield surface of the constitutive soil model, a widely used hypothesis is assuming normality – the yield surface coincident with the plastic potential. In this way, the yield surface can also be deduced by integration of $\dot{q}$. Accepting normality means assuming the increment vectors of plastic strain are orthogonal to the yield surface as well. Graham et al., (1983) carried out sets of triaxial compression tests using natural clay, and was able to determine the yield points and the corresponding plastic strain increments. The normalised yield surface based on the yield

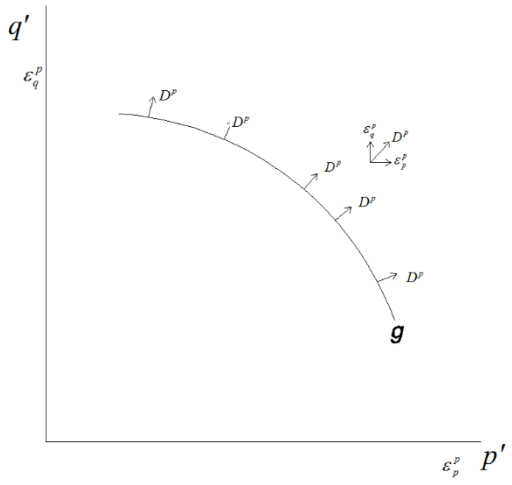

Figure 3.8 The pattern of plastic potential (integration of D^p).

points and the vectors of plastic strain increments are plotted in Figure 3.9 where $\sigma_{vc}^{'}$ is the applied vertical pre-consolidation pressure.

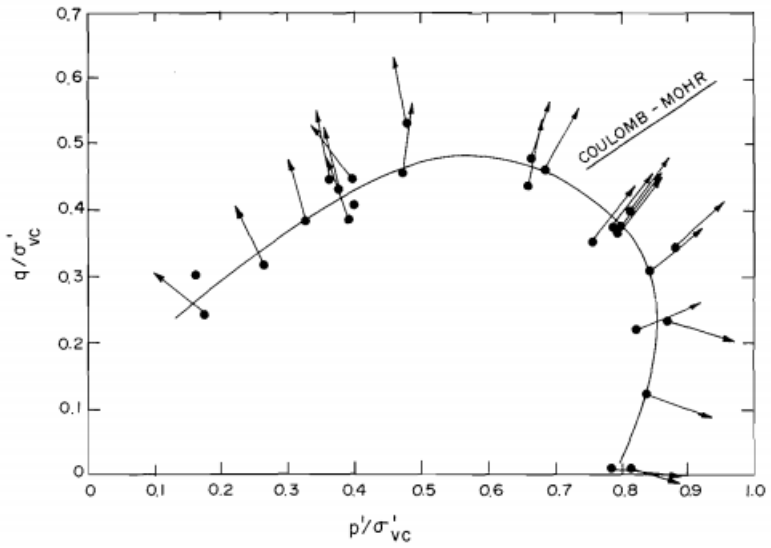

Figure 3.9 The normalised yield locus and vectors of plastic strain increment (Graham & Houlsby 1983).

It is not hard to conclude that in Figure 3.9 the increment vectors are roughly perpendicular to the normalised yield surface although some scatter remains. Through further investigations, Graham et al., (1983) claimed that most of the deviation angles between the normal to the normalised yield surface and the plastic strain increment vectors are within the value of $\pm 20^{\circ}$, which is an acceptable relative small deviation. Yet some other cases (Poorooshasb et al., 1966; Lade, 1977; Vermeer, 1982) illustrate that, for sand, the deviation between plastic potential and yield surface is much larger than for cohesive soil, and that for constitutive and numerical modelling of sand, it is more convenient and reasonable to use a yield surface that is fundamentally developed from the stress-dilatancy behaviour of the sand itself rather than an artificially defined curve, which might introduce extra laboratory tests and be numerical difficult (for example the man-made Hvorslev yield surface for soil brings calculative problems when implemented into numerical software due to its discontinues shape [Gens and Potts, 1988]), even it might be closer to the reality. It is of course always better to use yield surface that is closer to the data, thus the exploring of yield surfaces in constitutive modelling of sand is worth further research. In this study the original Norsand yield surface which assumes normality will be applied. From the definition of stress ratio η, $\dot{q}$ can be expressed as:

$$\dot{q} = p'\dot{\eta} + \eta\dot{p}' \qquad [3.10]$$

Assuming normality, the plastic strain increment being normal to stress increment gives:

$$\frac{\dot{q}}{\dot{p}'} = -D^p \Rightarrow \dot{q} = -D^p \dot{p}' \qquad [3.11]$$

From Equation [3.9], [3.10] and [3.11]

$$\frac{\dot{p}'}{p'} + \frac{\dot{\eta}}{M_i} = 0 \qquad [3.12]$$

As M_i is a function of state parameter ψ and other input parameters, it can be treated as a constant in the integral of Equation[3.12]. Integration of Equation[3.12] gives:

$$\ln p + \frac{\eta - M_i}{M_i} = K \qquad [3.13]$$

Theoretically the value of K can be any constant as different values of K illustrate different position on the yield surfaces. The Norsand model applies the solution on the image point where $\eta_i = M_i$, therefore $K = \ln p_i$. Taking the substitution of K into Equation[3.13]:

$$\frac{\eta}{M_i} + \ln\left(\frac{p'}{p_i}\right) - 1 = 0 \qquad [3.14]$$

The above equation is the orthogonal of the plastic strain increment vectors – the plastic potential g (p', q, ξ), where ξ is a parameter that indicate the size of current plastic potential. In Equation [3.14]ξ is taken as p_i. Again, accepting normality, the yield surface f (p', q, p_i) of Norsand is:

$$f(p', q, p_i) = \mathbf{g}(p', q, p_i) = \frac{\eta}{M_i} + \ln\left(\frac{p'}{p_i}\right) - 1 = 0 \qquad [3.15]$$

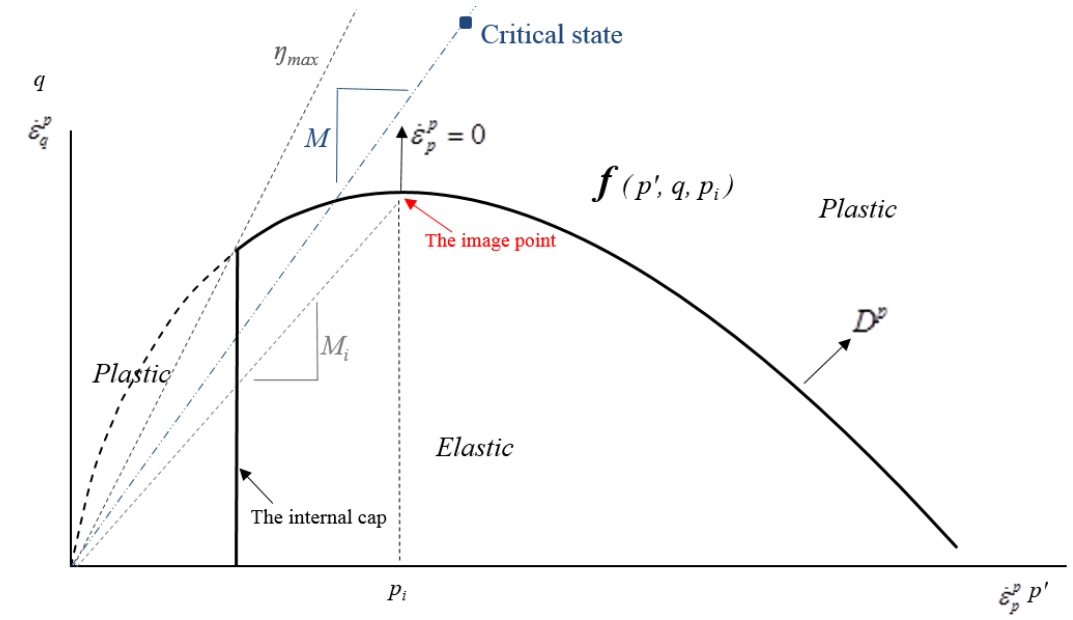

Figure 3.10 Norsand yield surface and internal cap for dense sand. *The internal cap will be discussed in section 3.2.7.

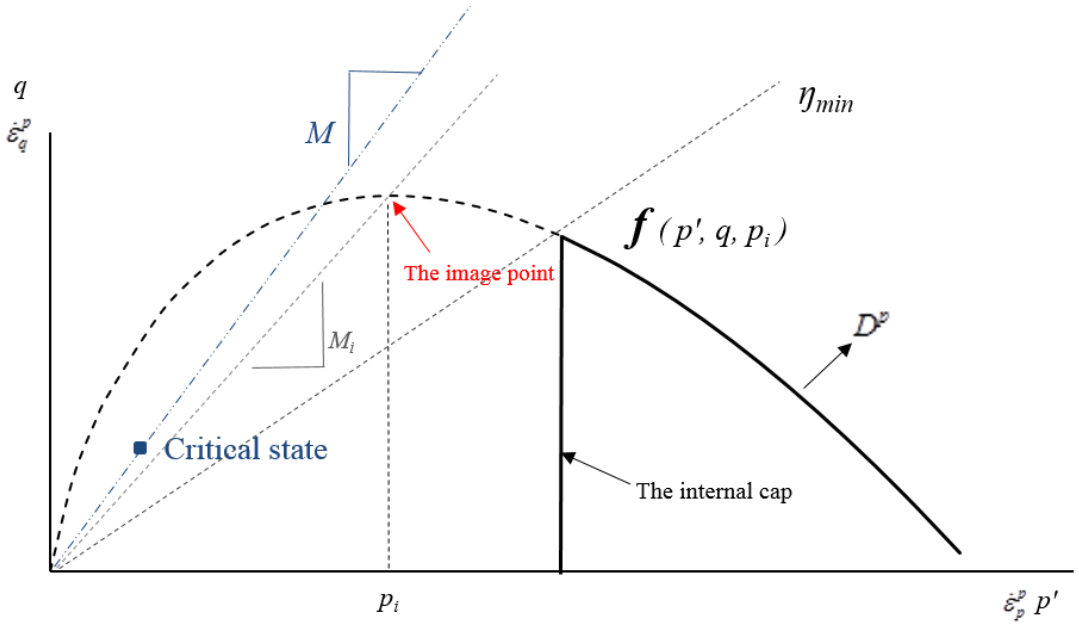

Figure 3.11 Norsand yield surface and internal cap for loose sand.

The process of deducing the yield surface of Norsand actually followed the same approach used for deducing the yield surface for Cam Clay. The yield surface Equation [3.15] is plotted in Figure 3.10. The different part of Norsand yield surface from the Cam Clay surface is the use of the stress ratio at the image point (M_i) instead of the stress ratio at the critical state (M).

Apart from relating yield surface to the state parameter, another valuable point of using M_i is that proper dilatancy behaviour of sand can be described. For example, for dense sand, when the soil dilated to the situation where D^p=0, the Cam Clay yield surface will take this situation as the critical state, therefore ultimate deviatoric plastic strain will occur accompanied by zero plastic volumetric strain. However, according to the definition of critical state, zero plastic volumetric strain ε_p^p=0 is only one of the two necessary conditions to reach the critical state, the trend of plastic volumetric change $\dot{\varepsilon}_p^p$ should also be zero on the CSL. The different between the image condition and the critical state can be clearly seen from Figure 3.10 where M_i does not coincide with M.

For dense sand, as shown in Figure 3.10, the image point (top of the yield surface) is located on a lower stress level compared to the critical state point. The soil needs further hardening (expansion of the yield surface) to make M_i coincide M, so as to reach the critical state. For loose sand (Figure 3.11), the image point is on a higher stress level compared to the critical state point, thus making the image point intersect the critical state needs further softening (shrink of the yield surface). This phenomenon also indicates how p_i controls the size of f (p', q, p_i). The Cam Clay model, which uses the stress ratio at critical state M in deducing the yield surface, automatically assume the sample is a mid-density soil as the image point always intersects the critical state point ($M \equiv M_i$), thus is a special case of Norsand. The internal stress cap in Figure 3.11 is considered as part of the yield surface and will be discussed in Section 3.2.7.

3.2.6 A case of shearing

An example of how the image state point controls the hardening and softening of the yield surface, and how the concept of infinite NCLs is applied in hardening is now presented. It should be understood that the image state where $D^p = 0$ exists at only one point on each yield surface, however, this does not satisfy the Axiom of the critical state only if $\dot{D}^p = 0$, which means the tendency of dilatancy change must also be zero. This is important when the infinity of the NCL is applied (the image point in the Cam Clay models coincide the critical state). An example of how the image point controls the hardening and softening of the yield surface is illustrated in Figure 3.12. Consider a sand sample that has been isotropically normally consolidated to point A, this situation gives the yield surface illustrated by surface a. Shear stress is then applied, as the strain increment vector is on the right side of the image point,

thus positive $\dot{\varepsilon}_p^p$ generates contraction. The sample is contracted up to point B, accordingly the yield surface is now progressed to surface b (where $p_i = p'$). Although the current condition meets $p_i = p'$ and $\dot{\varepsilon}_p^p = 0$, the current value of $|p_i\text{-}p'|$ is zero (the internal stress cap is not touched yet), so the soil begin dilating during further hardening of yield surface. The hardening does transit to softening until the internal stress cap is reached (the maximum off set of p_i from p'). This transition point is denoted by surface *c* and stress state point C. Further softening generates soil dilation as the current plastic increment vector is on the left side of the image point, thus giving negative volumetric strain increment. The critical state is reached when the yield surface is softened to surface *d* (same size as surface *b*) where the image point and the CSL coincide at stress point D. The soil can then experience ultimate shear strain increments without either stress change or further softening/ hardening. Now, the only difficulty is to find out the maximum offset of p_i from p (where hardening turns to softening; where the peak shear strength is).

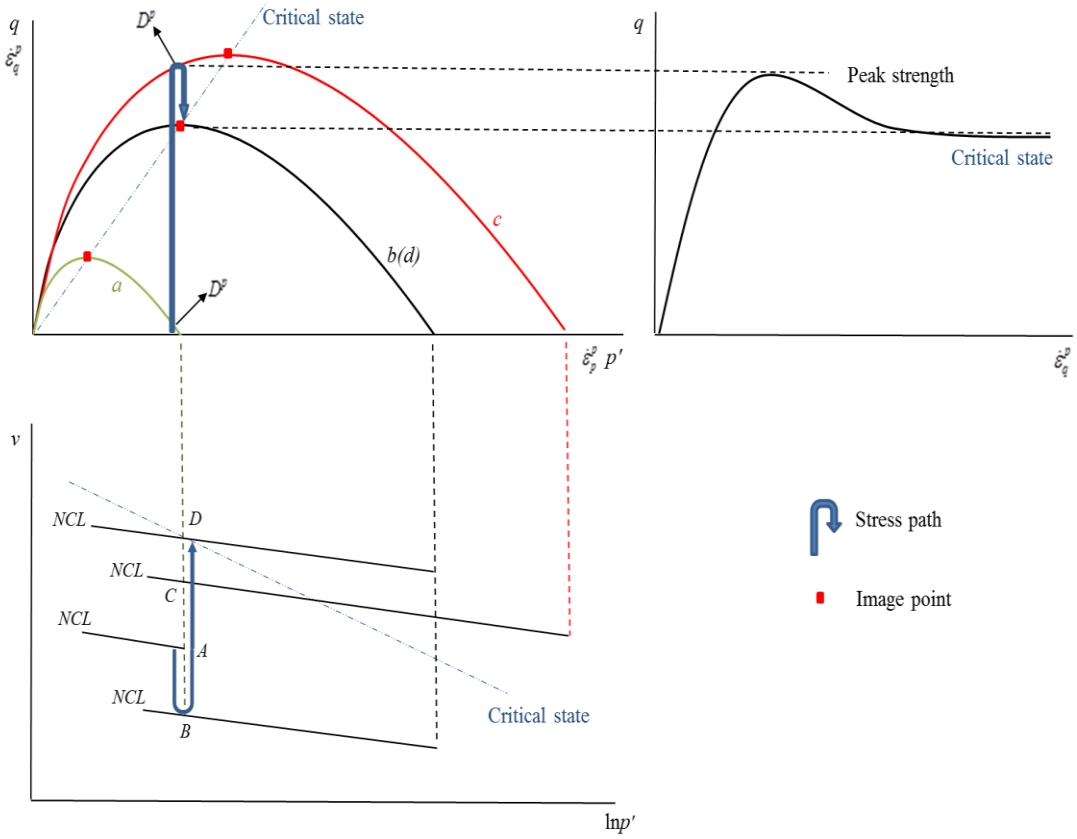

Figure 3.12 Hardening and softening of the yield surface during shearing.

3.2.7 Internal cap

As has been studied by many conventional laboratory tests on dense sand, the dilation of dense sand will be limited by a value where the peak shear strength is reached (Wood & Belkheir 1994; Salgado et al. 2000) After this limit condition, the shear strength gradually decreases to a steady level which is believed to be the critical state. In other words, the peak strength is the transaction point of hardening and softening of the yield surface, also the inflection point of dilation and contraction. The pattern of the yield surface softening to the critical state after peak strength is reached is shown in Figure 3.13. In terms of the strain increment vector, the inflection point is where the minimum volumetric strain increment $\dot{\varepsilon}^{p}_{p\min}$ is reached (minimum because negative volumetric change is taken as contraction) for current confining stress level, thus the dilatancy here is minimum: $D^{p}_{\min}$.

As discussed in Section 3.2.5, the stress value at the image point p_i is the parameter that controls the size of the yield surface in Norsand; it is straightforward to consider p_i as the reference in determination of the hardening limit of yield surface. By substitute the stress dilatancy Equation [3.9] into the yield surface Equation[3.15], the yield surface can be determined from the image stress p_i as:

$$p_i = p'\exp\left(\frac{D^p}{p'}\right) \qquad [3.16]$$

Taking the direct shear test as an example, according to Figure 3.13, the maximum size of yield surface is achieved when the dilation rate reaches its minimum value for current stress level (D^p pointing left indicates contraction). Equation[3.16], under the transition condition, therefore can be expressed as:

$$\left(\frac{p_i}{p'}\right)_{\max} = \exp\left(\frac{-D^{p}_{\min}}{M_i}\right) \qquad [3.17]$$

The yielding limit is preferably written in the form of stress ratio (Equation[3.17]) or stress difference, in order to geometrically clarify that the maximum offset of current stress *p'* from the image stress p_i indicates the limit (peak strength/ peak size of yield surface). Now the only remaining uncertainty for determining the hardening limit is the value of $D^{p}_{\min}$. An idea for determining $D^{p}_{\min}$ is to associate the state parameter with it. However each state parameter is

associated with one set of yield surfaces, thus the state parameter for the current image stress state ψ_i is used. As for each image state there is only one unique stress limit, under triaxial compression, $D^p_{\min}$ can be determined though the following relationship:

$$D^p_{\min} = \chi_i \psi_i \qquad [3.18]$$

where χ_i is an internal model parameter. Derivations of χ_i and ψ_i will be discussed in the following section. The reader may have noticed that the hardening limit is defined as one simple stress limit of p' (a vertical line in the p'-q plane as shown in Figure 3.10). The reason for using a stress limit is that, for the current yield surface, no dilation ratio smaller than $D^p_{\min}$ is allowed, to prevent any stress state from occurring on the left side of $D^p_{\min}$ (the curved dashed line in Figure 3.13). The stress limit is introduced to replace the dashed line as a new part of the current yield surface, thus any stress approaching the left side of the current $D^p_{\min}$ and crossing the current stress limit will act as the new stress limit, then cause softening of the current yield surface. For simplicity, the internal stress cap is summed as a straight vertical line. However, the actual shape of the stress cap remains uncertain and obviously need further study (the shape of the stress cap affects the direction of the strain increment during plastic softening).

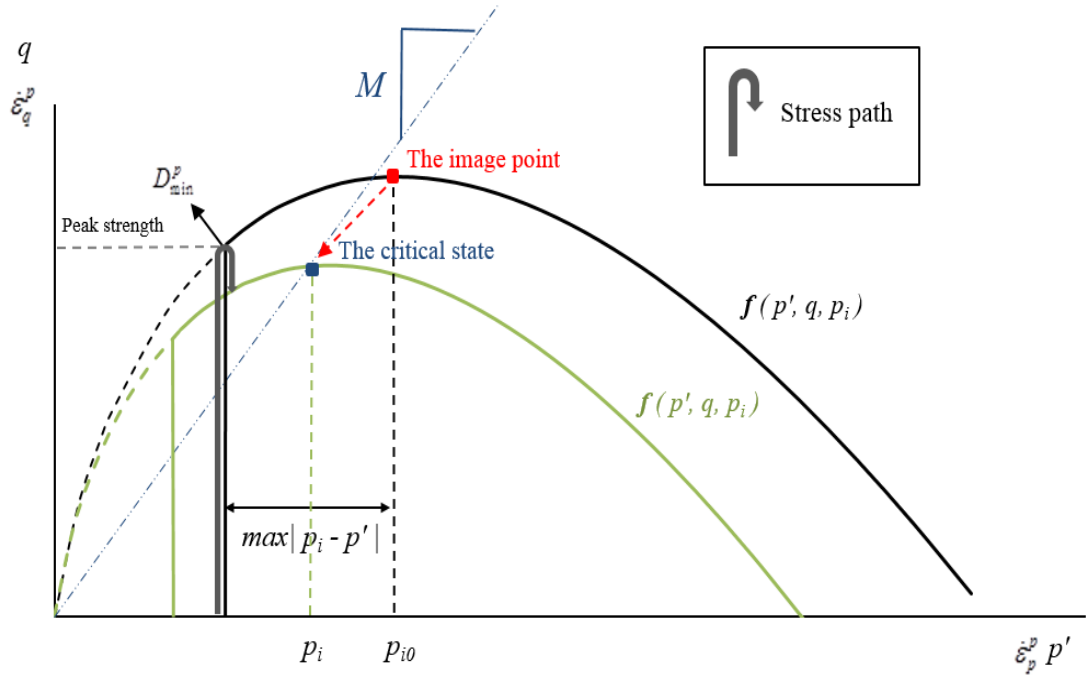

Figure 3.13 Approaching the critical state of dense sand in shear.

3.2.8 Image parameters

There are three internal model parameters that relate to the image point in Norsand: the model parameter χ_i, the state parameter at the image point $\psi_i$and the stress ratio at the image point M_i.

- the state parameter at the image point ψ_i;

As the stress state moves along the yield surface, the corresponding state parameter will change according to the confining stress level. Based on the definitions of the critical state, Equations [3.1] and [3.2], the state parameter for the current image stress will be:

$$\psi_i = \psi - \lambda \ln\left[\left(\frac{p_i}{p'}\right)_{\max}\right] \qquad [3.19]$$

$$\psi_i = \psi - \lambda_c \ln\left[\left(\frac{p_i}{p'}\right)_{\max}\right]^{\xi} \qquad [3.20]$$

Equation[3.19] is deduced according to the linear critical state while Equation[3.20] comes from the curved critical state locus. Both approaches will be implemented in the numerical codes for comparison purposes.

- Internal model parameter χ_i;

From Equation[3.18], χ_i is the slope of $D^p_{\min}$ against the image state parameter ψ_i. Since χ_i is an internal model parameter which cannot be directly measured though tests, it is reasonable to firstly determine the slope of $D^p_{\min}$ over the current state parameter, and then relate this slope to χ_i. The triaxial compression test is taken as the tool to measure the slope of $D^p_{\min}/\psi$. From the above discussion:

$$\chi_i \psi_i = \chi_{tc} \psi = D^p_{\min} \qquad [3.21]$$

where χ_{tc} is a input parameter, and is the slope of $D^p_{\min}/\psi$ under the triaxial compression condition. By introducing the expression of the image state parameter (Equation [3.19], or [3.20] if the curved critical state is used) and the stress limit (Equation [3.17]) into Equation [3.21] we have

$$\chi_i = \frac{\chi_{tc}}{1 - \frac{\lambda \chi_{tc}}{M_{tc}}} \qquad [3.22]$$

if the curved critical state is applied then

$$\chi_i = \frac{\chi_{tc}}{1 - \frac{\lambda_c \chi_{tc} \xi}{M_{tc}}} \qquad [3.23]$$

where M_{tc} is the stress ratio at critical state; the subscript indicates that this value is deduced under triaxial compression condition. It should be noticed that, in Equation [3.22] and [3.23], according to the strict derivation, the stress ratio used should be M_i but not M_{tc}. The reason to apply such a simplification is that M_i itself is χ_i dependent which makes it difficult to deduce χ_i. Given the fact that the stress ratio at the image point M_i is reasonably close to M (Figure 3.13), current approximations of χ_i (use M_i instead of M_{tc}) are used.

- the stress ratio at the image point M_i.

According to the famous Nova's flow rule (Nova, 1982), the maximum dilation can be expressed as:

$$D^p_{\min} = \frac{M - \eta_{\max}}{1 - N} \qquad [3.24]$$

where N is an input model parameter that can be derived from triaxial compression tests. Substituting Equation [3.24] for $D^p_{\min}$ into [3.21] and by combining Equation [3.9]

$$M_i = M + N \chi_i \psi_i \qquad [3.25]$$

By considering the effect on shear strength due to the lode angle θ (effect of intermediate stress), M_i becomes (Jefferies & Shuttle 2002)

$$M_i = M(\theta)\left(1 + \frac{N \chi_i \psi_i}{M_{tc}}\right) \qquad [3.26]$$

where the critical stress ratio considering lode angle is (Jefferies & Shuttle 2011)

$$M(\theta) = M_{tc} - \frac{M_{tc}^2}{3 + M_{tc}} \cos\left(\frac{3\theta}{2} + \frac{\pi}{4}\right) \quad [3.27]$$

where the lode angle is measured in radians. Note that in the derivation of M_i, a dense sand case (ψ_i<0) was assumed. For loose sand where ψ_i>0, it has been proved that a symmetric case of Equation [3.26] has a good fit to the data (Been & Jefferies 2004), thus a general version of Equation [3.26] for both dense and loose sand case is derived as

$$M_i = M(\theta)\left(1 - \frac{N \chi_i |\psi_i|}{M_{tc}}\right) \quad [3.28]$$

Two simpler definitions of M_i for general sands are also widely accepted:

$$M_i = M(\theta)\exp(\mathrm{m}\psi) \text{ (Li \& Dafalias 2000)} \quad [3.29]$$

$$M_i = M(\theta) + \mathrm{m}\psi \text{ (Manzari \& Dafalias 1997)} \quad [3.30]$$

where m is usually taken as 4 for sands.

3.2.9 Hardening and softening law

So far the boundaries (yield surface and the internal stress cap) between elasticity and plasticity, and the final destinations of strain increments (the critical state) are determined. The remaining problem is how these boundaries evolve with strains – the hardening rules.

- Hardening of the yield surface

The basic idea of the hardening rule can be summarised as, when using deviatoric strain increment $\dot{\varepsilon}_q^p$ as the integration step, the deference between the current size p_i of the yield surface and the maximum allowed size $p_{i,max}$

$$\dot{p}_i = H\left(p_{i,\max} - p_i\right)\dot{\varepsilon}_q^p \quad [3.31]$$

where H is one of the input model parameters. As the stress increment ratio $\dot{p}_i / p_i$ will be used in the later deducing of the plastic strain increments, for convenience, the hardening rule is preferred to be written as the form of a stress ratio:

$$\frac{\dot{p}_i}{p_i} = H\left(\frac{p'}{p_i}\right)\left(\frac{p_{i,\max}}{p'} - \frac{p_i}{p'}\right)\dot{\varepsilon}_q^p \qquad [3.32]$$

It can be see that because the shear strain increment $\dot{\varepsilon}_q^p$ is used, the plastic strain vectors can safely pass the image point before reach the critical state during hardening while the hardening is forced to stop at the image state (where $\dot{\varepsilon}_p^p = 0$) if the volumetric strain increment is used. The term $p_{i,\max}$ in the hardening rule does not indicate the limit size of the yield surface but the maximum p_i value for the current stress state (the yield surface can still harden). Taking consideration of the lode angle and the shear stress, and for a better fit of the experimental data, Equation [3.32] is further improved as

$$\frac{\dot{p}_i}{p_i} = H\left(\frac{p'}{p_i}\right)^2\left[\exp\left(\frac{-\chi_i\psi_i}{M_{i,tc}}\frac{p_i}{p'}\right)\right]\dot{\varepsilon}_q^p \qquad [3.33]$$

where the term $M_{i,tc}$ is the value of M_i under the condition of triaxial compression and can be approximated as $\chi_{tc} / \mathrm{M}_{\mathrm{tc}} \approx \chi_i \mathrm{M}_{i,tc}$ (see Equation [3.21]). The Norsand hardening rule differs from the hardening rules of conventional critical state models by using H and p_i instead of λ (the slope of the critical state), which gives the capability of modelling contraction and dilation according to the state parameter but not the unique critical state, thus the strain increment vectors can safely pass the image state before reaching the critical state.

- Softening on internal cap

To prevent the stress state from touching the dashed curve in Figure 3.13, as discussed in Section 3.2.7, the stress limit is assumed to be a vertical line (the internal cap) which should be counted as part of the yield surface. Stress evolution on the internal cap can be induced by both unloading and constant loading (for example increase of pore pressure with constant overall load under undrained conditions). Yielding of the internal cap will shrink the size of yield surface and cause softening, and should be related to the previous loading step that generated the current internal cap. Therefore a softening rule of the internal cap derived by Jefferies (1997) based on the sand behaviour will be included in the present model

$$\dot{\varepsilon}_p^p = -\frac{1}{H_u}\frac{\dot{p}'}{p'}\ln\left(\frac{p_{w0}}{p'}\right) \qquad [3.34]$$

where H_u is the softening parameter for unloading and is set as an input parameter; p_{w0} is the stress wall where the internal cap is reached for the previous loading step. According to the above softening rule, the larger the difference between the current stress level and the stress point of first yield, the quicker the plastic strain grows. To avoid the problem of D^p being close to zero causing infinite plastic shear strain increment, Equation [3.34] is rearranged as the form of using $\dot{\varepsilon}_q^p$ as the increment step:

$$\dot{\varepsilon}_q^p = \frac{1}{H_u}\frac{\dot{p}'}{p'}\ln\left(\frac{p_{w0}}{p'}\right) \qquad [3.35]$$

Again, for the convenience in deducing the plastic strain increments, the softening rule is preferred to be written as the form of stress ratio, from Equation[3.17]:

$$\dot{p}_w = \frac{\dot{p}_i}{\exp\left(-D_{\min}^p / M_i\right)} \qquad [3.36]$$

During yielding of the internal cap, the confining stress equals to the current internal cap, therefore

$$\frac{\dot{p}'}{p'} = \frac{\dot{p}_w}{p_w} \qquad [3.37]$$

From Equation [3.35] to [3.37]

$$\frac{\dot{p}_i}{p_i} = \frac{H_u}{\ln\left(\frac{p_{w0}}{p'}\right)}\dot{\varepsilon}_q^p \qquad [3.38]$$

It should be noted that during yielding of the internal cap, normality no longer applies, as the direction of the plastic strain increment is obviously not normal to the internal cap (a vertical straight line) anymore, thus the plastic potential is not consistent with the internal stress cap. During unloading, the Norsand considers not only elastic strains, but also plastic strains due to yielding of the internal cap which is already a big advantage compared to other conventional elasto-plastic models, however, Equation [3.38] is no more than an approximation of the actual softening rule for sand, because the recovery of non-elastic stored energy is not considered (Jefferies 1997). The non-elastic energy can be generally explained as the released energy from sand particles falling back to their original positions due to

relaxation of the stress during unloading, this energy is non-elastic during stress relaxation because it cannot be calculated according to the strain increments. Also, there is very little test data on researching the internal cap available thus the softening rule of the internal cap needs further study and refining.

3.2.10 Elasticity

So far there are only seven input parameters introduced in the sand model, all of them fundamentally linked with the sand plastic behaviour and have physical meanings. As for the plasticity, the elastic part is assumed to be isotropic to avoid unnecessary complexity. It is true that the more detailed the more geotechnical aspects can be covered, however, currently for practical underground engineering purposes, an isotropic sand model with fewer input parameters which is simple in application and implementation is likely to be more attractive than a complicated anisotropy model with dozens of input parameters.

The elastic property of Norsand involves isotopic shear modulus and bulk modulus. A stress dependent shear rigidity I is adopted to produce the shear strains:

$$I = \frac{G}{p'} \qquad [3.39]$$

where G is the elastic shear modulus that can be determined from various of laboratory tests.

From Figure 3.6, it can be seen that the unloading-reloading describes the dimensionless bulk modulus of the soil. By assuming isotopy we can easily conclude that:

$$\frac{\kappa}{1+e} = \frac{p'}{K} \qquad [3.40]$$

where κ is the slope of the unloading-reloading line in Figure 3.6; K is the elastic bulk modulus. Using a constant Poisson's ratio v, the two elastic modules can be related by:

$$K = I\frac{2(1+\nu)}{3(1-2\nu)}p' \qquad [3.41]$$

3.3 Determination of input parameters

For numerical modelling of sand behaviour, the Norsand model requires eight input parameters to describe the soil behaviour over ranges of accessible initial void ratios (varying

ψ_0 values). The parameters Γ and λ are used to define the critical state (where the sample experiences infinite shear strain without change of volumetric strain) of the soil sample. Four properties: M_{tc}; N; H_h (H_u during unloading) and χ_{tc} define the plastic behaviour after the yield surface / internal cap reached. Two parameters I (or G) and Poisson's ratio v define the elasticity. All the eight parameters can be determined from conventional drained triaxial compression tests. The input model parameters of the Toyoura sand which is a typical Japanese lab sand will be determined in the following sections by using the standard procedures, together with discussion of the determinations of the input model parameters. The test data used in this study is from the open source data base of a civil engineering consulting company – Golder Associates. The full test data set is downloadable from http://www.golder.com/.

3.3.1 The critical state line (CSL)

As Γ and λ are the altitude (the void ratio when $\ln p_0$ =1kPa) and the slope/ curvature of CSL respectively, the determination of Γ and λ is actually the process of determine the critical state. The following two phases can be used as a standard procedure to locate the CSL:

Phase 1: Three undrained tests at initial void ratios equivalent to a relative density of 10%, 20% and 30% (Jefferies & Been 2006). Initial confining stress of these undrained tests is suggested to be around 350 kPa. Two drained tests are then performed with initial void ratios equivalent to 20% of the reference density; One with an initial confining stress of 200 kPa while another one with an initial confining stress of 800 kPa. The lower stress drained test can be used as a check and the end of the test should locate close to the critical state defined by the previous undrained tests. The high stress drained test is there to extend the critical state to a stress level of about 1000 kPa, which is the upper bound of usual practical interest.

Phase 2: Further three or so tests with initial void ratios and confining stresses well spread throughout the range of the estimated critical state line defined by previous tests. The purpose of these tests is to give a uniform distribution of the data points to draft the CSL and to give higher level of accuracy on positioning the CSL.

Following the above procedure, for determining the critical state of the Toyoura sand, data from six undrained triaxial compression tests with initial void ratio ranges from 0.89 to 1.09 and confining pressure at 500 kPa and 600 kPa are used. Five drained triaxial tests with initial void ratio ranges from 0.65 to 0.84 are involved (Details of the procedure can be seen in

Figure 3.17). All the selected tests are with confining pressure below 1000 kPa, as for tunnelling in soft ground it is unlikely that a mean stress *p'* larger than 1000 kPa can be encountered. For discussion, data from two undrained tests are plotted in Figure 3.14 (a) and (b) followed by a drained test plotted in Figure 3.16. Note that contraction is taken as negative volumetric strain in the following discussions.

The triaxial test procedure is well developed, thus the accuracy of the test can be guaranteed. However the determination of the critical state involves subjective judgment on the test data thus variations may occur during the determination. It is inevitable that the critical state locus derived by different people may vary to some extent even with same test soil sample, because of different judgement on the critical state, the testing conditions and, mistaking a steady state as the critical state.

According to the undrained data of test GIU_G911 in Figure 3.14 (a), the peak drained shear strength is reached when the axial strain (ε_1) is around 1% followed by softening. At around axial strain is of 10%, the ultimate steady state is reached where it can be concluded that the critical state is achieved. Although certain variation of volumetric strain can occur after 10% axial strain, the amount is relative low and the instability of the soil state is negligible. Therefore the final state of the soil, in the current study, can be obtained by taking the mean values of the test data from after the final steady point is reached (which is the mean values after 10% axial strain in test GIU_G911). For test like CIU_G917 in Figure 3.15(b), the first steady state comes around 7% of the axial strain, but with further progressing of the test, the final steady state is reached when the axial strain is about 17%. The former steady state can be seen as a 'quasi-steady state' (Alarcon-Guzman et al. 1988) and should not be treated as the critical state. For this kind of sample it is important to progress the test to a higher level of strain to avoid missing the real critical state.

The situation for the drained triaxial tests is simpler as the aim is to find the ultimate shearing condition where the increment of the volumetric strain is zero. For instance, in the drained test CID_CPO2 in Figure 3.16, the constant volume condition is reached around ε_1 = 12% which demonstrates the critical state. The details of the triaxial tests used in determination of the CSL are plotted in Appendix A.

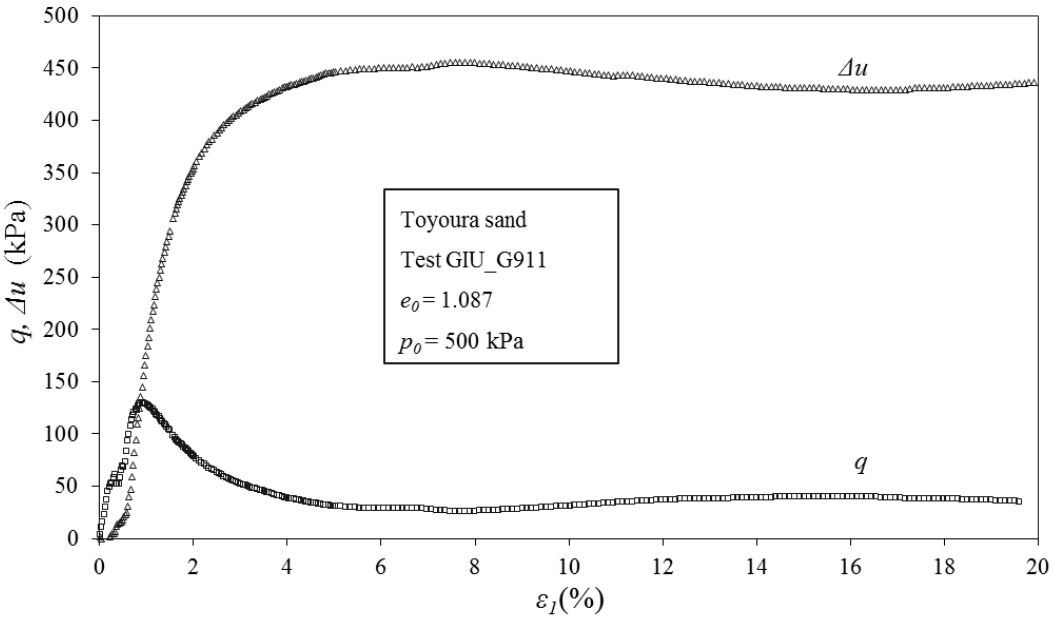

(a)

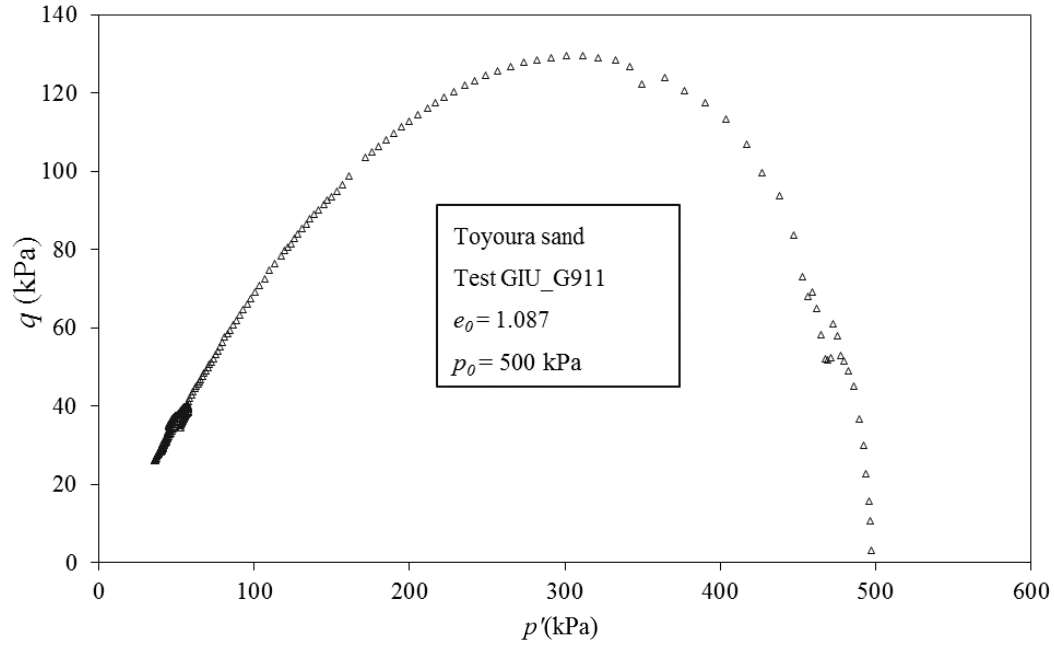

(b)

Figure 3.14 Undrained triaxial tests for determining the critical state.

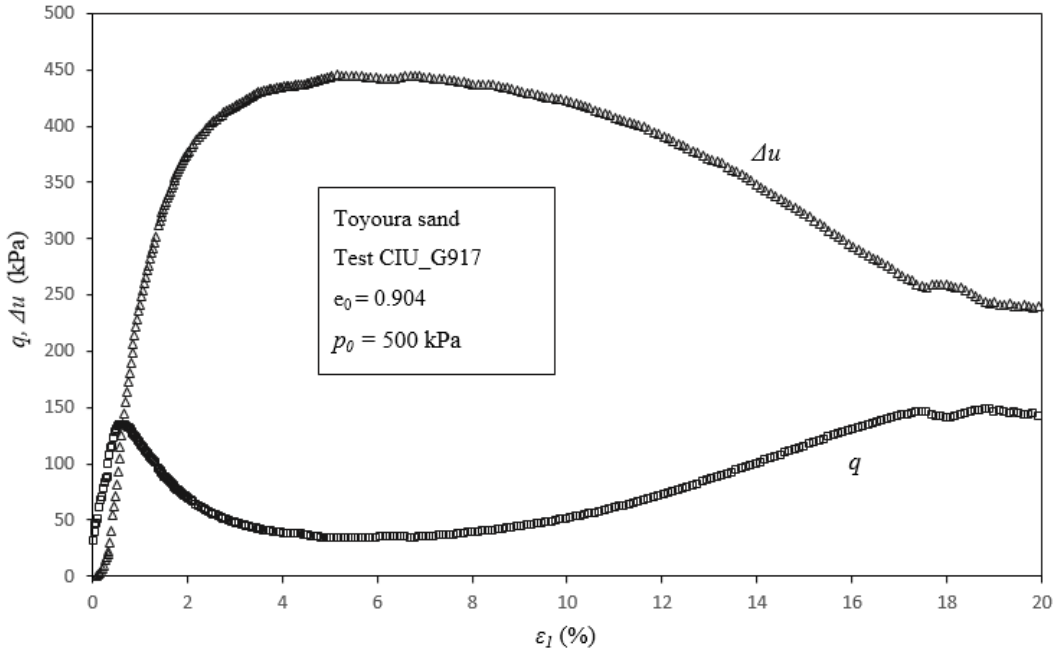

(a)

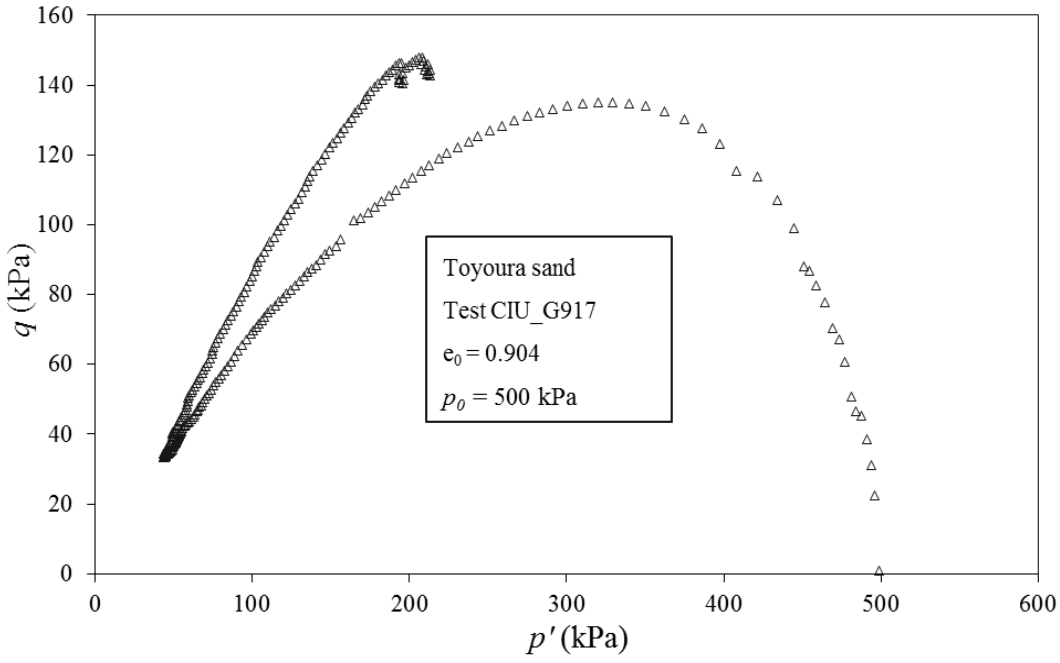

(b)

Figure 3.15Undrained triaxial tests for determining the critical state

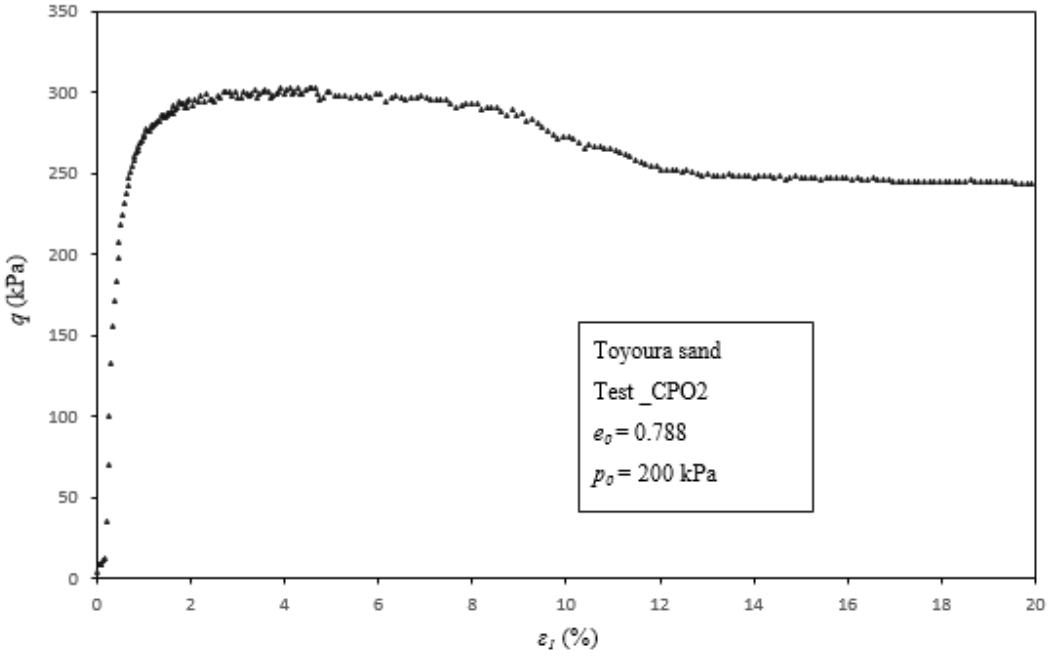

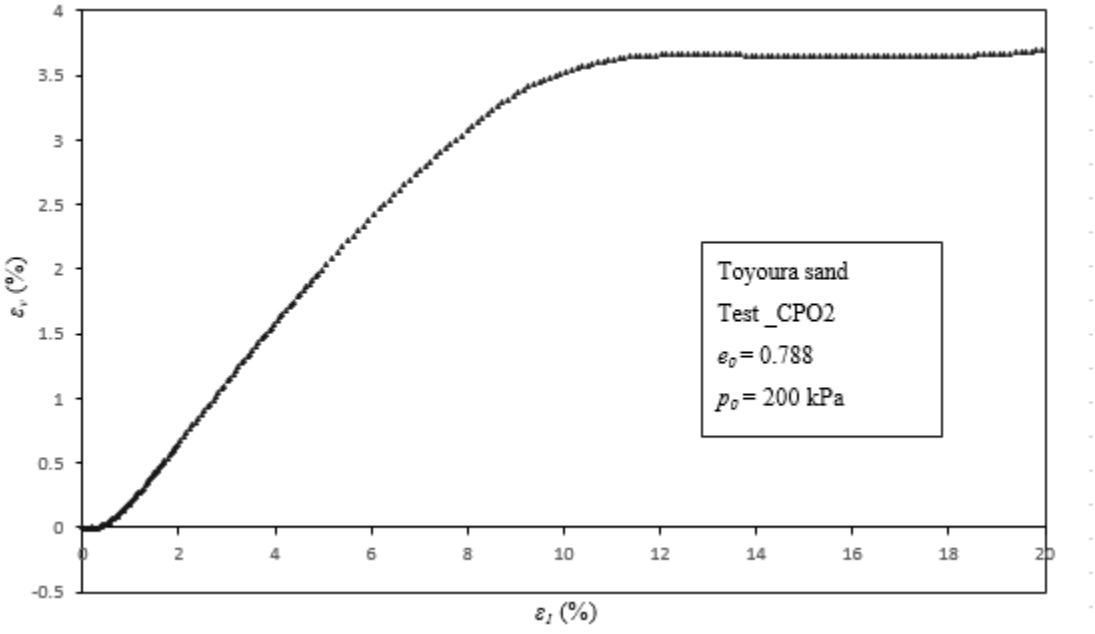

Figure 3.16 Drained triaxial tests selected for determining the critical state.

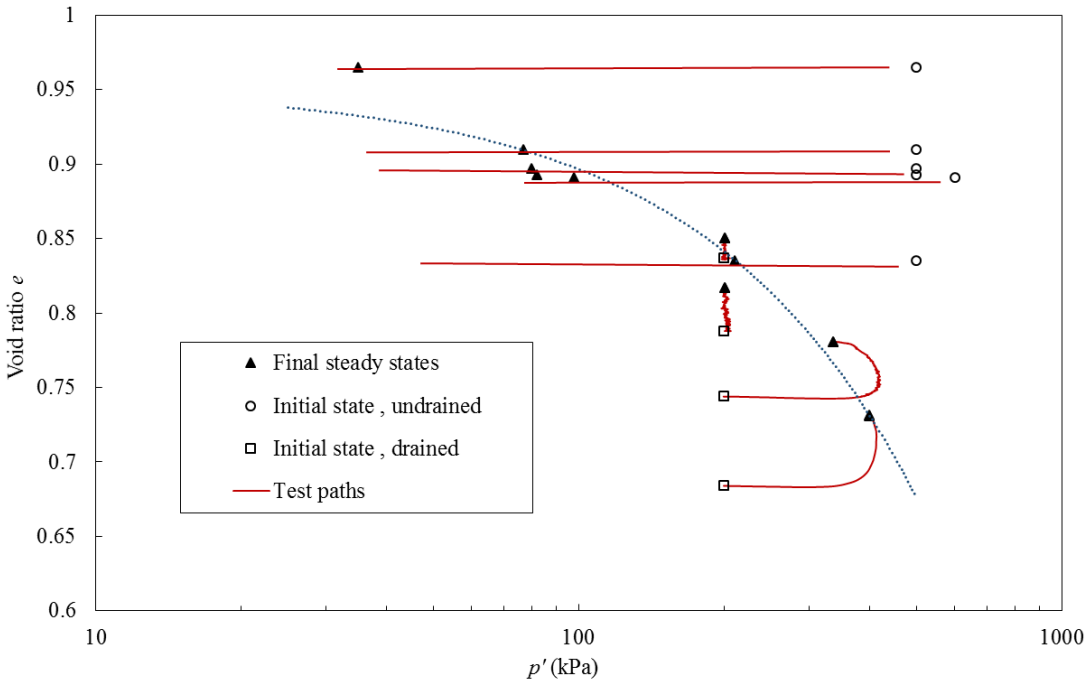

Figure 3.17 Determination of the critical state line in the *e-p'* plane.

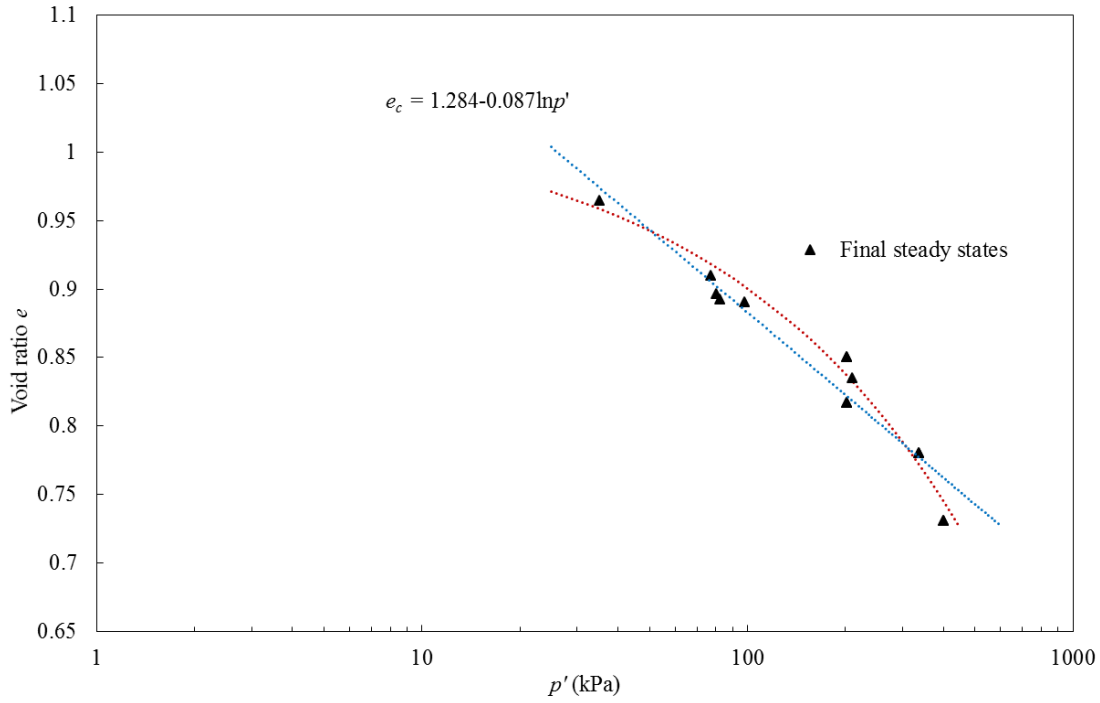

Figure 3.18 The critical state locus in *e*-ln*p'* plane.

Table 3.1 The drained and undrained tests of Toyoura sand used for determination of the critical states (Data from Golder Associates).

Test	Drainage type	Initial conditions			Critical state		
		Preparation method	Initial void ratio v_0	Initial stress p_0 (kPa)	Final steady stress p' (kPa)	Final steady stress q (kPa)	Final steady void ratio v_c
CIU_G911	Undrained	Moist tamped	1.021	500	35	40	0.957
CIU_G915	Undrained	Moist tamped	0.997	500	80	56	0.897
LIQ_905	Undrained	Moist tamped	0.956	600	98	140	0.891
CIU_G917	Undrained	Wet pluviation	0.904	500	210	145	0.835
CIU_G912	Undrained	Moist tamped	1.006	500	77	69	0.91
CIU_G913	Undrained	Moist tamped	0.967	500	82	48	0.893
CID_2A	Drained	Wet pluviation	0.744	200	336	404	0.781
CID_CP6	Drained	Wet pluviation	0.837	200	201	214	0.851
CID_CPO2	Drained	Wet pluviation	0.788	200	201	244	0.817
CID_G460	Drained	Moist tamped	0.684	200	400	603	0.731

The data involved in determination of the critical state is summarised in Table 3.1, and accordingly, the best fit locus of the critical state for Toyoura sand is plotted in Figure 3.17 in the *e-p'* plane. The final steady state values (the critical state values) in Table 3.1 are obtained by taking the average values of data from after the final steady point is reached (for example the critical state void ratio v_c for test CIU_G917 is taken as the average value of v from ε_1 = 17% to ε_1 = 20%). It can be seen from Table 3.1 that a variety of sample preparation methods are used before testing, however there is no large deviation observed from the derived critical locus in Figure 3.17, thus CSL seems to be insensitive to the sample preparation method. Theoretically this makes sense as the ultimate shearing condition for a sand sample should only be related to the texture and shape of the sand particles and the confining pressure in the test, none of which is affected the preparation method.

The determined critical states are plotted in Figure 3.18 and the data fitted with the linear CSL Equation [3.1] and the curved CSL Equation [3.2]. Both of the fittings give generally good agreement with the test data. The coefficient of determination R^2 for the linear relationship is 0.945, while the curved locus gives a better fit of 0.954. Accordingly, the input parameter Γ and λ derived from the fitting is:

- with linear CSL: Γ = 1.284; λ = 0.087
- with curved CSL: Γ_c = 1.03; λ_c = 0.13; ξ = 0.57

3.3.2 The critical stress ratio M_{tc}

Instead of using the widely known friction angle ϕ with constant volume, the Norsand uses a stress ratio to describe the critical state. The critical stress ratio M is expressed as q_c/p_c. From the experience of determination of the critical friction angle ϕ_c, it has been concluded that ϕ_c increases by certain degree in plane strain conditions while under the triaxial extension condition, ϕ_c decreases compared to reality (Jefferies & Been 2006). Because of this variation, it is reasonable to take the triaxial compression condition as the reference condition to determine the critical friction angle ϕ_c. Similarly, take triaxial compression as the reference condition of defining the critical friction stress ratio M_{tc}, where the subscript *tc* indicates the triaxial compression condition. The determination of M_{tc} can be simply done by sets of triaxial drained compression tests on sand samples with different densities. Knowing that

minimum dilatancy occurs at the same point as the sample reaches peak strength (peak stress ratio η_{max}), a value of minimum dilatancy D_{min} at peak stress ratio η_{max} can be deduced from each drained test. According to Equation [3.24], projecting the trend line of the results to zero dilatancy will give the value of M_{tc} and the volumetric coupling coefficient N, as shown in Figure 3.19. The critical stress ratio M_{tc} (intersection of the trend line on the vertical axis) is then derived as 1.31. The parameter N is 0.5. The test data used in Figure 3.19 is summarised in Appendix A.

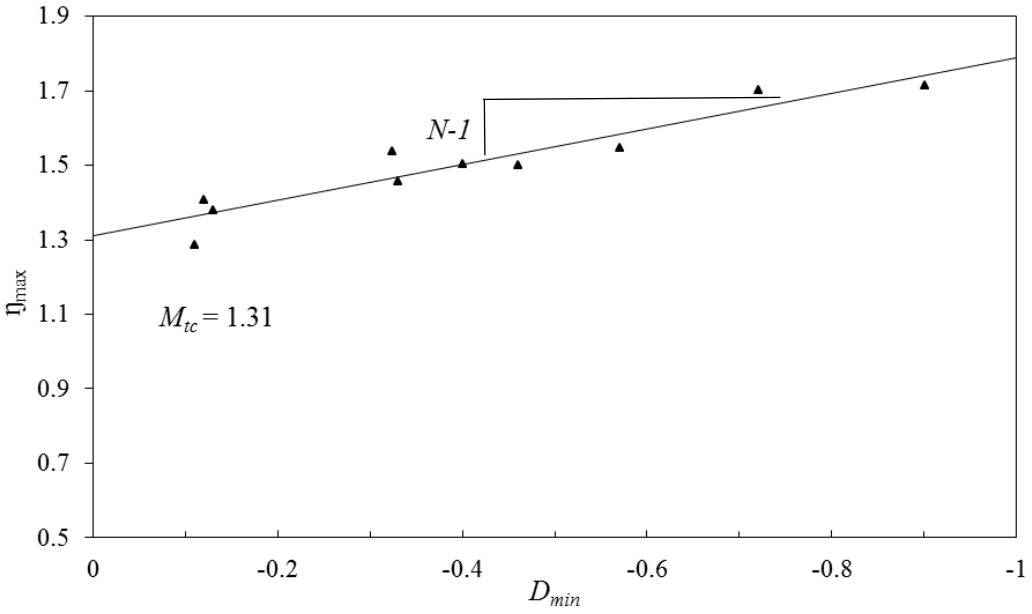

Figure 3.19 Relationship between peak stress ratio and peak dilatancy of Toyoura sand in triaxial compression.

3.3.3 State-dilatancy χ_{tc}

For a sand element that is not on the critical state, in other words the initial state parameter ψ_0 of this sample is not zero, during shearing its volume must change until it reaches the critical state void ratio. From Been and Jefferies (1985), experimental evidence shows that the relationship between the maximum dilation D_{min} (contraction positive in this thesis thus maximum dilation gives minimum value of D) and the initial void ratio is unique, thus it is straightforward to define a relationship between the initial state parameter ψ_0 and the maximum dilation D_{min}. However, dilation is a kinematic result of shearing, the rate of volume change is dependent on the particle geometry and the degree of difficulty of sand particles to move relative to each other, which is affected by the current void ratio (for example well-graded soils are more sensitive to the effect of volumetric strain due to less free

space for particle moving). Therefore it is more reasonable to relate D_{min} with the current state parameter (the void ratio at maximum dilation) as illustrated by Equation[3.21].

From the conventional drained tests, the state parameter at D_{min} can be calculated as the sum of the volumetric strain increments from the start of the test to the moment the maximum dilation is reached. The state dilatancy parameter χ_{tc} can then be obtained by plotting the minimum dilation D_{min} against the state parameter at peak strength ψ_p as shown in Figure 3.20 (theoretically maximum dilation occurs at the same time when the peak stress ratio η_{max} is reached). The test data used for determination of χ_{tc} and the involved calculations are summarised in Table 3.2.

It should be noticed that the peak strength state parameter ψ_p is the difference between current void ratio and the critical void ratio for the current stress level, thus different definitions of the CSL involve various values of χ_{tc}. With the semi-log linear CSL, the derived χ_{tc} is 3.6. As shown in Figure 3.20 χ_{tc} with the power law curved CSL, the data is more scattered and a value of χ_{tc} = 3.2 is given.

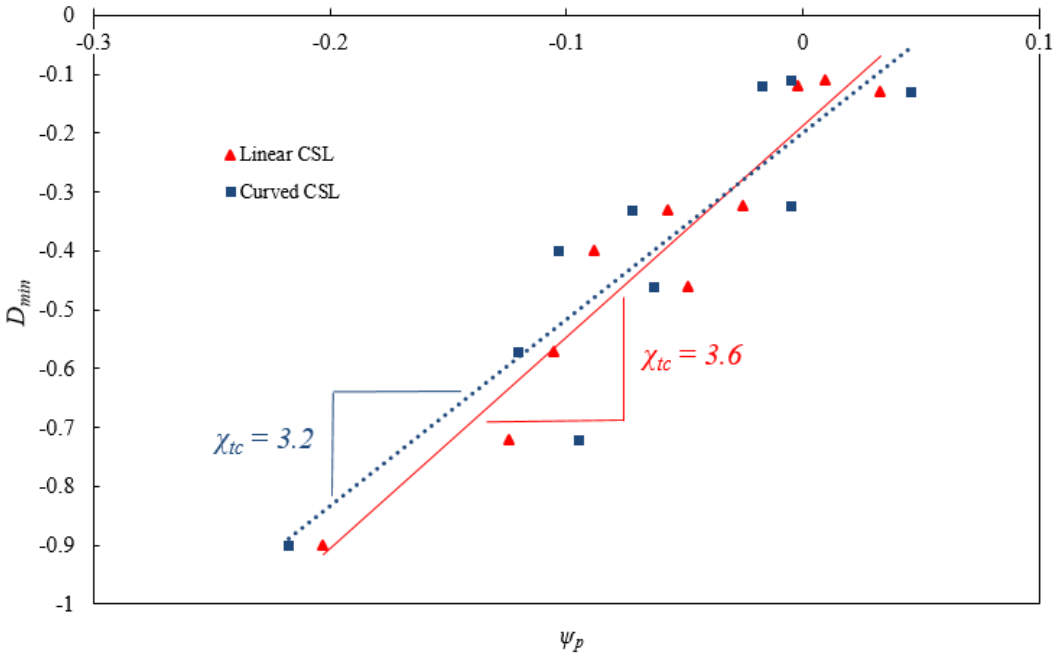

Figure 3.20 Derivation of the input parameter χ_{tc} for Toyoura sand.

3.3.4 The plastic hardening modulus *H*

The hardening modulus H_h for sand typically ranges from 25 to 500. The approximation of H_h can be simply done by taking the value that gives the best fit with the test data. However, to avoid any numerical difficulty, theoretically there is a lower limit for the value of H_h. Although the normal consolidation line – NCL is often assumed to be parallel with the CSL in *v-p'* plane, a fundamental behaviour of sand in reality is that under isotropic compression, eventually the soil will reach the critical state. This phenomenon can be expressed as the NCL in *v-p'* space is necessarily intersected with the CSL as shown in Figure 3.6 (b). Therefore in terms of plastic volumetric stiffness, the NCL should be harder than the CSL:

$$K^p > \frac{1-e}{\lambda-\kappa} p' \qquad [3.42]$$

where K^p is the plastic bulk modulus of normal consolidation and λ and κ are the slopes of CSL and URL in Figure 3.6 (b) respectively. To link K^p with the plastic hardening modulus H_h, with the use of Equation[3.33] and [3.42], after several steps the following limit for H_h can be achieved:

$$H_h > \frac{1}{2(\lambda-\kappa)} \qquad [3.43]$$

3.3.5 Shear modulus *G*

The initial shear modulus G_0 is usually measured on site or through laboratory tests such as bender element or hydrostatic triaxial compression. Onur et al. (2014) summarised several empirical approaches for determining G_0 from different researchers. An empirical expression can be concluded as

$$G_0(\text{kPa}) = A\frac{(B-e_0)^2}{1+e_0} p'^C \qquad [3.44]$$

where *A*, *B* and *C* are empirical constants that depend on the soil type and test conditions. Typically, *A* has a range of 3000 ~ 9000; *B* and *C* are often taken as 2.17 and -0.5 respectively for sands. According to resonant column test data (Onur et al. 2014), the initial shear modulus of Toyoura is measured as around 50MPa ~ 150 MPa with *p'* ranging from 50 kPa to 250 kPa. Although there are studies about the dependence of *G* on both stress and strain level, and

detailed empirical equations were presented by Oztoprak and Bolton (2012), for simplicity of using the constitutive sand model, Norsand applies stress-dependent elastic shear modulus G

$$G = G_0 \left(p' / p_0 \right)^{G\exp} \qquad [3.45]$$

where G_{exp} is the exponent effect of stress level on the shear modulus G_0 during shearing. G_{exp} often taken as 0.5 for sands. An alternative approach to determine the elasticity is to measure the elastic bulk modulus K, which can be directly related to G_0 by using Equation[3.41].

3.3.6 Summary

So far, the major input parameters for the model and the approaches to determine them have been presented. The parameters for Toyoura sand determined using both semi-log linear CSL and the curved CSL are listed in Table 3.3. The typical values of the parameters for normal types of sand are also given. Most of the model input parameters can be determined from triaxial drained and undrained compression tests.

Table 3.2 Drained tests for determination of χ_{tc} (data from Golder Associates).

Tests	Test condition					Semi-log CSL		Power law CSL	
	D_{min}	Volumetric strain ε_p (%)	Initial void ratio e_0	Stress at peak strength p_c(kPa)	Peak strength void ratio e_p	Critical void ratio e_c	State parameter ψ_p	Critical void ratio e_c	State parameter ψ_p
CID_2A	-0.32	1.3	0.744	414	0.734	0.760	-0.025	0.739	-0.005
CID_CP6	-0.11	0.5	0.837	200	0.833	0.823	0.010	0.838	-0.005
CID_CPO2	-0.46	1.7	0.788	200	0.775	0.823	-0.048	0.838	-0.063
CID_3	-0.72	3.5	0.649	460	0.626	0.751	-0.124	0.722	-0.095
CID_CP7	-0.4	1.39	0.745	200	0.735	0.823	-0.088	0.838	-0.103
CID_CPO1	-0.33	1.8	0.78	200	0.766	0.823	-0.057	0.838	-0.072
CID_1	-0.13	1.1	0.81	375	0.801	0.768	0.033	0.755	0.046
CID_CP1	-0.12	1.35	0.832	200	0.821	0.823	-0.002	0.838	-0.017
CID_CP2	-0.57	2.47	0.737	198	0.719	0.824	-0.105	0.839	-0.120
CID_CP3	-0.9	3.3	0.64	203	0.619	0.822	-0.203	0.836	-0.218

The semi-log CSL: e_c=1.284-0.087lnp_c; the power law CSL: e_c=1.03-0.13$(p_c/101)^{0.57}$.

Peak strength void ratio e_p= e_0 - 0.01ε_p* e_0. State parameter ψ_p= e_p-

Table 3.3 Input parameters of Norsand

Parameters	Toyoura sand	Typical values	Remark
Linear CSL			
Γ	1.284	0.9~1.4	'Altitude' of CSL
λ	0.087	0.01~0.07	Slope of CSL
χ_{tc}	3.6	2~5	State-dilatancy
Curved CSL			
Γ_c	1.03		'Altitude' of CSL
λ_c	0.13		Shape factor of curved CSL
ξ	0.57		Shape factor of curved CSL
χ_{tc}	3.2	2~5	State-dilatancy
Plasticity			
H_h	25~500	25~500	Use $H_h=4/\lambda$ as a first attempt of estimation
H_s	50	50	H modulus during unloading. Use 50 as first estimation
M_{tc}	1.31	1.2~1.5	Critical stress ratio
N	0.5	0.2~0.5	
Elasticity			
G_0	50~150Mpa	G_0/p'=100~600	$G = G_0\left(p'/p_0\right)^{G\exp}$
v	0.2	0.1~0.3	

3.4 Applications

Both linear and curved CSL will be used to simulate triaxial drained and undrained tests. The application involves the tests that were used in the determination of input model parameters of Toyoura sand. The input parameters that will be used for Toyoura sand test are the same as shown in Table 3.3. Of course, using different 'best fit' parameters for each single test will give better predictions, however, one reasonable constant set of model parameters for each type of sand may be more meaningful and practical from the view of civil engineers. A Visual Basic code for triaxial test simulation is used in the following discussion. The three commonly used expressions for M_i Equation [3.28] to [3.30] are included in the code with free choice of approach. Equation [3.28] is found to give reasonable fit to most of the data for Toyoura sand and therefore is applied in the following application. The maximum axial strain is set in the code as 0.2 ($\varepsilon_{1,max}$=20%) and the total number of increments is set as 3700 (a number considering the calculation time and continuity of the plots). These two constants can be easily changed in the code according to the study need.

3.4.1 Drained compression tests

To explore the capabilities of Norsand with curved and linear CSL in predicting the drained behaviour of dense sand, four drained triaxial compression tests conducted on dense Toyoura sand are applied in the following validations.

For a certain confining stress level, the theoretical critical void ratio for the curved CSL case is slightly larger than the critical void ratio for linear CSL (within the confining stress range of 50kPa~350kPa for Toyoura sand according to Figure 3.18), thus the initial state parameter ψ_0 applied in these two cases should be adjusted accordingly based on the original test report. Four drained triaxial compression tests are used in the validations. The initial conditions of the tests are summarised in Table 3.4.

Table 3.4 Input initial conditions for numerical modelling of triaxial compression

Test	Initial confining pressure p_0	Initial void ratio e_0	ψ_0 for linear CSL	ψ_0 for curved CSL	Hardening modulus H_h
CID_2A	200	0.744	-0.167	-0.25	120
CID_3	200	0.657	-0.262	-0.389	120
CID_G460	200	0.684	-0.233	-0.335	120
CID_G462	270	0.857	-0.061	-0.1	120

In test CID_3 (Figure 3.21), the laboratory data, interestingly, shows a sudden drop of the shear strength at around ε_1 = 10%, before which the numerical data is generally good. The volumetric strain also tends to become steady after this strength drop. However the numerical result continues with its smooth trend. This quick arrival of the critical state can also be seen in some other tests like CID_CP7 and CID_CP3 (see Appendix A), thus should not be considered as an error in the test procedure. The numerical predictions have not captured these quick arrivals to the critical state, however this type of phenomenon occurs at very large strain level which is way larger than common engineering strain level.

For test CID_2A in Figure 3.22, the numerical result gives slightly lower value of peak strength compared to the test data. After reaching the peak strength, both numerical and test results tend to give gradually decreased deviatoric stress as the soil is softening to the critical state. The data fitting of volumetric strain is generally good. The test data shows a small amount of contraction followed by continuous dilation, which is well represented by the numerical results. Neither the test nor the numerical simulation shows a clear final steady state, this is because the soil has not yet reached the critical state at end of compression where ε_1 = 20%.

Test CID_G460 (Figure 3.23) gives general good agreement between test data and numerical simulation. The only deviation is that the numerical simulation reaches the peak strength slower than the test.

The initial state parameter ψ_0 in test CID_G462 (Figure 3.24) is very close to zero, thus is initially close to the critical state. The numerical simulation predicted the hardening perfectly and reaches the critical state at exactly the same time as the test did. Because the magnitude of the volumetric strain is quite small due to an original ‘close to CSL’ position, thus the

deviations of volumetric behaviour of the three sets of data are relative large compared to the absolute values of ε_v.

Overall, both the linear and curved CSL methods give generally good agreements with the test data. All of the tests had negative initial state parameter, thus the sand samples experienced contraction followed by dilation, but this crucial volumetric aspect of sand behaviour is well modelled by the numerical simulation. One of the tests quickly reach the critical state after a sudden reduction of shear strength while the numerical approach needs more axial strain steps to reach the final destination. However this type of sudden strength drop happens around ε_1 = 10%, which is far beyond general civil engineering concerns.

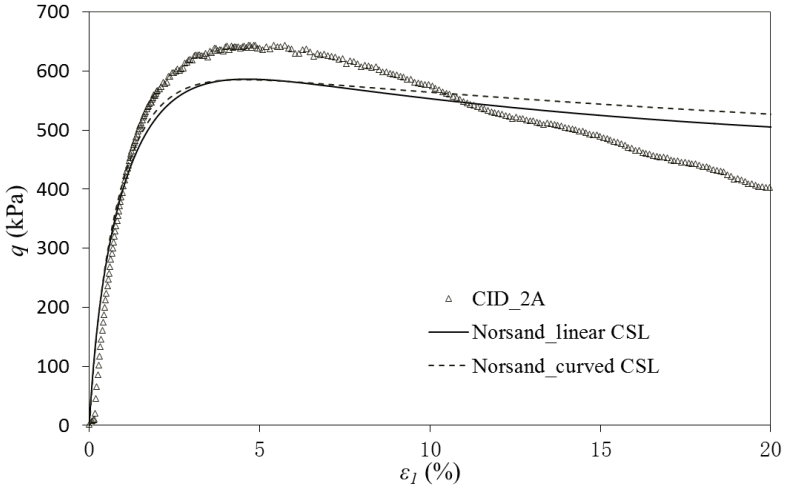

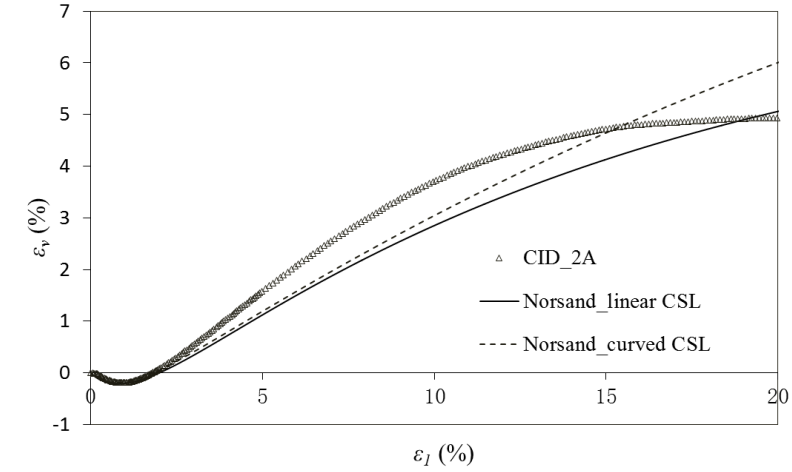

Figure 3.22 Triaxial compression test CID_2A

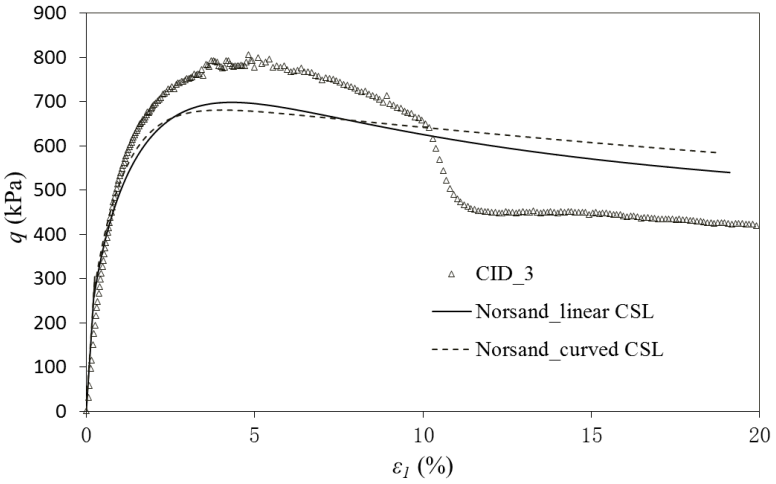

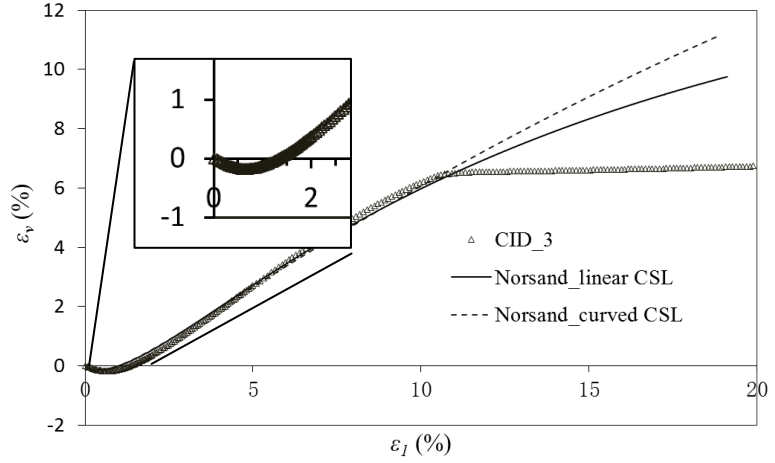

Figure 3.21 Triaxial compression test CID_3

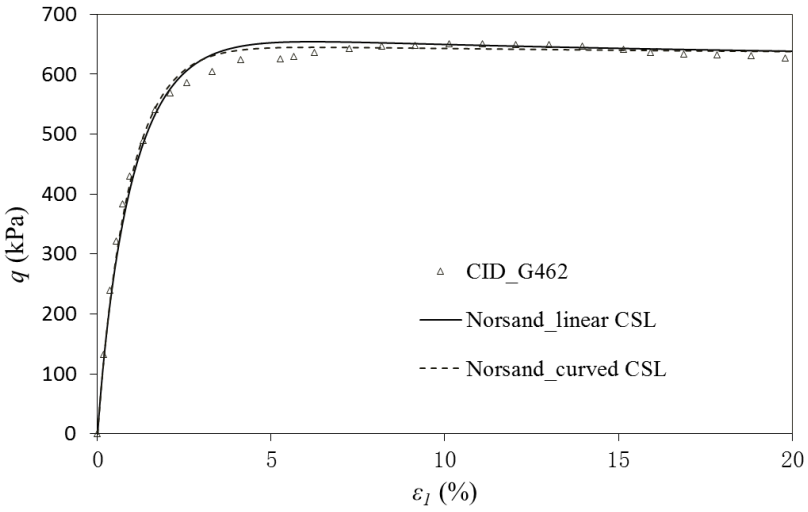

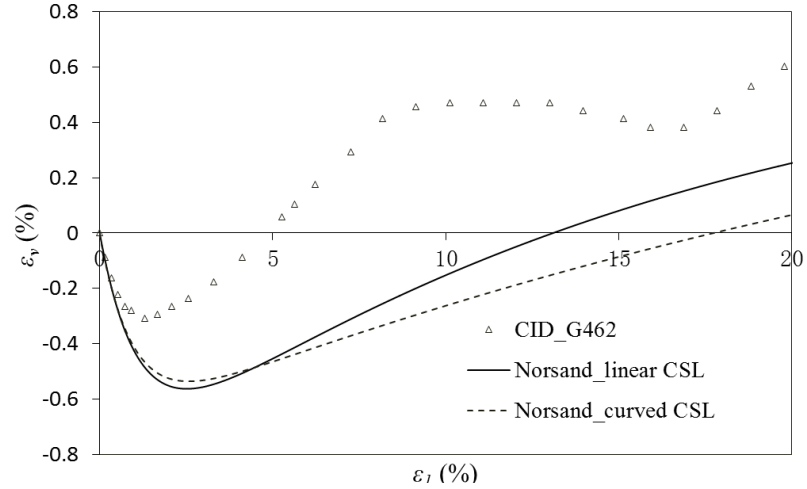

Figure 3.24 Triaxial compression test CID_G462

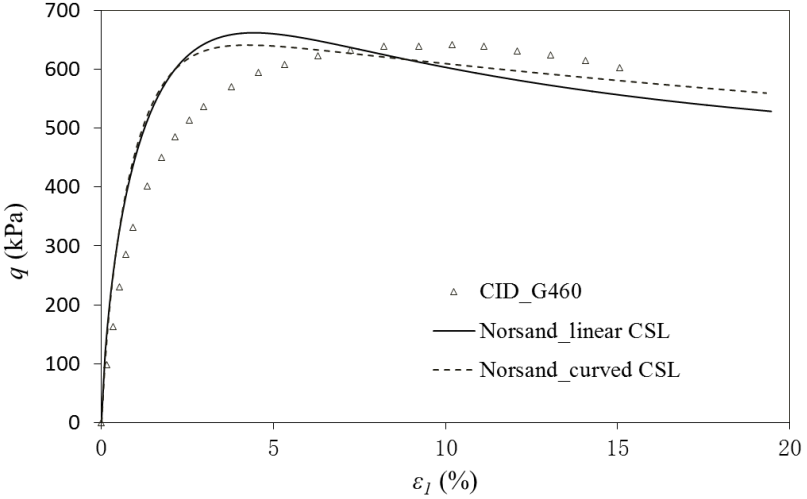

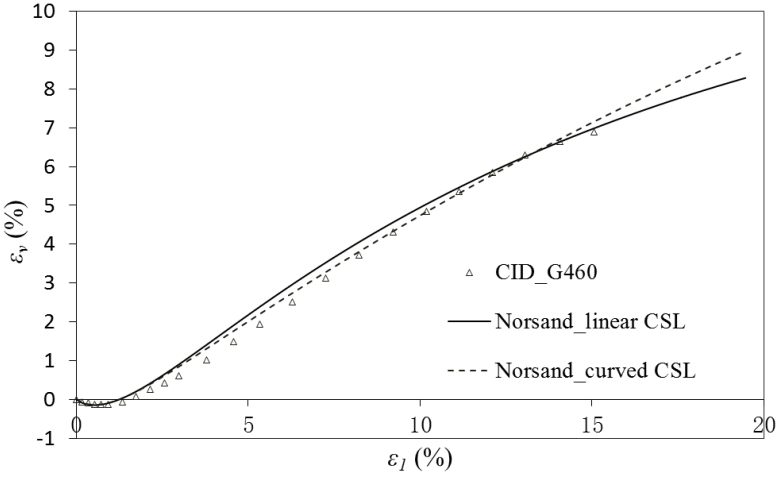

Figure 3.23 Triaxial compression test CID_G460

3.4.2 Undrained compression tests

For undrained conditions, the initial state parameter ψ_0 for linear and curved CSL should also be adjusted accordingly, as in drained triaxial simulations. Three undrained triaxial compression tests are presented here. The initial conditions of the tests are summarised in Table 3.5. Other input parameters remain the same as determined in Section 3.3. The hardening modulus H_h is taken as 65 for the undrained condition of the Toyoura sand to give reasonable numerical predictions. The same value of H_h is applied to all three undrained tests as done to the drained tests. It is meaningless to use different input parameters for the same type of soil just to obtain better data fittings.

Table 3.5 Input initial conditions for numerical modelling of undrained triaxial tests

Test	Initial confining pressure p_0	Initial void ratio e_0	ψ_0 for linear CSL	ψ_0 for curved CSL	Hardening modulus H_h
CIU_G919	500	0.913	-0.05	-0.1	65
CIU_G908	600	1.087	0.11	0.18	65
GIU_G911	600	0.956	0.21	0.295	65

Figure 3.25 ~ Figure 3.27 illustrate the stress path and stress-strain relationships of the undrained tests of Toyoura sand. Test GIU_G919 is with an initial state parameter smaller than zero whereas tests GIU_G908 and GIU_G911 both have positive ψ_0 values (initially looser than the critical state void ratios) thus have similar stress paths and stress strain curves. The numerical prediction also shows these phenomena.

The numerical simulation predicts the stress strain relationship very well when the strain level is smaller than 3%. The stress strain curves of the undrained tests all, to a certain extent, show a temporary steady state – the quasi-steady state before reaching the critical state stress q. Norsand hardly captures this feature so the three sets of data become more scattered at larger strain levels. In tests GIU_G919 and GIU_G911, the linear and curved CSL approaches tend to form an envelope (linear CSL as the upper bound with curved CSL forming the lower bound) within which the critical stress q is finally located.

The stress paths predicted by both linear CSL and curved CSL agree quite well with the test data. The critical stress ratio of all three tests is concentrated at the value of 1.31, which is the exact theoretical value used for the input parameter M_{tc}.

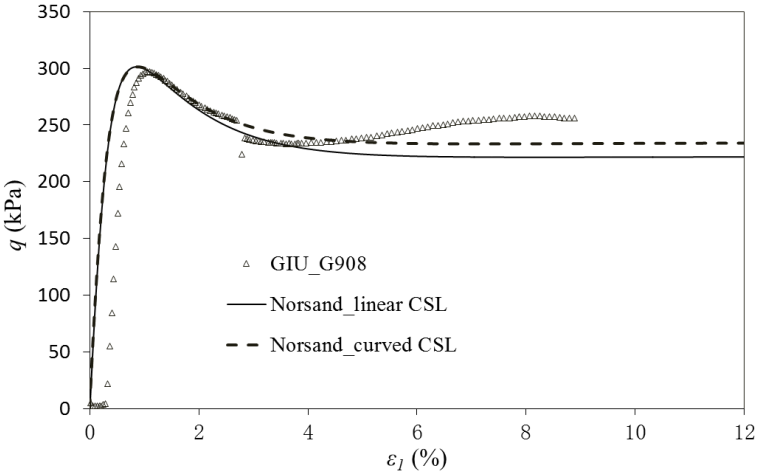

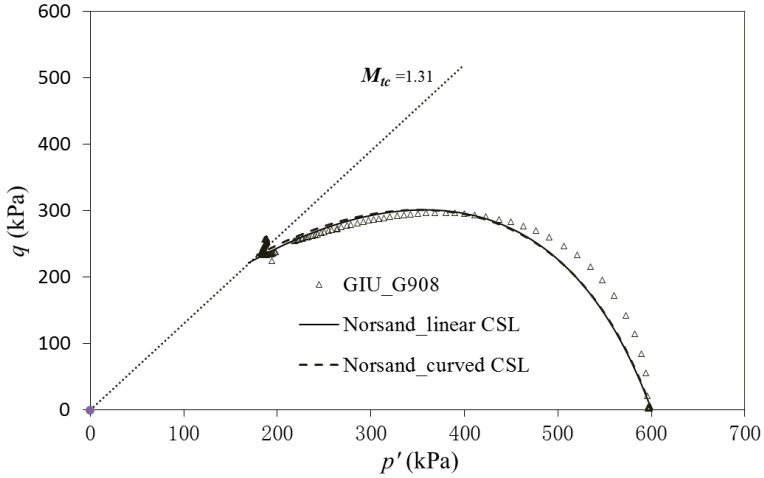

Figure 3.26 Undrained triaxial test GIU_G908

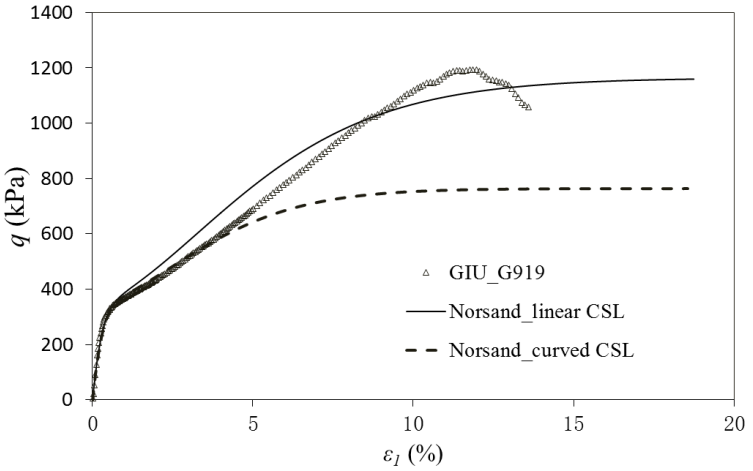

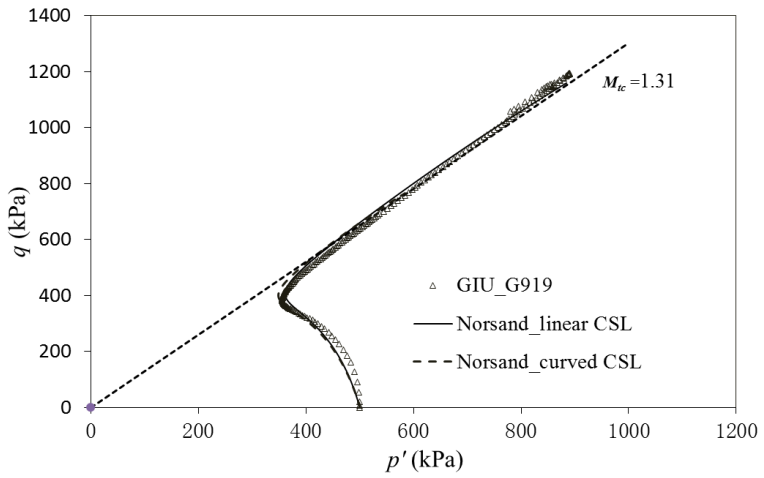

Figure 3.25 Undrained triaxial test GIU_G919

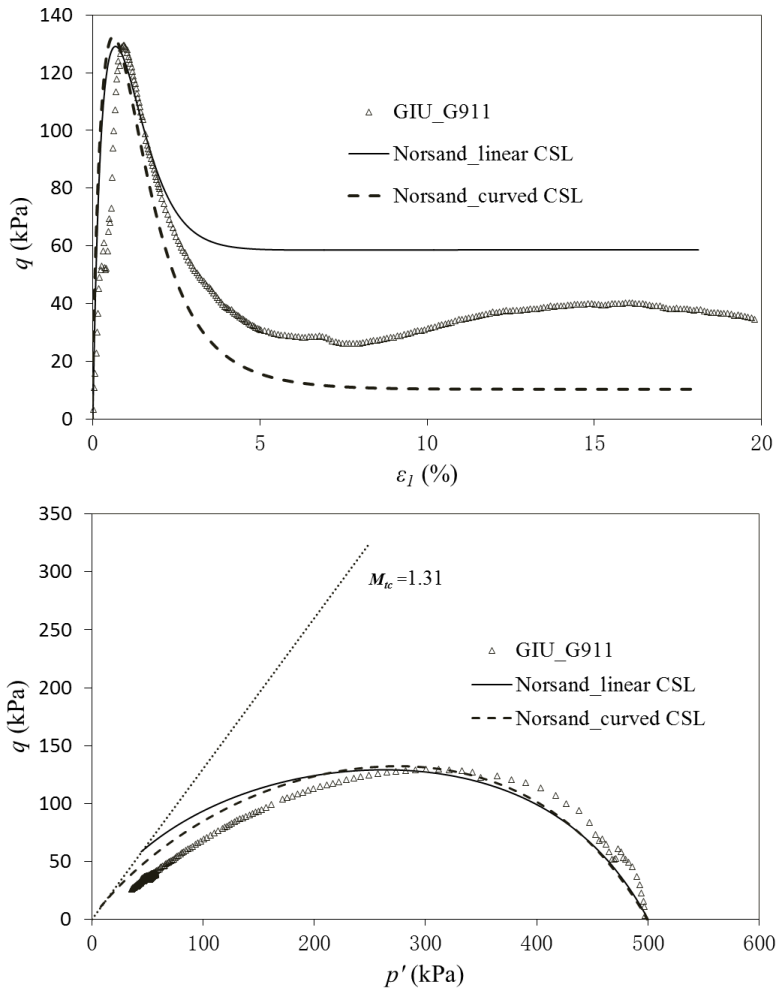

Figure 3.27 Undrained triaxial test GIU_G911

3.5 Summary

The starting point of developing and validating a constitutive soil model is to assume it will be applied to realistic industrial projects, where fewer and simpler parameters are preferred. The original Norsand model introduces only eight parameters to describe the fundamental features of sand behaviour such as stress dilatancy, critical state (ultimate shearing) and softening during unloading. All these input parameters have clear physical meanings and can be determined from simple laboratory tests. Based on laboratory data, without severely losing accuracy, certain approximations were made for the purpose of simplicity and feasibility:

- The internal stress limit is simplified as a vertical straight line in the p'- q / $\varepsilon_p^p - \varepsilon_q^p$ plane.
- In the derivation of the softening rule, the non-elastic strain-independent energy dissipation during shearing is ignored.
- Anisotropy is not considered.

Both linear and curved CSL are considered in this study and all the input parameters of the model are summarised in Table 3.3. Determination of the input parameters is quite straightforward, most of them can be determined from conventional triaxial tests. Although the judgement of the exact critical state may vary to a certain extent, it is crucial that the quasi-steady state is not taken as the critical state.

The Norsand with both linear CSL and curved CSL have shown good ability to simulate the drained and undrained behaviour of sand. The peak values of shear strength and subsequent softening are properly replicated by both drained and undrained simulations. The unexpectedly quick approach to the CSL in drained tests and the quasi-steady states in undrained tests are not captured and thus remain for further theoretical study. Overall, within practical engineering strain level, Norsand with either curved or linear CSL is capable to give meaningful predictions of drained and undrained sand behaviour. There is no obvious evidence telling which type of CSL is better; the choice is totally dependent on which locus fits the available data better. It is crucial to remember that the values of initial state parameter ψ_0 for linear CSL and curved CSL approaches are different, thus should be adjusted accordingly before switching the applied method.

Chapter 4. A proposed sand model

4.1 Introduction

A description of Norsand and its formulation have been presented in the previous chapter. The linear and curved critical concepts have also been applied in the triaxial simulations. Besides the well-developed critical state and plastic rules, the original Norsand applies a simple stress dependent elasticity (bulk modulus K and shear modulus G). This elastic constitutive behaviour may be considered as insufficient when modelling underground construction issues, where small stain elasticity of soil should be accounted (Burland 1989), as change in direction of the stress evolution, i.e. the reversal of loading, is a commonly seen phenomenon in tunnelling. Many researchers have made certain improvements regarding small strain elasticity to existing constitutive soil models (Hegedus & Cowin 1976; Bolton et al. 1994; Kuwano & Jardine 2002; Kung et al. 2007) and explored the effect of small strain elasticity in tunnelling cases (Brinkgreve et al. 2006 and Kung et al. 2007 among others).

To include the considerations of small strain effect, both small strain elastic stiffness and a stress reversal criteria (the starting point of small strain development) will be added in the original Norsand model. In addition, as the internal stress cap will be reached frequently in tunnelling due to unloading, the associated plastic potential surface in Norsand will be replaced by a non-associated surface to make the model more capable in describing the sand behaviour during plastic softening.

4.2 Elasticity in the proposed model

As discussed in the literature review section 2.4.1, the change of stress direction, or in other words, the stress history, has certain impact on the profile of tunnelling-induced ground movements. However, after monotonic loading, the stress state immediate after the stress direction change is very likely to be located within the yield surface, thus the stiffness of soil is usually treated as linear under this circumstance which conflicts with real soil behaviour. On the other hand, the effect of the stress direction change on the stiffness will gradually decrease as the strain level goes further from the direction change point (Atkinson et al. 1990). Therefore, the stiffness immediately after a stress direction change can be considered as ‘small strain stiffness’ in terms of monotonic loading even though the total strain level may not be small in absolute terms.

4.2.1 The small strain elastic modulus

Many studies have tried to use different approaches to fit empirical expressions to the experimental data of small strain stiffness of soil (Burland, 1989;Clayton & Heymann, 2001; Oztoprak & Bolton, 2012). It is clear that the small strain stiffness should be density and stress dependent, thus, in this study it will be related to the current void ratio *e* and the current confining stress *p'*. From the idea of relating the small strain stiffness to void ratio, it is reasonable to start with adding a stress reversal point (large change in direction of stress path, will be mathematically defined in section 4.2.4) related by a factor to the elastic bulk modulus *K*. This idea can be expressed as

$$K = (1+e)\frac{p'}{\rho_r} \qquad [4.1]$$

where ρ_r is a stress reversal factor that is related to the distance between the current stress level *p'* and the stress reversal point in the stress plane. Through detailed studies on the small strain volumetric behaviour of clay and sand, Pestana-Nascimento (1994) developed the following expression for the parameter ρ_r which fits well with the experimental data

$$\rho_r = \frac{(1+\omega_s\zeta_a)}{C_s}\left(\frac{p'}{p_{ref}}\right)^n + D_s\left(1-\zeta_b^r\right) \qquad [4.2]$$

where C_s and ω_s are material constants that control the slope of the shear stiffness – stress curve (The effect of C_s and ω_s is negligible under isotropic loading condition where $\xi_a = 0$; C_s is larger than 1000 for general soil thus $1/C_s$ is negligible when $\xi_a = 0$); D_s and r are material properties which define the slope of the swelling line under isotropic loading condition; n is an exponent index which is often taken empirically as 0.5 for sands. The subscript s indicates the small strain elastic behaviour. p_{ref} is the reference stress value which often set as the atmospheric pressure 101kPa. The parameters ξ_a and ξ_b are used to indicate the distance (this was the original motivation of introducing ρ_r) between the current stress state and the stress reversal point in the following way

$$\zeta_a = |\eta - \eta_{rev}| \qquad [4.3]$$

$$\zeta_b = \frac{\min\left\{p', p'_{rev}\right\}}{\max\left\{p', p'_{rev}\right\}} \qquad [4.4]$$

where η is the current stress ratio; η_{rev} is the stress ratio q/p' at the stress reversal point and p'_{rev} is the confining stress p' at the stress reversal point. It can be seen that at the stress reversal point where $\xi_a = 0$ and $\xi_b = 1$, according to Equation [4.2], the elastic bulk stiffness of soil will only be affected by the material constant C_s. With continuous monotonic loading, the stress state gradually moves away from the stress reversal point and the impact of the increasing offset from the stress reversal point is reflected by ω_s and D_s.

By assuming isotropic and a constant Poisson's ratio v, the elastic shear modulus G is related to the bulk modulus K as

$$G = \frac{1-2v}{1+v} K \qquad [4.5]$$

thus by using Equations [4.1] and [4.2] G can be expressed as

$$G = \frac{(1-2v)}{(1+v)} \frac{p'(1+e)}{\left(\frac{(1+\omega_s \zeta_a)}{C_s} \left(\frac{p'}{p_{ref}} \right)^n + D_s \left(1-\zeta_b^r\right) \right)} \qquad [4.6]$$

At the stress reversal point or the beginning of loading where $\xi_a = 0$ and $\xi_b = 1$, the very small strain shear modulus G_0 becomes

$$G_0 = \frac{(1-2v)(1+e)}{(1+v)} C_s p_{ref}^n p'^n \qquad [4.7]$$

The above equation can be plotted in the logarithmic coordinate of stiffness G_0 against stress level p' in Figure 4.1, which illustrates that the distribution is close to linear (Oztoprak & Bolton 2012).

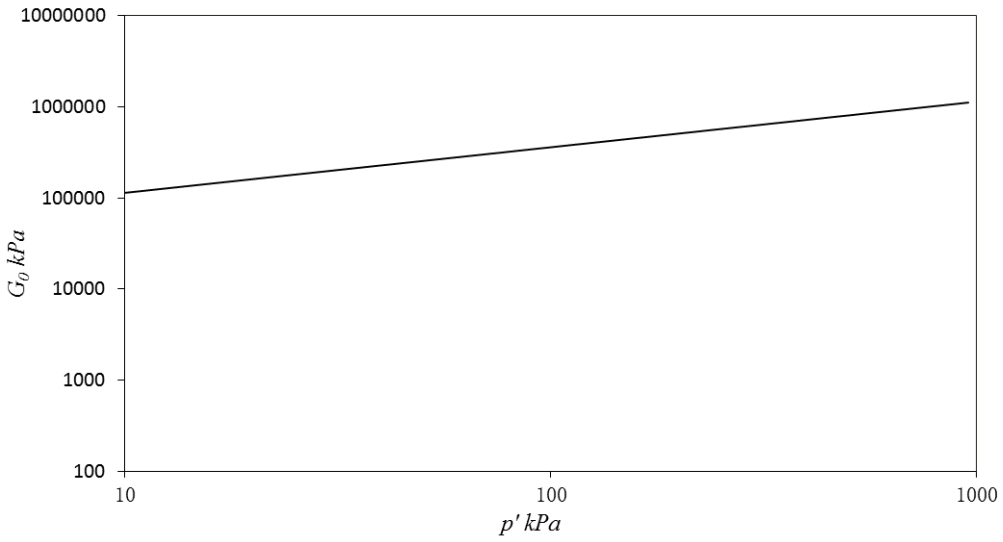

Figure 4.1 Very small strain shear modulus against stress level

4.2.2 The non-linear elastic shear stiffness

From the previous section, there are four small strain stiffness parameters that are needed to be determined before numerical modelling: C_s; ω; r and D_s. Theoretically they can be determined by fitting the elastic swelling line in the *v-p'* space or the stress strain curve in the ε_1-*q* space. As researchers have been much more focused on the small strain shear modulus of different sands, it is more reasonable that the determination of the parameters starts from fitting the experimental G_0 data.

- C_s

Equation [4.7] is a stress and void ratio dependent very small strain (close to the stress reversal point or the start point of monotonic loading) stiffness where the magnitude of the stiffness is controlled by C_s. Oztoprak and Bolton (2012) reviewed more than 70 literatures on small strain stiffness of sands, within which experimental data from 454 tests is presented. The relationships between stress and very small strain stiffness (strain level from 0.0001% to 0.001%) are plotted in the following logarithmic figures, where the vertical axis is G_0v^3/p_{ref} with the stress ratio p'/p_{ref} as the horizontal axis.

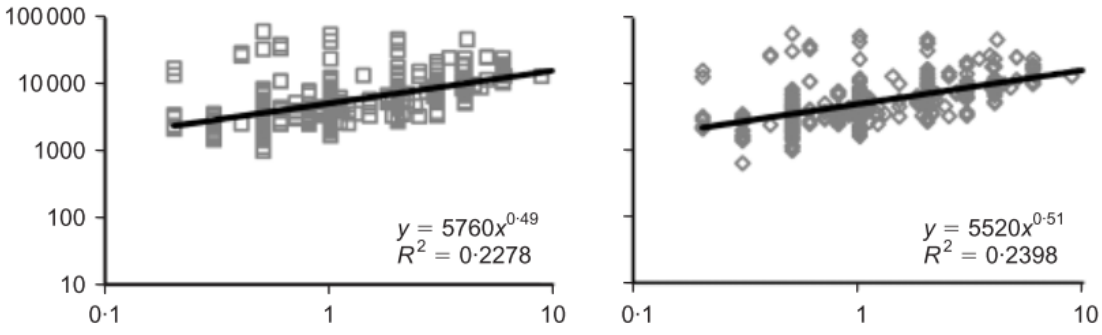

(a) (b)

Figure 4.2 Shear modulus against stress level (Oztoprak & Bolton 2012); (a) ε_1=0.0001%; (b) ε_1=0.001% .

As shown in Figure 4.2 the distribution of the test data from different types of sands together form a linear stiffness/stress distribution, as illustrated by Equation[4.7]. In addition, the average value of the exponent *n* is 0.5 which matches well with the empirical value. Taking the average value of (5760+5520)/2=5640; (G_0v^3/p_{ref} = $5640p'^{0.5}/p_{ref}^{0.5}$) into Equation [4.7], the value of C_s for sands is deduced as

$$C_s = C_i \frac{(1+\nu)}{(1-2\nu)} \cdot \frac{1}{(1+e)^4} \qquad [4.8]$$

where C_i is an empirical shear modulus index which is taken as 5640 for general sands. Therefore, the typical values of the very small strain stiffness G_0 for normal sands can be illustrated in Table 4.6.C_i is set as an input model parameter whose value can be adjusted according to the experimental data or back calculated from known values of G_0 and corresponding confining stress level *p'*.

Table 4.6 Typical values of the very small strain stiffness $G_0$with C_i = 5640.

	p'= 50 kPa			*p'*= 150 kPa			*p'*= 250 kPa		
e	0.6	0.7	0.8	0.6	0.7	0.8	0.6	0.7	0.8
C_s	1721	1351	1075	1721	1351	1075	1721	1351	1705
G_0 (MPa)	97.37	81.17	68.38	168.64	140.60	118.44	217.71	181.51	152.91

- ω_s

During the determination of C_s, the effect of $\omega_s$is negligible, as the stress state is at the stress reversal point (or the start point of loading) where $\xi_a \rightarrow 0$. As the strain level increases, the small strain stiffness become ω_s dependent, thus the value of ω_s can be

derived from fitting the experimental G- ε_1 curve with Equation [4.6]. From Equation [4.2] and [4.4], the effect of D and ξ_b can be isolated by using constant confining stress p' ($p' = p'_{rev}$) during shearing so that the term $D\,(1 - \xi_b^r) = 0$.

The G- ε_1 data from 454 tests presented by Oztoprak and Bolton(2012) covered various types of sands including Toyoura sand, Ottawa sand, Ishikari sand and so on; the database includes a wide range of densities of sand samples from very dense to loose samples; the confining pressure p' ranges from 50kPa to 600 kPa with a mean value of p' = 150 kPa. Therefore the database can be used as a reference for small strain behaviour of general sandy soil. Although a wide variety of samples are included, the scatter of the data is relatively low thus a clear hyperbolic zone can be seen in Figure 4.3.

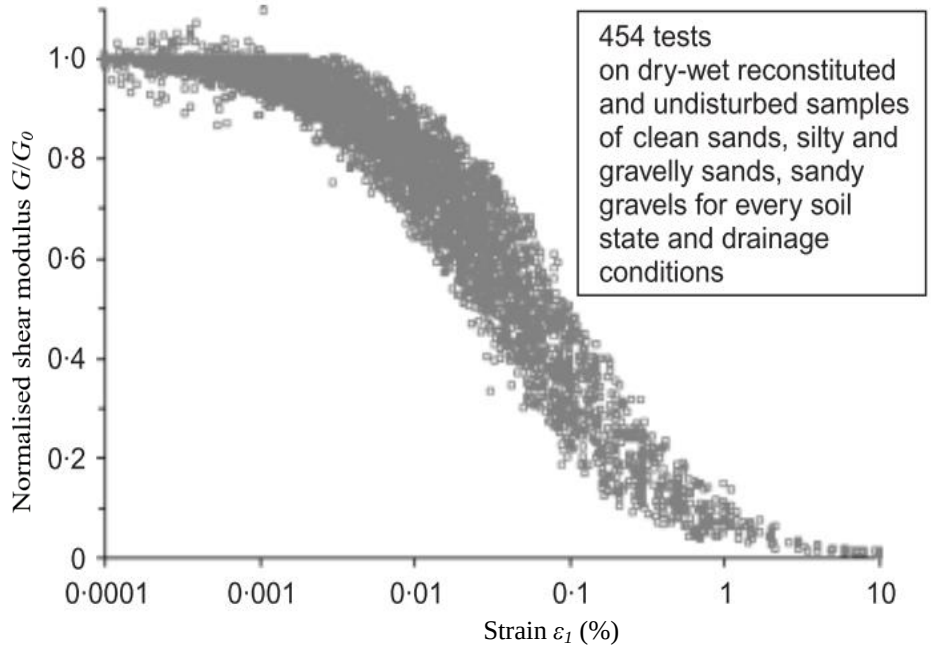

Figure 4.3 Shear modulus versus strain level data. (Oztoprak & Bolton 2012)

In order to mathematically describe the shear modulus degradation zone given in Figure 4.3, a set of best-fit relationships was proposed by Darendeli(2001) as the following hyperbolic form

$$\frac{G}{G_0} = \frac{1}{\left[1 + \left(\frac{\varepsilon_1 - \varepsilon_e}{\varepsilon_r}\right)^{0.88}\right]} \qquad [4.9]$$

where ε_e is a threshold parameter indicating beyond which strain level the shear modulus starts decreasing from its maximum state G_0; ε_r is the reference strain level where G/G_0

= 0.5. To fit the degradation zone in Figure 4.3, the following values of ε_e and ε_r need to be applied:

Upper bound: ε_e = 0.003%; ε_r = 0.1%

Lower bound: ε_e = 0; ε_r = 0.02%

Mean value: ε_e = 0.0007%; ε_r = 0.044%

Note that for $\varepsilon_e > \varepsilon_1$, $G=G_0$ is applied. The above relationships are plotted in Figure 4.4 which illustrates that the hyperbolic equation represent well the experimental data of small strain stiffness.

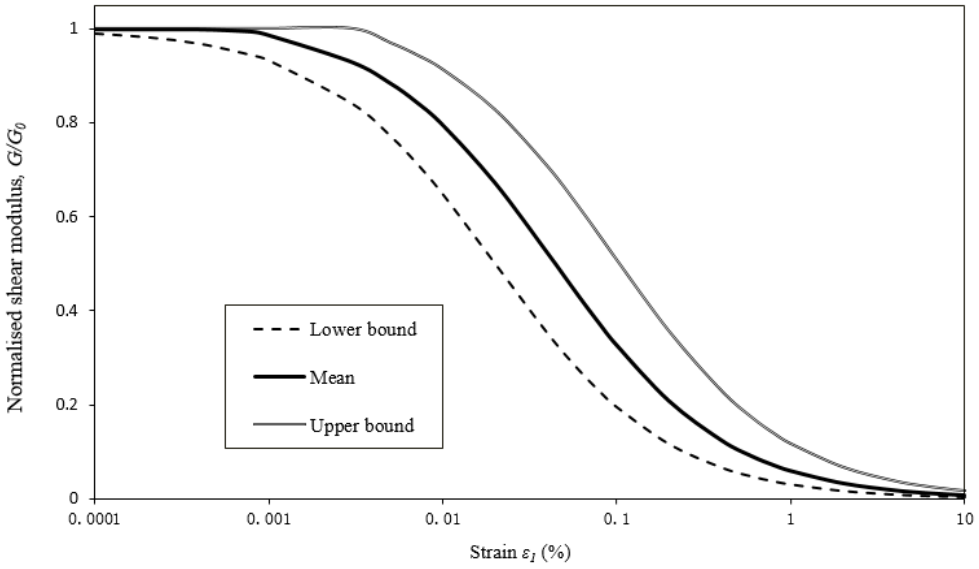

Figure 4.4 The hyperbolic description of small strain shear modulus.

Assuming a direct shear situation, where a constant p' ($p' = p_{ref}$) is applied, by combining Equation [4.6], [4.7] and [4.9], the parameter ω_s is then deduced as

$$\omega_s \cdot \zeta_a = \left(\frac{\varepsilon_1 - \varepsilon_e}{\varepsilon_r} \right)^{0.88} \qquad [4.10]$$

4.2.3 The non-linear elastic bulk stiffness

- D_s and r

With the typical values of C_s in Table 4.6, during isotropic loading, the first term of Equation [4.2] becomes negligible, thus under isotropic loading conditions, the elastic volumetric behaviour of sands can be simplified as the following form (Henkel 1959)

$$\log(\dot{e}) = \kappa\left[\log(p_0^{'}) - \log(p^{'})\right] \quad [4.11]$$

$$\kappa = D_s\left(1-\zeta_b^r\right) \quad [4.12]$$

Equation [4.12] illustrates that under isotropic condition, D_s and r control the slope of the elastic unloading line in *v-p* space. To determine the values of the small strain parameter D_s and r, data of isotropic unloading starting from the normal consolidation line (NCL) would be useful, as the point where the unloading-reloading line (URL) intersects with the NCL (see Figure 3.6b) can be treated as a stress reversal point. The unloading-reloading lines described by Equation [4.12], and how D_s and r affect the curvature of URL is presented in Figure 4.6. Noticing that D_s and r only control the curvature of the unloading line, the values of confining stress and void ratio at the stress reversal point are input values in numerical modelling and can be obtained directly from a previous step of calculation. From Figure 4.6, D_s defines the final slope of the unloading reloading line, r controls how fast the URL is reaching its final slope.

Jefferies and Been (2000) carried out detailed isotropic loading – unloading tests using Esksak 330/0.7 sand and obtained clear unloading-reloading lines as shown in Figure 4.5. In addition, it is worth to mention that Figure 4.5 gives a great example of the infinity of the NCL, as discussed in Chapter 3.

Equation [4.12] was originally developed based on laboratory data from saturated clays, where the slope of the URL is monotonically increasing, with a maximum value of D_s, as the stress level is decreasing. However for sands, as shown in Figure 4.7, as the confining stress approaches low stress level during unloading, the rate of volumetric change tends to decrease, and for those URLs starting from higher stress levels and terminating at low stress levels, the volumetric strain change rate at high stress level is much lower than at the starting point of unloading. Therefore the URLs predicted by Equation [4.12] may not fit the volumetric behaviour for sandy soils. In order to describe the non-linear elasticity of sand, the following relationships are proposed by the Author

$$\begin{aligned} \kappa &= D_s\left(1-\zeta_b^{\alpha}\right) \\ \alpha &= r\cdot\xi_b^m \end{aligned} \quad [4.13]$$

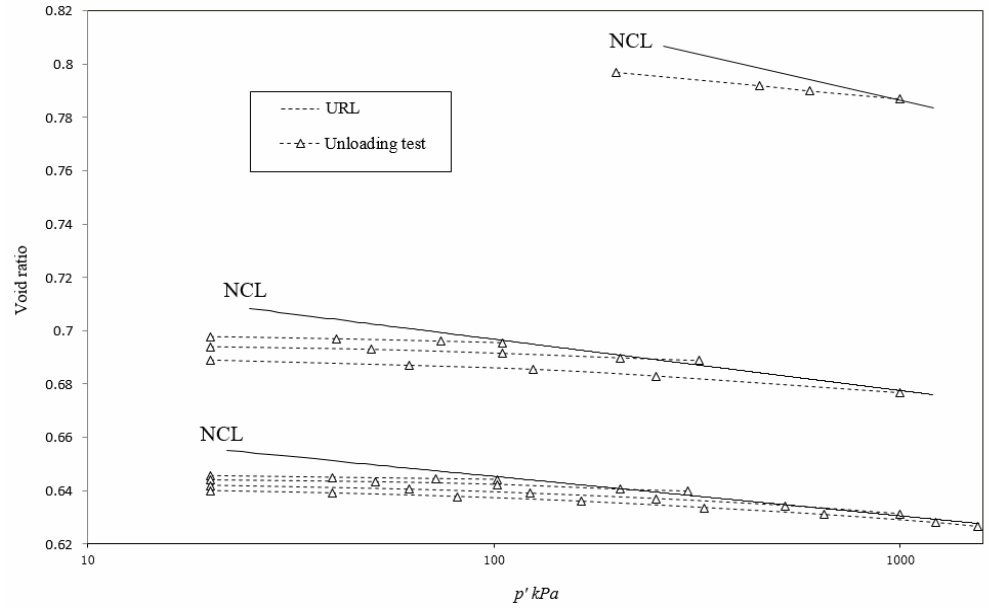

Figure 4.5 Isotropic consolidation and unloading of Esksak 330/0.7 sand. Data from Jefferies and Been (2000)

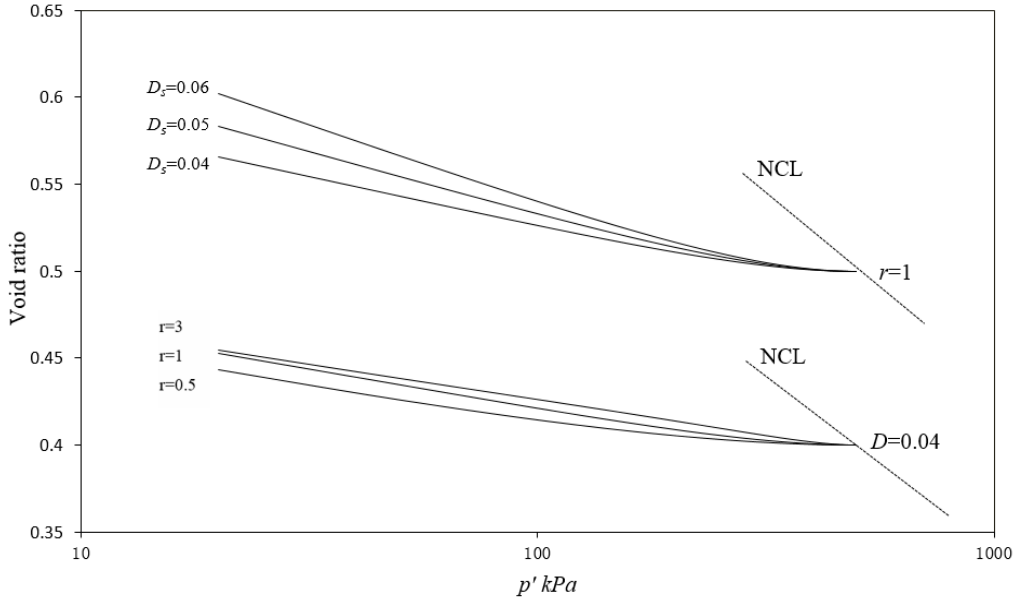

Figure 4.6 The unloading reloading line starting from p' = 500 kPa predicted by Equation [4.12] with stress reversal points at e=0.4 and 0.5 respectively.

where κ is, as usual, the slope of URL, m is an empirical parameter which is taken as 0.55 in this study based on Esksak sand test data. The advantage of using Equation [4.13] instead of [4.12] is that the effect of small strain stiffness is still controlled by the stress state factor ξ_b, while the decreasing slope of URLs of sands is effectively represented by α, thus the non-linearity during unloading can be better predicted. Note that the slope factor κ corresponds to the log$e$-logp' space in this study as most of the literature data was presented in a log-log manner. Comparison between test data and Equation [4.13] is plotted in Figure 4.7, where each sub-figure contains URL(s) generated from one single NCL. Figure 4.7 shows that despite a little scatter, the URLs with void ratio ranges from 0.55 to 0.8 and stress level from 20 kPa to 1600 kPa are generally well predicted by Equation [4.13].

For relatively short unloading paths (short in terms of the difference between the confining stress values at starting point of unloading and end of unloading), the rate of volumetric change increment tends to be constant like the top one or two unloading paths in each of the sub-figure in Figure 4.7. For longer unloading paths, the starting slopes are generally much greater, however they gradually become flat when approaching low stress levels. This makes sense in reality because, for one NCL, it is impossible that a later generated URL intersects with an earlier generated URL, no matter how long the stress span travelled by the later URL.

To cover the general non-linear elastic behaviour of sand, it is unpractical to use a constant pair of D_s and r. For different stress levels and void ratios, different values of D_s and r need to be applied. As illustrated in Figure 4.7, to fit the given test data, r ranges from 0.8 to 3 while D_s has a much smaller magnitude of 0.003~0.05. It can be seen that the parameter r is related to the void ratio; D_s is both void ratio and stress level (the stress reversal point of the URL) dependent. The Author suggests the following approaches for deducing the values of D_s and r,

$$r = r_1 \exp\left(r_2 e\right) \qquad [4.14]$$

$$D_s = D_1 \exp\left[D_2 \ln\left(\frac{p'}{e^3}\right)\right] \qquad [4.15]$$

where r_1, r_2D_1 and $D_2$are empirical parameters for determining r and D_s respectively. Equation [4.14] and [4.15] are plotted in Figure 4.9 and Figure 4.8 together with the best fit values of D_s and r from Figure 4.7.

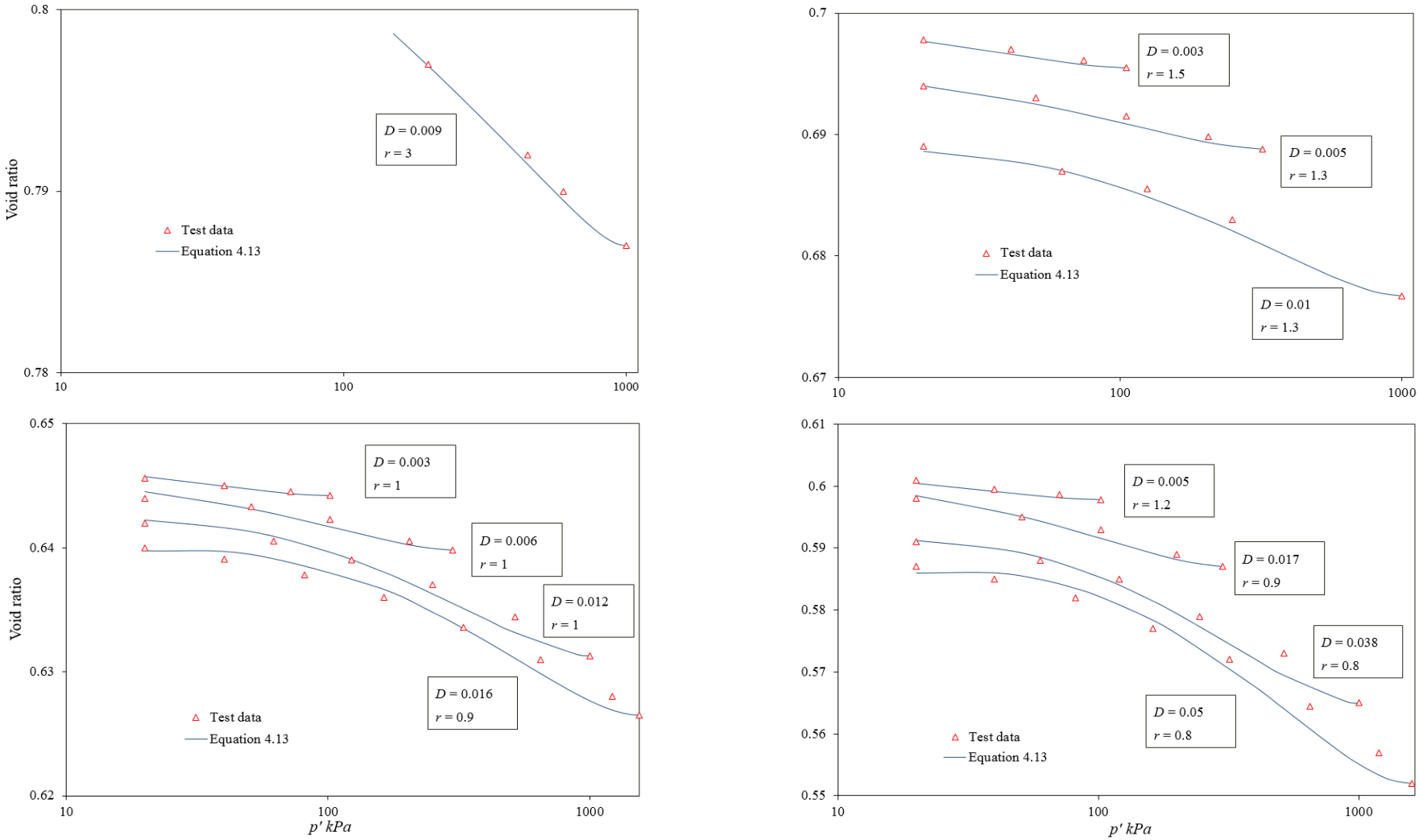

Figure 4.7 URLs experimental data and predictions of non-linear elasticity of sand using Equation [4.13]; m=0.55. Test data from Jefferies and Been (2000)

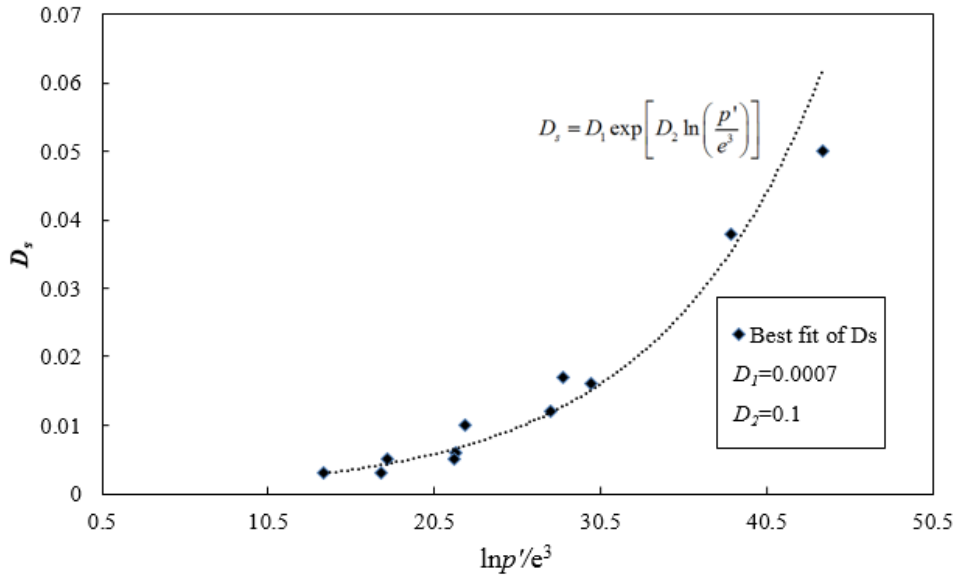

Figure 4.9 The dependence of D_s on stress level and void ratio

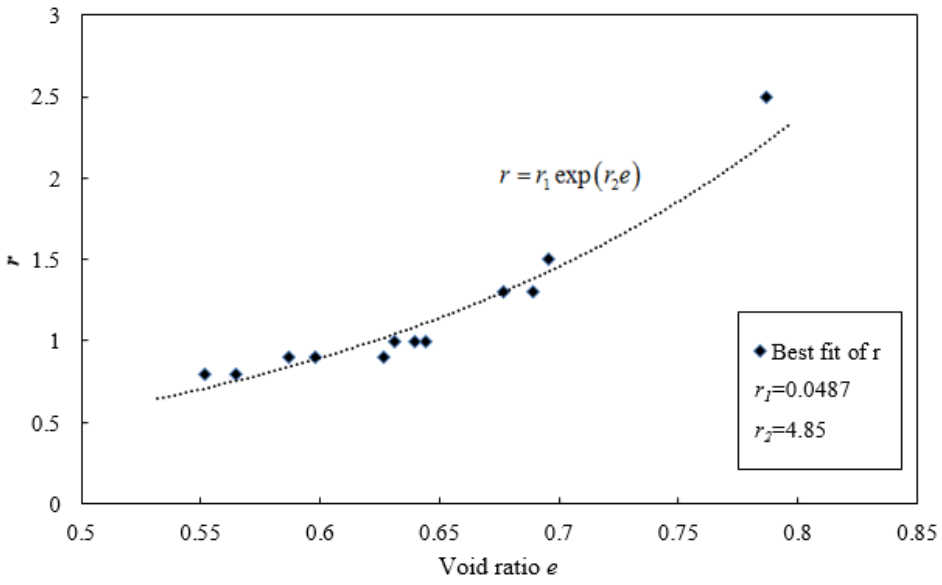

Figure 4.8 The relationship between r and void ratio e.

From Figure 4.8, r_1 is the altitude (where the void ratio is zero) of the r-e curve while r_2 controls the shape. The fitting of r to Equation [4.14] is generally good despite a little scatter where r = 2.5. From Figure 4.9, D_s can be well predicted by relating it exponentially with the lnp'/e^3 ratio. Note that the stress level p' here indicate the stress reversal point where the URL diverts from the NCL. The values of r_1, r_2, D_1 and D_2 should be defined according to the experimental data of isotropic unloading. These parameters will be set as input parameters in numerical modelling.

4.2.4 Change of stress path direction

To apply the non-linear elastic relationships discussed in the previous section, an indication of the stress reversal point is needed. Theoretically this indication can be described by a large stress direction change in the *p'-q* stress space, or a large direction change of strain increment vector in the ε_p-ε_q space. The stress direction change at the reversal point is not necessarily 180 degrees as in isotropic compression changing to unloading. Through laboratory stress path tests on London Clay, Atkinson et al. (1990) concluded that for stress rotation greater than 90 degrees, the subsequent stress strain curve behaves highly non-linearly; the stiffness immediately after the stress direction change is dependent on the stress rotation angle, and can be one magnitude of order higher than the stiffness before the stress rotation. With further loading, the stiffness reduces rapidly, and the effect from the degree of the stress rotation is negligible. This phenomenon can be perfectly described by the stress reversal factor ξ_a and ξ_b discussed in Section 4.2.1. In this study, a stress direction change larger than 90 degree is treated as a stress reversal, the indication of this reversal can be expressed as the following form

$$\left(\dot{p}'_{n+1}-\dot{p}'_{n}\right)^2+\left(\dot{q}'_{n+1}-\dot{q}'_{n}\right)^2\begin{cases}\geq \dot{p}'^2_{n+1}+\dot{p}'^2_{n}+\dot{q}'^2_{n+1}+\dot{q}'^2_{n}, & I_R=True\\ < \dot{p}'^2_{n+1}+\dot{p}'^2_{n}+\dot{q}'^2_{n+1}+\dot{q}'^2_{n}, & I_R=False\end{cases} \qquad [4.16]$$

where n and n+1 represent previous and current load integration steps respectively; I_R=True indicates that stress reversal occurs and the very small strain stiffness (ξ_a = 0 and ξ_b = 1) should apply.

4.2.5 Summary

So far the small strain and nonlinear elasticity have been presented. These concepts will be applied into the Norsand model to give more detailed predictions of small strain stiffness and nonlinear unloading of sand. Note that at the first step of stress integration, the stress state should be treated as a stress reversal point so that the very small strain stiffness applies at the beginning of loading. The author proposed Equation [4.14] and [4.15] to predict the unloading reloading line of sands. Note that the URL here differs the conventional linear unique URL in *v-p* space, as under cyclic loading conditions, the *v-p* curve produced by reloading does not coincide with the *v-p* curve produced by unloading. Although the cyclic loading condition hardly occurs in tunnelling, the stress reversal point will be triggered at least three times in tunnelling cases – (i) initial compression of ground; (ii) unloading induced by excavation; and (iii) reloading caused by installation of supporting system, thus a conventional unique unloading reloading locus does not apply.

From Equation [4.14] and [4.15], the stress reversal factor ρ_r becomes

$$\rho_r = \frac{(1+\omega_s\zeta_a)}{C_s}\left(\frac{p'}{p_{ref}}\right)^n + D_s\left(1-\zeta_b^{\alpha}\right) \qquad [4.17]$$
$$\alpha = r\cdot\xi_b^m$$

The above expression will be applied for deriving the elastic modulus G and K in this study instead of using Equation [4.2] which was originally proposed for Clay. Seven additional input parameters are added in the proposed model

- C_i is the empirical shear modulus index that is related to the very small shear modulus G_0 (sometimes referred as G_{max} by some researchers), a mean value of 5460 for general sands can be applied. Alternatively, C_i can be back-calculated by using known values of G_0 at certain stress level according to Equation [4.7] and [4.8].
- ε_e and ε_r define the elastic shear modulus ratio G/G_0; a set of empirical mean values: ε_e = 0.0007%; ε_r = 0.044% can be applied for general sandy soils.
- D_1, D_2r_1 and r_2 control the elastic bulk modulus during unloading and reloading; the parameter values can be determined by fitting Equation [4.14] and [4.15] with the experimental data of the conventional URLs.

4.3 Numerical implementation of the proposed model

The constitutive equations of Norsand with curved CSL discussed in chapter 3, together with the small strain and nonlinear elastic stiffness presented in the previous section will be implemented into the commercial finite element analysis software Plaxis 3D (creation and revision of constitutive models can be conveniently done in this software, in addition, an implemented constitutive model in a commercial FEM software can be easily accepted by the industry). This chapter will present the process of numerical implementation of the proposed model that has been done in this study. The presentations follow a logic of: stress integration – hardening of yield surface – softening of yield surface. In section 4.3.3 a new plastic potential is applied for a better description of sand behaviour. Details of coding of the proposed sand model using the theory presented in this chapter are given in Appendix E.

4.3.1 Stress increment

The elastic predictor – plastic corrector (EP-PC) method is applied here to deduce the stress increments for each calculation step. The stress increment is firstly calculated based on the elastic stiffness matrix $\mathbf{D^e}$, then corrected to its real value if any plastic strain occur:

$$\dot{\varepsilon}^e = \dot{\varepsilon} - \dot{\varepsilon}^p \qquad [4.18]$$

$$\dot{\sigma} = D^e\left(\dot{\varepsilon} - \dot{\varepsilon}^p\right) \qquad [4.19]$$

where the superscript*e* and *p* indicate elasticity and plasticity respectively, σ is the effective stress tensor. The elastic stiffness matrix $\mathbf{D^e}$is defined in the isotropic manner as

$$\begin{bmatrix} \dot{\sigma}_{xx} \\ \dot{\sigma}_{yy} \\ \dot{\sigma}_{zz} \\ \dot{\sigma}_{xy} \\ \dot{\sigma}_{yz} \\ \dot{\sigma}_{zx} \end{bmatrix} = \frac{E}{(1-2\nu)(1+\nu)} \begin{bmatrix} 1-\nu & \nu & \nu & 0 & 0 & 0 \\ \nu & 1-\nu & \nu & 0 & 0 & 0 \\ \nu & \nu & 1-\nu & 0 & 0 & 0 \\ 0 & 0 & 0 & 1/2-\nu & 0 & 0 \\ 0 & 0 & 0 & 0 & 1/2-\nu & 0 \\ 0 & 0 & 0 & 0 & 0 & 1/2-\nu \end{bmatrix} \begin{bmatrix} \dot{\varepsilon}_{xx} \\ \dot{\varepsilon}_{yy} \\ \dot{\varepsilon}_{zz} \\ \dot{\varepsilon}_{xy} \\ \dot{\varepsilon}_{yz} \\ \dot{\varepsilon}_{zx} \end{bmatrix} \qquad [4.20]$$

where E is the effective Young's modulus which is related to the non-linear elastic shear modulus and bulk modulus discussed in Section 4.2 as following

$$G = \frac{E}{2(1+\nu)} \qquad [4.21]$$

$$K = \frac{E}{3(1-2\nu)} \qquad [4.22]$$

The new stress for current step is then simply presented as:

$$\sigma_n = \sigma_{n-1} + \dot{\sigma} \qquad [4.23]$$

The total strain increment is an input parameter for current calculation step, thus the problem reduces to deducing the plastic strain increment. For simplicity, and to keep consistently with the constitutive discussions in chapters 3 and 4, stress and strain are better represented in the *p*'-*q* and volumetric - deviatoric manner respectively, and can be related to the numerical outputs as follows:

$$\dot{p}' = \left(\dot{\sigma}_{xx} + \dot{\sigma}_{yy} + \dot{\sigma}_{zz}\right)/3 \qquad [4.24]$$

$$\dot{q} = \sqrt{\frac{1}{2}\left[\left(\dot{\sigma}_{xx} - \dot{\sigma}_{yy}\right)^2\right] + \left[\left(\dot{\sigma}_{xx} - \dot{\sigma}_{zz}\right)^2\right] + \left[\left(\dot{\sigma}_{yy} - \dot{\sigma}_{zz}\right)^2\right]} \qquad [4.25]$$

$$\dot{\varepsilon}_v = \dot{\varepsilon}_{xx} + \dot{\varepsilon}_{yy} + \dot{\varepsilon}_{zz} \qquad [4.26]$$

$$\dot{\varepsilon}_q = \sqrt{\frac{2}{9}\left[\left(\dot{\varepsilon}_{xx} - \dot{\varepsilon}_{yy}\right)^2 + \left(\dot{\varepsilon}_{yy} - \dot{\varepsilon}_{zz}\right)^2 + \left(\dot{\varepsilon}_{zz} - \dot{\varepsilon}_{xx}\right)^2 + \frac{1}{3}\left(\dot{\varepsilon}_{xy}{}^2 + \dot{\varepsilon}_{yz}{}^2 + \dot{\varepsilon}_{zx}{}^2\right)\right]} \qquad [4.27]$$

where the subscripts *x* and *y* represent horizontal; *z* represents vertical in the FEM model.

4.3.2 Consistency condition during hardening

During hardening of the yield surface, as discussed in chapter 3, assuming normality:

$$f\left(p', q, p_i\right) = \mathbf{g}\left(p', q, p_i\right) = \frac{\eta}{M_i} + \ln\left(\frac{p'}{p_i}\right) - 1 = 0 \qquad [4.28][3.15]$$

As the plastic strain increment vectors are always perpendicular to the yield surface (plastic potential), the plastic strain increment vectors are expressed as

$$\dot{\varepsilon}_p^p = \lambda_h \frac{\partial f}{\partial p'} \qquad [4.29]$$

$$\dot{\varepsilon}_q^p = \lambda_h \frac{\partial f}{\partial q} \qquad [4.30]$$

where the subscripts p and q stand for volumetric and deviatoric respectively, and λ_h is the plastic multiplier during hardening, which controls the magnitude of the plastic strain increment for each integration step. From Equation [4.28], the partial differentials of the yield surface function with respect to p' and q are

$$\frac{\partial f}{\partial p'} = M_i - \eta \qquad [4.31]$$

$$\frac{\partial f}{\partial q} = 1 \qquad [4.32]$$

By combining Equations [4.29], [4.30], [4.31] and [4.32], the plastic volumetric strain increment and the plastic deviatoric strain increment are presented as

$$\dot{\varepsilon}_v^p = \lambda_h \left(M_i - \eta \right) \qquad [4.33]$$

$$\dot{\varepsilon}_q^p = \lambda_h \qquad [4.34]$$

The plastic multiplier can be deduced by using the consistency condition during yielding. During expansion of the yield surface, the stress state can never 'cross' the yield surface, thus is always on the yield surface which gives $\dot{f} = 0$. The consistency condition is then expressed as

$$\dot{f} = \frac{\partial f}{\partial p'} \dot{p} + \frac{\partial f}{\partial q} \dot{q} + \frac{\partial f}{\partial p_i} \dot{p}_i = 0 \qquad [4.35]$$

The partial differential with respect to M_i is neglected because, although the term M_i is a variable in the yield surface equation, according to Equation 3.28 – 3.30, it is mainly lode angle θ and state parameter ψ dependent, during stress integrate. $\dot{M}_i$ is therefore of less importance compared to $\dot{p}'$, $\dot{q}$ and $\dot{p}_i$, thus is a second order term. From Equation [4.28], the partial differential of the yield surface function with respect to the stress at image point is

$$\frac{\partial f}{\partial p_i} = -\frac{M_i p'}{p_i} \qquad [4.36]$$

The consistency condition of the yield surface is then expressed as

$$\dot{f} = \left(M_i - \eta \right) \dot{p}' + \dot{q} - \frac{M_i p'}{p_i} \dot{p}_i = 0 \qquad [4.37]$$

The term $\dot{p}_i / p_i$ is the hardening rule of the plasticity Equation [3.33]. On collecting the hardening rule Equation [3.33]; the partial differential terms [4.31], [4.32] and [4.36]; the EP-PC process [4.18] and [4.19]; and the consistency condition [4.37], the plastic multiplier during hardening is calculated as

$$\lambda_h = \frac{3G\dot{\varepsilon}_q + K\dot{\varepsilon}_v D^p}{3G + H\exp\left(1-\frac{\eta}{M_i}\right)\left(\frac{(p_i/p)_{\max}}{p_i/p}\right)pM_i + K(M_i-\eta)^2} \qquad [4.38]$$

4.3.3 Consistency condition during softening

The derivation of λ_h assumed that the yield surface coincides with the plastic potential (the direction of plastic strain increment vectors are always normal to the yield surface f). However, during softening, under which condition the stress state is on the vertical internal stress cap, assuming overlapped yield and potential surfaces becomes unrealistic. Therefore, a

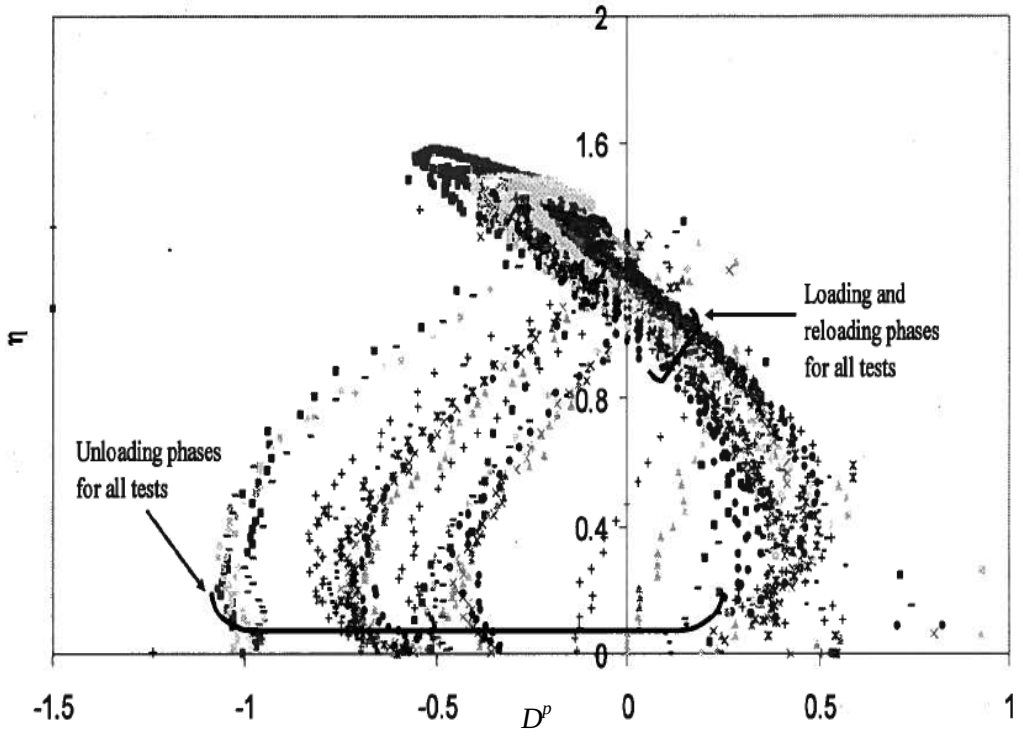

Figure 4.10 The flow rule of Erlsak sand during loading and unloading. (A.E.Dabeet 2008)

reasonable plastic potential surface during softening needs to be mathematically defined.

According to the drained triaxial tests data of Erlsak sand (A.E.Dabeet 2008), as shown in Figure 4.10, the flow rule (stress – dilatancy curve) of the unloading process is generally

perpendicular to the flow rule during hardening. Recall the flow rule of Norsand during hardening discussed in chapter 3

$$D^p = M_i - \eta \qquad [4.39]\ [3.9]$$

assuming the flow rule of softening is normal to that of hardening makes the former one become negative of the later one

$$D_s^p = \eta - M_{is} \qquad [4.40]$$

where D_s^p is the dilatancy ratio ($D_s^p = \dot{\varepsilon}_p^p \big/ \dot{\varepsilon}_q^p$) during softening; M_{is} is the image stress ratio (q / p') during softening. By following the same methodology of deriving the plastic potential during hardening, combining Equation [3.10], [3.11]and [4.40] gives

$$\frac{\dot{p}'}{p'} + \frac{\dot{\eta}}{2\eta - M_{is}} = 0 \qquad [4.41]$$

Integration of Equation [4.41] with respect to mean stress p' gives

$$\ln p' + \frac{1}{2}\ln\left|2\eta - M_{is}\right| = C \qquad [4.42]$$

where C is a random constant. Theoretically the value of C can be any constant, different values of C represent different positions on the plastic potential surface during softening. Following the same process applied in deriving the hardening potential surface, the stress state at $\eta = M_{is}$ is taken as the solution which gives the potential surface during softening, as follows

$$g\left(p', q, p_{is}\right) = \ln\left(\frac{p'}{p_{is}'}\right) + \frac{1}{2}\ln\left|\frac{2\eta}{M_{is}} - 1\right| = 0 \qquad [4.43]$$

where p_{is} is the confining stress at the image point of plastic potential surface during softening. Similar to the situation during hardening, the plastic strain increment vectors during softening is expressed as

$$\dot{\varepsilon}_p^p = \lambda_s \frac{\partial g}{\partial p'} \qquad [4.44]$$

$$\dot{\varepsilon}_q^p = \lambda_s \frac{\partial g}{\partial q} \qquad [4.45]$$

where λ_s is the plastic multiplier during softening. Note that the plastic potential $\boldsymbol{g}$ is used here instead of the yield surface function, as f no longer coincides with $\boldsymbol{g}$ during softening. The plastic multiplier can be deduced by taking the partial differential of $\boldsymbol{g}$

$$\dot{g} = \frac{\partial g}{\partial p'}\dot{p} + \frac{\partial g}{\partial q}\dot{q} + \frac{\partial g}{\partial p_{is}}\dot{p}_{is} = 0 \qquad [4.46]$$

As during hardening, the partial differential with respect to M_{is} is neglected as it is of second order importance during differentiation. For the convenience of differentiation, the plastic potential function Equation [4.43] can be rewritten as

$$g\left(p', q, p_{is}\right) = \ln p' - \ln p_{is} + \frac{1}{2}\ln\left|\frac{2\eta}{M_i}\right| - \frac{1}{2}\ln\left(M_i p'\right) = 0 \qquad [4.47]$$

From Equation[4.47], the partial differential of the plastic potential surface function with respect to p' , q and p_{is} are derived as

$$\frac{\partial g}{\partial p'} = \frac{\eta - M_i}{2q - M_i p'} \qquad [4.48]$$

$$\frac{\partial g}{\partial q} = 1 \qquad [4.49]$$

$$\frac{\partial g}{\partial p_{is}} = -\frac{1}{p_{is}} \qquad [4.50]$$

The consistency condition of the plastic potential surface during softening is then expressed as

$$\dot{g} = \frac{\left(\eta - M_i\right)\dot{p}'}{2q - M_i p'} + \dot{\mathrm{q}} - \frac{\dot{p}_{is}}{p_{is}} = 0 \qquad [4.51]$$

The term $\dot{p}_{is} / p_{is}$ is the softening rule during plastic unloading as described by Equation [3.38]. On collecting the softening rule Equation [3.38]; the plastic strain increments vectors Equation [4.44] and [4.45]; the partial differential terms[4.48], [4.49] and [4.50]; the EP-PC process [4.18] and [4.19]; and the consistency condition [4.51], the plastic multiplier during softening can be derived as

$$\lambda_s = \frac{3G\dot{\varepsilon}_q - \frac{K\left(M_i - \eta\right)}{2q - p'}\dot{\varepsilon}_p}{3G + \frac{H_u}{\ln\left(p_w / p'\right)} + \frac{K\left(M_i - \eta\right)^2}{\left(2q - M_i p'\right)^2}} \qquad [4.52]$$

As during hardening, the plastic multiplier during softening can be calculated based on the total strain increments $\dot{\varepsilon}_p$ and $\dot{\varepsilon}_q$ which are inputs for the current calculation step.

4.3.4 Calculation flow in FEM

The proposed constitutive equations are implemented into the commercial FEM software Plaxis 3D as a subroutine attached into the user-defined soil model package. In the FEM calculation process, each calculation step inherits the imbalanced force ΔF from the previous step, then the displacement is derived accordingly; thus the strains become input parameters for the current calculation step. The new stresses (new imbalanced force) are then calculated based on strains and the proposed constitutive equations. The calculation flow of the proposed model in the FEM programme can be summarised as shown in Figure 4.11.

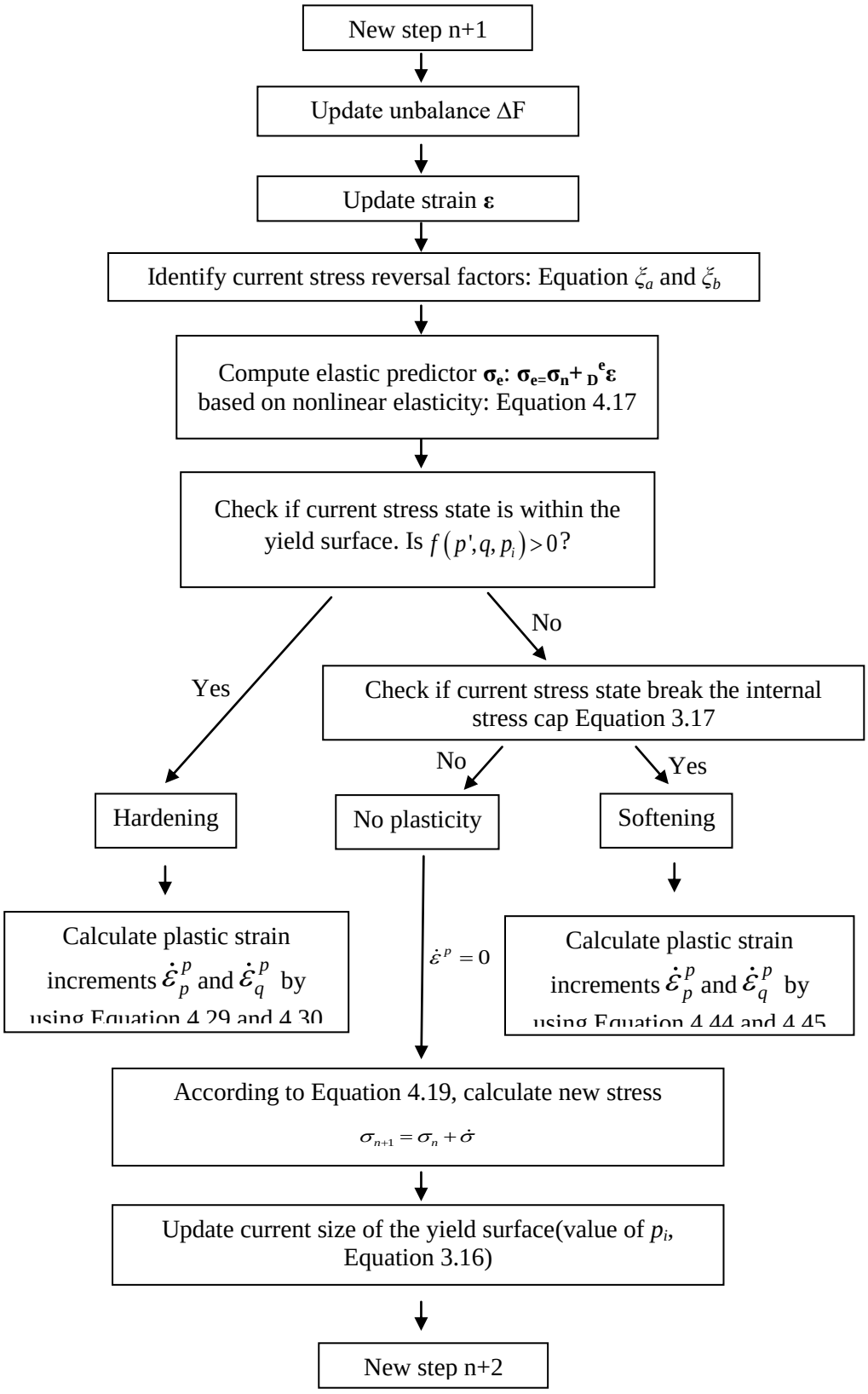

Figure 4.11 The calculation flow of the proposed model in FEM

4.4 Comparison between the proposed model and the Norsand

Although through conventional triaxial validations (where the stress reversal point is automatically treated as the beginning of tests) it is hard to identify the impact induced by considering the stress reversal point, however, it is useful to look at the consequence of considering the small strain and non-linear elasticity of sand proposed in section 4.2. This section demonstrates the comparisons between the numerical predictions of drained/ undrained triaxial tests by using the original Norsand model and the proposed Norsand with nonlinear elasticity model. The linear critical state locus is applied in this section. Apart from the small strain and nonlinear elastic input parameters listed in Table 4.7, the original Norsand input model parameters for Toyoura sand are kept consistent with those determined in the previous chapter. The initial conditions of the drained and undrained tests listed in Table 3.4 and Table 3.5 are applied.

Table 4.7 Input parameters for small strain and nonlinear elasticity

C_i	ε_e	ε_r	r_1	r_2	D_1	D_2
2000	0.0007%	0.0044%	0.0487	4.85	0.0007	0.1

- Drained triaxial compression

From test CID_2A (as shown in Figure 4.12; ψ_0 = -0.167), the volumetric behaviour predicted by the proposed model and the original Norsand model are almost identical, in which case the initial contraction is well predicted while the following dilation is slightly under estimated. The predicted stress strain curve is much improved by the proposed model, with a very precise peak strength calculated, in addition, the stress strain behaviour of the sand sample is perfectly overlapped by the numerical prediction given by the proposed model until the axial strain reaches around 9%, after which strain level the proposed model prediction become over estimating.

From Figure 4.12, the deviation between the predictions from the two models gradually decreases after passing the peak shear strength, so they are very likely to meet each other at very large strain level. This is because as the strain level increases, during which process $\xi_a \rightarrow 0$ and $\xi_b \rightarrow 1$, the effect of the small strain elasticity is vanishing, thus the stress strain curve gradually become solely plastic hardening law dependent, as in the original NorSand. On the other hand, the stress-strain and ε_v-ε_1 curves predicted by the two models theoretically meant to meet each other when the critical state is reached, because the same CSL is applied, thus same 'destination' of shearing is reached.

Similar conclusions can be drawn from test CID_3 in Figure 4.13 (ψ_0 = -0.262). Better prediction of stress strain behaviour is achieved by the proposed model at the strain level of 0%~9% compared to the original Norsand model. The original Norsand underestimated the peak shear strength compared to the proposed model. The stress strain curves predicted by the two models tend to join each other at very high strain level. Despite the sharp approaching of the critical state from the test data, both the proposed model and the original Norsand model give quite good predictions of the volumetric behaviour of Toyoura sand.

For test CID_G462 (Figure 4.14), with a value of the initial state parameter much closer to zero (ψ_0 = -0.061), the consequence of considering small strain and nonlinear elasticity becomes negligible. The stress-strain and ε_v-ε_1 curves predicted by the two models nearly coincide with each other. This is due to the absence of a peak shear strength and the following softening. It is reasonable to conclude that the closer the initial state to the critical state (in which case the effect of the peak shear strength is less), the less the deviation between the numerical predictions of the original Norsand and the proposed model with consideration of small strain and nonlinear elasticity.

For test CID_G460 (Figure 4.15), with an initial state parameter ψ_0 = -0.233, theoretically a peak shear strength should be firstly reached followed by softening. However the test data strangely shows a monotonic increasing of shear strength (an unobvious peak strength seems to appear at late stage of test), thus leading to overestimated numerical results. Nevertheless the predictions from the two models tend to meet the test data at very large strain level.

- Undrained triaxial compression

As in chapter 3, three undrained compression tests CIU_G919, CIU_G908 and GIU_911 are used for comparison here with initial state parameters of -0.05, 0.11 and 0.21 respectively. From Figure 4.16 to Figure 4.18, the undrained behaviours of Toyoura sand predicted by the two models are very similar, and the deviations between the two groups of numerical results are negligible. The small strain and nonlinear elasticity considered by the proposed model has very limited effects on predictions of undrained behaviour of sand.

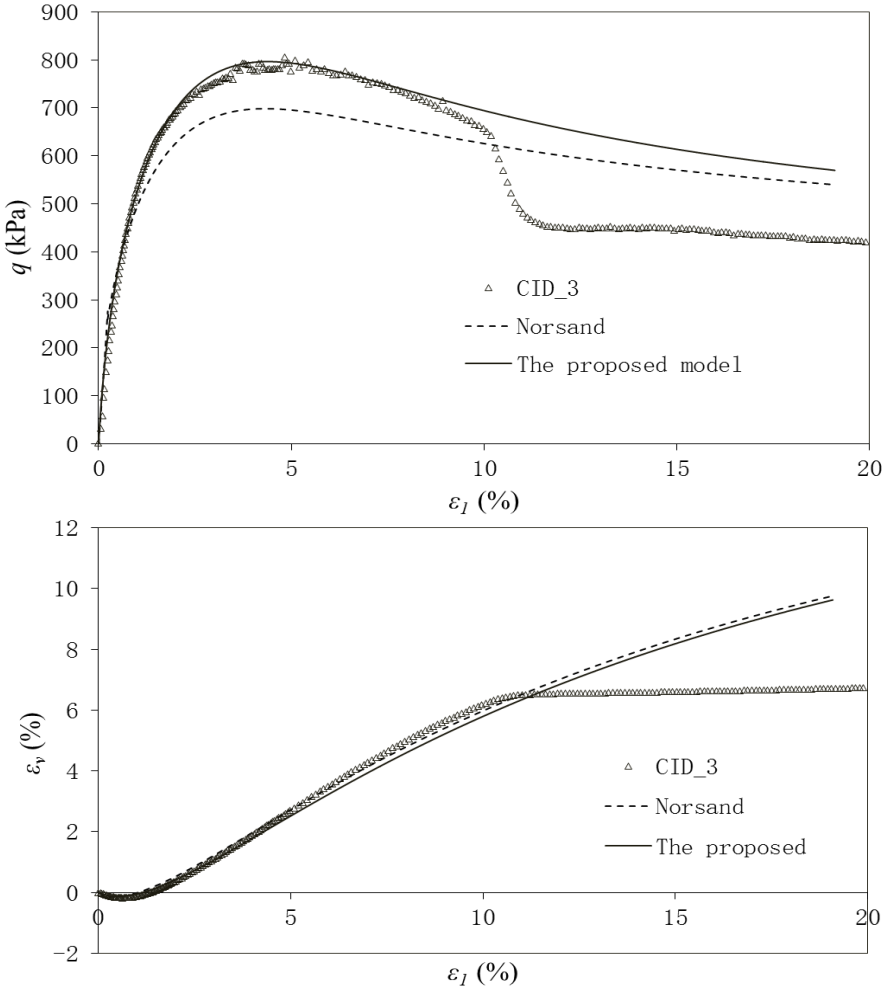

Figure 4.13 Numerical modelling with and without small strain & non-linear elasticity - Triaxial compression test CID_3

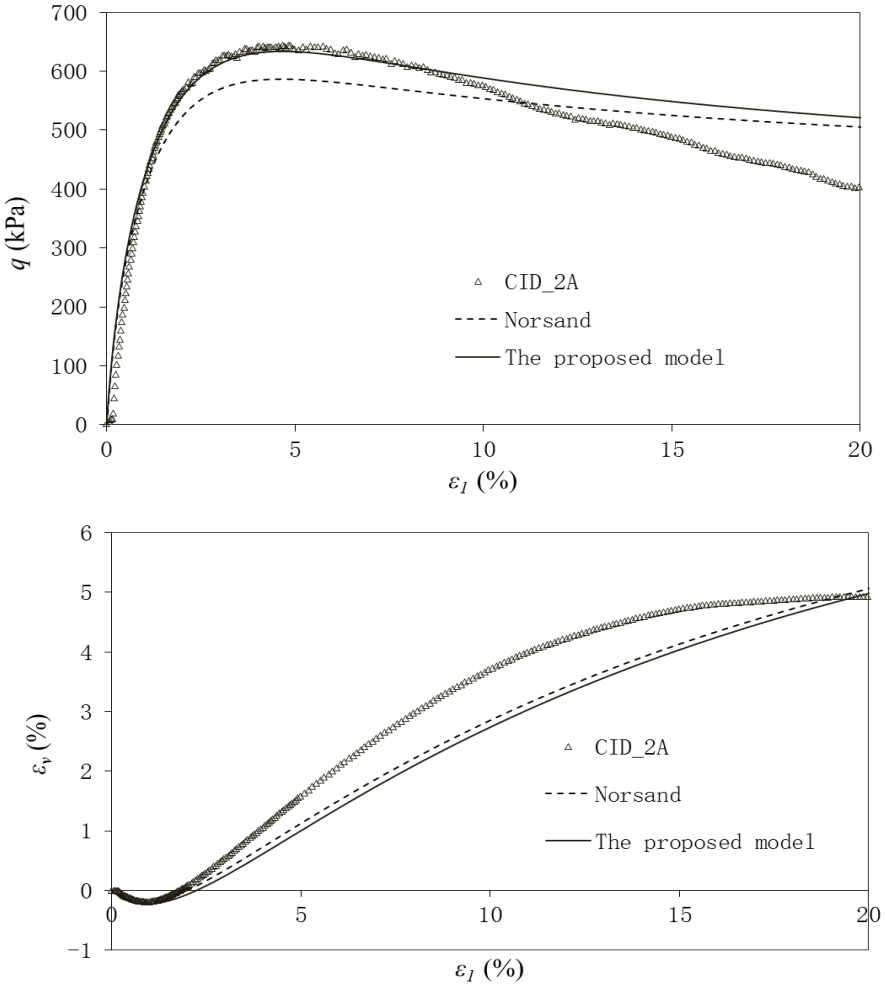

Figure 4.12 Numerical modelling with and without small strain & non-linear elasticity - Triaxial compression test CID_2A

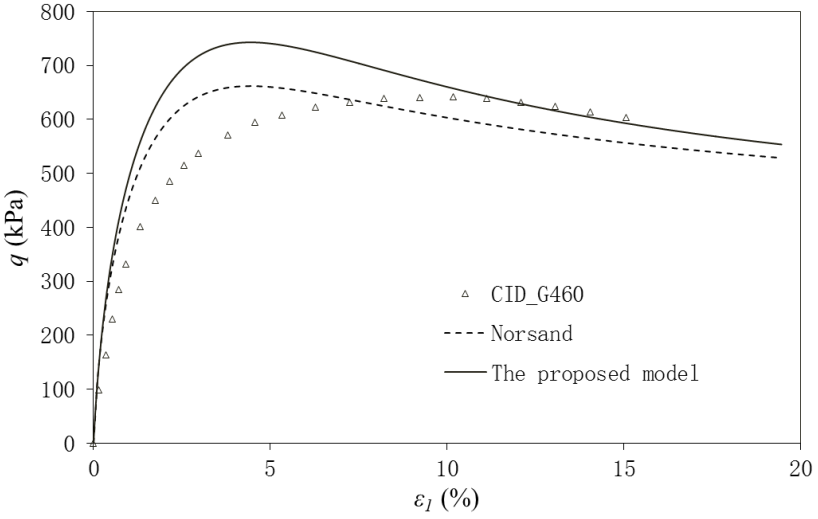

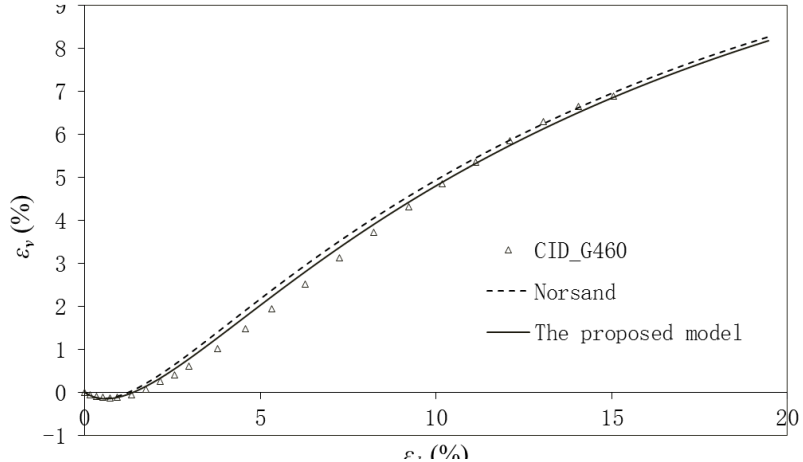

Figure 4.15 Numerical modelling with and without small strain & non-linear elasticity - Triaxial compression test CID_G460

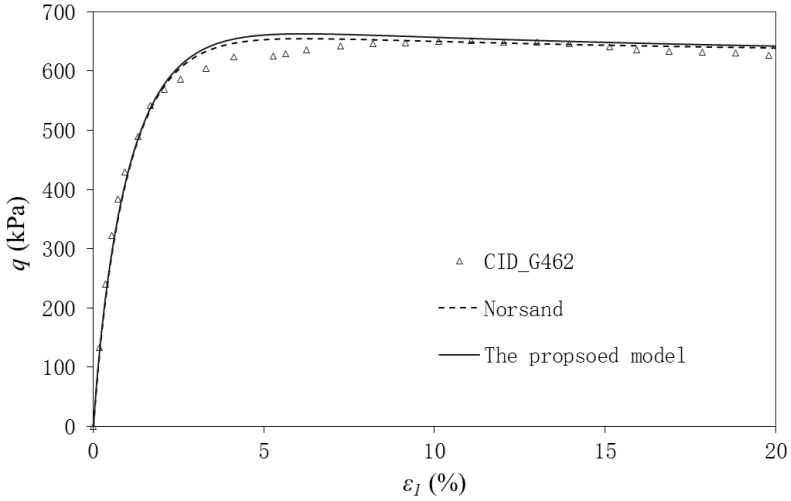

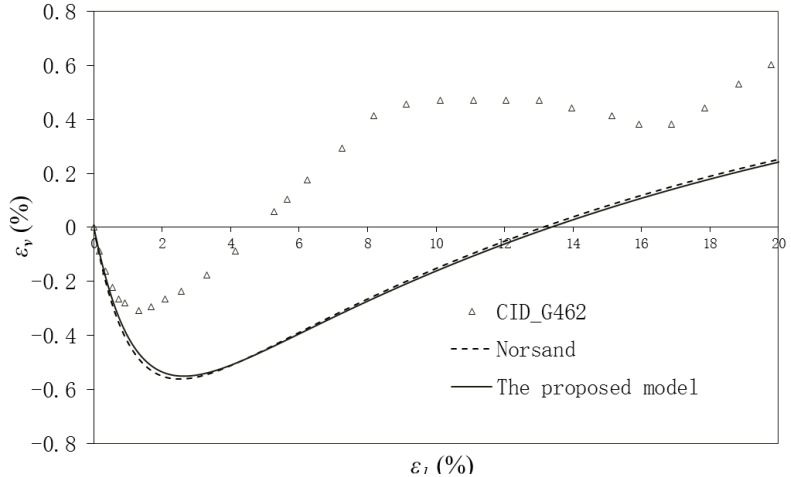

Figure 4.14 Numerical modelling with and without small strain & non-linear elasticity - Triaxial compression test CID_G462

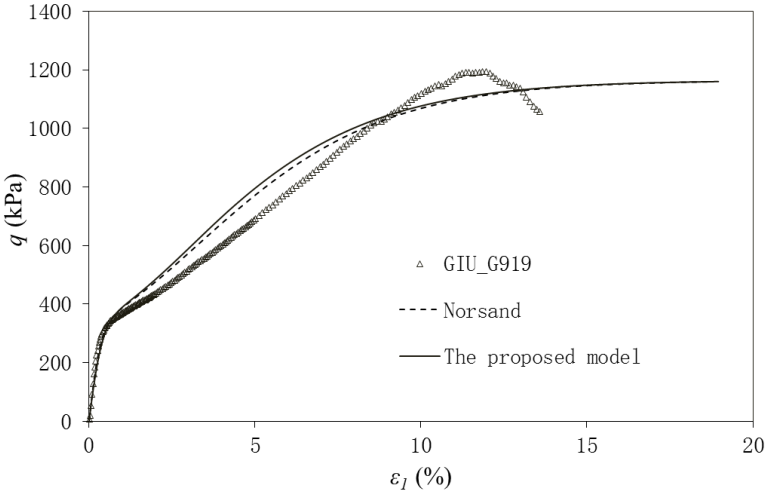

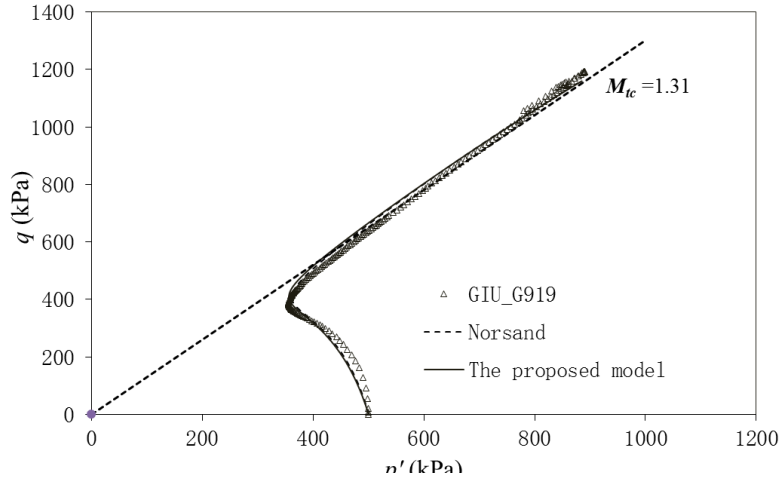

Figure 4.17 Numerical modelling with and without small strain & non-linear elasticity - Triaxial compression test CIU_G908

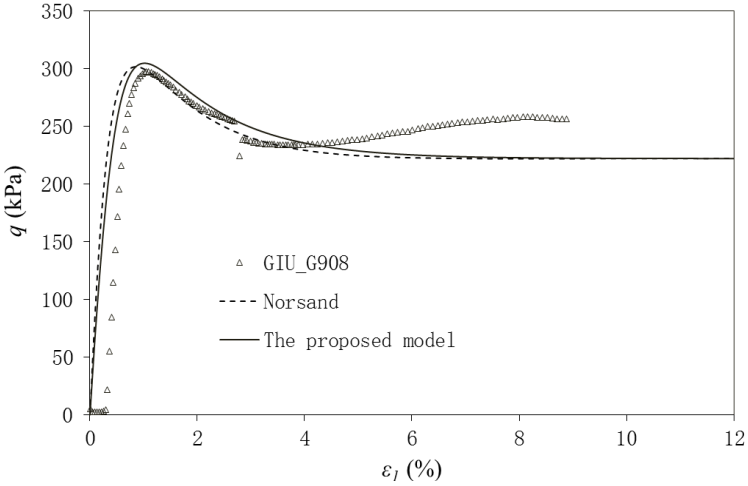

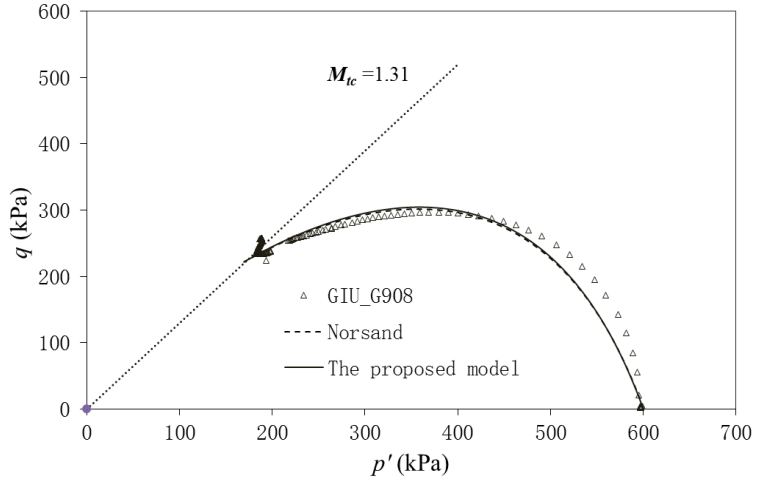

Figure 4.16 Numerical modelling with and without small strain & non-linear elasticity - Triaxial compression test CIU_G919

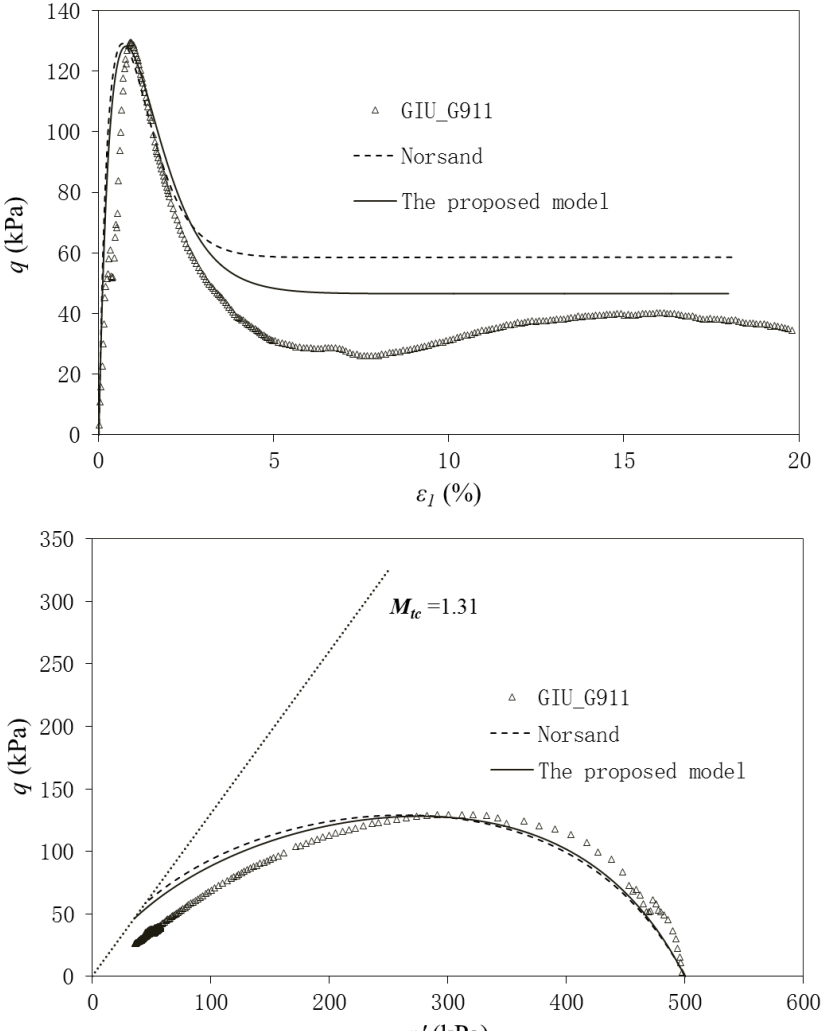

Figure 4.18 Numerical modelling with and without small strain & non-linear elasticity - Triaxial compression test CIU_G911

4.5 Effect of nonlinear elasticity and model parameters

The proposed model, when a linear CSL is applied, in total has 16 input model parameters, 9 of which are inherited from the original Norsand model, while the remaining 7 parameters control the small strain and nonlinear elasticity. All the input parameters can be easily determined from conventional triaxial drained and undrained tests. It is now helpful to look at the effect of the major input parameters on the calculated sand behaviour. In the following sections, base parameters shown in Table 4.8 are applied, and the values of some major input parameters will be changed accordingly to analyse the induced effect. As the proposed model is dimensionless, thus it is more convenient to present the numerical results normalised by the initial confining pressure p_0'. As the undrained behaviour of sand is of less importance during tunnelling, the following analysis only considers the drained condition.

Table 4.8 Base parameters applied for the analysis of the effect from input parameters

Initial state		**Elasticity**	
Γ	1.2	C_i	2000
λ	0.08	ε_e	0.0007%
ψ_0	-0.1	ε_r	0.044%
Plasticity		D_1	0.0007
H_h	120	D_2	0.1
H_s	120	r_1	0.05
M_{tc}	1.3	r_2	5
N	0.5	v	0.2
χ_{tc}	3.6		

*H_s does not have impact in triaxial compression, thus the value of H_s is kept as the same as H_h

4.5.1 Influence of initial state

The influence of initial states are shown in Figure 4.19Figure 4.21. The altitude of the CSL (Γ) produces minor effect. Higher value of Γ induces slightly longer period of contraction (wider range of axial strain ε_1) in triaxial compression. The slope parameter λ of CSL generate large impact on the volumetric behaviour. Larger λ significantly reduces the maximum dilation, as larger λ makes the soil much more compressible, thus the upper limit of dilation is constrained by a more inclined critical sate locus. The initial state parameter ψ_0 dominates the sand behaviour in both strength and volumetric terms. A peak shear strength followed by softening is introduced by a negative ψ_0, in which the soil will firstly contract and then dilate as

expected for relatively dense sand. Larger positive ψ_0 represents relatively loose sand thus much lower stiffness and monotonic contraction will be expected. A misunderstanding that can easily be made is that, expecting $\psi_0 = 0$ leading to zero volumetric strain as the initial state is already on the critical state. However, small amount of contraction happens during compression as shown in Figure 4.21 because of the confining pressure level increases, thus the soil state will move downwards along the CSL in the *v-p'* space.

4.5.2 Influence of elasticity properties

The elastic parameters C_i, ε_e and ε_r have relatively minor influence, as the plastic properties dominate the soil behaviour after the initial stage of loading (see Figure 4.22~ Figure 4.23). The small strain shear modulus factor C_i affects the rate of approaching to the peak shear strain to some extent. Larger range of volumetric strain change is also expected from smaller values of C_i; this is because shear stiffness is directly related to the volumetric strain by the stress dilatancy D^p. The bulk elastic parameters D_1, D_2, r_1 and r_2 matter more in the unloading process, the effect of these input parameters during unloading can be seen in Figure 4.7.

4.5.3 Influence of plasticity properties

The hardening parameter H_h, similar to the shearing stiffness parameter C_i, affects the approach to the peak shear strength; the volumetric strain is also affected because of stress dilatancy D^p (see Figure 4.25 **错误!未找到引用源。**). As expected, the critical stress ratio M_{tc} defines the peak strength and the critical state strength of the soil sample, thus higher values of M_{tc} lead to larger shear strengths. The state dilatancy parameter χ_{tc} controls the dilation ratio at peak shear strength, thus it is not a surprise that it has affected the volumetric strain ratio, as shown in **错误!未找到引用源。**.

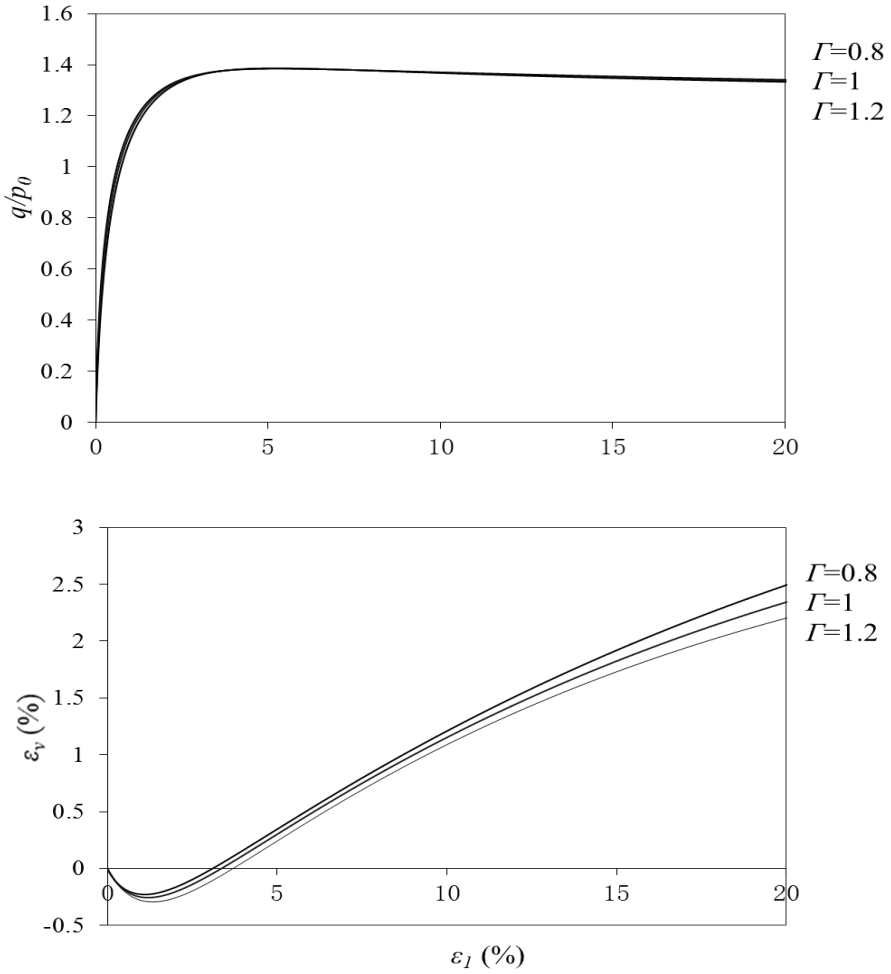

Figure 4.20 Effect of critical state altitude Γ

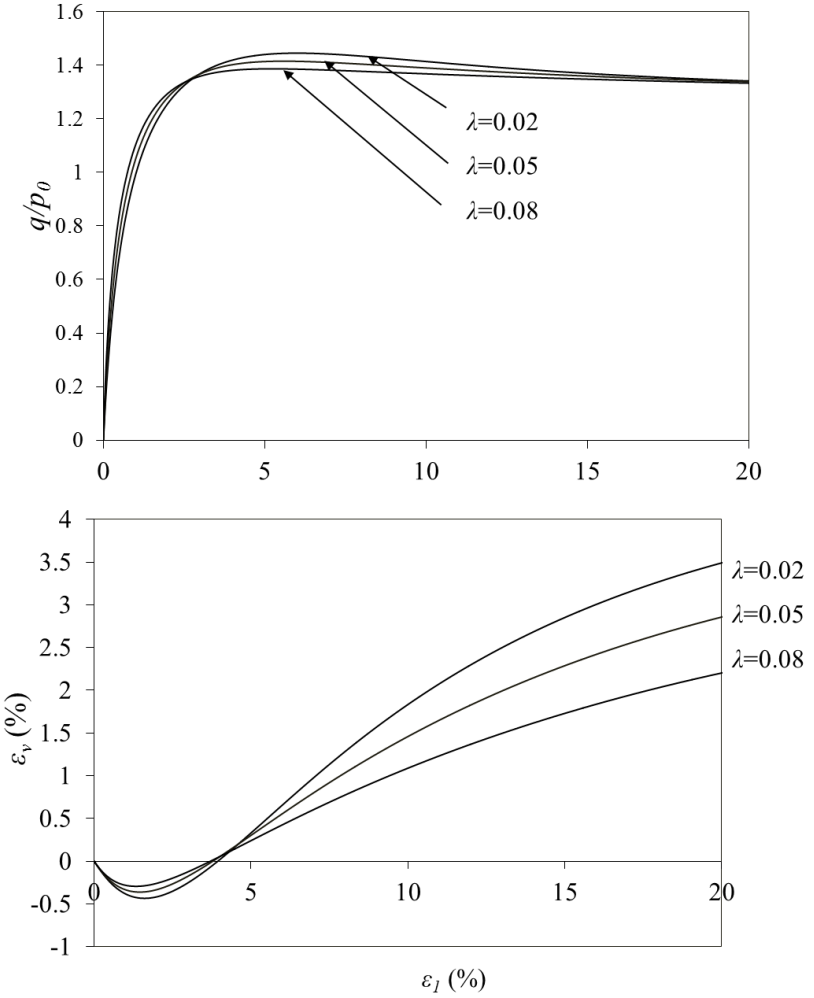

Figure 4.19 Effect of critical state slope λ

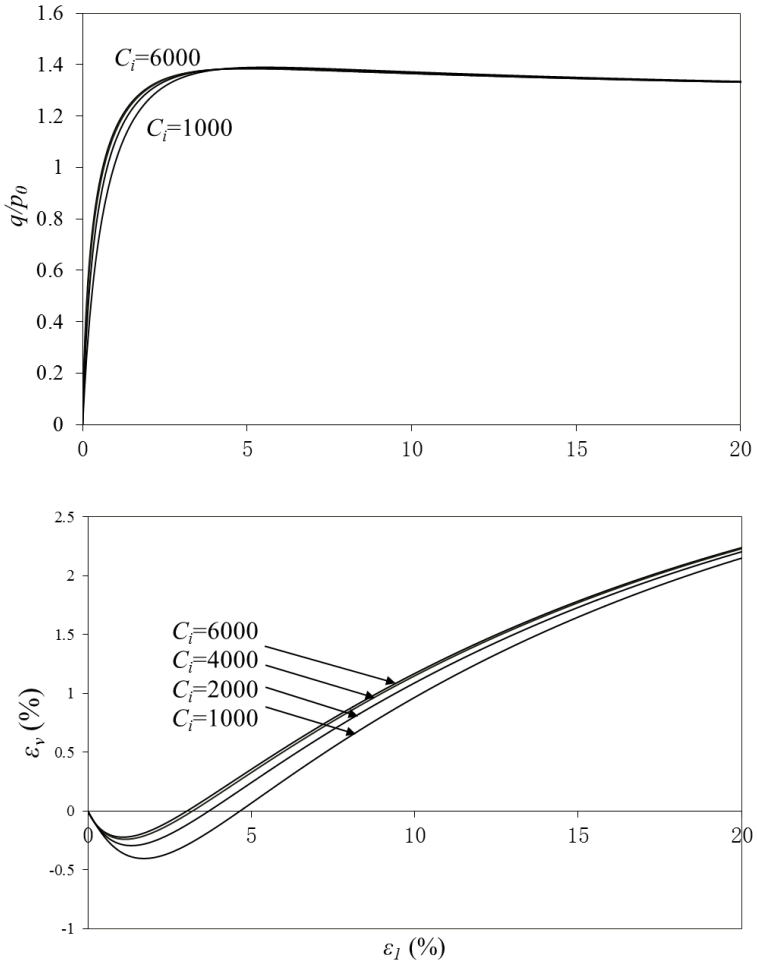

Figure 4.22 Effect of shear modulus index C_i

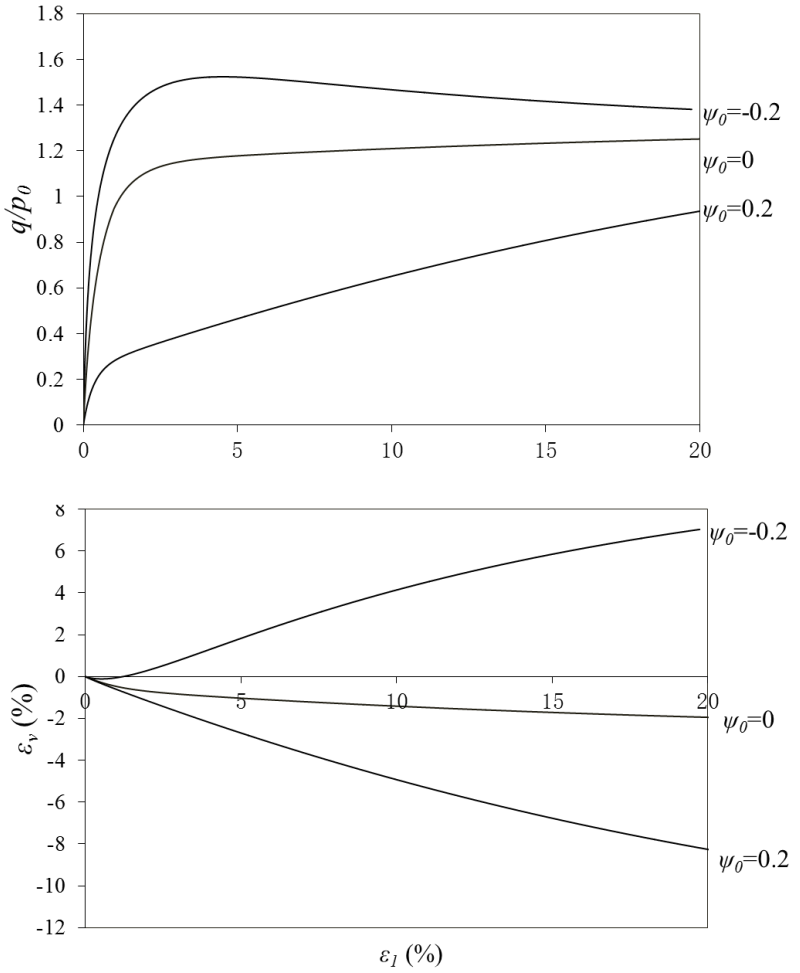

Figure 4.21 Effect of initial state parameter ψ_0

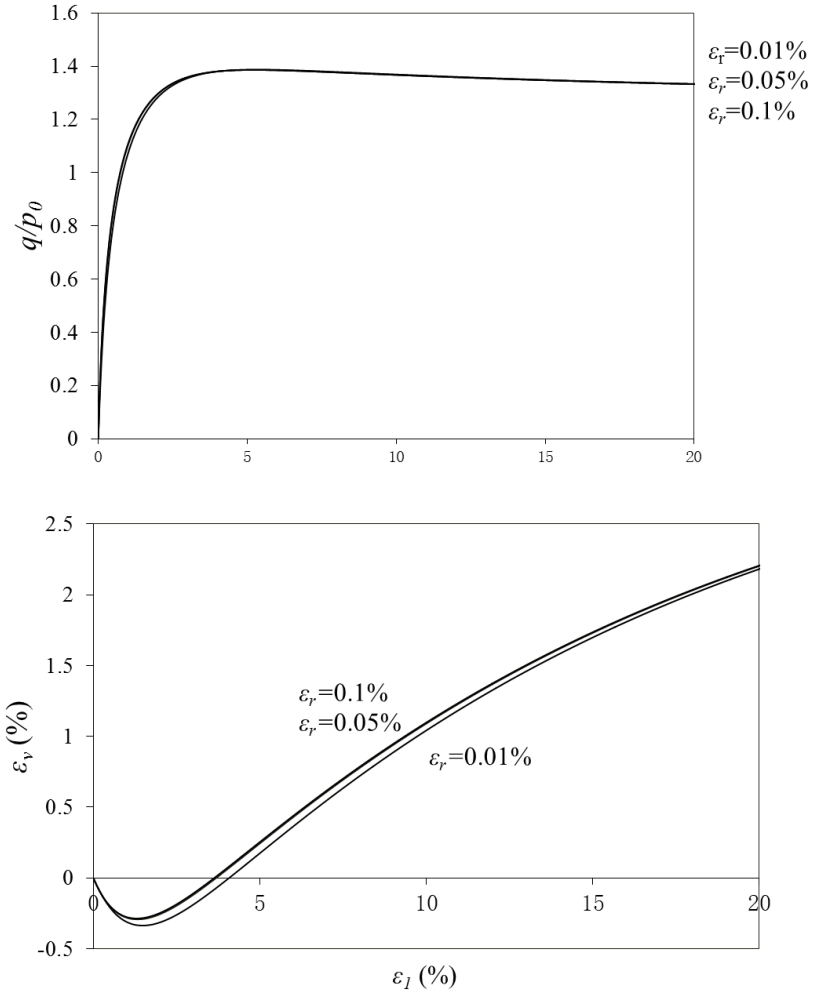

Figure 4.24 Effect of the elasticity reference strain parameter ε_r

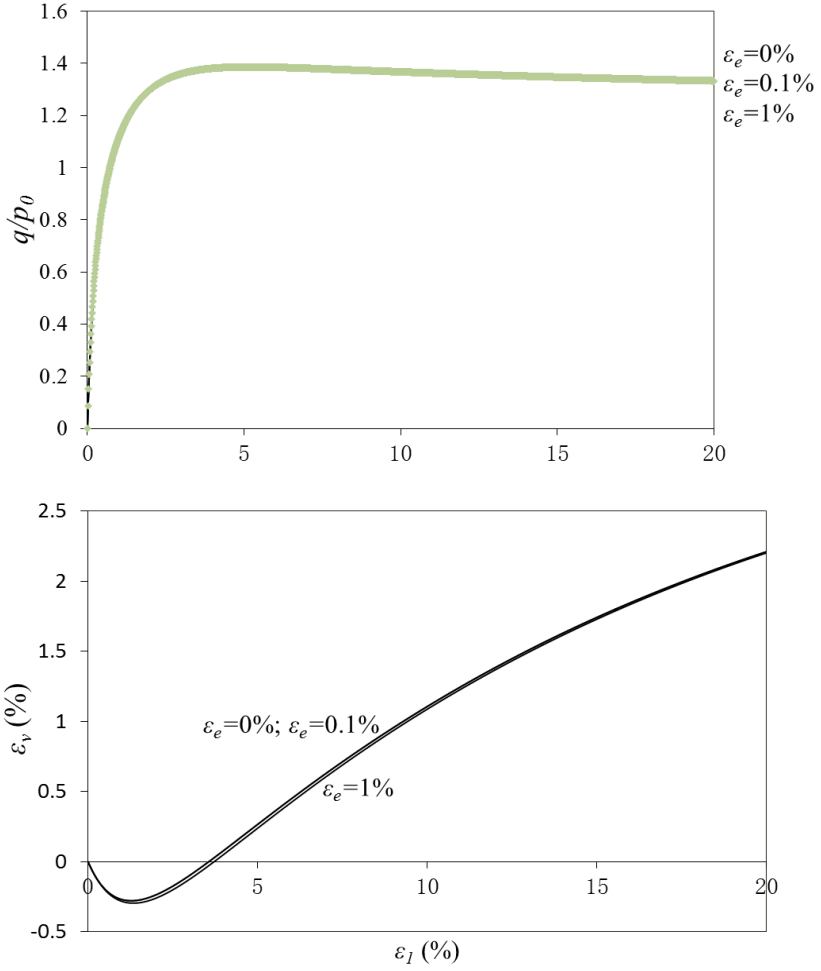

Figure 4.23 Effect of the elasticity threshold parameter ε_e

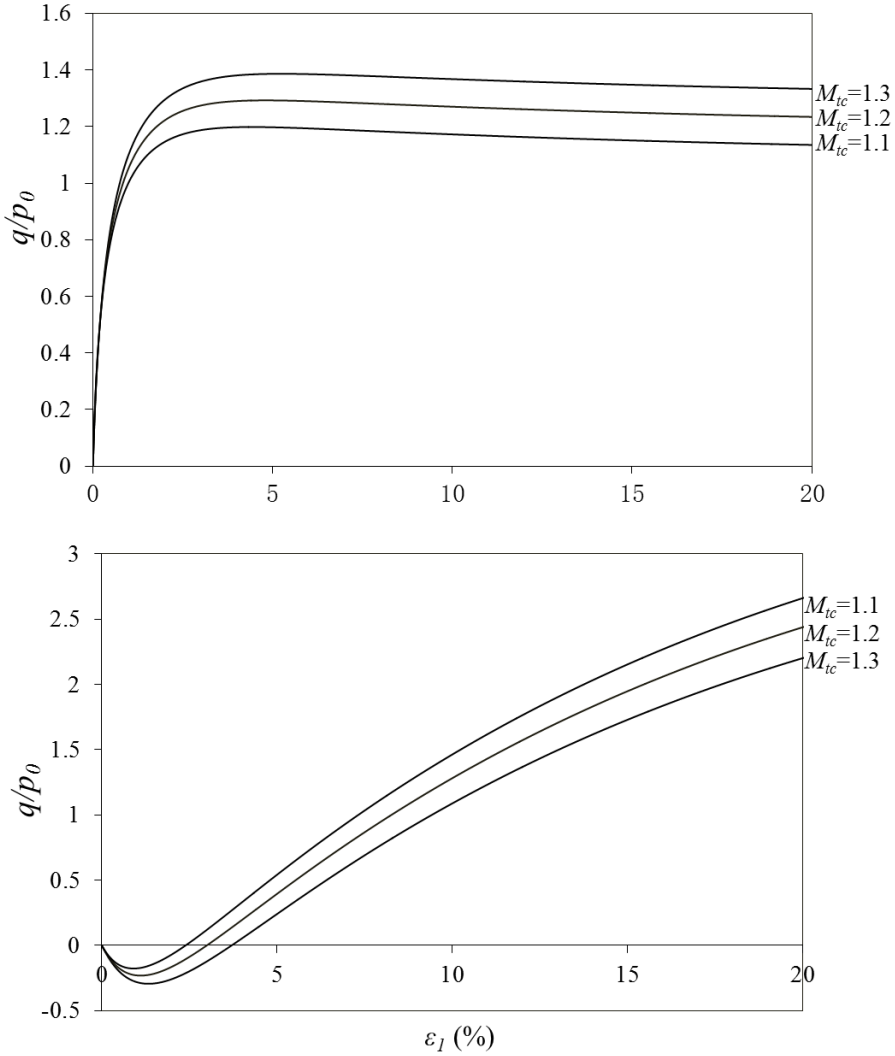

Figure 4.26 Effect of the critical stress ratio M_{tc}

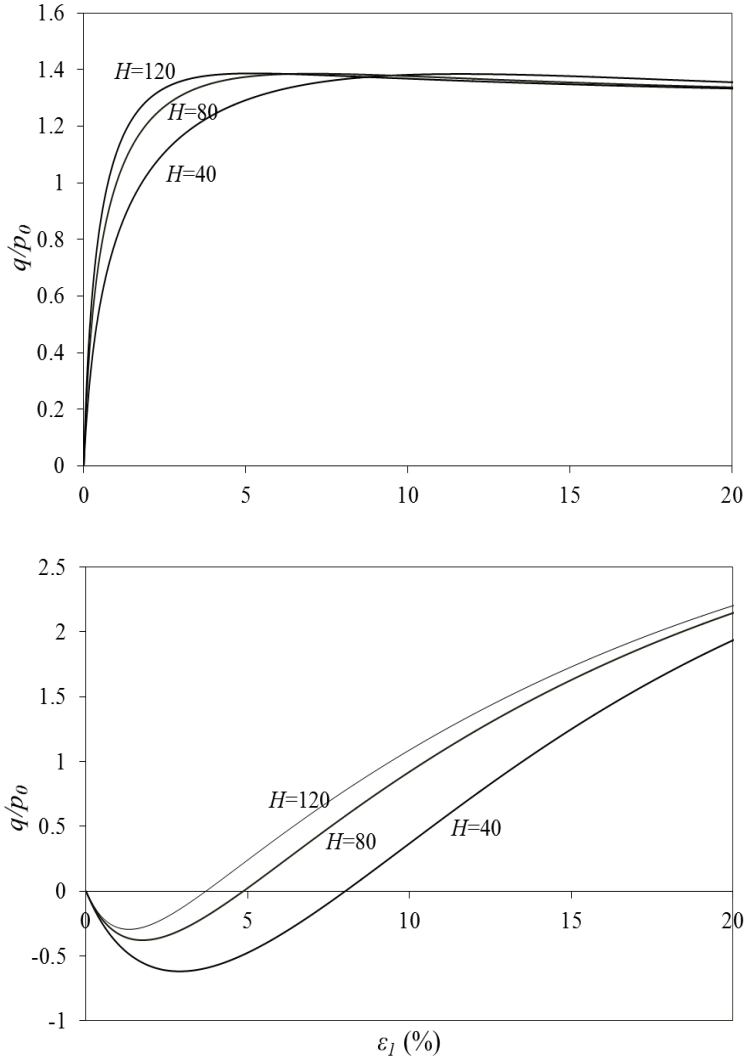

Figure 4.25 Effect of the hardening parameter H_h

4.6 Summary

Based on the relationships between the flow rules during loading and unloading of Erlsak sand (A.E.Dabeet 2008), a plastic potential surface during softening of the internal stress cap is applied in the proposed model. Correspondingly, the plastic multiplier λ_s, which is needed in calculating the new stresses $\boldsymbol{\sigma}_{n+1}$ during softening, is deduced. The flow rule during unloading is assumed to be normal to the flow rule during loading in the proposed model, yet further unloading reloading tests on other types of sands may be needed.

The numerical predictions of the drained and undrained triaxial compression tests demonstrate that both Norsand and the proposed model are capable of giving reasonable results. For drained behaviour, the proposed model shows better capability in calculating the stress strain relationships and predicting the peak shear strength compared to the original Norsand. The volumetric behaviour predicted by the two models are quite similar. For undrained tests, both models gave reasonable predictions, in addition, the deviations between the numerical results provided by the two models are negligible.

Among the 16 input model parameters, the initial state parameter ψ_0 dominates the behaviour of soil as it defines whether the soil is relatively dense or loose compared to the critical state. Therefore, giving a reasonable and precise value to the initial state parameter is a crucial stage in determination of the input parameters and the promise of producing meaningful numerical results. The plastic hardening parameter H_h and the shear modulus parameter C_i also play crucial rules in the input parameter determination process, as they have relatively large influence on the predicted sand behaviour. What's more, the determination of H_h needs a curve fitting process.

Chapter 5. FEM analysis of a centrifuge tunnelling prototype in sand

5.1 Introduction

This chapter explores the capability of using the proposed Norsand-based constitutive model to predict tunnelling induced ground movements and stress change in sandy ground. Of particular relevance to this study is the centrifuge tunnel prototype (Marshall 2009) modelling TBM construction in sand. The sets of centrifuge tunnel tests are replicated in the commercial FEM software Plaxis 3D. Firstly, the proposed Norsand based constitutive sand model is applied in the FEM simulation, the effects induced by varying certain important input parameters are analysed. The Hardening Soil model (existing soil model in Plaxis) is also applied in section 5.5, the numerical ground movement results calculated by the proposed model and the Hardening Soil model will then be discussed and compared with the centrifuge data. Some widely used analytical and empirical methods in predicting tunnelling induced ground movements will also be discussed for the purpose of comparison.

The recorded and discussed numerical results in this research mainly include:

- Surface and subsurface transverse vertical ground settlement troughs. This is probably the most obvious and meaningful numerical outcomes that be compared with the measured centrifuge data and the empirical predictions.
- Transverse horizontal ground movement troughs. Although these troughs were not measured in the centrifuge test, they demonstrate the impact of the some important input model parameters。
- Stress developments above and around the tunnel. Stresses were not measured in the centrifuge test but demonstrate the coordinate of the studied area in the stress space, and more importantly, demonstrate the relative position to the critical stress state.
- Strain developments around the tunnel. The shear and volumetric strains at different stages of tunnel deformation will be compared with the measured centrifuge data.

5.2 The centrifuge tunnel prototype

Tunnel prototype geometry, boundary conditions and the characters of the applied ground material will be briefly described in this section. Details of the tunnel volume loss control procedure in the centrifuge test will also be given as this procedure is actually modelling the excavation process in

TBM tunnel construction, therefore, in order to achieve meaningful numerical results, it is extremely important to precisely replicate this volume loss control process in the FEM modelling. This section only cover the issues that matter in the later FEM simulations， more detailed descriptions of the centrifuge test can be found in Marshall's (2009) work.

5.2.1 The geometry and boundary conditions

As shown in Figure 5.1, the centrifuge scheme considers a green field tunnelling condition. The centrifuge box has a height of 311mm, with its width and length been set as 147.5mm and 770mm respectively (the size refers to the inside of the box, therefore the thickness of the centrifuge box is not included). The scaling factor N of this centrifuge test is set as 75, thus the centrifuge box represents a block of ground with the size of 77m * 23.325m * 11.0625m. The diameter D_r and the tunnel axis level z_t of the prototype tunnel are 62mm and 182mm respectively, which stands for a 4.65m diameter tunnel with axis depth of 13.65m.

In order to avoid any disturbance induced by on-surface equipment, the centrifuge box is designed in a way that all the measurements of surface ground displacements are made by using image based equipment so that the surface settlement troughs are only affected by the tunnel volume loss. The measurements of subsurface ground displacements are done by using the linear variable differential transformers (LVDT) as shown in Figure 5.1. The lasers and LVDTs are kept in a certain distance within the boundaries of the centrifuge box so that the effect induced by the friction between the sand particles and the vertical walls is limited to a minimum.

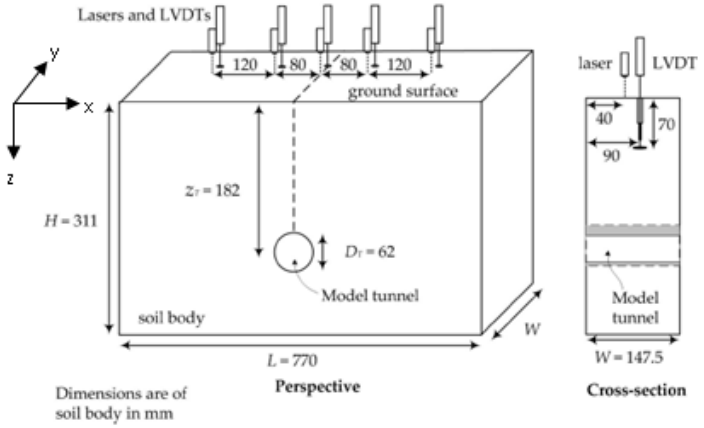

Figure 5.1 The centrifuge tunnel prototype package (Marshall 2009).

A U-shape welded steel frame forms the base and side walls of the centrifuge box. The back wall is made up of 25mm thick steel, the front wall is made up of 80mm thick Perspex wall which is transparent, thus imaging observation of the cross section of the ground becomes possible during

testing. The materials of the centrifuge box are stiff enough that the deformation of the box boundaries during testing can be neglected. Therefore, the four sides of the ground are fixed normal to the boundaries (the soil particles next to the side boundaries are allowed to move in parallel with the walls). The bottom of the ground is fixed vertically, as the excavation face is not considered in this test, thus this case can be seen as a 2-D problem which leads to zero ground movement in all three directions at the bottom of the ground. As laser measurements are made on the surface level, the surface of the ground is free to move in all directions.

5.2.2 Characters of the ground material

The soil used in the centrifuge test is the dry Leighton Buzzard Fraction E silica sand which is a commonly used type of soil for laboratory tests on sand. This sand has an initial void ratio of 0.68 (Vorster et al. 2005). The unit weight of the soil is around 16.0 kN/m^3 (Zhao 2008). An automatic sand poring technique is involved in filling the centrifuge box with sand. The box is placed on its front before sand pouring, then the sand is then poured in layer by layer. When the sand pouring is finished the box is then placed back on its upright position. The 'ground' in the box, therefore, can be assumed as isotropic as the sand is evenly poured, no localised texture is supposed to be made. The poured sand finally reaches approximately 90% relative density.

5.2.3 Details of volume loss control

As discussed in the literature chapter, the construction of TBM (which is usually necessary for tunnelling in sandy ground) tunnels will encourage most of the ground movement to occur above the tunnel crown because of the downwards movement of the TBM and the after-excavation installed segmental lining. The final deformed ground around the excavation can be simplified in the manner illustrated in Figure 2.2. To replicate this ground deformation mechanism, the tunnel prototype is designed as shown in Figure 5.2. The entire tunnel is sealed by a 1mm thick latex membrane with a brass cylinder within, fixed on the front and back wall of the centrifuge box crossing the entire width of the ground (length of the prototype tunnel is 148.5mm). The tunnel axis is positioned at a depth of 182mm. Fluid is filled between these two cylindrical surfaces so that the excavation induced volume loss can be simulated by extracting fluid from inside the sealed cylinder. It is straightforward that the volume of the extracted fluid is directly related to the tunnel volume loss $V_{l,t}$ of the prototype tunnel.

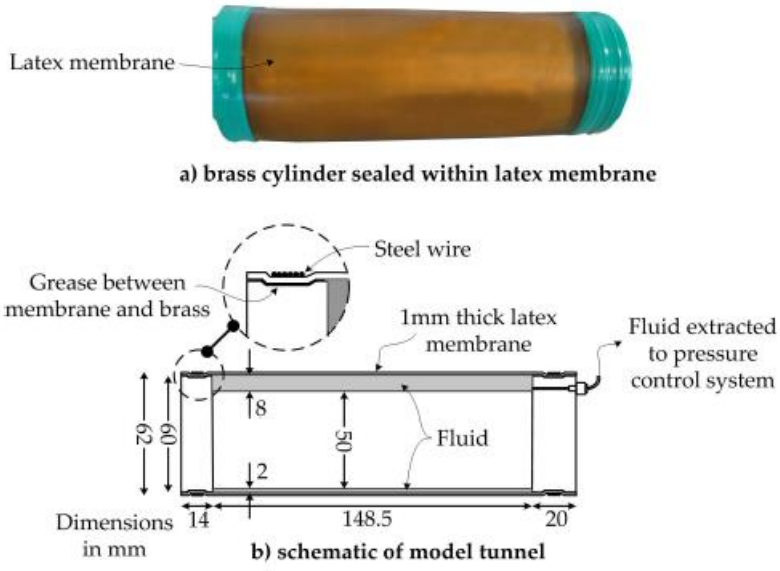

Figure 5.2 The tunnel prototype (Marshall & Mair 2009).

The extraction of the fluid is controlled by using an electric powered piston system. Moving of the piston within the sealed cylinder will continuously pull a volume of fluid out of the grey area in Figure 5.2 (b). The movement of the piston is measured, and the extraction scheme is calibrated in a manner that the movement of the piston can be directly related to the volume of extracted fluid. In order to achieve a steady tunnel deformation process, the rate of tunnel volume loss (rate of extracting fluid) is set to 3%/min by setting the movement of the piston at a speed of 0.64mm/min.

Dimensions and relative positions of the two rings shown in Figure 5.2 (b) illustrate how ground displacement is encouraged to occur predominantly above the tunnel. It should be noted that the diameter of the excavation profile should be taken as 62mm rather than 50mm.

5.3 The FEM model

All the numerical research in this study is carried out by using the commercial finite element software Plaxis 3D. The FEM calculation equations follow the basic continuum mechanics. The deformations are limited in a sense that only small deformation is considered so that the original unreformed mesh can always be referred. Details of the FEM theories and formulation can be found in Brinkgreve et al. (2013).

5.3.1 Model geometry

As shown in Figure 5.3, the geometry of the FEM model is consistent with the centrifuge model. The soil only is modelled with its boundaries fixed as assumed in the centrifuge model.

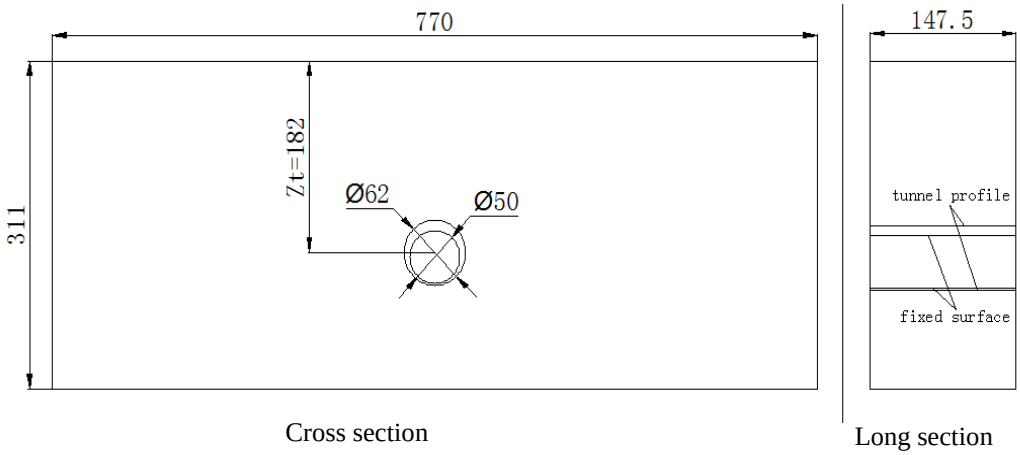

Figure 5.3 Geometry of FEM model (all dimensions in millimetres)

The axis level of the inside and outside cylinders is located at z = - 182mm. The diameter of the outside deformable membrane is 62mm with a 50mm diameter cylinder fixed in all three directions inside. The gaps left between the two surfaces at crown and bottom are 8mm and 2mm respectively as was the situation in the centrifuge tunnel box. Thicknesses of the cylinders are ignored in this study.

5.3.2 Element type and meshing

In Plaxis 3D, the soil is modelled by 10-node tetrahedral elements which give second-order interpolation of displacements. This type of element has three local coordinates (η, ξ and ζ) as shown in Figure 5.4, thus the soil elements have three degrees of freedom. The two cylinders are modelled by the 6-node triangle plate elements which have two local coordinates (η and ξ) as illustrated by Figure 5.5. As structural elements, each node of the plate elements has six degrees of freedom instead of three for soil elements including three translational degrees and three rotational degrees. These plate elements are directly integrated by using three-point Gaussian integration, the positions of the three integration points are shown in Figure 5.5 as ×.

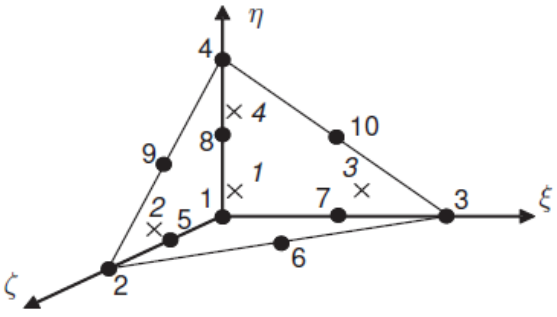

Figure 5.4 The tetrahedral soil element with three local coordinates and its numbering of the nodes.

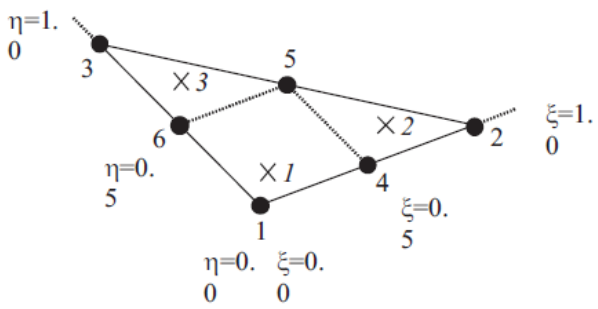

Figure 5.5 The triangle plate element with two local coordinates, six nodes and three integration points (×).

The mesh of the FEM model is shown in Figure 5.6. The meshing procedure uses the 'very fine mesh' option in Plaxis3D which leads to 56959 soil elements and 81145 nodes. The soil particles are assumed to move with the deforming cylinder membrane. In other words, no relative movements between the ground and the shell elements are generated, therefore, the soil elements and the plate elements of the outside cylinder share the same nodes; the interface is not modelled. This assumption makes sense in reality as the friction between the segmental lining and the soil particles is so large that the soil particles are unlikely to 'slide' on the lining surface.

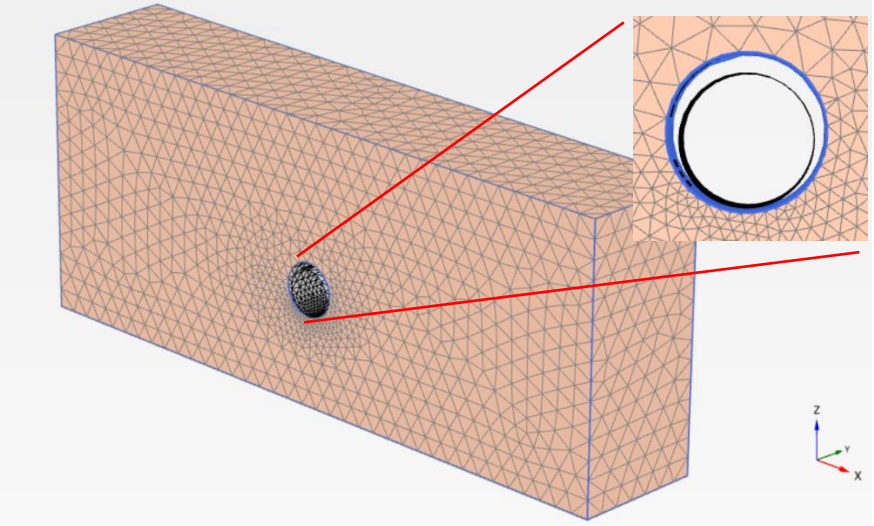

Figure 5.6 The FEM model in Plaxis 3D.

5.3.3 Boundary conditions

In numerical simulation, two types of boundary conditions should be applied which are pore pressure boundary conditions and displacement boundary conditions. As the dry Leighton Buzzard sand is used in the centrifuge test, the ground water flow and the pore pressure are absent from the test, thus in the FEM model, pore pressure and drainage boundary conditions are not applied.

Ideally, to simulate the real tunnelling projects, the model boundaries should be as far as possible from the excavation so that the boundary effect is limited to the minimum. In the centrifuge tests, the distance between the excavation profile and the side walls is 354mm which is approximately six times of the tunnel diameter, these are not 'very far' boundaries, thus the effect of the normally fixed side boundaries may still have certain effect on the ground movements and stress path developments around the tunnelling area, however, the purpose of this numerical study is to model the ground response in the centrifuge test, thus to replicate the boundary situation in the centrifuge box, the four side boundaries are fixed normally; the bottom of the ground is fixed in all three directions; the surface is free to move in all three directions. The boundary settings in the numerical model are shown in Figure 5.7 (model coordinates illustrated in Figure 5.6).

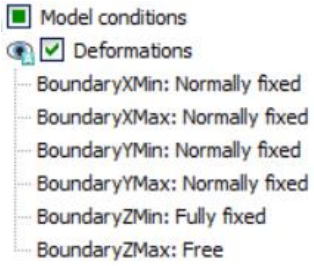

Figure 5.7 Displacement boundary conditions of the FEM model.

5.3.4 Modelling the volume loss

5.3.4.1 The volume loss control process

As discussed in the literature chapter Section 2.6.1, to simulate the tunnel volume loss $V_{l,t}$ during excavation, four methods are commonly used in numerical modelling. The possible ways to apply these four methods in this study are (the soil within the inside fixed cylinder is removed in all cases):

a. Convergence deconfinement

The soil between the two cylinders are firstly removed, a set of stress that equilibrates the initial in situ ground stress is perpendicularly applied from inside the tunnel periphery to support the ground.

The tunnel volume loss procedure can be simulated by gradually reducing the supporting stress until the desired tunnel volume loss is reached.

b. Soil softening

The soil between the two cylinders is kept in situ. In order to reduce the volume of this block of soil the bulk modulus K is gradually reduced. The soil left in between the two cylinders is then compacted.

c. Controlling $V_{l,t}$

The soil between the two cylinders is removed, a prescribed convergence is applied on the outside cylinder before the calculation. The outside cylinder will need certain stiffness to avoid further unreasonable deformations and tunnel collapse. In this case the tunnel volume loss value is the prescribed percentage of the convergence.

d. The gap parameter method

This method encourages the majority of the deformation to occur above the tunnel crown; the bottom of the excavation profile (the outside cylinder in this case) is fixed in all three directions. The volume loss process can be done by either reducing the bulk modulus of the soil left in between the cylinders or decreasing the supporting stress from inside the tunnel periphery. The tunnel volume loss can be related to the vertical displacement (the gap parameter g) of the tunnel crown.

In the centrifuge test, the outside cylinder is made of flexible latex membrane, and is free to deform in all directions. As the water was extracted with a reasonably low rate, the tunnel pressure (water pressure) is maintained consistent during tunnel deformation. It can be seen that to replicate this tunnel deforming process in the centrifuge test, none of the four methods can be directly applied. This study applies a combined c-d method:

As the tunnel volume loss $V_{l,t}$ should be a controllable value in the analysis, a prescribed surface contraction is applied on the outside cylinder before the volume loss control process. Certain values of Young's modulus and shear modulus are given to the outside cylinder to keep the cylinder flexible and to avoid tunnel collapse. It should be noted that the assigned surface contraction value should not be treated as the final tunnel volume loss as the outside cylinder is flexible, further deformation occurs after the prescribed surface contraction. The dominant deformation around tunnel crown is achieved by positioning the two cylinders in the way illustrated in Figure 5.6. To replicate the steady water extraction process, each calculation step in the volume losing phase is assigned with 0.1% additional surface contraction. In this way, an equilibrium condition can be reached after each step of calculation, in addition, whether or not the desired tunnel volume loss is reached can be checked at all times.

It is for sure that 0.1% surface contraction each step sacrifices certain precision in obtaining the target tunnel volume loss value; smaller percentage of surface contraction each step is preferred theoretically. However, it is a reasonable compromise to apply 0.1% contraction each step considering practicability and accuracy. The calculation of the tunnel volume loss is carried out by AutoCAD by using the extracted tunnel peripheries from Plaxis 3D. The points used for calculating the tunnel volume loss are located evenly on the tunnel periphery as shown in Figure 5.8, the coordinates of these points are updated in AutoCAD after each step of simulation to form the current deformed tunnel periphery. The displacements throughout the numerical analysis of the monitored points are discussed in Section 5.6.1 and detailed listed in Appendix B. $V_{l,t}$ is identified by calculating the area difference between the original tunnel periphery and the current deformed one.

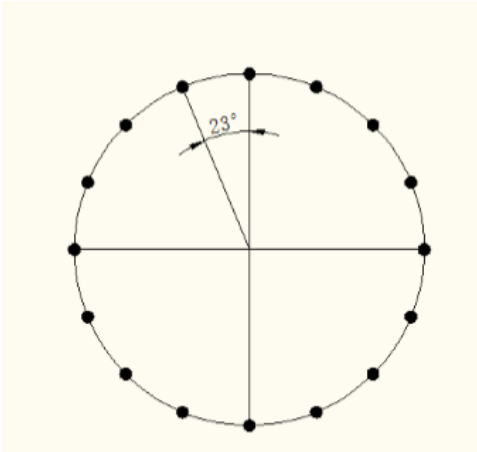

Figure 5.8 Points used for calculating the tunnel cross section area.

The tunnel volume loss control process in the numerical modelling can be summarised as the following five phases (also see Figure 5.9):

- Pre-calculation: Remove soil elements Ⅰ; Active cylinder 1(fixed in all directions).
- Initial phase: Reset ground displacements to zero.
- Volume loss control phase 1: Remove soil elements Ⅱ; Active plate elements on cylinder 2.
- Volume loss control phase 2: Step 1. Apply 0.1% surface contraction to cylinder 2.
  Step 2. Check tunnel volume loss
- Repeat Volume loss control phase 2 until the target $V_{l,t}$ is reached. .

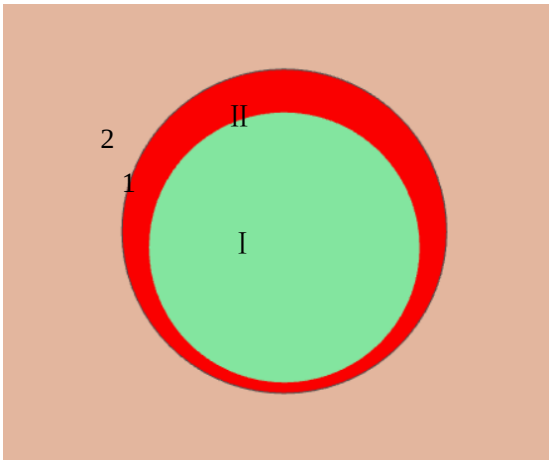

Figure 5.9 Volume loss control process in FEM

5.3.4.2 The flexible tunnel periphery

The selection of the material parameters of the plate elements should be done cautiously. The Young's and shear modulus of cylinder 2 cannot be too large that the bending resistance of the cylinder becomes far larger than that of the latex membrane, thus the deformation pattern of the cylinder becomes nearly uniform convergence, on the other hand, cylinder 2 has to have certain stiffness to avoid early tunnel collapse (tunnel collapse never happens in the centrifuge box as consistent water pressure was kept between the two cylinders) before the target tunnel volume loss values are reached.

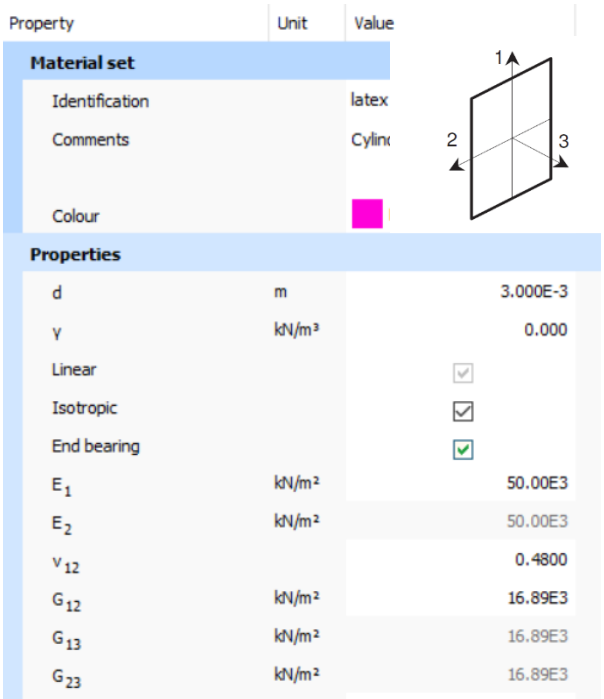

Figure 5.10 Input material parameters of the plate elements on cylinder 2.

In this study, the plate elements on cylinder 2 are isotropically assigned with 50 MPa Young's modulus to avoid early tunnel collapse, the Poisson's ratio is set as 0.48 which lead to 16.9 MPa shear modulus. The input parameters of the tunnel periphery plate in Plaxis are illustrated in Figure 5.10, where the subscripts 1, 2 and 3 are the local coordinates of the plate elements. This combination of plate material parameters is proven to be able to give a similar tunnel deformation pattern (see Section 5.6.1) as in the centrifuge test.

5.3.5 The applied constitutive models and input parameters

Two constitutive soil models will be involved in the numerical simulations: the Hardening Soil model and the proposed sand model. The Hardening Soil model is an existing soil model in Plaxis 3D, and is the suggested model for simulating tunnelling cases in sandy ground according to industrial experience (Brinkgreve et al. 2013).The proposed sand model has been implemented as a sub routine using FORTRAN 90, and been combined with the Plaxis user-defined soil model routine. Both constitutive models apply a K_0 of 0.53 which is the realistic K_0 value of Leighton Buzzard Sand Friction E sand (Gao et al. 2014).

5.3.5.1 The Hardening Soil model

The Hardening Soil model is called 'hardening' because the enlargeable yield surface distinguishes this model from other elastic perfectly plastic models in which case the boundary between elasticity and plasticity is fixed. In the Hardening Soil model, the yield surface, in the principal stress space, may expand due to compression and shearing. The Hardening Soil has been widely used in numerical modelling and can give reasonable numerical results for simulating the behaviour of both soft and stiff type of soils (Schanz et al. 1999). Furthermore, it is suggested for analysing deep excavation cases in sandy ground by the Plaxis manual .

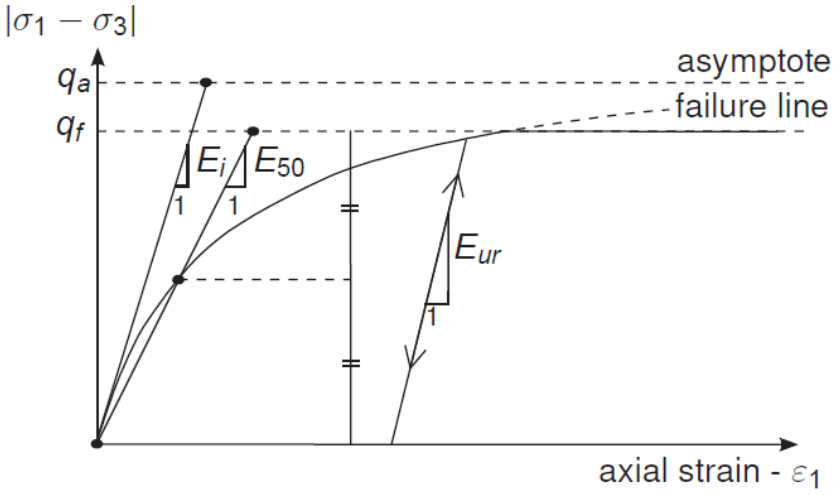

Figure 5.11 The basic idea of the Hardening Soil model in a triaxial compression version (Brinkgreve et al. 2013).

One of the basic features of the Hardening Soil model is the hyperbolic relationship between the axial strain $\varepsilon_1$and the deviatoric stress q under triaxial compression condition as indicated in Figure 5.11, where q_a is the critical state strength at very large strain level, q_f is the ultimate deviatoric stress at a practical engineering strain level. q_f is related with q_a by $q_f = R_f$ and q_a (R_f is a reference factor and is set as 0.9 in Plaxis by default). E_i is the initial stiffness, in other words, the small strain stiffness of the soil. E_{50} is the stiffness where the deviatoric stress reaches 50% of its ultimate value q_f. E_{ur} is the unloading reloading elastic stiffness of the soil. The initial stiffness E_i can be related to E_{50} by

$$Ei = \frac{2E_{50}}{2 - R_f} \qquad [5.1]$$

Another basic feature of the Hardening Soil model is that the stiffness is stress dependent, which means that the characteristic stiffnesses E_{50} and E_{ur} cannot be simply set as input parameters, as their values change with the stress development, thus need to be related to current stresses and other input model parameters. Some basic input parameters of the Hardening Soil model in Plaxis are:

- E_{50}^{ref} - the reference deviatoric stiffness .
- E_{oed}^{ref} - the reference compressive stiffness (under oedometer condition)
- E_{ur}^{ref} - elastic unloading reloading stiffness.
- m- a power law that governs the stress dependence of the stiffness.
- C', φ' and ψ' - cohesion, friction angle and dilation angle (same meanings as in the Mohr-Coulomb failure criterion).

The stiffnesses E_{50} and E_{ur} can be related to the input parameters and the current stress level through following relationships:

$$E_{50} = E_{50}^{ref}\left(\frac{c\cos\varphi - \sigma_3 \sin\varphi}{c\cos\varphi + p^{ref}\sin\varphi}\right)^m \quad [5.2]$$

$$E_{ur} = E_{ur}^{ref}\left(\frac{c\cos\varphi - \sigma_3 \sin\varphi}{c\cos\varphi + p^{ref}\sin\varphi}\right)^m \quad [5.3]$$

where p^{ref} is a reference pressure and often taken as 100kPa.

Based on Zhao (2008)'s laboratory studies on the Leighton Buzzard Fraction E sand, the input parameters of the Hardening Soil model in this study are applied with the values shown in Table 5.9. It is noted that the unit weight of the soil is set as 1200 kN/m^3, because by considering the scaling factor N in the centrifuge test, the unit weight of the soil in the numerical modelling should be 75 times (N = 75 in the centrifuge test) of its usual value in normal gravity condition. The dilatancy cut-off option in Plaxis is set as active so that the void ratio does not exceed the maximum void ratio 0.97 of the Leighton Buzzard Fraction E sand.

Table 5.9 Input parameters of the Hardening Soil model (relate Leighton Buzzard Fraction E sand)

Parameter		**Value**	**Unit**
Unit weight	γ	1200	kN/m^3
Reference deviatoric strength	E_{50}^{ref}	30	kN/m^2
Reference compressive strength	E_{oed}^{ref}	30	kN/m^2
Elastic stiffness	E_{ur}^{ref}	90	kN/m^2
Cohesion	c	0	kN/m^2
Friction angle	φ	41	°
Dilatancy angle	ψ	10	°
Maximum void ratio	e_{max}	0.97	
Power law factor	m	0.5	
Poisson's ratio	v	0.2	

5.3.5.2 The proposed model

The proposed soil model has been implemented as a user defined soil model in Plaxis soil model library in both 32-bit and 64-bit forms, thus can be used under most of the PC operating systems.

This model requires 14 input parameters (15 parameters when applying the curved CSL) in Plaxis 3D (the soil property parameters including unit weight and maximum void ratio are shared by all applied constitutive models in Plaxis 3D). The determinations of the input parameters for Leighton Buzzard Fraction E sand follows the same procedure described in Chapter 3.

Property		Unit	Value
DLL file			norsand small strain.dll
Model in DLL			Norsand
Parameters			
Gamma	Γ		0.9720
Lambda	λ		0.05400
Mtc	M_{tc}		1.240
HH	H_h		75.00
chi	χ_{tc}		3.800
N	N		0.5000
Ci	C_i		6000
Hu	H_u		75.00
nu	ν		0.2000
psi0	ψ_0		0.000
$p_{i\,min}$	p_{i_min}	kN/m²	1.000
EpsilonE	ε_e	%	0.7000E-3
EpsilonR	ε_r	%	0.04400
DD1	D_1		0.7000E-3
DD2	D_2		0.1000
RR1	r_1		0.04870
RR2	r_2		4.850

Figure 5.12 Input parameters of the proposed Norsand based model in Plaxis 3D

It has been proven in chapter 4 that the selection of the type of CSL (curved or linear in the logarithmic *v-p* plane) is dependent on the available laboratory data and the studied range of stresses. The significant change of the CSL type from linear-curve to curve happens around p' = 1000 kPa, before which value the CSL can be reasonably described by both approaches. In this study, the tunnel level is around 180 mm deep which gives a mean effective stress of approximate 200 kPa (considering the scaling factor *N*). The values of the linear CSL altitude Γ, CSL slope λ, critical stress ratio M_{tc} and the state-dilatancy χ_{tc} are directly available from the Golder Project laboratory database (Jefferies & Been 2006). Therefore, the linear CSL will be applied in the following simulations. The CSL input parameters in Plaxis are shown in Figure 5.12.

The hardening modulus H_h ranges from 25 to 500 for commonly seen sandy soils, $H_h=4/\lambda$ is often used as a first attempt of estimation which gives H_h = 75 for Leighton Buzzard sand. As the value of H_h will be changed for the purpose of parametric study, it should be noted that there is a limit of the minimum value of H_h:

$$H_h > \frac{1}{2(\lambda - \kappa)} \qquad [5.4]$$

where κ is the slope of the elastic unloading reloading line. In the proposed model, the slope of URL is curved and is related to the non-linear elasticity parameters, current stress level and void ratio as discussed in Section 4.2.3, therefore κ is not constant anymore. By considering the initial void ratio of the Leighton Buzzard Fraction E sand and the approximate stress level 0~200kPa from surface to tunnel level of this study, according to Figure 4.7, κ is estimated as 0.002 which leads to a minimum H_h of 10.

The softening modulus H_u and the volumetric coupling coefficient N are set as 50 and 0.5 respectively (Jefferies & Been 2006) for general sands.

The initial state parameter ψ_0 is the most important input parameter as it defines whether the soil is relatively dense or loose, thus leading to different types of volumetric behaviour of the soil. ψ_0 is initially set as zero which indicates a normal compressed condition.

The elastic parameters D_1, D_2, r_1, and r_2 are assigned with the empirical values determined in Chapter 4. To match the 30 MPa initial shear stiffness G_0 of Leighton Buzzard Fraction E sand at 200kPa, with an initial void ratio of 0.68, according to the discussion in Section 4.2.2, the input parameter C_i is set as 2600.

The 14 input parameters of Leighton Buzzard Fraction E sand in Plaxis are shown in Figure 5.12. Due to coding issues in the FORTRAN 90, in the Plaxis input parameter window, the parameters are not shown as their original forms. The corresponding original signs used in this thesis are listed as bold font in Figure 5.12.

5.3.6 The monitoring points

Both surface and subsurface ground displacements are studied in the FEM result evaluation section. In order to compare with the ground displacement results in the centrifuge test, the numerical displacement results on the surface level, z = -70mm, z = -120mm and the tunnel central line from surface to tunnel crown are recorded (black dashed line in Figure 5.13). As the ground movements

further than 300mm away from the tunnel central line are negligible in both centrifuge test and numerical simulation, only the data within 300mm from the tunnel central line are presented.

The stress developments experienced by soil elements around the tunnel are continuously recorded during the tunnel volume loss simulation process. Five points are marked for stress data recording as shown in Figure 5.14. The stress paths are illustrated in the form of the effective deviatoric stress q against the effective principal stress p.

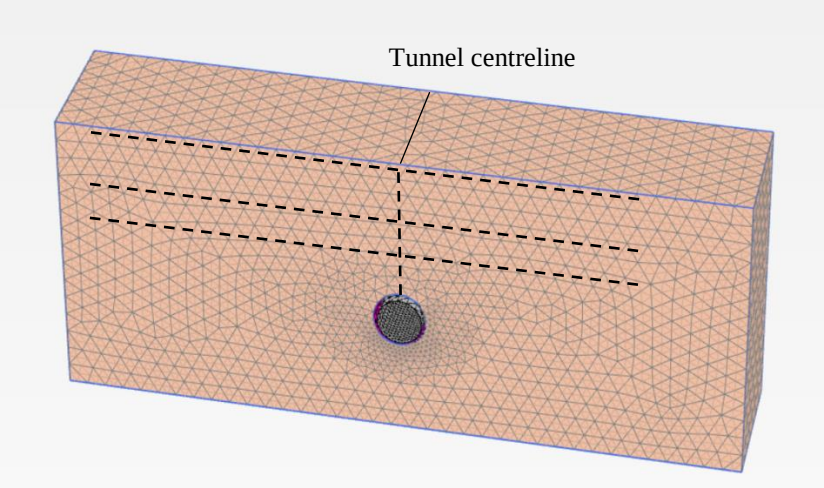

Figure 5.13 Sections for ground displacement analysis.

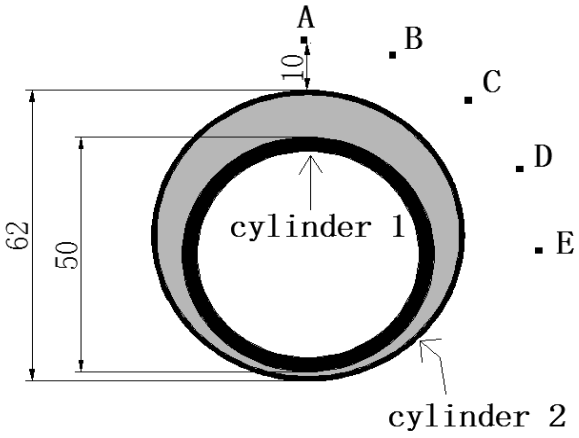

Figure 5.14 Points for stress development examination (dimensions in mm).

5.4 Parametric study of the initial state parameter ψ_0

This section describes the analysis carried out for studying the influence of the input parameter ψ_0 of the proposed constitutive sand model. Most of the input parameters for sands are directly determined from laboratory databases, thus should not be varied during numerical modelling. As discussed in

chapter 3, during excavation, volumetric variation distinguishes tunnelling in sand cases from the cases in general soft soils. The key factor which affects the volumetric behaviour of sand is determined as the initial state parameter ψ_0, which stands for the initial density of soil, which affects the hardening and softening of the yield surface. In addition, the determination of ψ_0 is based on current void ratio, stress level and the critical state void ratio for corresponding stress level. This requires high consistency of soil conditions between the in situ soil sample and the sample used for establishing the laboratory database. Therefore the theoretical determined value of ψ_0 may not perfectly reflect the behaviour of the studied in situ sand involved in the excavation.

As the state parameter was not the research interest in the centrifuge test (Marshall 2009), the state parameter of the soil before and after the tunnel deformation is unknown. In the centrifuge test, to reach the final 75g condition (scaling factor N = 75), the gravity was gradually increased by 10g each increment. It is reasonable to speculate that the state of the soil remains on the normal consolidation line before deformation of the tunnel prototype, thus the initial state parameter is very possible to have a negative or near-zero value as the soil has been considerably compacted in the gravity increasing process. Four ψ_0 values including -0.2, -0.1, 0 and 0.1 are applied in the following study. These ψ_0 values correspond to initial void ratio of 0.48, 0.58, 0.68 and 0.73 under 200kPa confining stress of Leighton Buzzard Fraction E sand.

5.4.1 Vertical settlement troughs

The calculated transverse ground settlement troughs at tunnel volume loss of 0.5%, 1.0%, 2.5% and 2.5% using the proposed model with ψ_0 = 0, ψ_0 = -0.1 and ψ_0 = -0.2 are plotted in Figure 5.15 ~ Figure 5.18 and compared with the centrifuge data. The settlements are normalised by their maximum values as illustrated in Figure 5.15 ~ Figure 5.18 to indicate the shape of the settlement trough. As the vertical settlement troughs calculated by ψ_0 = 0.1 shows relatively large deviation compared to the centrifuge data and the troughs calculated by other initial state parameter values, it is not included in the following figures. Overall, ψ_0 = 0.1 over estimates the settlements at all depths and tunnel volume loss levels although the shape of the settlement troughs is reasonable compared to the centrifuge data. This deviation is due to a very loose state of sand is given by ψ_0 = 0.1, thus lead to large amount of ground contraction (see section 5.4.4). Details of the predicted vertical settlements by using ψ_0 = 0.1 are given in Appendix C.

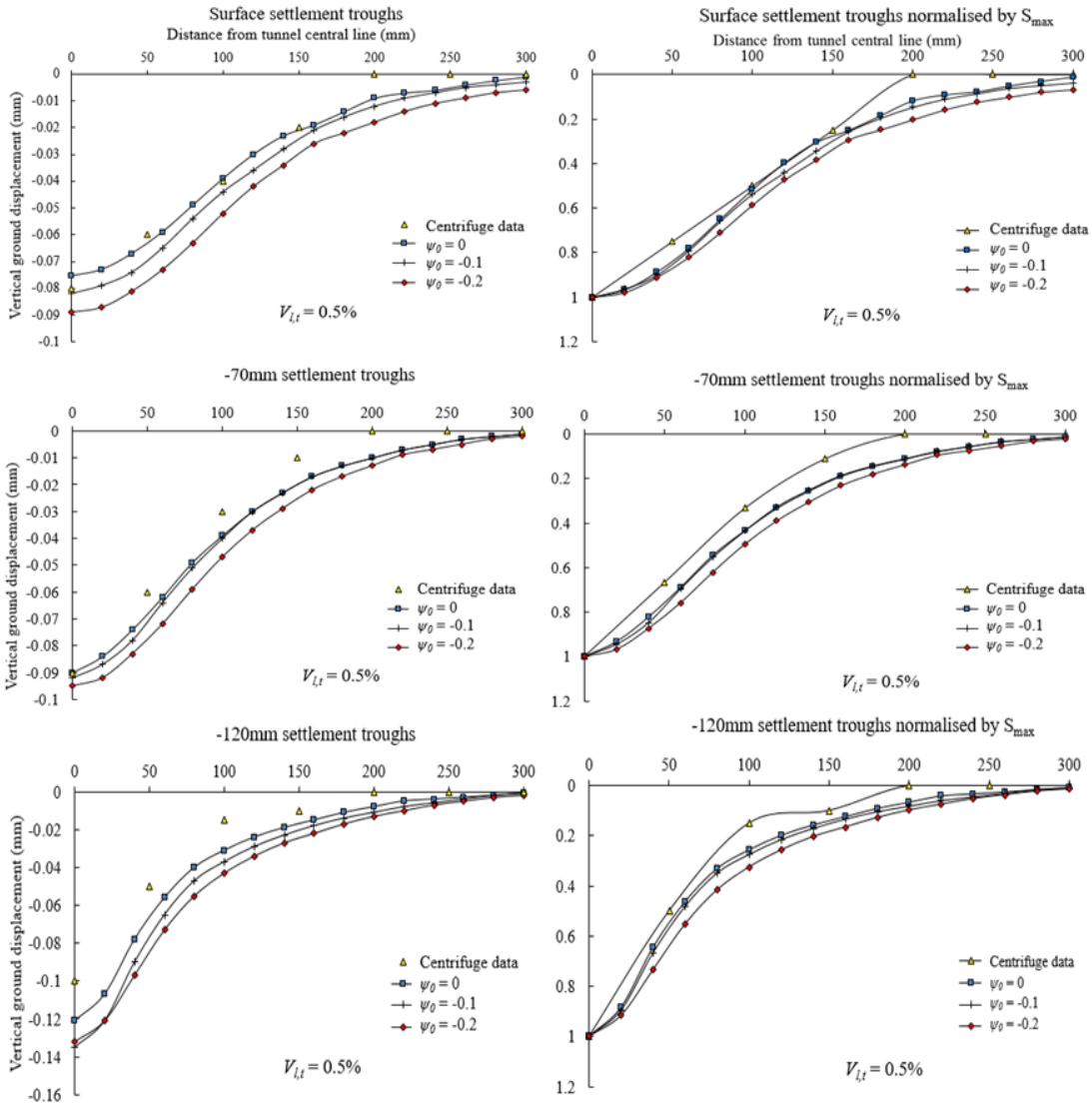

Figure 5.15 Vertical settlement troughs at three depths (surface, -70mm and -120mm) calculated by the proposed model with $V_{l,t}$=0.5%.

From Figure 5.15, at $V_{l,t}$ = 0.5%, the calculated maximum settlement values at surface and 70mm depth show good agreements with the centrifuge data. Lower initial state parameters tend to give larger maximum settlement values. At 120mm depth, all initial state parameter values slightly overestimate the settlement. The widths of the settlement troughs become narrower as the depth increases according to the centrifuge data, this feature is well demonstrated by the numerical results. ψ_0 = -0.2 gives slightly wider settlement troughs compared to ψ_0 = 0 and ψ_0 = -0.1 although the difference between the calculated trough shapes is very small.

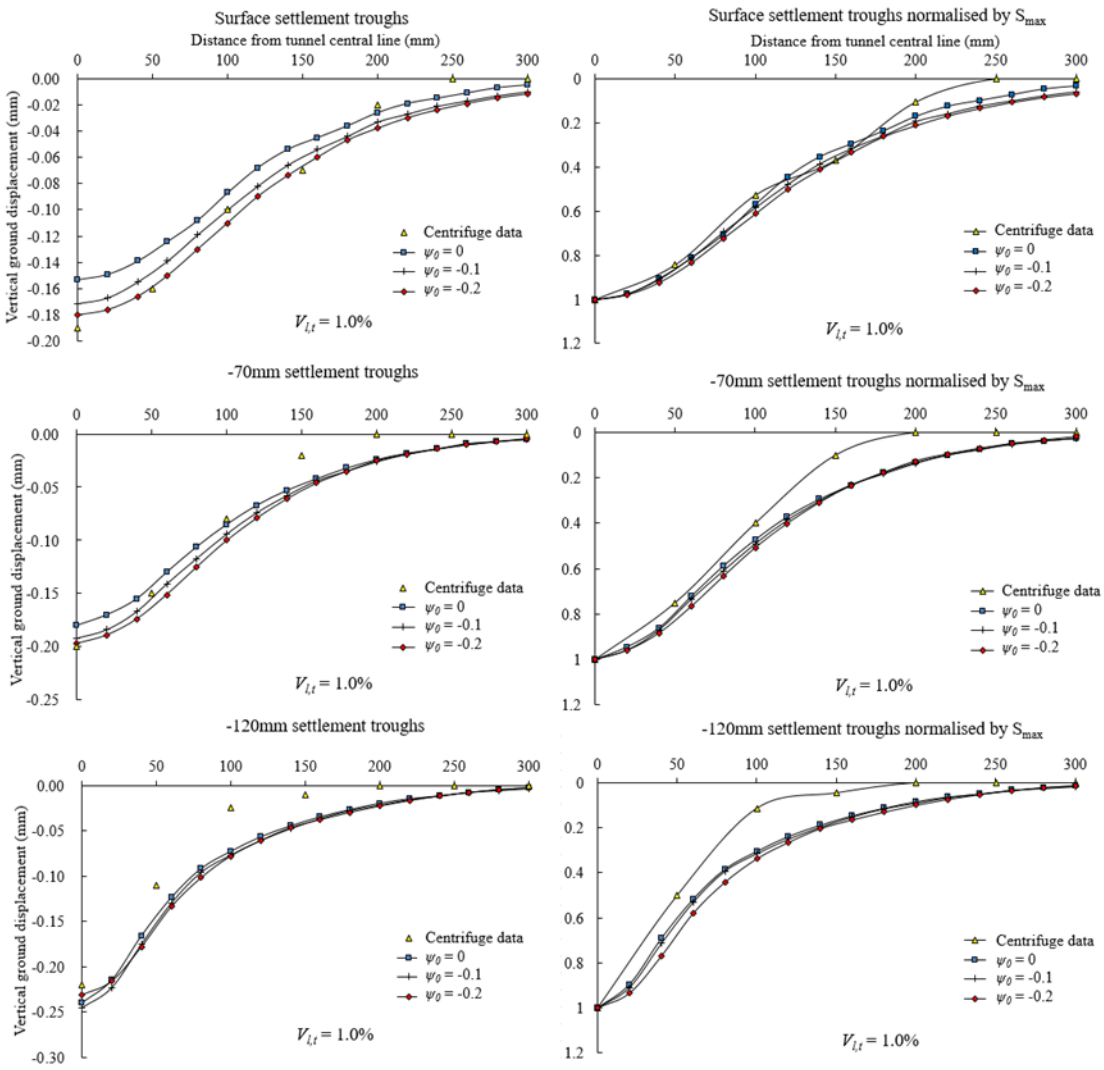

Figure 5.16 Vertical settlement troughs at three depths (surface, -70mm and -120mm) calculated by the proposed model with $V_{l,t}$=1.0%.

As $V_{l,t}$ increases to 1.0%, ψ_0 = -0.2 overall gives best predictions especially on the surface level where ψ_0 = 0 and ψ_0 = -0.1 underestimate the vertical settlement values as shown in Figure 5.16. This is due to the soil contraction at around surface area being better captured by a lower initial state parameter. Similar to the situation in the case of $V_{l,t}$ = 0.5%, the predictions of trough shapes closely match the centrifuge data, despite that the numerical calculated trough widths are a little wider than the trough widths measured in the centrifuge test.

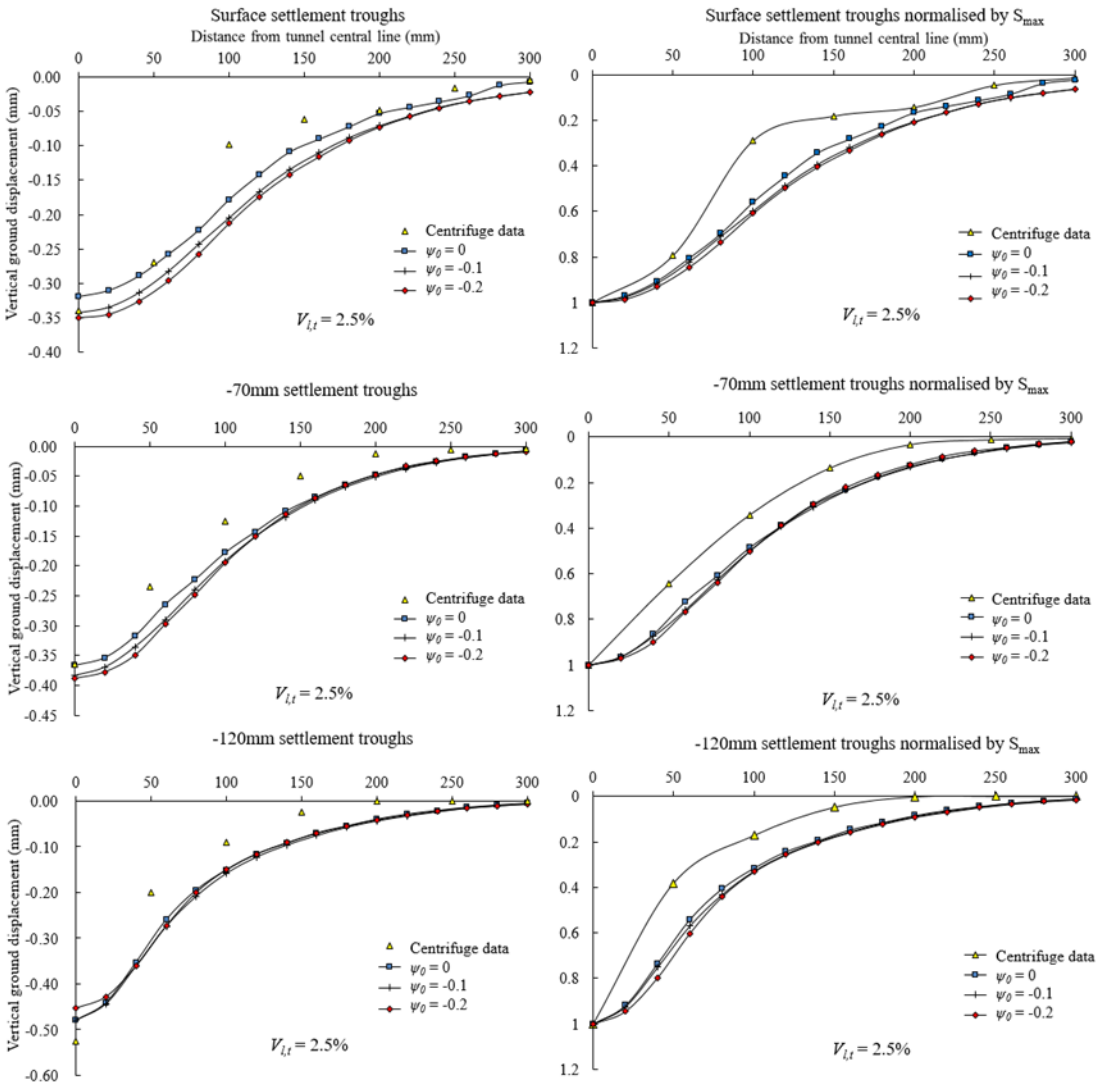

Figure 5.17 Vertical settlement troughs at three depths (surface, -70mm and -120mm) calculated by the proposed model with $V_{l,t}$=2.5%.

As illustrated in Figure 5.17, the maximum settlement values are well predicted at surface and 70mm depth when the tunnel volume loss reaches 2.5%. The discrepancy between the numerical results and the centrifuge data becomes larger at the depth of 120mm where the maximum vertical settlement value is underestimated by all initial state parameter values and the settlements further away from the centreline are over estimated. The calculated trough widths are becoming even wider relative to the measured data compared to the situations of $V_{l,t}$= 0.5% and 1.0%.

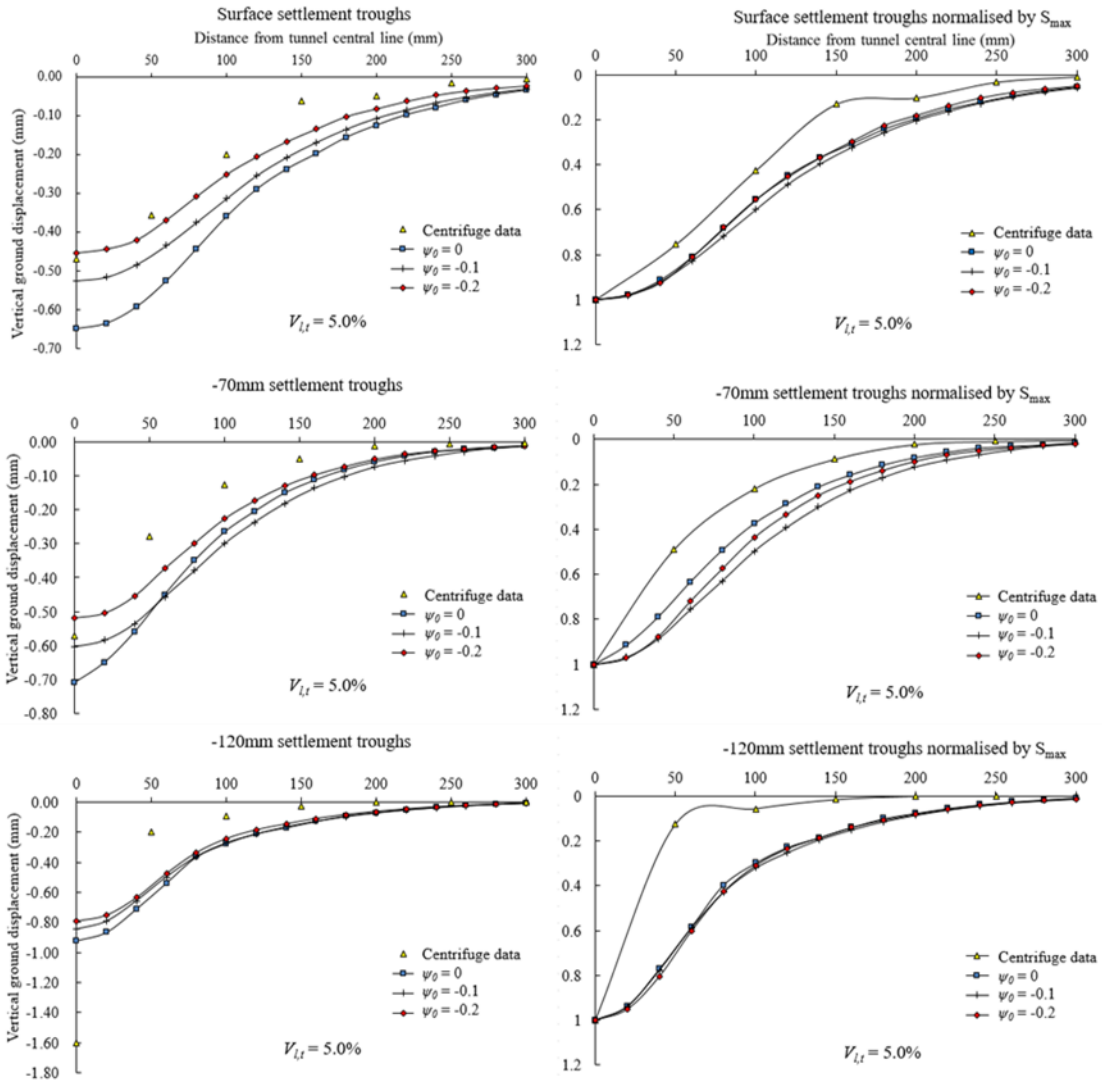

Figure 5.18 Vertical settlement troughs at three depths (surface, -70mm and -120mm) calculated by the proposed model with $V_{l,t}$=5.0%.

From Figure 5.18, the correlation between the width of settlement trough and depth becomes more clear at $V_{l,t}$=5.0%. The widths of settlement troughs measured in the centrifuge test continuously becoming narrower as the measurement level goes deeper. The inflection point of the settlement trough decreases from 150mm (three diameters) to 50mm (one diameter) from surface level to 120mm depth. This trend is also illustrated by the numerical results, however the absolute values of calculated trough widths are larger compared to the test data. At surface and 70mm depth, the vertical settlement values are severely overestimated by ψ_0= 0, and slightly over predicted by ψ_0= -0.1 while ψ_0= -0.2 gives relative reasonable settlement values at these depths. This phenomenon can be explained by the soil dilation that will be discussed in 5.6.6. When it goes closer to the tunnel at 120mm depth, the measured vertical displacement is considerably larger than the numerical predictions given by all ψ_0 values.

5.4.2 Horizontal ground displacement

As the linear variable differential transducers (LVDT) applied in the centrifuge model were not able to measure horizontal ground movement, the horizontal troughs were not stated in the centrifuge test, only horizontal displacement contours were imaged by the particle image velocimetry (PIV) technique. This section shows the calculated subsurface horizontal ground displacement troughs by using different initial state parameter values. The calculated horizontal ground displacement contours will be compared with the centrifuge data and further discussed in section 5.6.3. The numerical results from ψ_0 = 0.1 are shown in Appendix C. It should be noted that in Figure 5.19 ~ Figure 5.22, the horizontal size of the tunnel is not the real scale size, the tunnel periphery in the following figures aims to indicate the relative positions of the tunnel to the horizontal ground movement troughs.

The horizontal ground subsurface movements 15mm away from the tunnel are plotted in Figure 5.19. At 1% tunnel volume loss, the horizontal ground movement is negligible with maximum displacement of 0.05mm calculated by ψ_0 = 0 and -0.1. ψ_0 = -0.2 gives smallest horizontal ground movement with a maximum movement of 0.03mm located around the tunnel axis level. As tunnel volume loss increases to 5%, all ψ_0 values predict similar displacements with maximum horizontal movement of approximately 0.25mm (1/200 tunnel diameter) located at the tunnel axis level, which indicates the influence of the inwards movement of the tunnel periphery. At 30mm away from the tunnel the discrepancy between the calculated troughs become larger as illustrated in Figure 5.20. Smaller initial state parameters tend to predict less horizontal ground movement. It is noted that ψ_0 = -0.2 shows greater sensitivity to the movement of the tunnel periphery compared to other ψ_0 values. This feature can be clearly seen at 5% tunnel volume loss where ψ_0 = -0.2 gives larger ground movement towards the tunnel at tunnel axis level whereas it predicts less ground movement in other depths compared to the results from ψ_0 = 0 and -0.1.

The horizontal ground displacements at further distances, 45mm and 60mm away from the tunnel boundary, calculated by same ψ_0 do not show larger difference as indicated in 错误!未找到引用源。 and Figure 5.22. Similar to the situation in near tunnel area, smaller ψ_0 value predicts less horizontal ground movement. The effect from the tunnel movement becomes very limited because of the increased distance from the tunnel. It is noted that ψ_0 = -0.2 predicts certain negative horizontal ground movement (moving away from the tunnel), this is perhaps due to the fact that at very early simulation steps the tunnel boundary around tunnel axis level was firstly moving away from the tunnel centre (the tunnel was slightly squeezed vertically in very first calculation steps). As ψ_0 = -0.2 makes the ground more sensitive to the outward tunnel movement, and for this very dense sand, it is capable of arching across the tunnel which would create an arch that would prevent the soil at side of the tunnel from moving inward. Sadrekarimi and Abbasnejad (2010) carried out centrifuge tests and

numerical modelling to study the arching effect in soft soil. They find out that denser soils generate larger arching effects under isotropic condition, this may explain the reason that ψ_0 = -0.2 leads to less horizontal ground movements during tunnel deformation. The impact of negative tunnel boundary movement remains at the distance of 45mm and 60mm in later calculation steps, thus in the case of ψ_0 = -0.2, the negative horizontal ground movement still exists when tunnel volume loss reaches 5.0%.

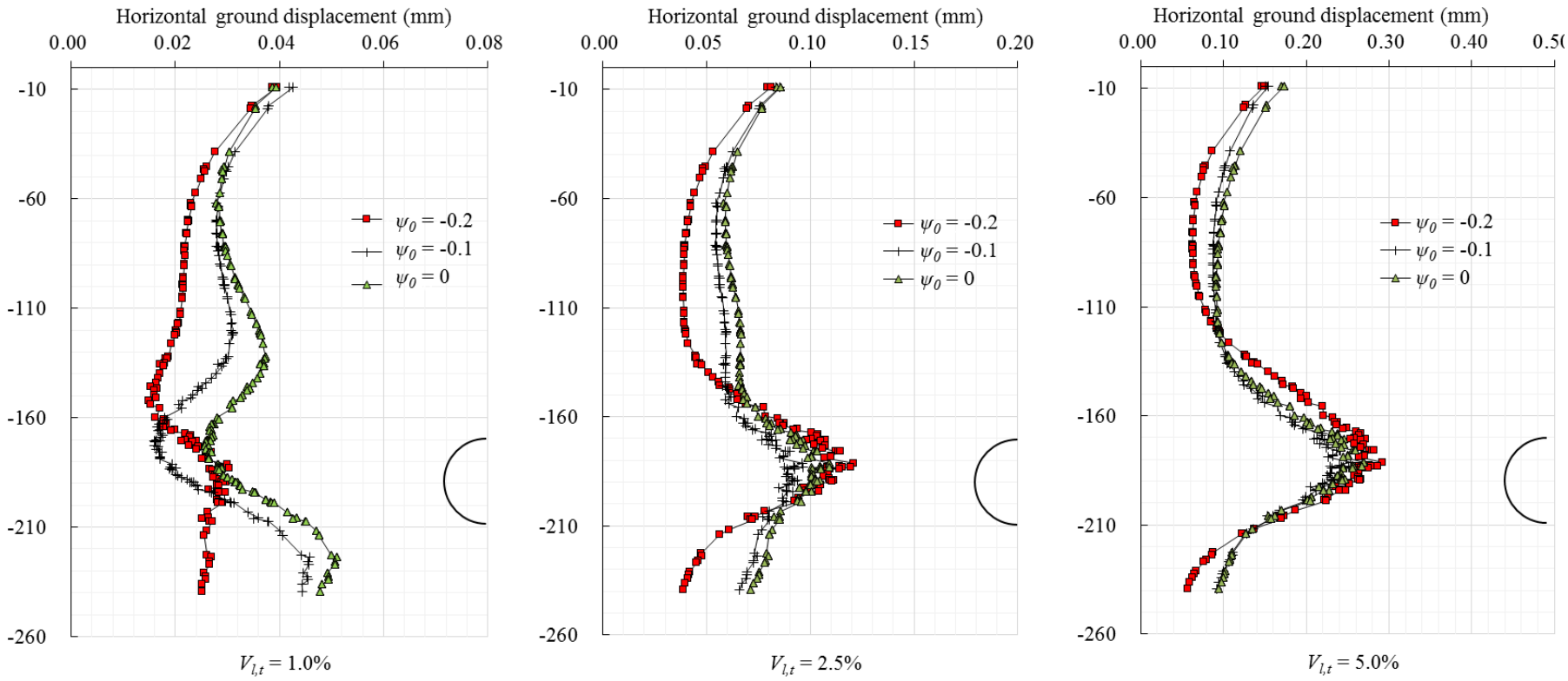

Figure 5.19 Horizontal ground displacements 15mm away from the tunnel periphery calculated by the proposed model.

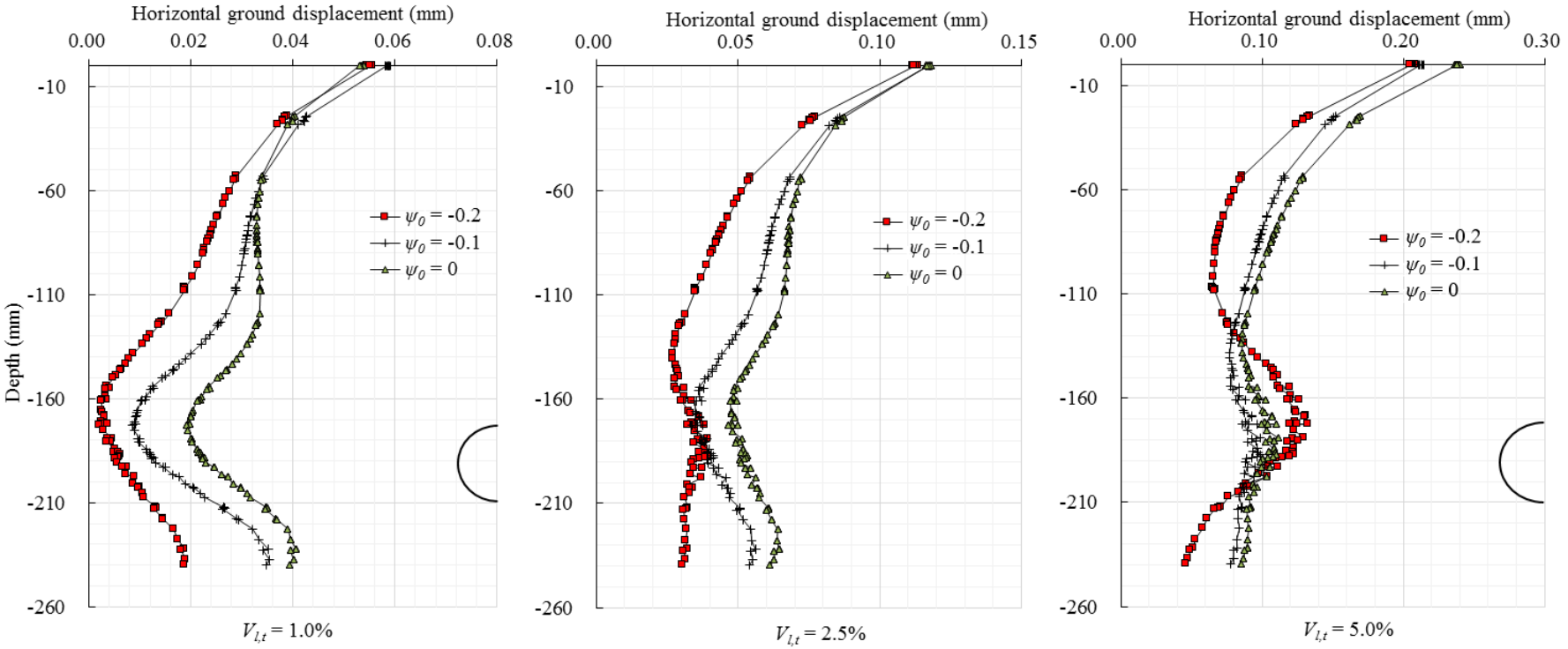

Figure 5.20 Horizontal ground displacements 30mm away from the tunnel periphery calculated by the proposed model.

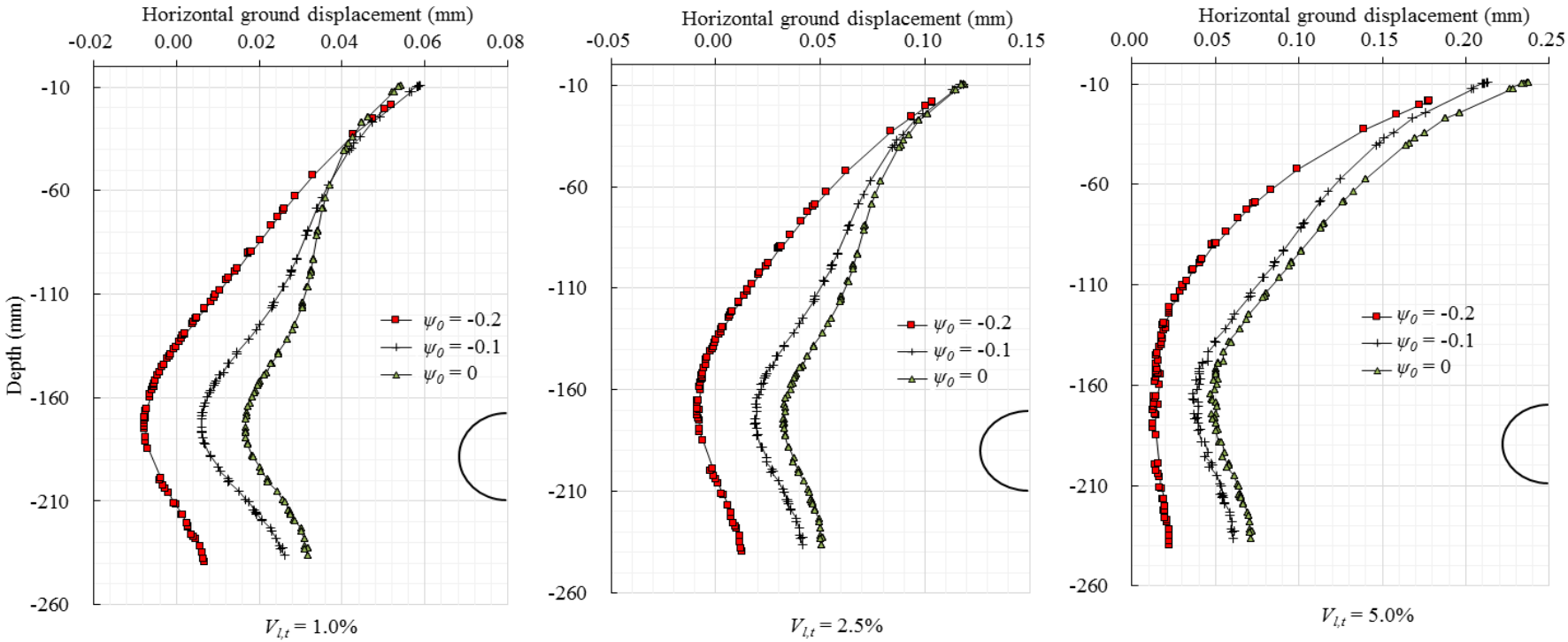

Figure 5.21 Horizontal ground displacements 45mm away from the tunnel periphery calculated by the proposed model.

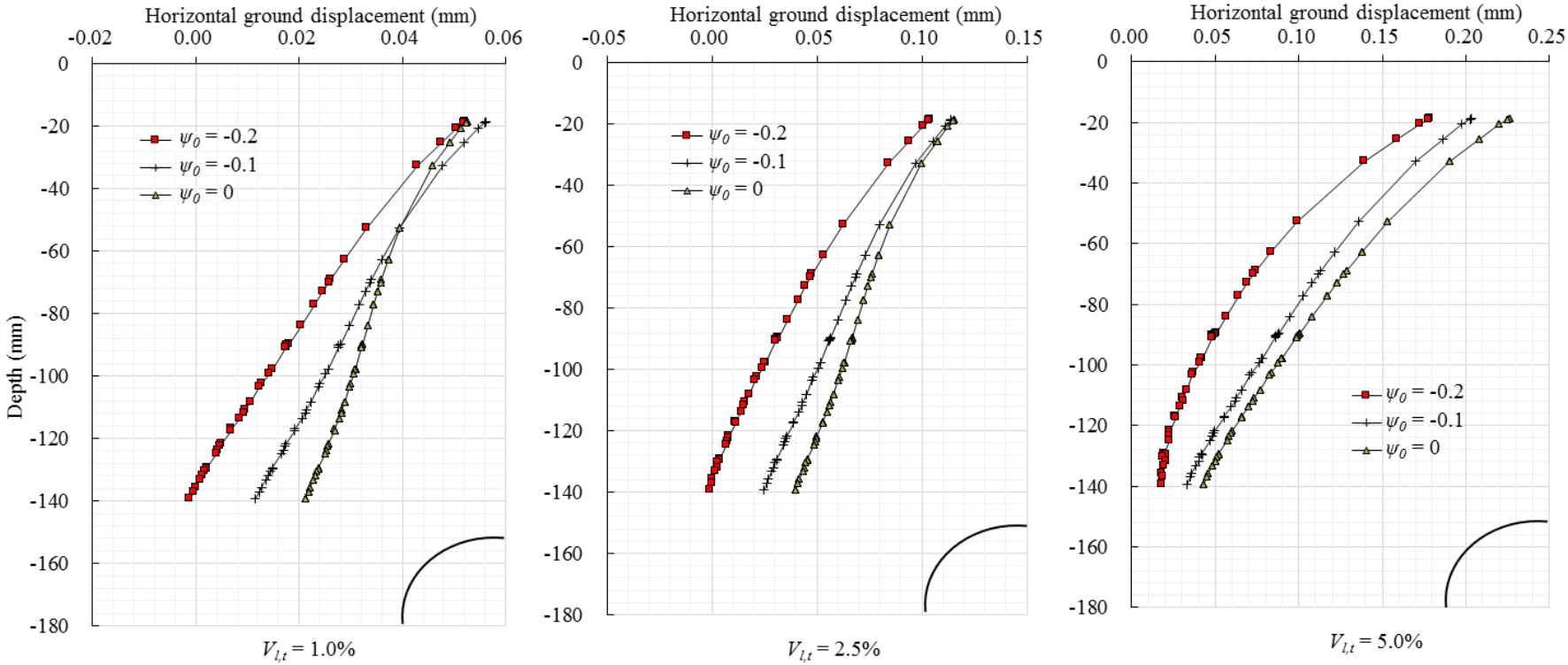

Figure 5.22 Horizontal ground displacements 60mm away from the tunnel periphery calculated by the proposed model.

5.4.3 Effect on stresses

5.4.3.1 Stress paths around tunnel

The stress paths from the numerical model are recorded at five points evenly deployed from tunnel crown to side as listed in Figure 5.14. The calculated stress paths by different initial state parameters are plotted in Figure 5.23 ~ Figure 5.27. It should be noted that the first 6 points are from the 'initialising stage' of numerical integration (before tunnel deformation process), thus fewer data is recorded compared to the tunnel deformation stages. It is not surprising that the stress paths calculated by different ψ_0 values share the same initial stress states as this state is only affected by the unit weight of the soil and K_0. It can be seen that the stress paths experienced by point A and B follow an approximate same trend: firstly decrease in shear stress with almost constant mean stress p' followed by a stress reversal point when the mean effective stress starts reducing considerably, accompanied by a sharp increase of shear stress. According to the numerical calculation data it is noted that the stress reverse happens around 0.45% tunnel volume loss. All calculated stress paths finally head to the position of critical state line while the magnitude of stress change calculated by ψ_0 = 0.1 differs greatly from the stress paths calculated by smaller $\psi_0$values. The normally consolidated soil (ψ_0 = 0), at its late deformation stage experiences an isotropic unloading process (decrease in confining stress p' with constant deviatoric stress q). In contrast, dense soils (negative ψ_0 values) at point A and B go through large increase in shear stress when approaching the critical states illustrated in Figure 5.23 and Figure 5.24.

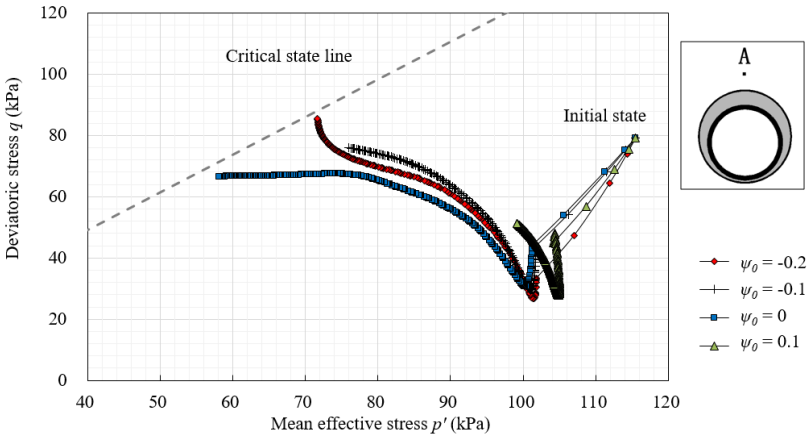

Figure 5.23 Stress paths at point A calculated by the proposed model.

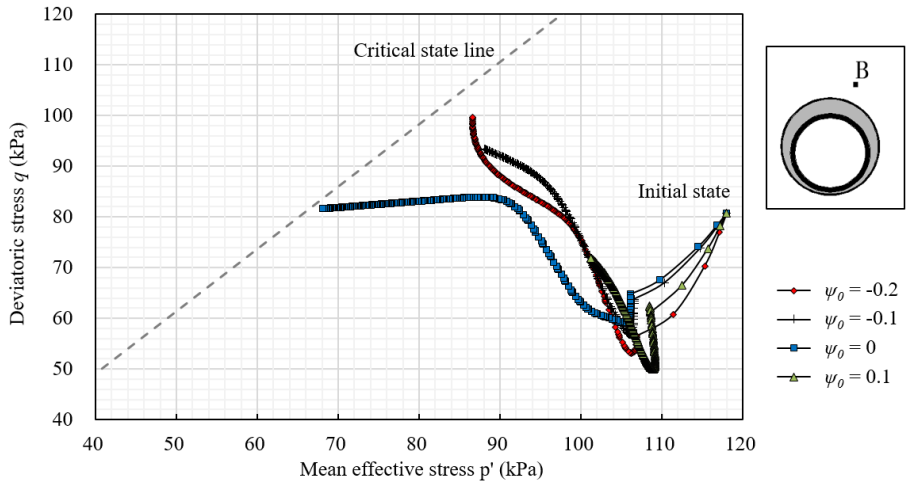

Figure 5.24 Stress paths at point B calculated by the proposed model.

It can be reasonably expected that at above the tunnel area (point A and B), the stress paths during tunnel deformation are mainly located within the yield surface according to the relative positions of the initial stress states and the elliptic shape of the yield surface. In contrast, expansion of yield surface and plastic stress strain behaviour should be found at point C, D and E according to Figure 5.25 to Figure 5.27. The discrepancy between the stress paths predicted by different ψ_0 values become larger at the plasticity zone, however more or less similar stress development trends can still be found at these points. The stress paths calculated by ψ_0 = 0 go pass the critical state line and continue the reduction of confining stress *p'* without change of shear stress at point C, D and E which indicates that ψ_0 = 0 predicts pure stress relaxation at all recorded points. At point C, D and E ψ_0 = -0.2 indicates sharp increase of shear stress after the stress paths go across the critical state line. The stress paths given by ψ_0 = -0.1 seem following same patterns predicted by ψ_0 = -0.2 at all five points, but with certain amount of delay in stress development stage, thus the calculated stress path are unable to go across the critical state line.

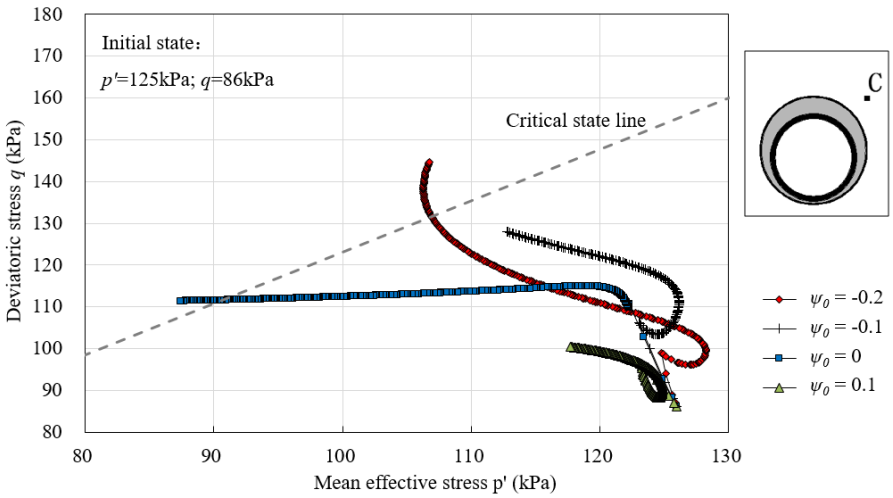

Figure 5.25 Stress paths at point C calculated by the proposed model.

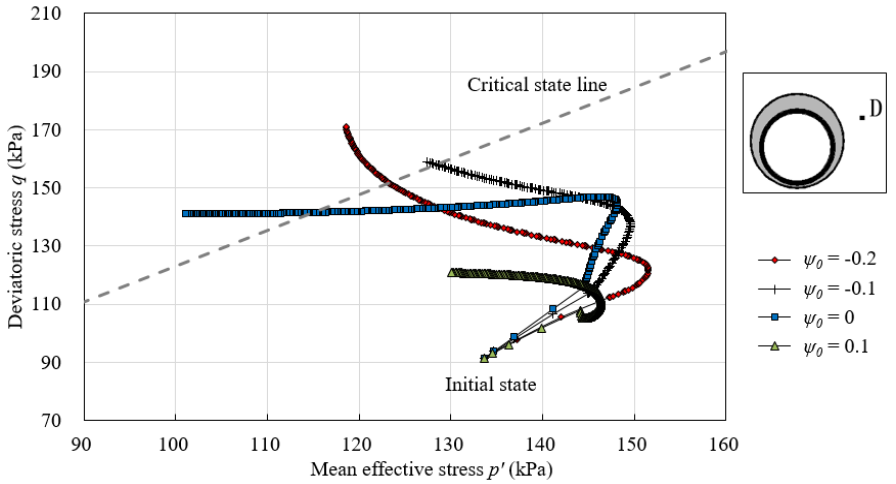

Figure 5.26 Stress paths at point D calculated by the proposed model.

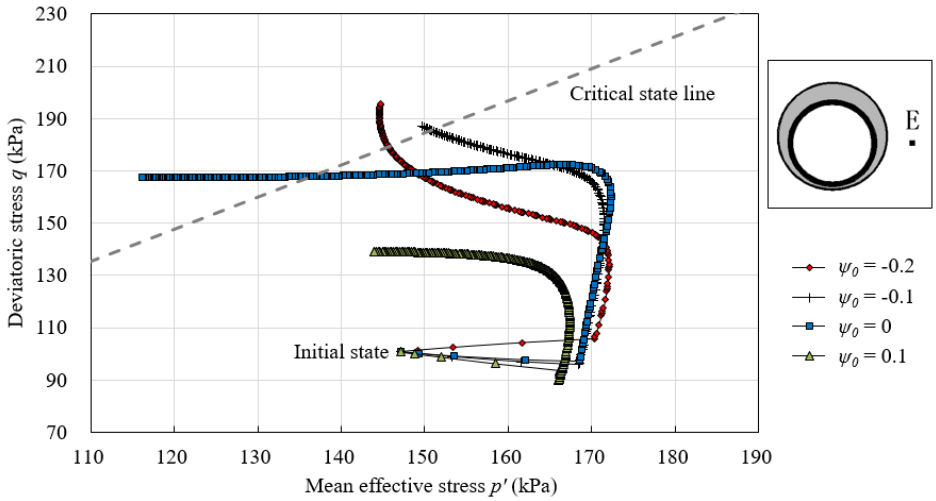

Figure 5.27 Stress paths at point E calculated by the proposed model.

5.4.3.2 Stress distribution above tunnel crown

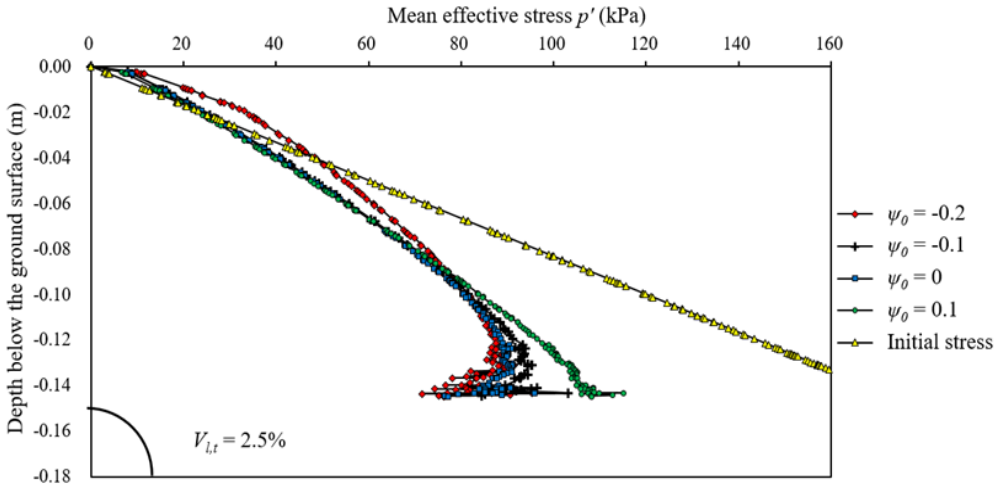

Figure 5.28 Mean effective stress above tunnel crown calculated by the proposed model

The calculated mean effective stress distributions above the tunnel crown at 2.5% tunnel volume loss are plotted in Figure 5.28. The figure illustrates that all ψ_0 values predict overall less mean effective stress compared to the original stress distribution, thus ground relaxation occurs at all depths (except the case with ψ_0 = -0.2) above the tunnel crown. It worth noticing that from surface to around 40mm below surface level ψ_0 = -0.2 shows increased mean stress *p'* which will theoretically lead to ground contraction. This may explain the reason that ψ_0 = -0.2 gives larger vertical settlement values at surface when $V_{l,t}$ = 1.0% and 2.5% compared to ψ_0 = 0 and -0.1 thus provides better predictions as shown in Figure 5.16 and Figure 5.17.

ψ_0 = 0.1 predicts monotonic stress increase from surface to tunnel crown level while other denser soil cases show a significant stress release close to the tunnelling area above the tunnel crown. The discrepancy between the stress calculated by ψ_0 = 0, -0.1 and -0.2 is negligible from 100mm depth to the tunnel crown level despite that smaller initial state parameter is likely to give smaller stress level close to tunnel area.

5.4.4 Effect on strains

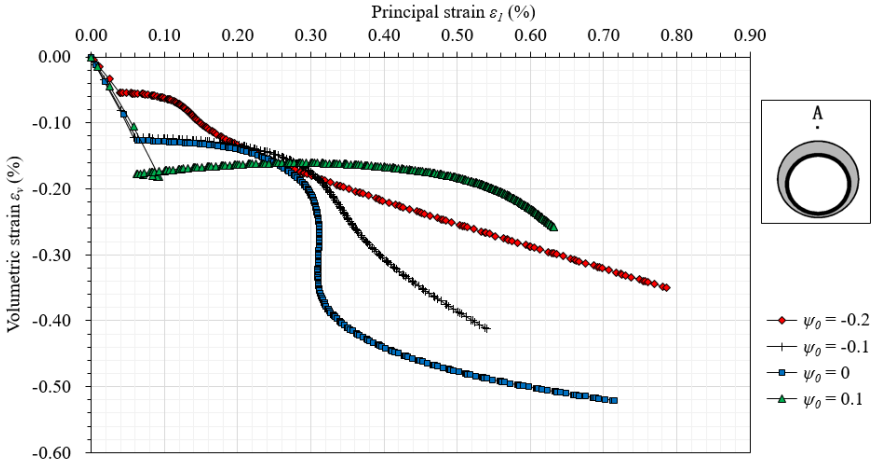

Figure 5.29 Volumetric behaviour of point A.

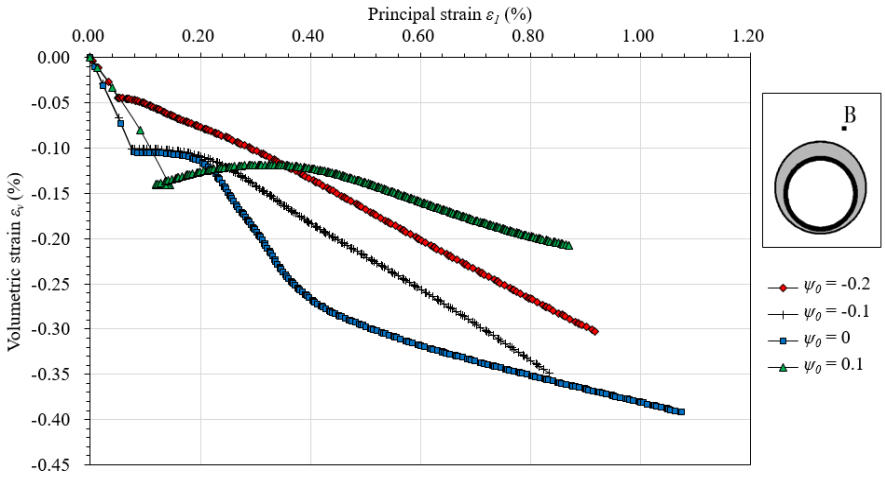

Figure 5.30 Volumetric behaviour of point B.

The volumetric strain developments at the recorded five points around the tunnel from zero to 5.0% tunnel volume loss are plotted against the increase of major principal strain in Figure 5.29 ~ Figure 5.33 where negative volumetric strain indicates soil dilation; positive volumetric strain stands for contraction. As a result of the stress relaxation above the tunnel crown, all predicted strain curves at point A and B overall illustrate monotonic increase of volume (dilation of soil) because the volumetric strain development is dependent on the elastic stiffness at above the tunnel crown area. Therefore the loose sand case predicted by ψ_0 = 0.1 produces smallest soil dilation due to less reduction of mean effective stress *p'* as shown in Figure 5.23 and Figure 5.24.

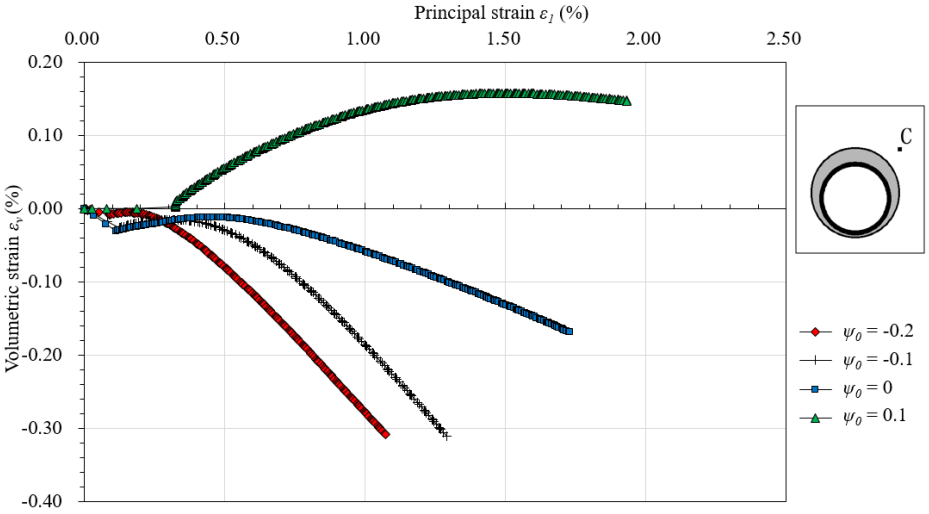

Figure 5.31 Volumetric behaviour of point C.

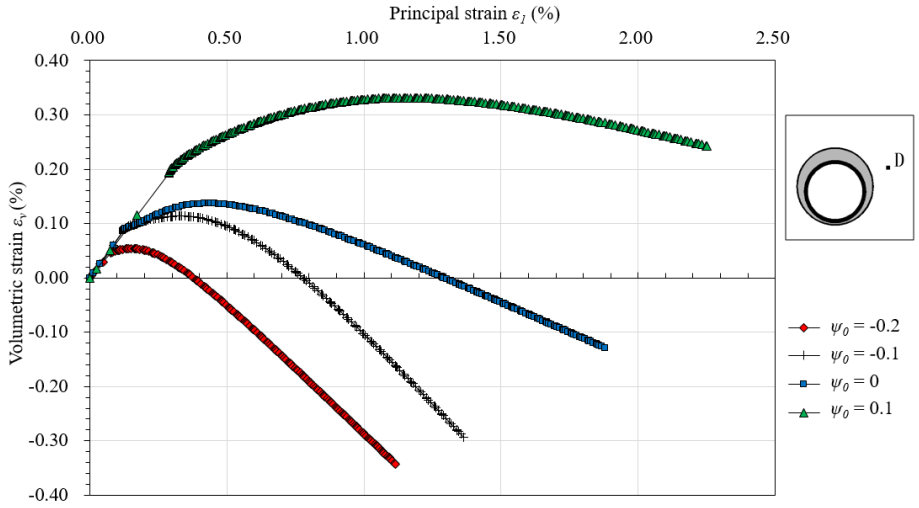

Figure 5.32 Volumetric behaviour of point D.

The calculated volumetric strain developments at point C illustrate clear difference between the behaviour of dense and loose sand under shearing. Dense sand (ψ_0 = -0.2 and -0.1) generates relatively large soil dilation with approximate -0.3% volumetric strain at end of simulation (around 5.3% tunnel volume loss). The normally consolidated soil (ψ_0 = 0) predict least volumetric change with -0.17% soil dilation at its maximum major strain level of 1.7%. The loose sand case shows a totally different story by predicting continuous contraction at point C. The predicted volumetric strains by different ψ_0 values at point D and E show similar trend: contraction followed by expansion, although the absolute values of volumetric change remain large deviations. Loose sand overall gives most decrease in volume, the transition between contraction and dilation happens around 1.25% and 0.75% principal strain levels at point D and E respectively which indicate the moment of passing the image point. ψ_0 = -0.1 and 0 generate relatively smaller ranges of volume change with earlier triggers

of transition between contraction and dilation compared to loose sand. ψ_0 = -0.2 firstly goes through a short process of contraction, and then switches to dilation at point D and E. The strain developments predicted at these two points by ψ_0 = -0.2 are very similar to the direct shear case discussed in section 3.2.6, where dense sand firstly experiences contraction, and then, after passing the image point, dilation occurs with continuous hardening.

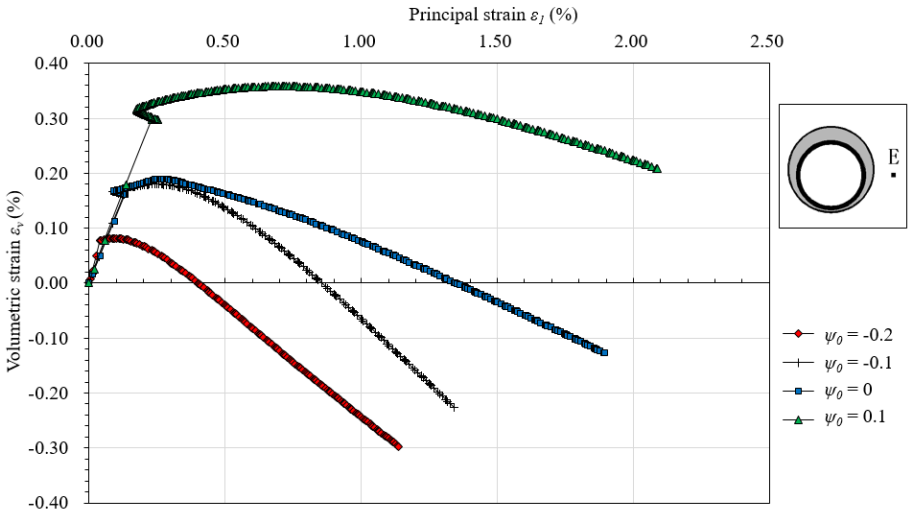

Figure 5.33 Volumetric behaviour of point E.

5.4.5 Summary

Generally the vertical ground movement predictions given by ψ_0= 0, ψ_0 = -0.1 and ψ_0 = -0.2 are reasonable compared to the centrifuge data when the tunnel volume loss is around 0.5%~2.5%. The benefit of using a dense state model (ψ_0= -0.2) can be seen in the predictions of surface ground movement at smaller $V_{l,t}$ values (where ground contraction happens, further discussion of ground contraction on surface see section 5.6.6), and the predictions at $V_{l,t}$ = 5.0%, although, all ψ_0 values fail to match the very large maximum vertical settlement value at the depth of 120mm when $V_{l,t}$ = 5.0%. In terms of horizontal ground movement all ψ_0 values predict similar trend of ground movement troughs whereas smaller initial state parameters tend to predict smaller horizontal ground movement, and are more sensitive to the impact from the restraint of tunnel boundary. According to the predicted stress and strain developments at five points around the tunnel, the stress paths and strain curves calculated by ψ_0 = -0.2 are found to clearly replicate the stress strain behaviour of dense sand under shearing discussed in chapter 3. Overall, ψ_0 = -0.2 gives better predictions of vertical ground movement and more specific features of sand behaviour, thus -0.2 is selected as the initial state parameter for further FE analysis.

5.5 Effect of K_0

According to Gao et al (2014), K_0 is determined as 0.53 for Leighton Buzzard Fraction E sand under normal consolidation states as shown in Figure 5.34, thus this K_0 value was applied in the previous parametric study of the proposed constitutive sand model. To explore the effect of varying K_0 on ground deformation and stress development around the tunnel, 0.4 and 0.6 are applied in the numerical modelling in this section with the initial state parameter of -0.2. The selection of these K_0 values is to cover the range of K_0 immediate after secondary compressions (up to 0.58, see Figure 5.34) and under overconsolidated conditions (down to 0.47). The calculated results are compared with the predictions given by K_0 = 0.53 and the measured data in the centrifuge test.

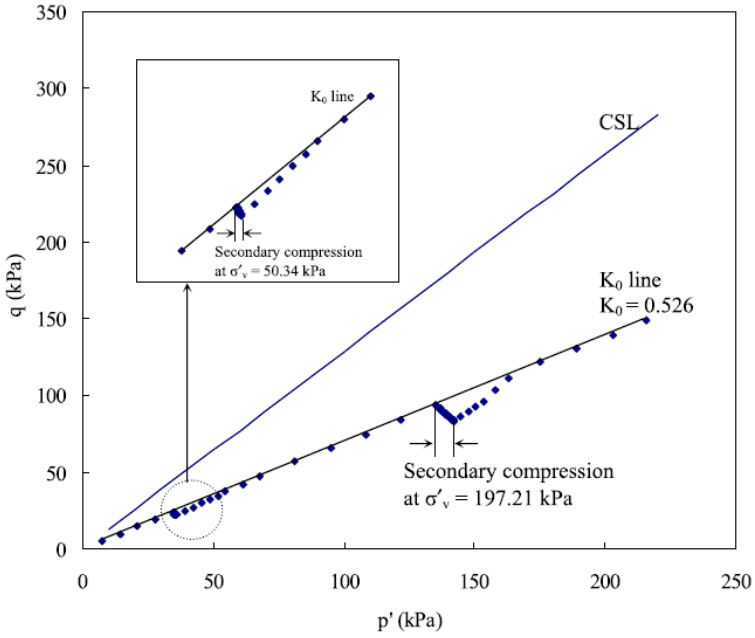

Figure 5.34 Evaluation of K_0 of the Leighton Buzzard Fraction E sand under normal consolidation state (Gao et al. 2014).

5.5.1 Effect on ground displacements

It is found that change of K_0 does not make significant variations on the ground displacements, therefore only the ground movement at the surface and 70mm depth with $V_{l,t}$ = 1.0% and 2.5% are reported. As the manners and trends of horizontal ground displacements calculated by the proposed model have been detailed in previous discussion, only selected parts of the recorded data are discussed in the following contents. Full details of the numerical predictions of horizontal ground movement from different K_0 values are given in Appendix D.

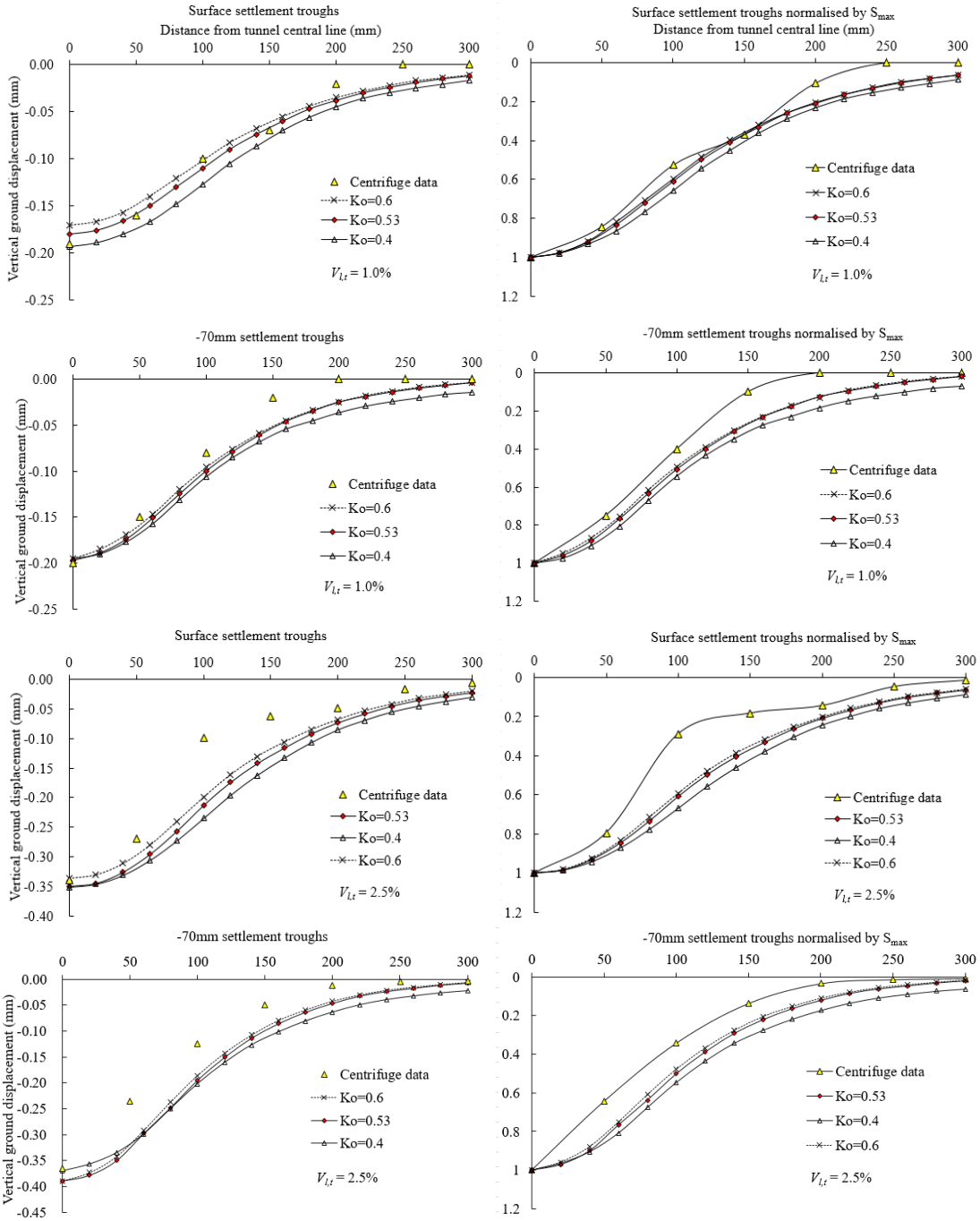

Figure 5.35 Effect of K_0 on vertical ground displacement.

The calculated transverse vertical settlement troughs by three different K_0 values are plotted in Figure 5.35. At surface level the increase in K_0 predicts less magnitude of vertical settlement with both $V_{l,t}$ = 1.0% and 2.5%. At 70mm depth, with $V_{l,t}$ = 1.0%, all three K_0 values give similar maximum settlement values which are closely matched with the measured centrifuge data. When the tunnel volume loss increases to 2.5% K_0 = 0.4 is found to give best prediction of vertical maximum settlement value at 70mm depth while larger K_0 slightly overestimates the settlement. Overall, K_0 =

0.6 predicts larger amount of change in the maximum vertical settlement value at same depth during the tunnel deformation progress.

The normalised vertical settlement is well predicted by all three K_0 values at surface when $V_{l,t}$ = 1.0%. As discussed in the previous section, the measured trough widths decrease with both depth and tunnel volume loss, whereas change of K_0 seems give very limited improvement on predicting this feature. Although the increased K_0 predicts relative narrower settlement troughs according to the figure, the magnitude of this change is not comparable with those found in the centrifuge test.

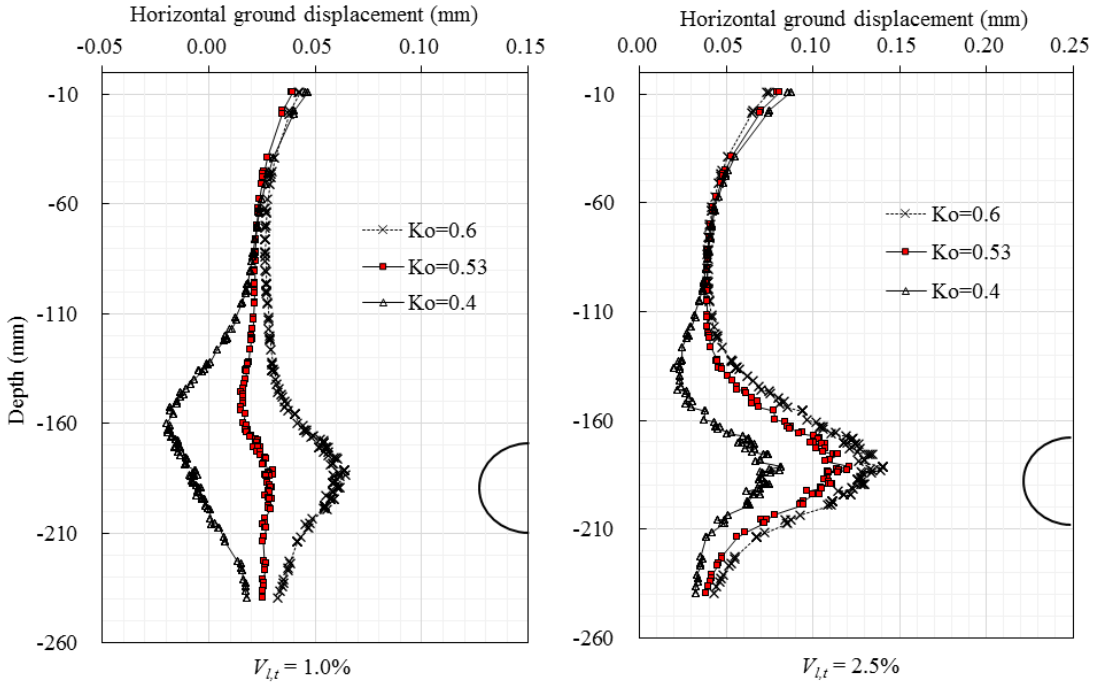

Figure 5.36 Effect of K_0 on horizontal ground displacement 15mm from tunnel periphery.

The calculated horizontal ground movement troughs with $V_{l,t}$ = 1.0% and 2.5% at 15mm away from the tunnel boundary are plotted in Figure 5.36. Larger horizontal ground movement is found to be given by K_0 = 0.6 which illustrates that the increase of K_0 enhances the sensitivity of the ground to the movement of tunnel boundary. However consistent horizontal ground movements are predicted by all K_0 values at surface level.

5.5.2 Effect on stresses

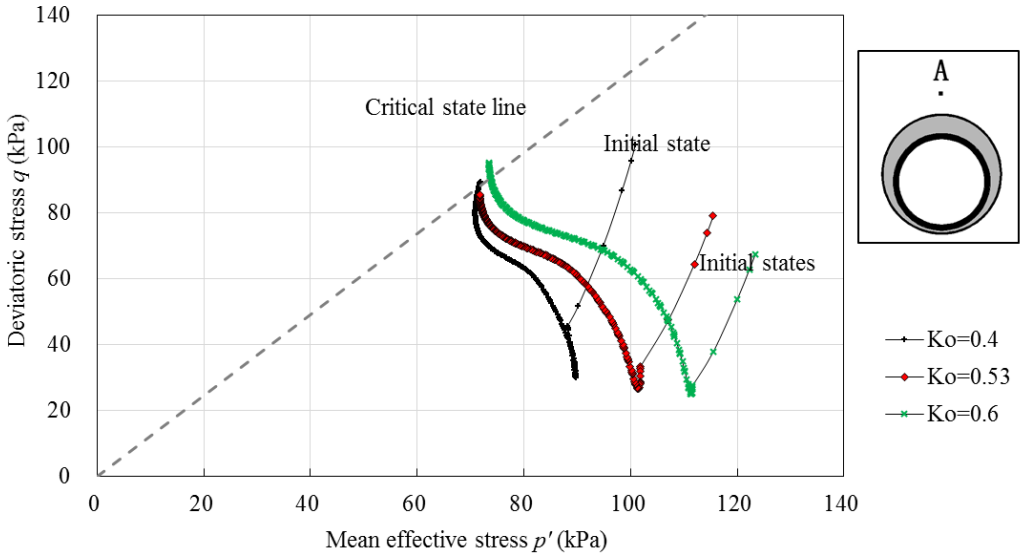

Figure 5.37 Effect of K_0 on stress path at point A.

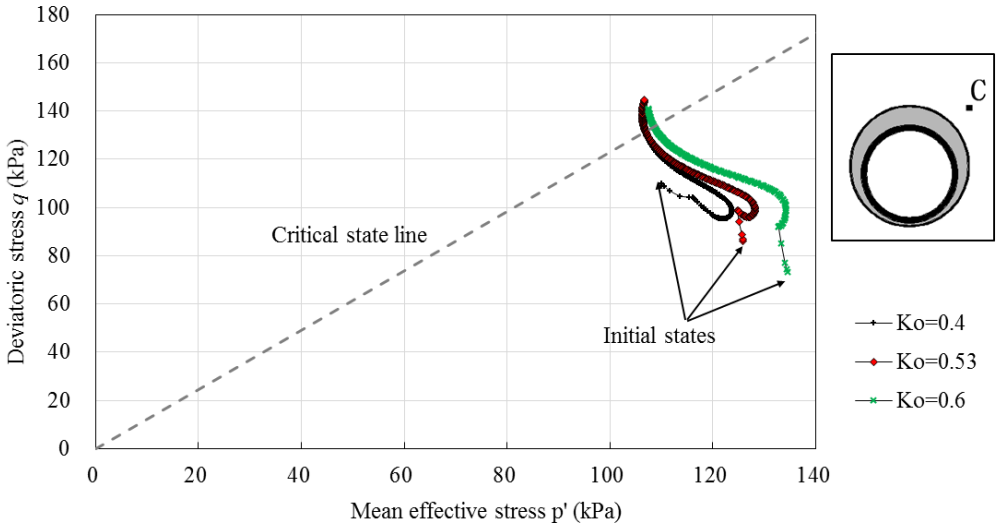

Figure 5.38 Effect of K_0 on stress path at point C.

The calculated stress path at point A (elastic zone) and point C (plastic zone) by different K_0 values are plotted in Figure 5.37 and Figure 5.38 respectively. The stress paths at point B, D and E can be found in Appendix D. It can be seen that reduction of K_0 introduces a lower initial mean stress state as expected, as smaller K_0 generates less horizontal stress at same depth compared to larger K_0 value. However, larger initial shear stress exists for smaller value of K_0. During tunnel deformation, similar trends of stress developments calculated using all K_0 values can be found at point A, whereas the

stress reversal point is missing at point C when applying K_0 = 0.4 in which case a smoother stress development is predicted. Overall, larger K_0 causes larger changes in both mean effective stress *p'* and deviatoric stress *q* which may explain why larger variations of the predicted vertical settlement can be found at a given depth when applying K_0 = 0.6. The discrepancies between stress paths at the same location become smaller as tunnel volume loss increases. At around the critical stress state where the stress paths terminated, the discrepancies between stress paths calculated by different K_0 values become negligible which indicates that K_0 does not necessarily affect the intersection point of the stress paths and the critical state.

5.6 Comparison of the proposed model and Hardening Soil

The Hardening Soil model with the input parameters concluded in section 5.3.5.1 is applied in the numerical simulations discussed in this section. The results predicted by the Hardening Soil are compared with the measured centrifuge data and the numerical results calculated by the proposed model with ψ_0 = -0.2. Both constitutive models apply a realistic K_0 value of 0.53 for Leighton Buzzard fraction E sand (Gao et al. 2014).

5.6.1 Deformation of the tunnel profile

The calculated deformed tunnel boundary at 1.0% and 2.5% tunnel volume losses is plotted in Figure 5.39 according to the changed coordinates of the 16 points located on the tunnel periphery (see Figure 5.8). Data of the tunnel boundary movements are listed in Appendix B. The deformations of the tunnel are plotted with ten times of its real scale for better illustrations.

Figure 5.39 shows similar tunnel deformation pattern as found in the centrifuge tunnel prototype (Marshall 2009) where most deformation occurs above the crown, thus matches the simplified tunnel deformation patterns concluded by previous studies (Lo and Rowe 1982, Rowe and Kack 1983 and Gonzalez and Sagaseta 2001). The deformed tunnels calculated by two constitutive models are almost overlapped at 1.0% tunnel volume loss. At 2.5% tunnel volume loss the deviation slightly increases by showing less distance between the tunnel crown and the invert in the proposed model case. This is due to larger mean effective stress predicted by the proposed model above the tunnel crown (see section 5.6.4.2) thus the tunnel undergo larger deformation in vertical direction.

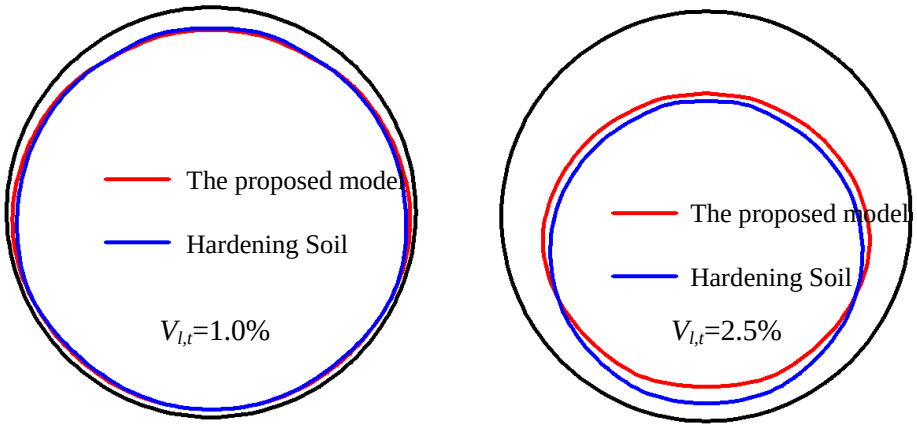

Figure 5.39 Original and deformed tunnel periphery in the FE model (undeformed tunnel plotted using black line).

5.6.2 Vertical ground displacements

5.6.2.1 Vertical settlement patterns

The predicted vertical ground deformation contours are compared with the centrifuge data (Marshall 2009) at $V_{l,t}$ =2.5% in Figure 5.40 and Figure 5.41. Overall both the proposed model and the Hardening Soil model give reasonable predictions of vertical ground deformations. Both models replicate the 'chimney' zone of around 0.3mm vertical settlement in sand. The numerical results give wider area of vertical ground movement as illustrated by both two models that will lead to wider vertical settlement troughs compared to the centrifuge data. This deviation could be partially because larger ground movements next to the sides and bottom of the tunnel boundary are calculated by the numerical models whereas the ground displacement next to the lower part of the tunnel profile is close to zero in the centrifuge test as shown in the following two figures.

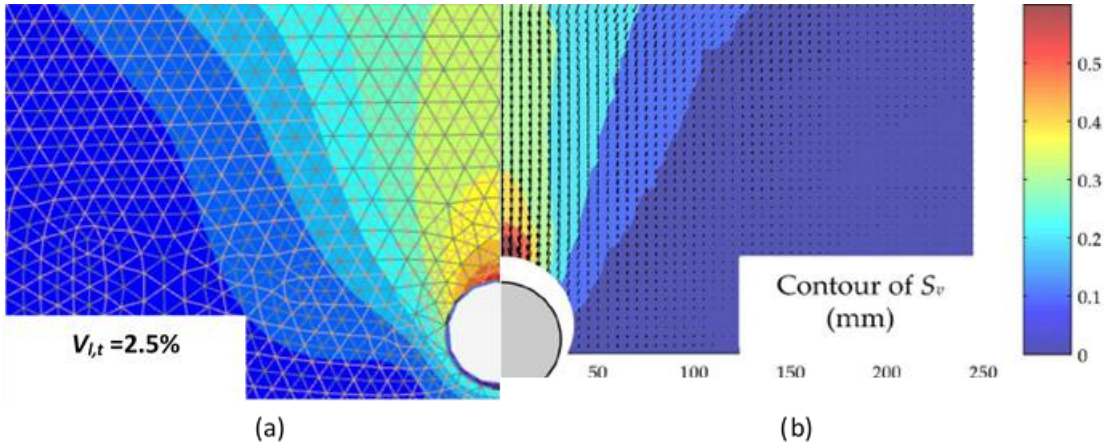

Figure 5.40 Vertical displacement contours of (a) FE model calculated by the proposed model, (b) centrifuge test (Marshall 2009).

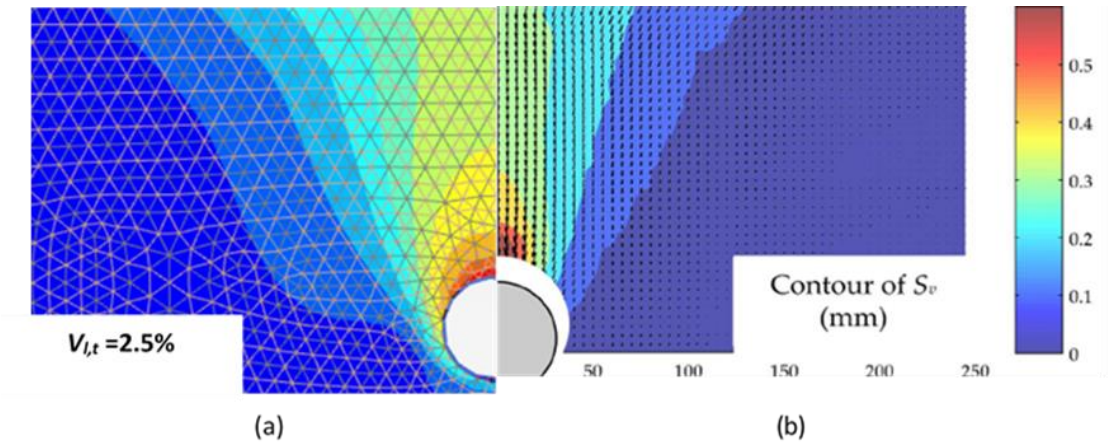

Figure 5.41 Vertical displacement contours of (a) FE model calculated by the Hardening Soil model, (b) centrifuge test (Marshall 2009).

5.6.2.2 Vertical settlement troughs

Comparisons between the calculated vetical settlement troughs by the proposed model with ψ_0 = -0.2 and the Hardening Soil model are plotted in Figure 5.42 ~ Figure 5.44.

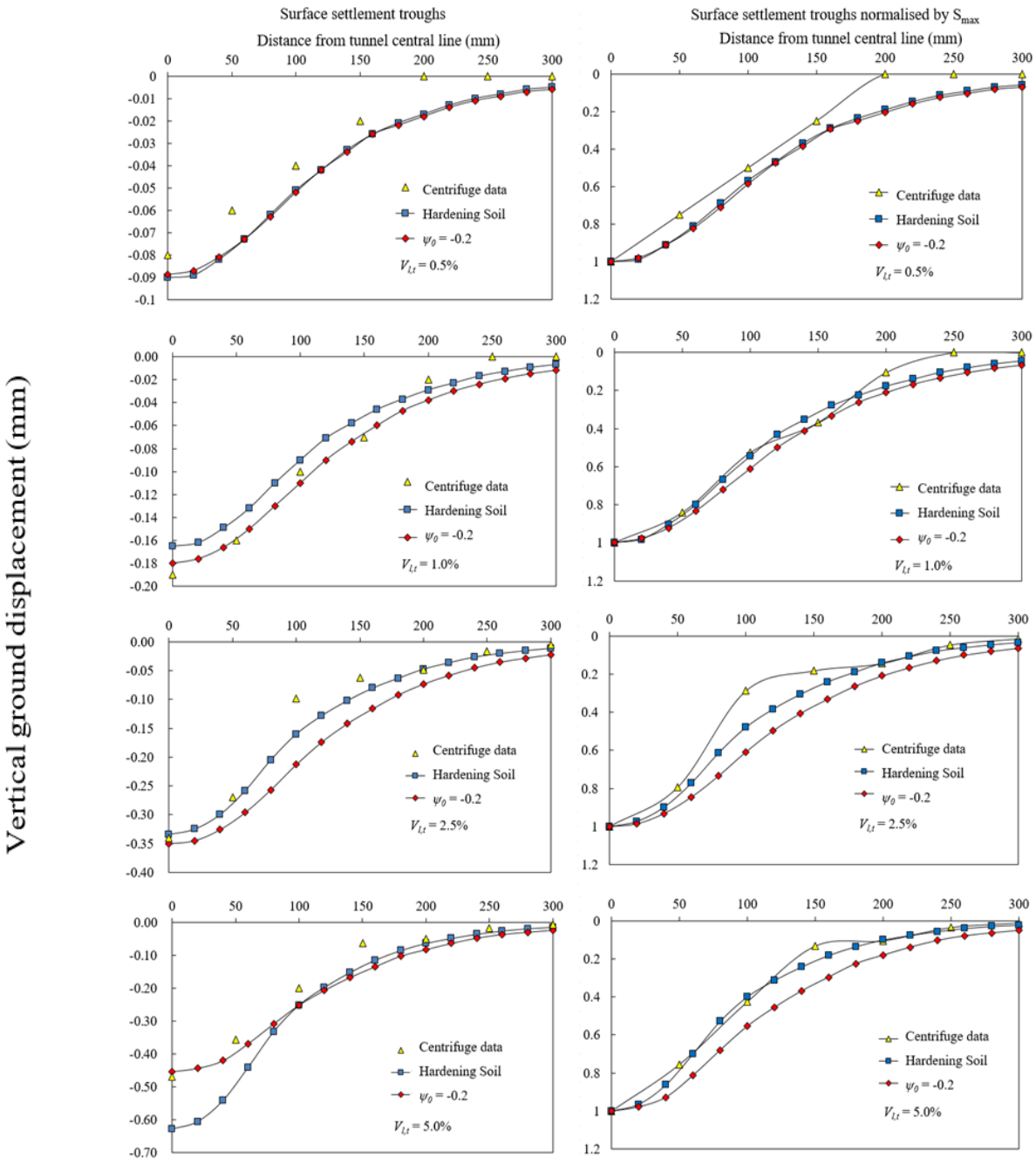

Figure 5.42 Surface settlement troughs.

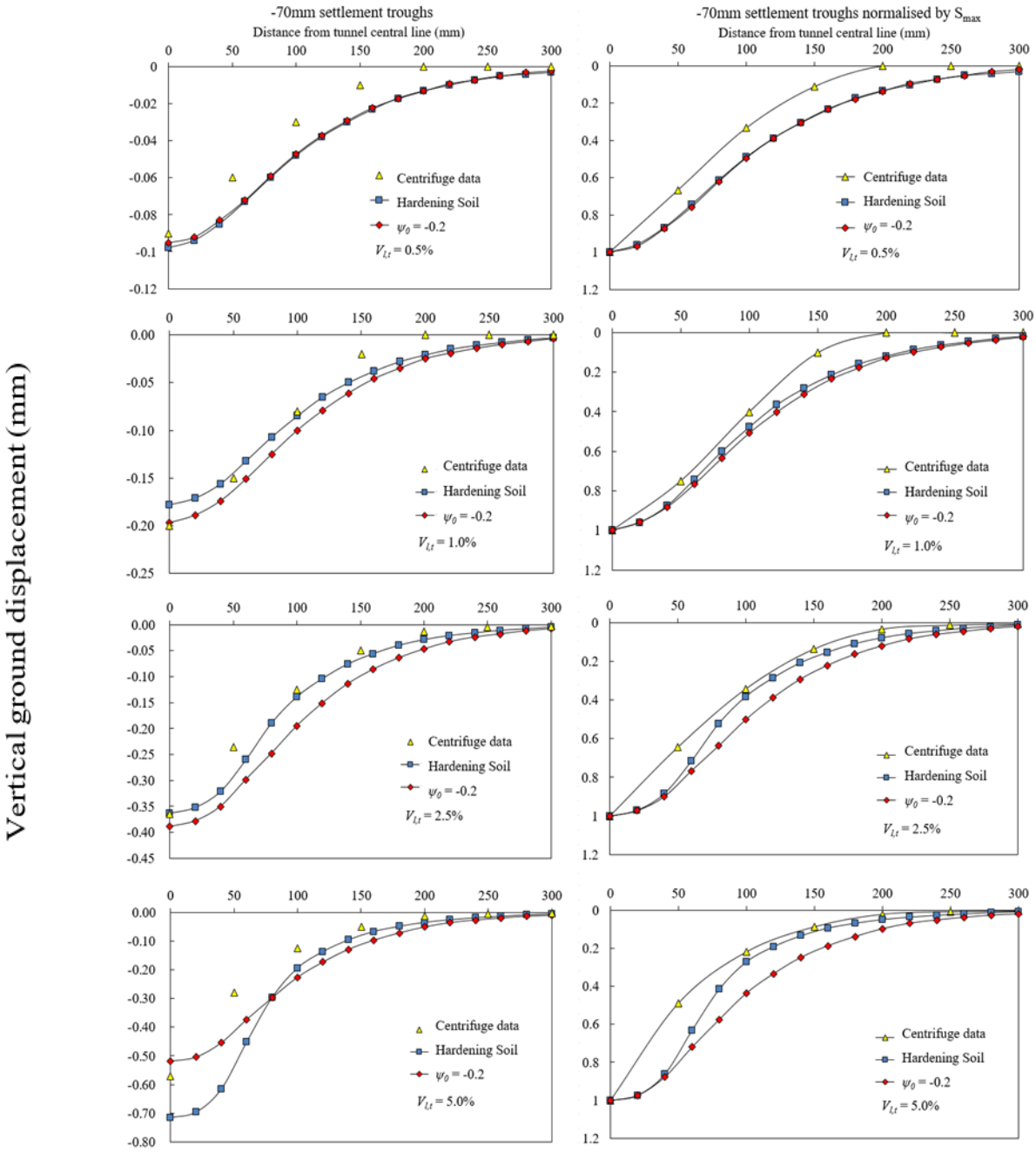

Figure 5.43 Settlement troughs at -70mm.

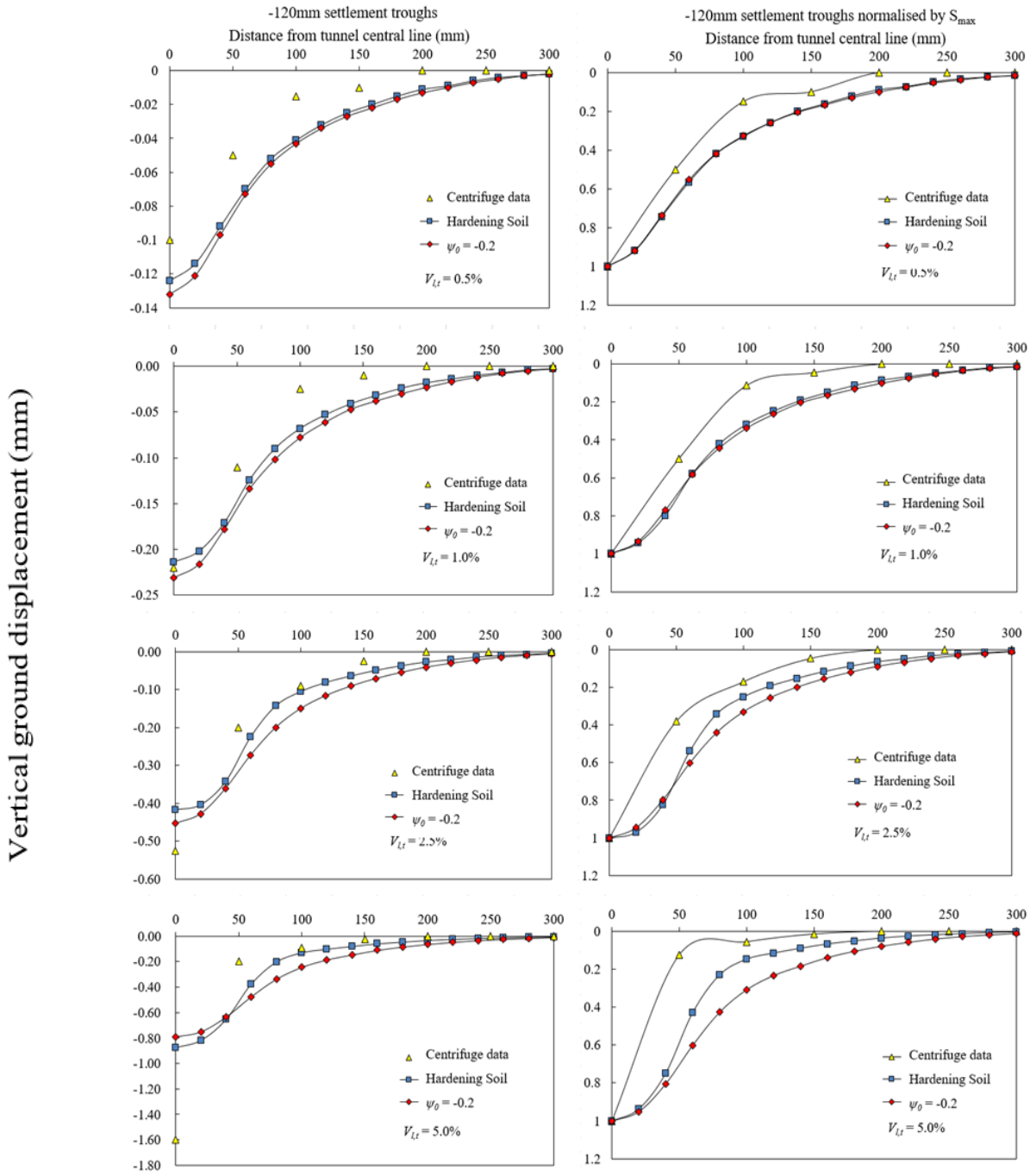

Figure 5.44 Settlement troughs at -120mm.

At surface level, the discrepancy between the vertical settlement magnitudes predicted by the Hardening Soil and the measured data become larger as the tunnel volume loss increases as shown in Figure 5.42. The Hardening Soil predicted vertical settlements overestimate the measured data at small tunnel volume loss level, the prediction then become underestimating at around $V_{l,t}$ = 1.0%. At $V_{l,t}$ = 5.0% the prediction given by the Hardening Soil model is significantly larger than the measured data. In comparison, the predicted vertical settlements provided by the proposed sand model give much better agreements with the measured data, especially at $V_{l,t}$ = 5.0% where the maximum vertical

ground displacement value is well captured by the proposed model. The normalised settlement troughs calculated by the Hardening Soil model are overall narrower than those predicted by the proposed model, thus are closer to the measured trough shape in the centrifuge test. This could be due to larger amount of tunnel deformation is predicted at side and bottom parts of tunnel by the proposed model when the tunnel volume loss is larger than 2.5%, therefore the disturbed area of ground is wider. It is noted that with $V_{l,t}$ = 1.0% the measured trough width is well predicted by both constitutive models.

At the depth of 70mm, similar to the situation at surface level, the Hardening Soil model underestimates the vertical settlements when the tunnel volume loss is smaller than 2.5%. At $V_{l,t}$ = 5.0%, the Hardening Soil model severely over predicts the maximum vertical ground displacement value. The proposed model again gives more reasonable predictions in general. The discrepancies between measured and calculated trough widths become larger compared to the situation at surface. The Hardening Soil model is found to give smaller trough widths compared to the proposed model at $V_{l,t}$ = 2.5% and 5.0%.

Closer to the tunnel, at the depth of 120mm, the overall accuracy of the numerical prediction provided by both constitutive models decreases compared to the situations at surface level and 70mm depth. The predictions of the vertical ground displacements at $V_{l,t}$ = 1.0% are improved compared to other tunnel volume loss values. The maximum vertical ground movement with $V_{l,t}$ = 5.0% is approximately two times the predicted values by both constitutive models. The predicted settlement troughs are wider at all $V_{l,t}$ levels compared to reality although the Hardening Soil continues to give the closer matches.

It is noted that the overall features of the predicted settlement troughs by using the Hardening Soil model are found to be similar to the calculated results by using the proposed model with ψ_0 = 0.1. Better predictions on the magnitudes of vertical settlement are given by the proposed model with ψ_0 = -0.2 is because the contraction and dilation process of dense sand is captured (further discussed in section 5.6.6).

5.6.3 Horizontal ground displacements

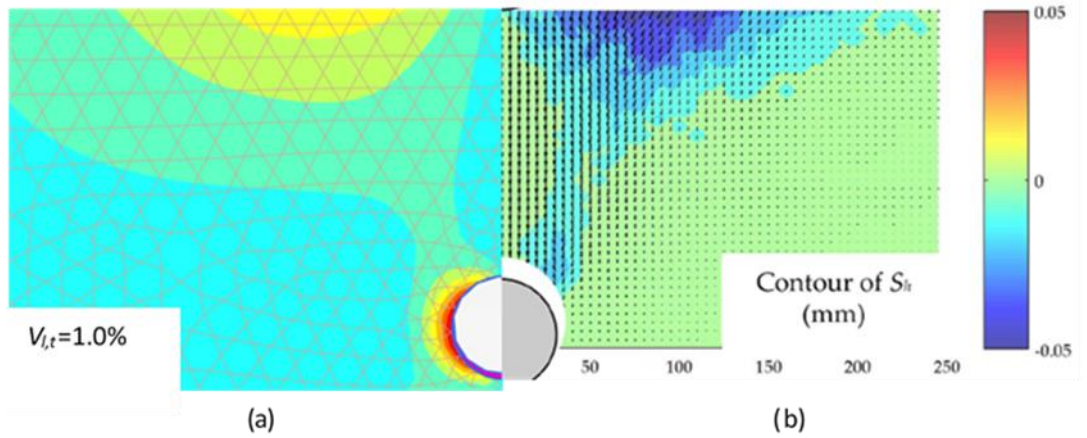

Figure 5.45 Horizontal displacement contours of (a) FE model calculated by the Hardening Soil model, (b) centrifuge test (Marshall 2009)

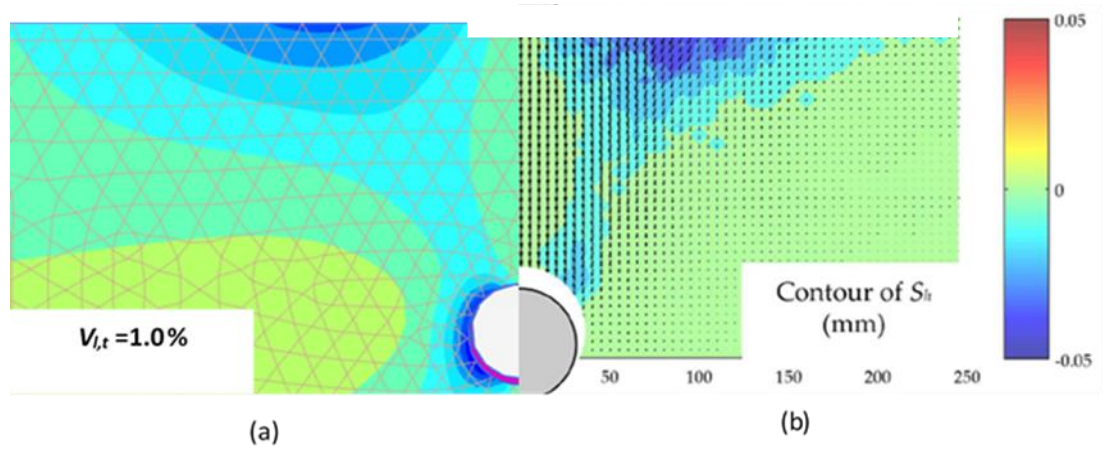

Figure 5.46 Horizontal displacement contours of (a) FE model calculated by the proposed model (note that legend should contrarily apply to numerical results in this figure due to setting issues in Plaxis3D), (b) centrifuge test (Marshall 2009)

The horizontal ground displacement contours with $V_{l,t}$ = 1.0% calculated by the two applied constitutive models are compared with the imaged contours in the centrifuge test in Figure 5.45 and Figure 5.46. It can be seen that the predicted contours by both constitutive models match the measured data well at around the surface area. Horizontal ground movements around tunnel axis level are found in both numerical predictions whereas this sort of movement is absent in the centrifuge test. This discrepancy is probably because larger horizontal tunnel deformation is generated in the numerical simulations.

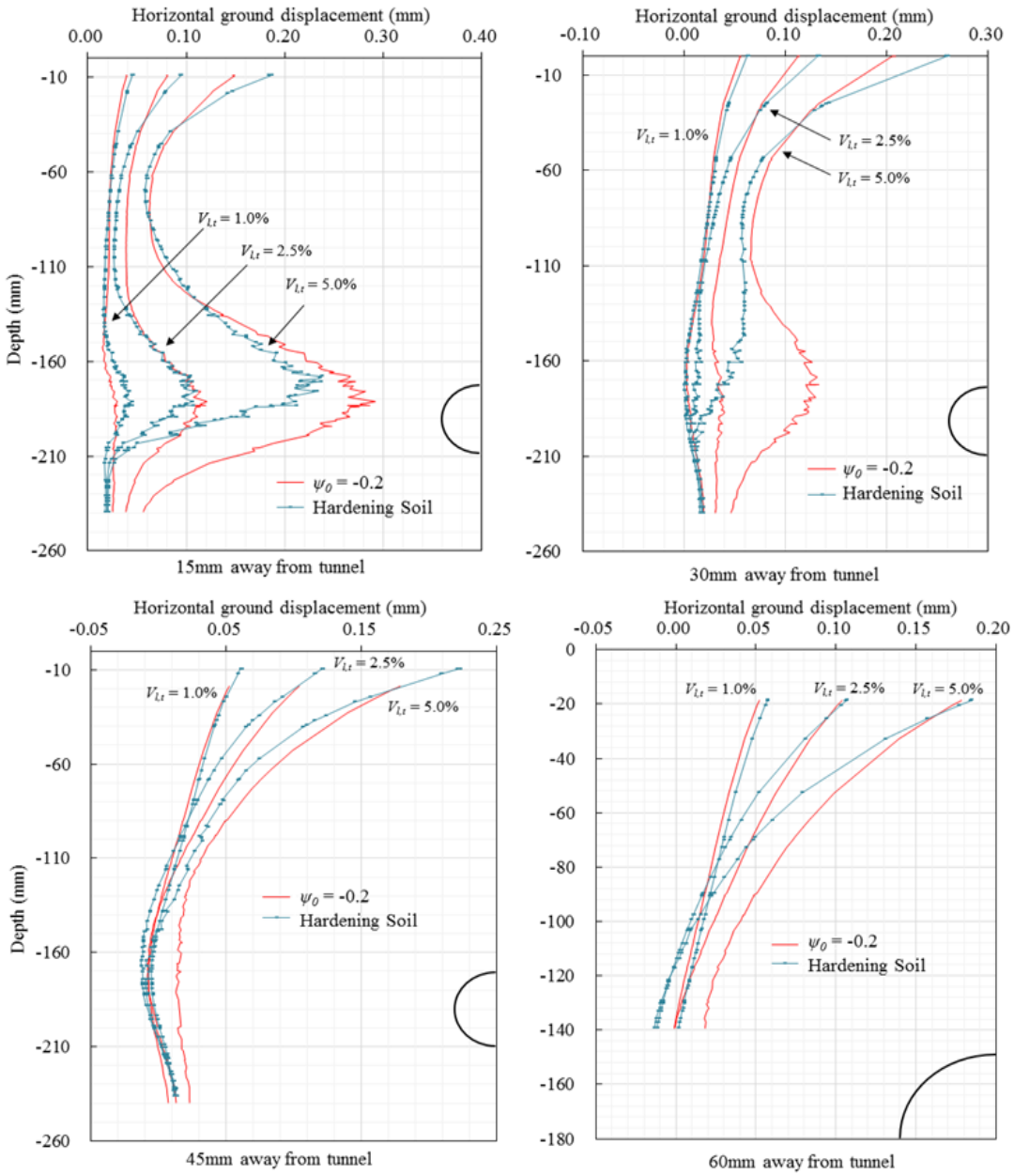

Figure 5.47 Horizontal ground displacements predicted by the FE model.

Full details of the predicted horizontal ground movement troughs at four different distances from the side boundary of the tunnel are plotted in Figure 5.47. Generally 1.0% tunnel volume loss does not result in much deviation between the two constitutive models. As tunnel volume loss increases, at 15mm and 30mm away from the tunnel, the figure shows very similar predicted profiles from surface to around 120mm deep by the two constitutive models with the Hardening Soil predicting slightly larger movement at surface. The movement of the tunnel boundary introduces more horizontal ground movement to the troughs predicted by the proposed model from 110mm depth to tunnel level. At 45mm and 60mm away from the tunnel, similar predicted horizontal movement values are found as at

surface level while overall larger predicted subsurface ground movements are found throughout the recorded depths when using the proposed model.

5.6.4 Stresses

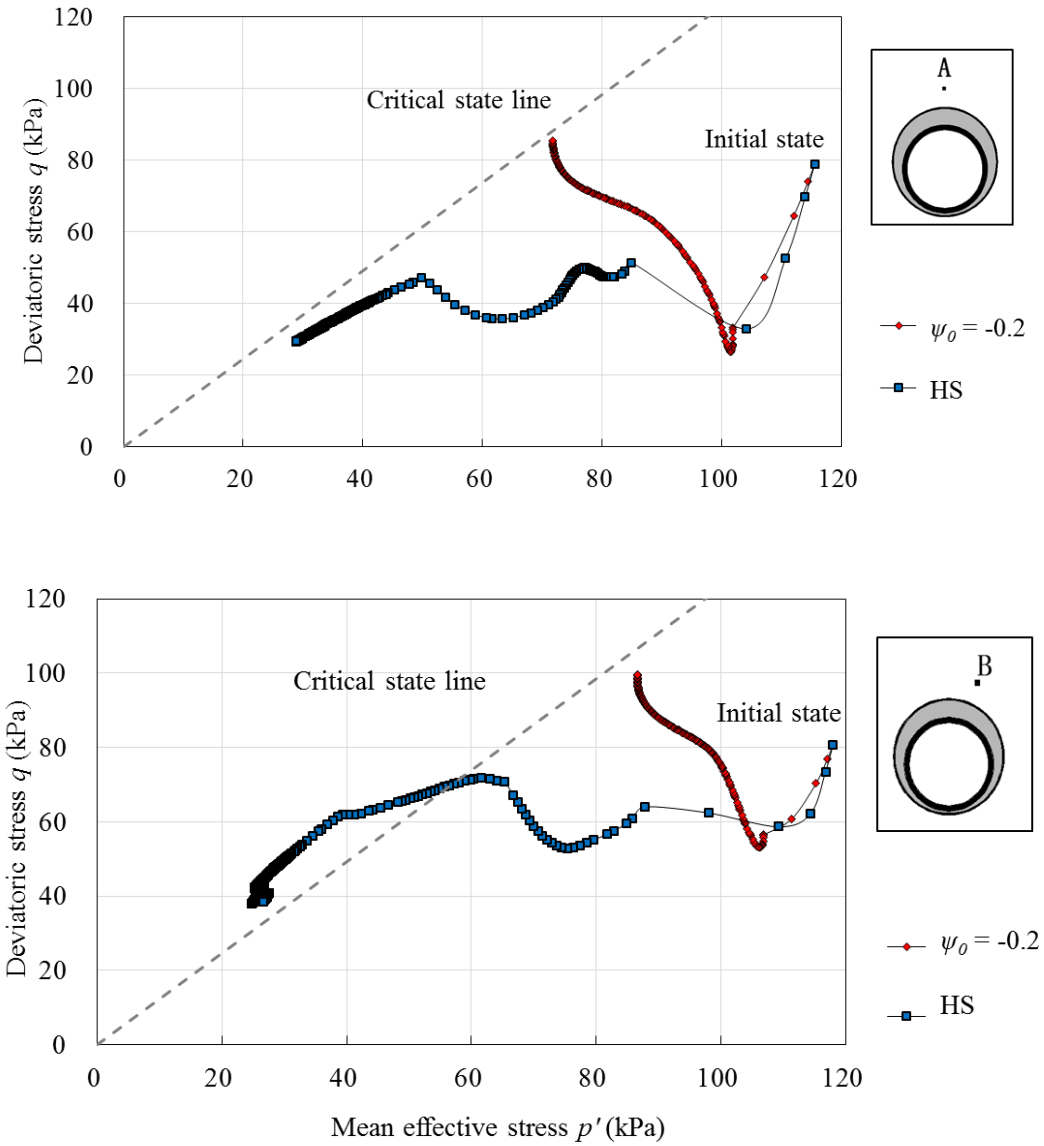

Figure 5.48 Calculated stress paths above tunnel.

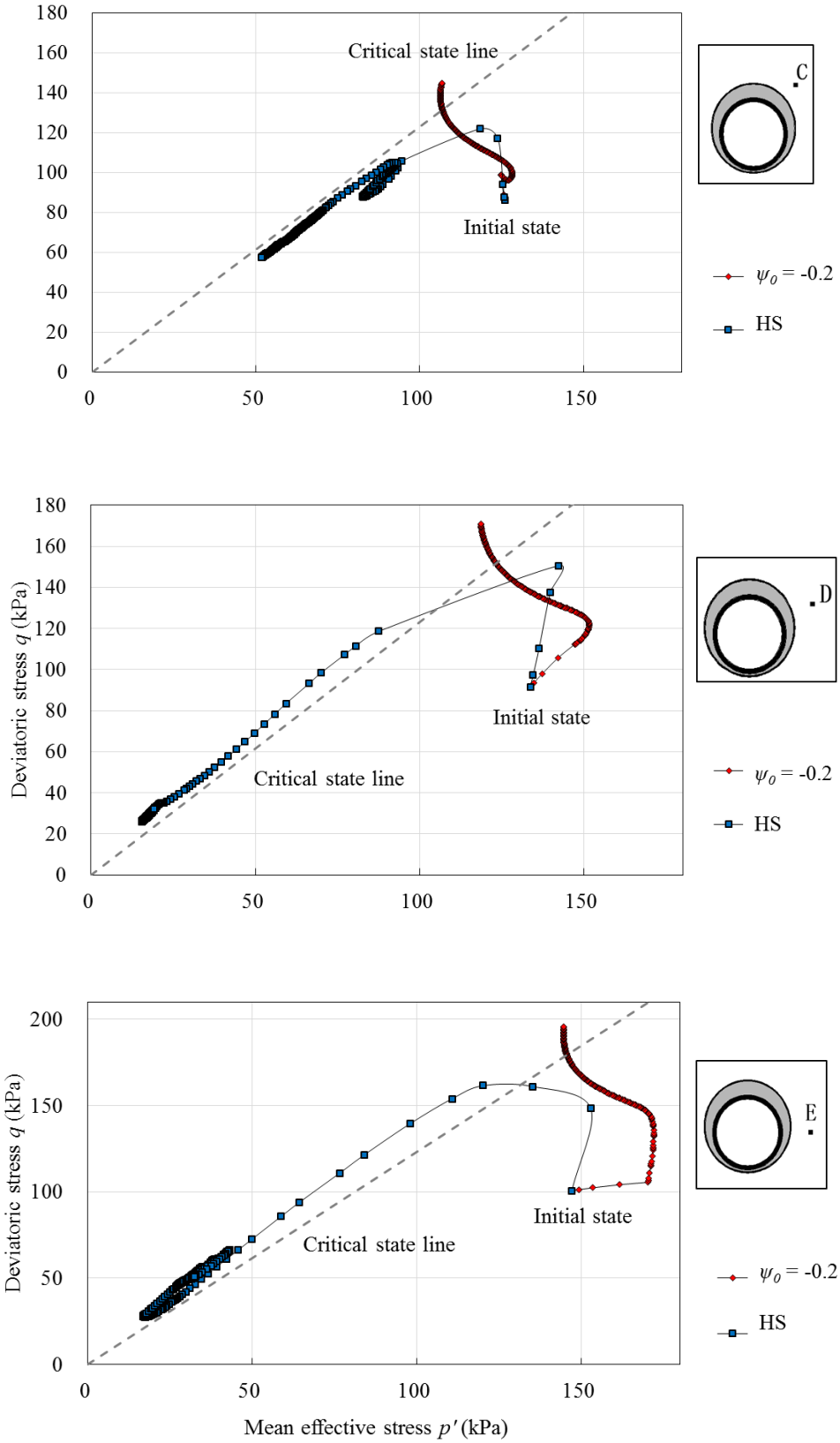

Figure 5.49 Calculated stress paths at side of tunnel.

5.6.4.1 Stress paths

The calculated stress paths around the tunnel are plotted in Figure 5.48 and Figure 5.49 where 'HS' stands for the Hardening Soil model. The Hardening Soil model overall predicts considerable reductions in both mean stress and deviatoric stress at all five recorded points while the proposed model produces increased deviatoric stress accompanied by a certain amount of reduction in mean stress as discussed in section 5.4.3.1. It is clear that two considerably different types of post tunnel deformation stress distributions are predicted by the two constitutive models. It is noted that although the critical stress parameter M_{tc} was not applied in the Hardening Soil model, the predicted stresses paths are roughly moving along the critical stress line at all five points after the starting stage of tunnel deformation.

Despite the discrepancy, certain similarities remain between the two groups of predicted stress paths. Both models give elastic stress relaxation at early stage of tunnel deformation above the tunnel as illustrated in Figure 5.48. Point C, D and E undergo plastic hardening during early stages of stress developments in both two cases, although the Hardening Soil model generates a long process of elastic unloading at these points after a short term of plastic hardening while the proposed model predicts hardening under approximately critical shearing conditions at large tunnel volume loss. When using the proposed model, the stress state can go through the critical state line and lead to further hardening before heading back to the critical state, because of the use of the concept of image state point in which case the top of the yield surface is not overlapping the critical state line as illustrated in section 3.2.5.

5.6.4.2 Stress above tunnel

The distributions of mean effective stress above the tunnel crown at different tunnel volume loss levels are shown in Figure 5.50. As $V_{l,t}$ increases, stress reductions compared to the original situations in the ground are predicted by both models. The amount of stress reduction increases with tunnel volume loss. The Hardening Soil overall gives a larger amount of stress relaxation from surface to tunnel level thus leads to less mean stress next to the tunnel crown, which is also demonstrated in Figure 5.48.

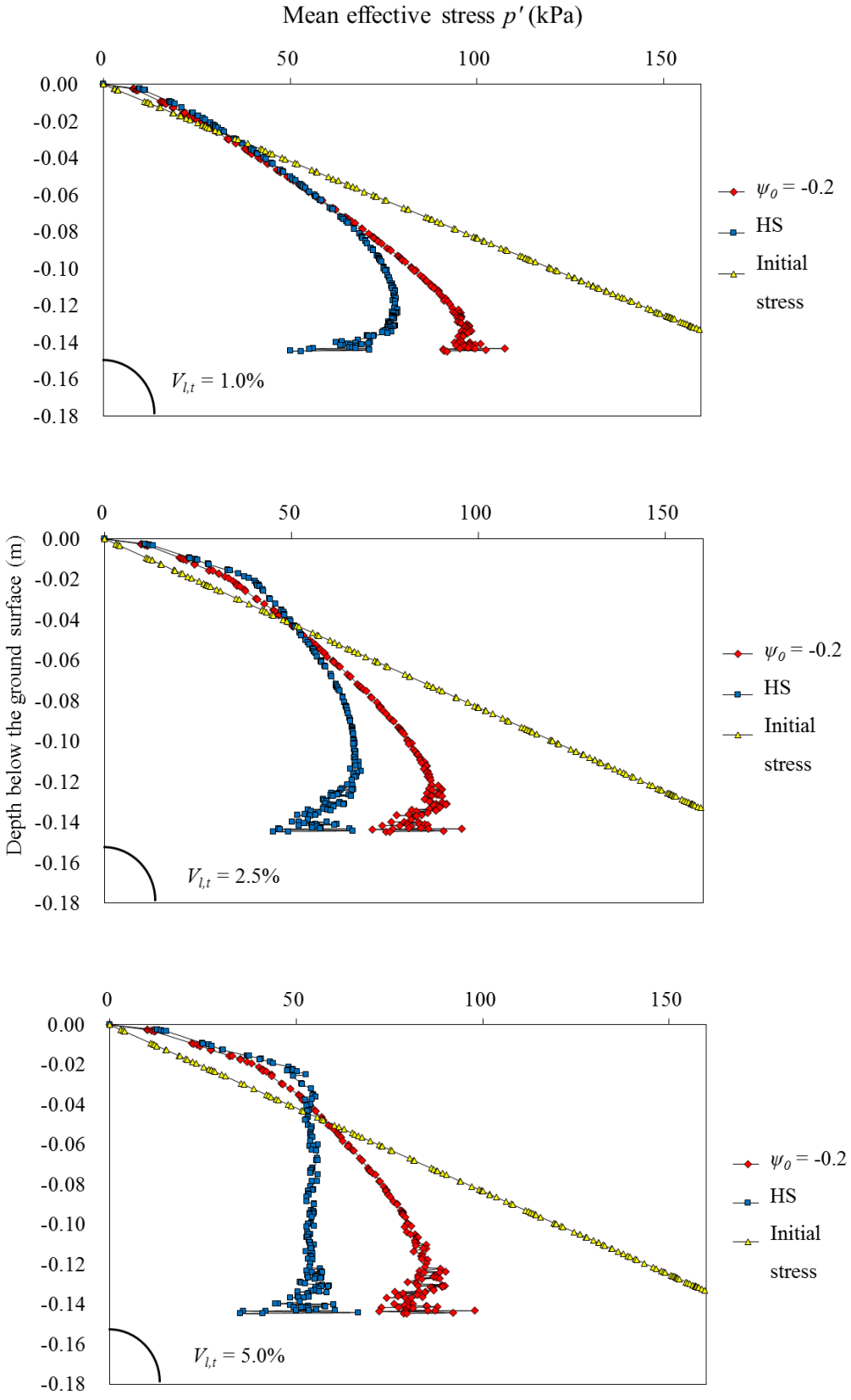

Figure 5.50 Calculated mean stress above tunnel crown.

5.6.4.3 Shear bands

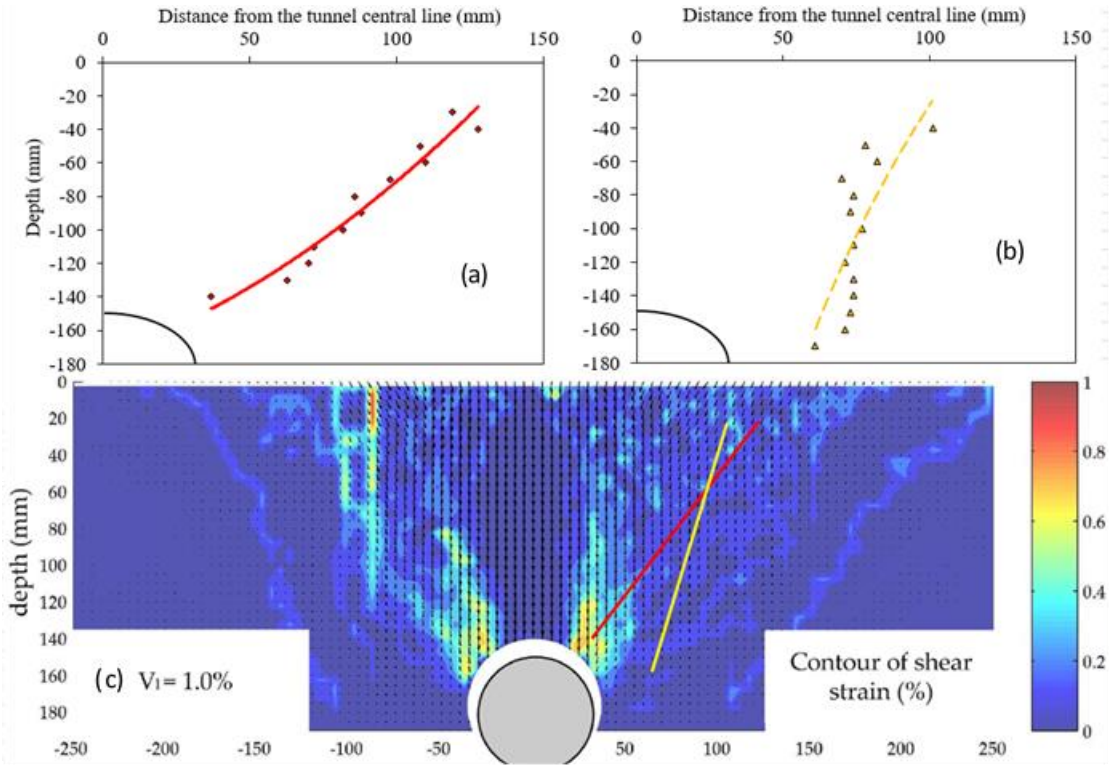

Figure 5.51 Shear bands in (a) FE model calculated by the proposed model; (b) FE model calculated by Hardening Soil; (c) the centrifuge model.

Localisation of shear strains, in other words the shear bands, is a unique feature of ground deformation during tunnelling in sandy ground. However due to the limitations of the finite element method, it is hard to replicate the measured multiple localised shear zones in FE analysis. Although various studies have tried to explore the possibilities of predicting the shear bands using FEM, it has been proven that the predicted shear strain zone is highly mesh dependent thus only rough trends of shearing zone are predicted (Arslan & Sture 2008) unless complicated modifications on the calculation process are made (Kristensson & Ahadi 2005). In reality, maximum shear stress does not necessarily generates maximum shear strain, however it is worthwhile to identify the predicted maximum shear stress area to illustrate the potential of using FE method in predicting localised shearing in sand. It should be clarified that the shear strain zones predicted by both two models are highly mesh dependent thus are not represented here.

The distributions of shear stress at every 10mm depth are recorded at $V_{l,t}$ = 1.0% (as the shear bands are more clear at this tunnel volume loss level in the centrifuge test), it is found by both constitutive models that there is an area of large shear stress at each depth. The predicted positions of maximum

shear stress at each depth are plotted in Figure 5.51(a) and (b). The predicted shear stress bands are then plotted on the measured shear strain contours of the centrifuge test in Figure 5.51(c). The figure illustrates that the close-to-tunnel starting position of the inside shear zone and the inclination of the outer shear bands are better predicted by the proposed model while the Hardening Soil predicted shear zone matches the inclination of the inside shear band.

5.6.5 Strain developments

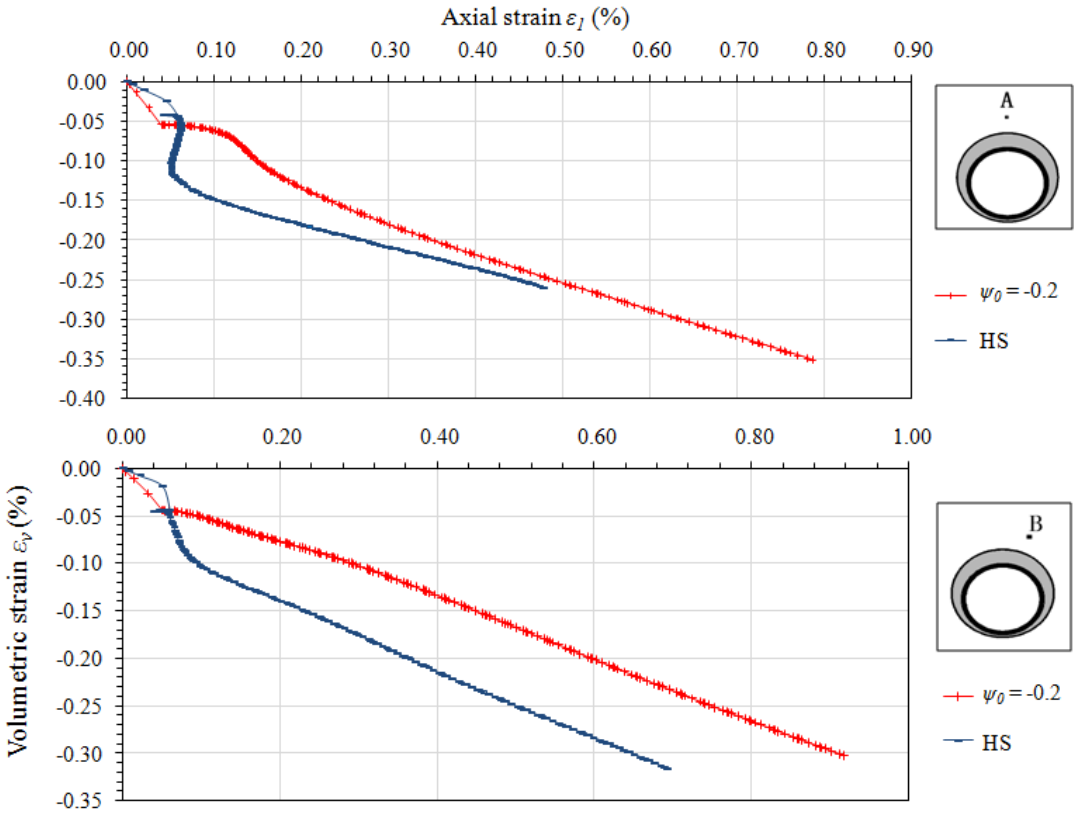

Figure 5.52 Calculated strain developments above tunnel.

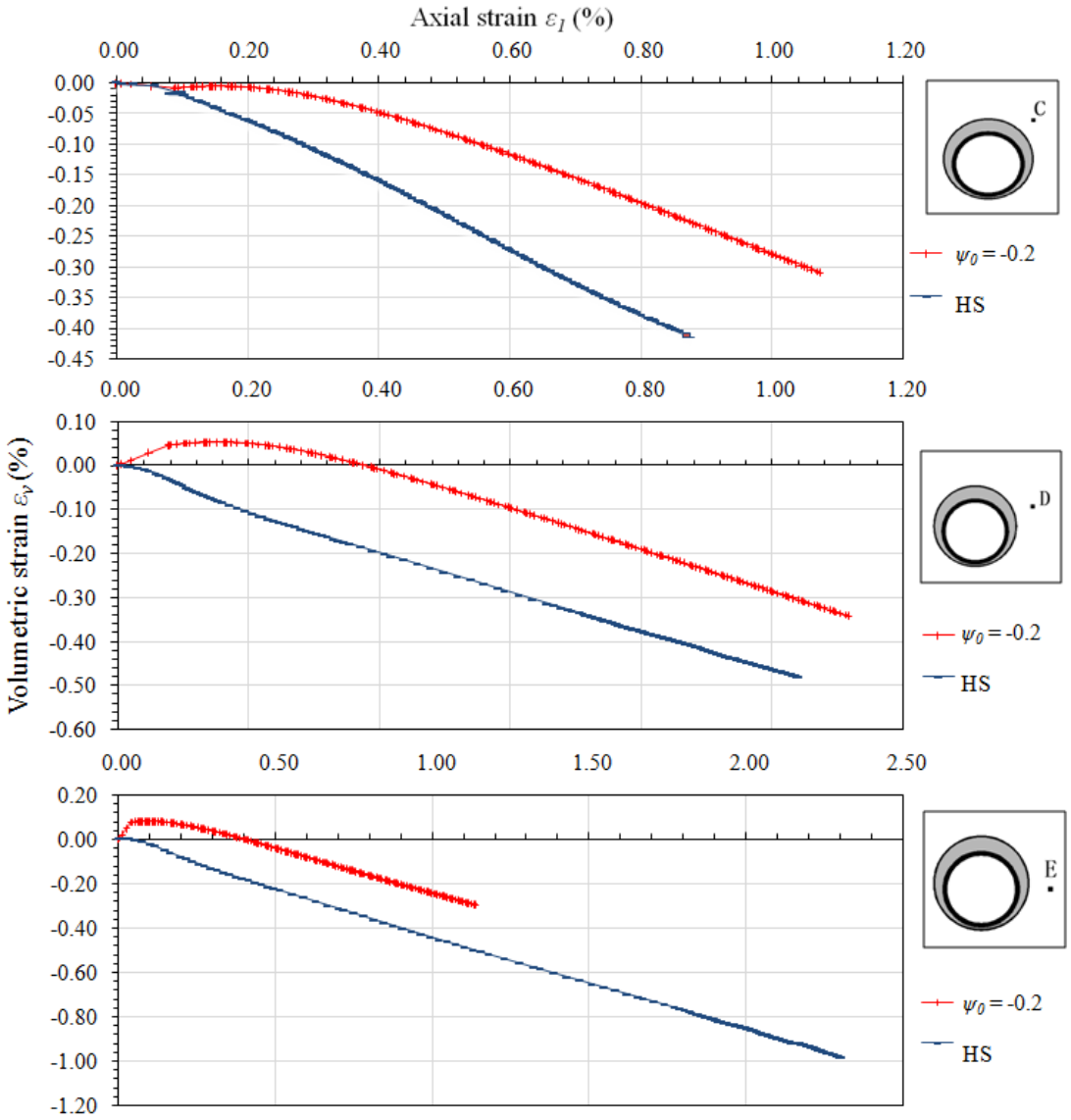

Figure 5.53 Calculated strain developments at side of tunnel.

The predicted developments of volumetric strain around the tunnel are illustrated in Figure 5.52 and Figure 5.53 where negative strain indicates expansion in volume. At points A, B and C, both constitutive models predict continuous expansion of ground with the Hardening Soil generating a larger amount of ground expansion. The deviation between the predicted ground expansions increases with the tunnel deformation process. At point D and E, the Hardening Soil continues to predict monotonic ground expansion whereas the proposed model firstly gives contraction at early stage of tunnel deformation, followed by ground expansion as the tunnel volume loss is increasing. The volumetric strain developed by the Hardening Soil mostly depends on the elastic matrix (thus depends on bulk modulus *K*) as elastic unloading is dominant as discussed in 5.6.4.1. In contrast, plastic hardening is more involved in the strain development predicted by the proposed model.

It is not difficult to imagine that, during tunnel deformation, a larger amount of ground expansion around the tunnel generates lower magnitude of vertical settlement at surface and subsurface area. In comparison, ground contraction around the tunnelling area induces a larger amount of vertical ground displacement. The volumetric strain developments illustrated in the above two figures may explain the discrepancies between the magnitude of the predicted vertical settlements by the two constitutive models discussed in section 5.6.2.2.

5.6.6 Dilation and contraction

This section further explores the influence of volumetric behaviour of sand on the magnitude of vertical ground displacement. Contour plots of volumetric strain calculated by the Hardening Soil model and the proposed model at $V_{l,s}$ = 2.0% and $V_{l,s}$ = 5.0% are shown in Figure 5.54Figure 5.55 respectively. The predicted ground soil volume loss $V_{l,s}$ (area of vertical ground movement at a depth) is compared with the measured centrifuge data in

Figure 5.56. For all tunnel volume loss ranges, in both centrifuge test and numerical modelling, the ground movement becomes negligible when the offset to tunnel centreline is larger than 300mm. Therefore, the soil volume loss is calculated by integrating the settlement curves within 300mm offset to tunnel centreline.

It can be seen from the centrifuge data, that at surface and the depth of 70mm, the soil firstly experiences contraction (slope of $V_{l,s}$ / $V_{l,t}$ larger than 1), then after around 2.5% tunnel volume loss the ground undergoes a dilative process (slope of $V_{l,s}$ / $V_{l,t}$ smaller than 1). This phenomena is predicted by the proposed model as illustrated in Figure 5.54Figure 5.55, however, the Hardening Soil model gives dilation at surface and -70mm.

At the depth of 120mm, the ground experiences approximate monotonic dilating process. Both Hardening Soil and the proposed model give small ground contraction at this area as shown in Figure Figure 5.55. According to

Figure 5.56，both Hardening Soil and the proposed model overestimate the magnitude of soil volume loss because a larger area of settlement is calculated by wider predicted settlement troughs. Due to limited capability in modelling volumetric behaviour of dense sand, it is not surprising that the trend of $V_{l,s}$ development predicted by Hardening Soil shows a discrepancy compared with the centrifuge data and the numerical results calculated by the proposed model.

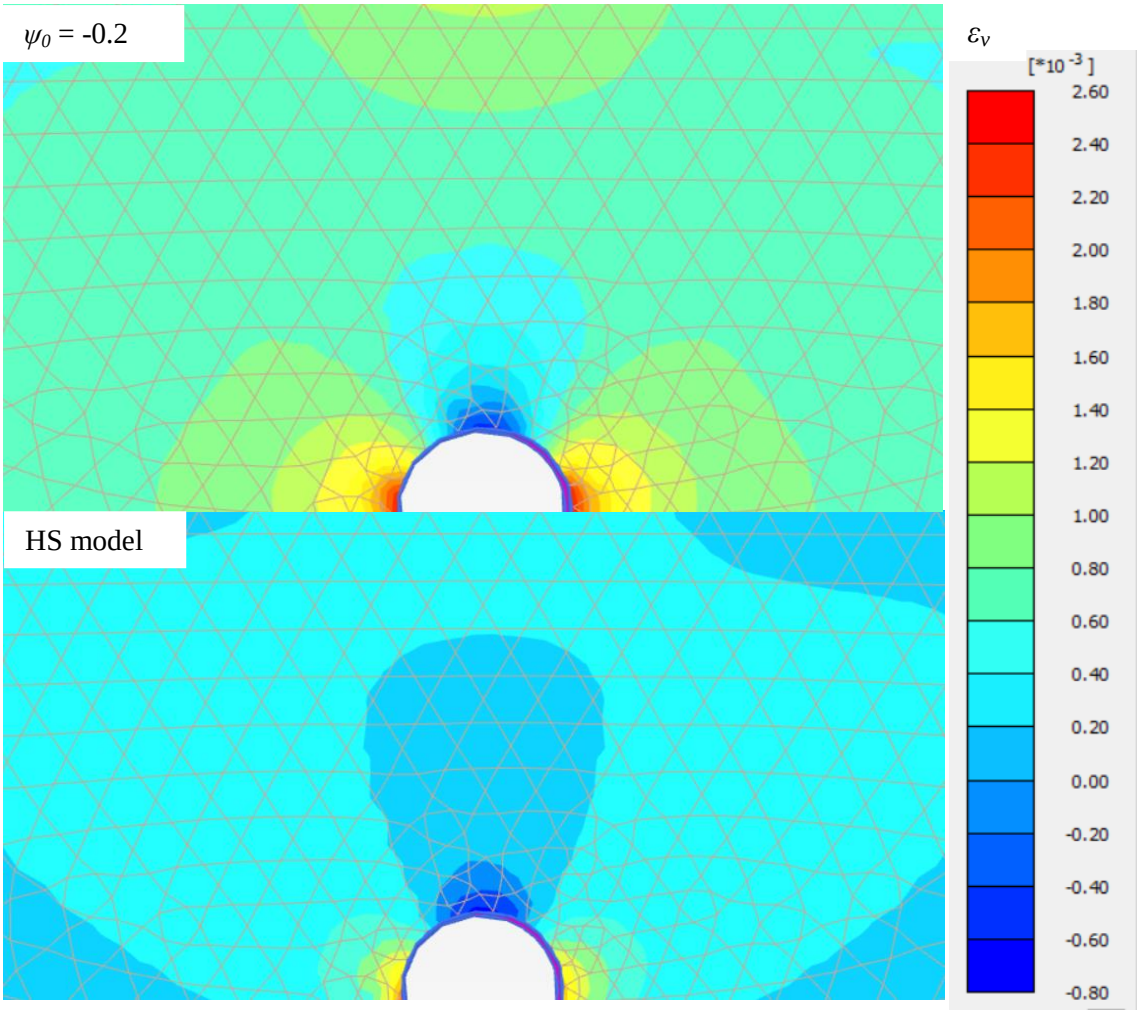

Figure 5.54 Contour plots of volumetric strain at $V_{l,t}$ = 2.0% (compression positive).

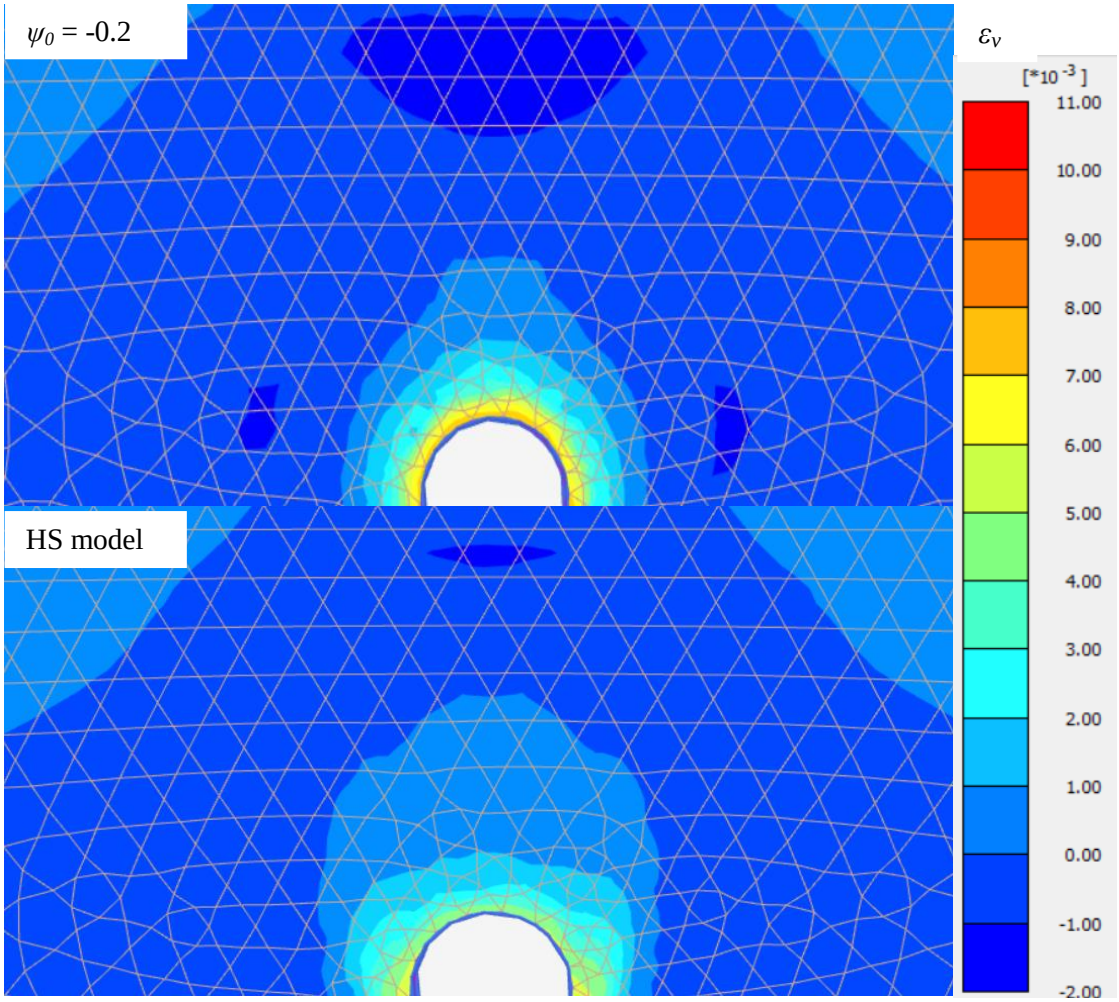

Figure 5.55 Contour plots of volumetric strain at $V_{l,t}$ = 5.0% (compression positive)

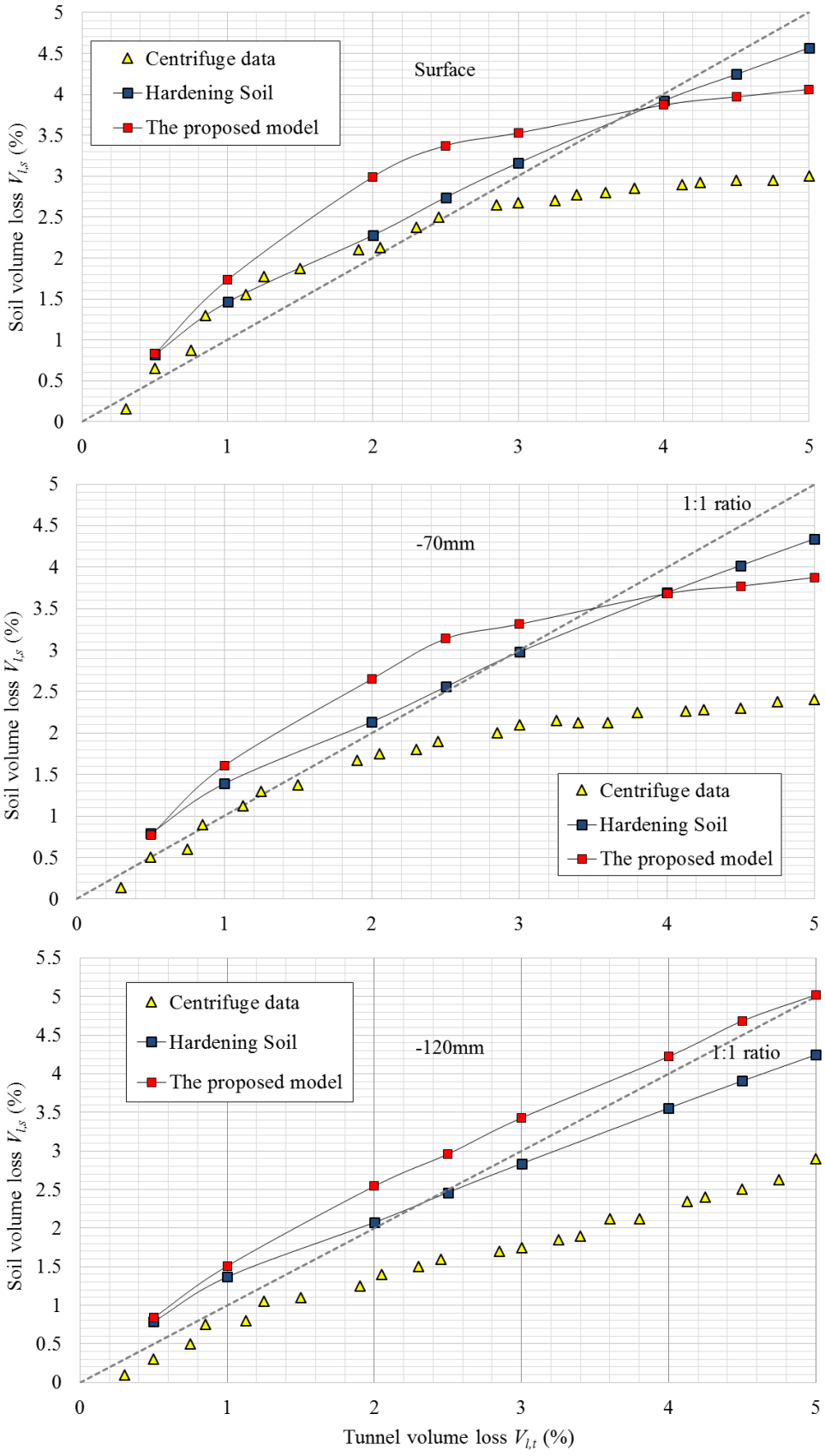

Figure 5.56 Ground volume loss induced by tunnel volume loss.

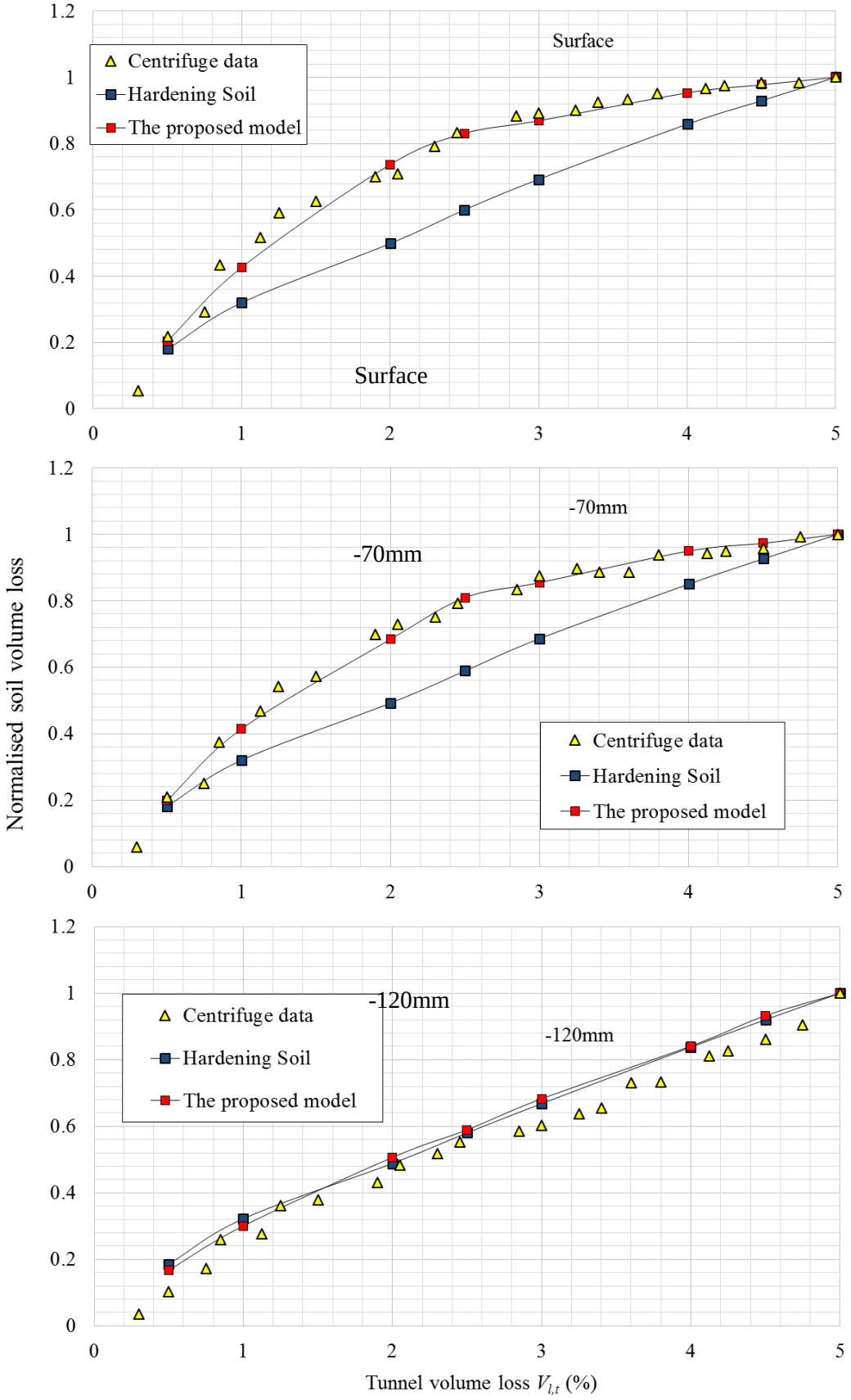

Figure 5.57 Normalised ground volume loss induced by tunnel volume loss.

$V_{l,s}$ is normalised by its maximum value in Figure 5.57 to illustrate the trend of $V_{l,s}$ development. It can be clearly seen that at surface level and the depth of 70mm, the contraction - dilation process of ground behaviour is well predicted by the proposed model while the Hardening Soil gives an approximate linear relationship. At the depth of 120mm, both predicted and measured curves show linear relationship between $V_{l,s}$ and $V_{l,t}$.

5.7 Evaluation of ground deformation prediction methods

Various empirical and analytical methods discussed in section 2.1 are applied in this section to predict the vertical surface and subsurface ground movement in the centrifuge test. The predicted results are compared with the numerical predictions calculated by the Hardening Soil and the proposed model with ψ_0 = -0.2.

5.7.1 Surface settlement troughs

The following three approaches discussed in the literature review are applied in predicting the vertical settlement troughs:

- The modified Gaussian curve (Vorster et al. 2005)

The parameter i and α in Equation [2.5] use the values that give the best fit to the measured data. V_s is calculated according to the tunnel volume loss value $V_{l,s}$ and the undeformed area of the tunnel.

- Verruijt and Booker (1996)

According to the discussions in section 2.3, the parameter δ and ε control the ovalization and the uniform convergence of the tunnel respectively. δ and ε are firstly determined so that the prediction gives the best fit of the maximum vertical settlement value, then δ is set to zero to eliminate the influence of ovalization.

- Loganathan and Poulos (1998)

The gap parameter g is firstly calculated by assuming the bottom of the tunnel is fixed thus zero movementoccurs at the tunnel invert. An optimised value of g is also applied to make the predicted maximum vertical ground movement match the measured data.

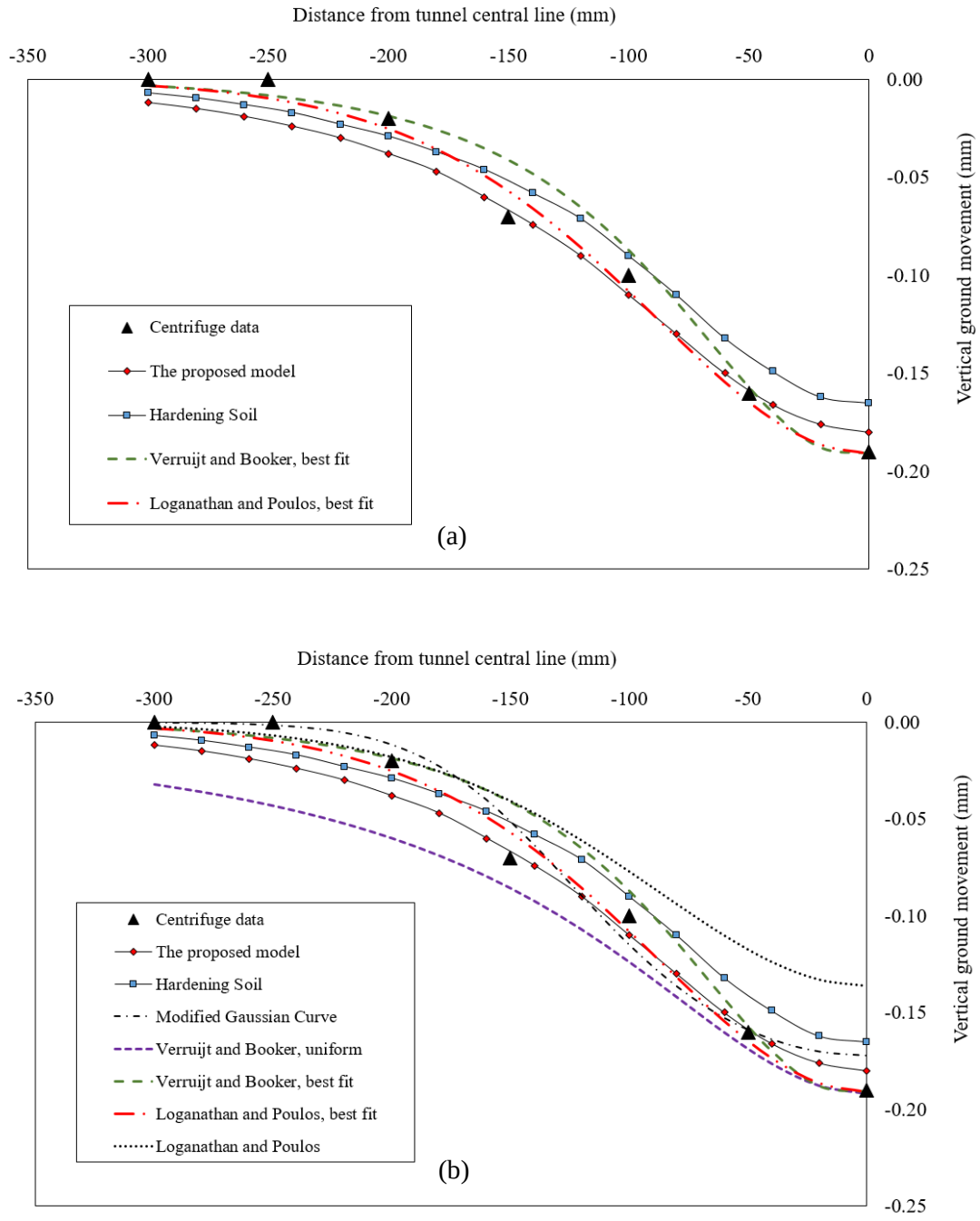

Figure 5.58 The predicted surface settlement troughs at 1% tunnel volume loss using (a) analytical methods with adjusted parameters; (b) all applied approaches.

The predicted transverse vertical ground movement troughs at surface with $V_{l,t}$ = 1.0% are plotted in Figure 5.58. It can be seen that most predicted curves reasonably matches the measured data. The Verruijt and Booker (1996) method with uniformly deformed tunnel and the Loganathan and Poulos (1998) approach using a back calculated value of g from the lower and upper boundary of the predictions respectively.

i = 125 and α = 0.5 are found to give the modified Gaussian curve the best fit of the trough width (the position of the inflection point), however, the prediction underestimates the maximum settlement value. In the Verruijt and Booker (1996) case, the uniformly deformed tunnel leads to an unreasonable wide settlement trough as too much horizontal tunnel deformation is generated while the combination of δ = 0.0058 and ε = 0.0035 is found to give better prediction. Although a fixed tunnel invert during tunnel deformation is a reasonable assumption, when applying the Loganathan and Poulos (1998) approach, this assumption lead to significantly underestimated maximum vertical settlement value. The predicted curve becomes valuable only when an unrealistic high value of g, 0.44 is applied (the physical meaning of the applied parameters of the analytical methods were discussed in Section 2.3.1).

Overall, the two analytical methods with optimised parameters give reasonable predictions of the vertical ground movement. The numerical results give slightly wider predicted troughs compared to the analytical approaches. However, when following the normal process of making predictions, in other words without the assistance of known measured data and optimisation of parameters, the predictions calculated by the analytical methods remain unreliable.

5.7.2 Subsurface settlement troughs

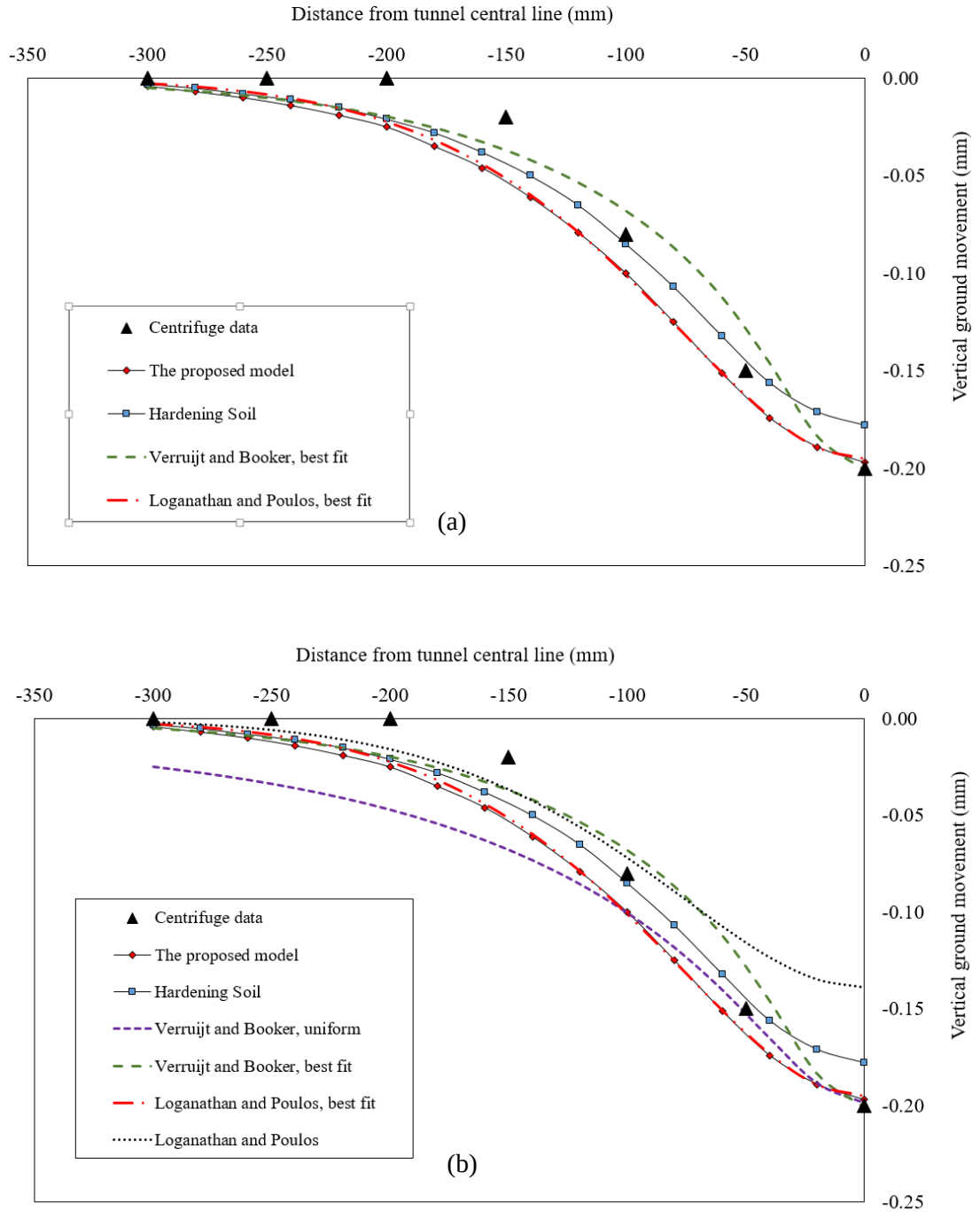

Figure 5.59 The predicted -70mm settlement troughs at 1% tunnel volume loss using (a) analytical methods with adjusted parameters; (b) all applied approaches.

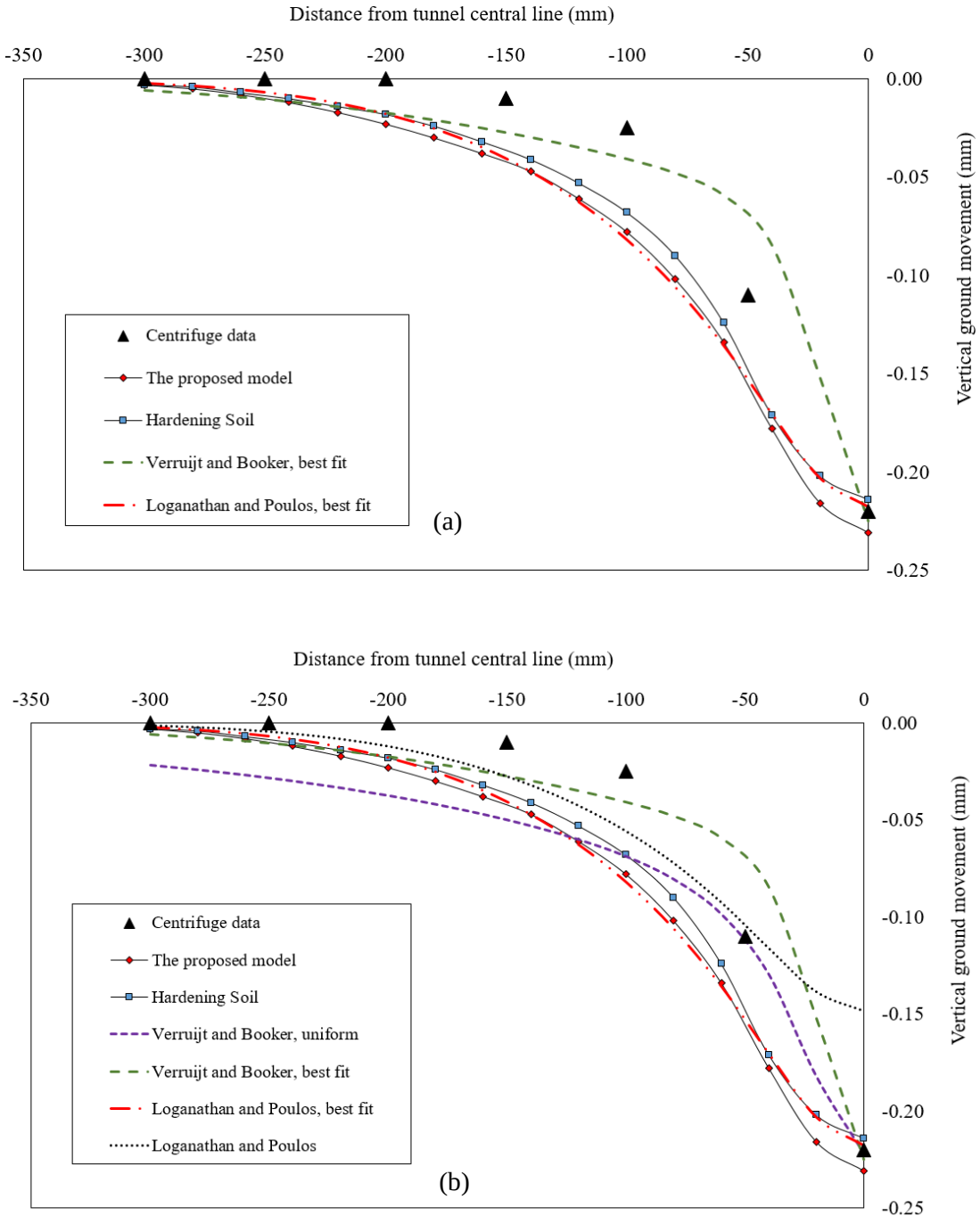

Figure 5.60 The predicted -120mm settlement troughs at 1% tunnel volume loss using (a) analytical methods with adjusted parameters; (b) all applied approaches.

The predicted subsurface settlement troughs are plotted in Figure 5.59 and Figure 5.60. To obtain the best fit, δ = 0.0055 and ε = 0.0033 are applied in Verruijt and Booker (1996) approach at the depth of 70mm; δ = 0.005 and ε = 0.0019 are applied at the depth of 120mm. For Loganathan and Poulos (1998) it is necessary to change the value of g from 0.44 to 0.46 at the depth of 120mm to match the

maximum vertical settlement value. The modified Gaussian curve does not predict subsurface settlement trough thus is absent from the above two figures.

Overall Verruijt and Booker (1996) and Loganathan and Poulos (1998) approaches with optimised parameters give reasonable descriptions of the subsurface settlement troughs. These approaches should be rather treated as 'descriptions' than 'predictions' when using optimised parameters to fit the measured data. Loganathan and Poulos (1998) is found to give similar curves with the predicted troughs calculated by the proposed model with ψ_0 = -0.2 at the depth of 70mm and 120mm.

5.8 Chapter summary

The numerical simulations of the centrifuge test using both constitutive models with different sets of input parameters have been successfully carried out. Tunnel failure did not happen within the studied tunnel volume loss range 0%~5.0%. The following findings can be drawn out according to the presented numerical and centrifuge data:

- The numerical results calculated by four selected initial state parameters are compared in Section 5.4. ψ_0 = -0.2 gives overall best predictions of the surface and subsurface vertical settlement troughs and the contraction/dilation of sandy ground among all applied initial state parameters, although all initial state parameters give wider settlement troughs compared to the measured centrifuge data.

- The effects of K_0 in predicting ground displacement and stress path are discussed in Section 5.5. Varying the value of K_0 in a reasonable range does have certain impacts on the predicted vertical and horizontal ground movement troughs. However the improvements caused by varying K_0 are not comparable with those discrepancies found when comparing the numerical results with the centrifuge data.

- Varying K_0 has greater effect at the early stage of stress development. The impact of K_0 become negligible when the stress state of the ground is around the critical state.

- The numerical predictions given by the proposed sand model and the Hardening Soil model are compared in Section 5.6. Similar tunnel deformation mechanisms are given by the proposed sand model and the Hardening Soil model. The proposed sand model give slightly more vertically squashed tunnel profile at 2.5% and 5.0% tunnel volume losses.

- The proposed sand model gives overall better predictions of the maximum surface and subsurface vertical settlements at all studied tunnel volume loss levels. Both the proposed sand

model and the Hardening Soil model give overall wider vertical settlement troughs compared to the measured centrifuge data.

- Similar patterns of horizontal ground movement are given by the two applied constitutive models.

- The two applied constitutive models predict two different patterns of stress development around the tunnel. The Hardening Soil model predicts overall stress relaxation around the tunnel. The stress paths around the tunnel calculated by the proposed model are approaching towards the critical state line. Stress reversal points are generated by the proposed model above the tunnel crown at around 0.45% tunnel volume loss.

- The contraction and dilation of the soil governs the magnitude of the vertical settlement. The proposed model gives better predictions of the contractive and dilative behaviour of sand induced by tunnel volume loss.

- The empirical and analytical approaches discussed in the literature review chapter are used in predicting the surface and subsurface ground movement. They are able to make reasonable predictions which are comparable with the numerical modelling only when using optimised input parameters based on known ground movement data.

Chapter 6. Conclusions

6.1 The proposed constitutive sand model

(1) Two types of CSL applied.

The Norsand model developed based on critical state soil mechanics is used as a theory base for analysing constitutive sand behaviour in this thesis. Two types of critical state in the algorithmic *v-p'* space have been applied in the numerical analysis: (i) a linear critical state line and (ii) a curved power law critical state line. It is found that both types of CSL are able to give reasonable predictions of drained and undrained triaxial compression tests on sand. The selection of which CSL to use should depend on which CSL gives closer fit to the measured critical states in laboratory tests.

(2) Small strain stiffness and nonlinear elasticity added in the proposed model.

According to the literature, small strain elasticity is involved in ground response to tunnelling in both cohesive and cohesionless soils. Therefore, the proposed sand model applies this feature in its elasticity part by considering the following three factors: (i) large changes of stress path directions during tunnelling, (ii) stress and strain dependent small strain elastic stiffness and (iii) nonlinear elasticity during stress relaxation. In addition, the plastic potential surface during softening in Norsand has been modified to make this surface more realistic compared to test data. The proposed sand model has been validated by simulating sets of drained and undrained compression tests using Toyoura sand. The numerical results calculated by the proposed sand model shows better predictions of drained compression tests at the early stage of deformation, although the discrepancies between the predictions given by the proposed model and the original Norsand model become negligible at large strain level. Both models give similar predictions of undrained triaxial compression tests.

6.2 FE modelling of tunnel volume loss induced ground response

A continuous surface contraction method is used for simulating the tunnel volume loss control process in the centrifuge test and shows similar tunnel deformation patterns compared to the centrifuge tunnel prototype and real tunnelling projects. 0.1% surface contraction per step is applied and results in good control of the tunnel volume loss in the FE model, thus the desired tunnel volume loss values are all closely achieved.

(3) ψ_0 = -0.2 (represents a very dense state) is found to give better predictions of the ground movement among all applied initial state parameters.

Four different values of initial state parameter are applied when using the proposed constitutive sand model in numerical simulations. It is found that ψ_0 = -0.2 gives good fitting of the transverse settlement troughs at 0.5% to 5% tunnel volume loss at the surface and most depths although the predicted troughs are wider in certain cases. However, the proposed model is not able to replicate the extreme localised large vertical ground movement at C/D=0.5 at large tunnel volume loss. The predicted stress paths and development volumetric strain around the tunnel predicted by ψ_0 = -0.2 indicate perfect stress strain features of dense sand under drained conditions discussed in chapter 3. The stress reversal points which will lead to small strain elastic effect are generated at point A and B by all initial state parameter values as a result of major unloading above the tunnel crown. Point A and B are found to behave elastically during the tunnel deformation, whilst at the sides of the tunnel plastic stress strain behaviour is determined. Overall ψ_0 = -0.2 is found to give good ground movement predictions of the centrifuge data, and replicate clearly thhe stress strain features of dense sand, thus was selected for further analysis.

(4) Varying K_0 does not sufficiently improve the numerical prediction.

The comparison between the numerical predictions given by various values of K_0 illustrates that varying K_0 has certain impact on the predicted maximum vertical settlement value. More importantly, larger K_0 tends to give narrower settlement troughs in sand at all depth and tunnel volume loss levels, however increase of K_0 provides very limited influence on improving the shape of the settlement troughs, thus wider troughs compared to the measured centrifuge data can still be found around C/D = 0.5~1.3 with large tunnel volume loss levels. The influence of K_0 on stress paths around the tunnel is mainly found in the beginning stage of tunnel deformation; the ultimate positions of stress paths relative to the critical state line are not effectively affected.

(5) Some widely used empirical and analytical approaches of predicting surface and subsurface vertical ground settlements are also applied. In order to give reasonable predictions, these methods are more or less reliant on optimisation of the parameters based on known data of the maximum vertical settlement. The approach proposed by Loganathan and Poulos (1998), when using optimised gap parameter g, is found to give similar settlement curves with the proposed sand model with ψ_0 = -0.2.

(6) Overall, the proposed model is able to replicate the unique features of volumetric strain behaviour of dense sand. Due to better predictions on modelling volumetric strain development under plastic shearing, it is not surprising that the proposed model gives better predictions on the development of ground dilation and contraction during tunnelling in sand compared to the Hardening Soil model. The following features are also concluded according to the comparison between the numerical results using the proposed model and the Hardening Soil model:

- The Hardening Soil predicts narrower settlement troughs compared to the proposed model and is found to give similar numerical results as calculated by the proposed model with $\psi_0 = 0$ in terms of settlement magnitude.

- Both applied constitutive models give reasonable predictions of horizontal ground movement around surface and near-surface areas. The ground deformation pattern at large depths predicted by the numerical simulations show certain discrepancy compared to the centrifuge data due to larger side-tunnel deformation in numerical modelling.

- Two different types of stress development around the tunnel are predicted by the Hardening Soil model and the proposed model with $\psi_0 = -0.2$, thus different stress distributions are generated after tunnel deformation. The Hardening Soil model more or less gives stress relaxations in both mean effective stress and shear stress around the tunnel, whereas the proposed model predicts a certain amount of reduction in mean effective stress around the tunnel but with plastic critical shearing.

6.3 Further research

Certain features have been added to the original Norsand model to improve its performance in modelling the stress relaxation process during tunnelling in sand. Formulations corresponding to elastic unloading and plastic softening based on laboratory data are involved. However, the laboratory data used in this thesis still remains insufficient to confidently cover the general behaviour of different types of sands. Further normal and cyclic triaxial compression tests are needed in the determinations of the nonlinear elastic stress strain relationships during unloading and plastic softening of the yield surface so that the input elastic parameters (r_1, r_2, D_1 and D_2) and the softening potential $\boldsymbol{g}$ can be fundamentally related to the critical state of soil so that various types of sands can be covered.

The proposed model has been validated at various stages in this thesis against triaxial testing and ground deformations induced by tunnelling in sand under green field condition. However, detailed assessments on the predictions of stresses are incomplete due to lack of laboratory or field data. More measurements (experimental or on site) on the stress path developments around the tunnel during tunnelling in sand under green field condition will provide crucial information about the critical state behaviour of sand during tunnelling.

Perhaps the most obvious shortcoming of numerical modelling of tunnelling in sand using FEM is that the predicted vertical settlement troughs are always wider than the measured data no matter what type of constitutive model or combination of input parameter are applied. A possible reason of this discrepancy is that the tunnel deformation pattern of the FEM model is still not close enough to real

projects and the centrifuge test. Too much deformation occurs at the sides and invert of the FEM tunnel. It would be an interesting and meaningful research to further explore the possible ways to solve this problem.

Although the numerical predicted localised shear stress zones are found to roughly match the shear bands measured in the centrifuge test, the localised shear strain zone (critical state achieved) observed in the centrifuge test remains hardly predictable using the finite element method. Thus, as has been stated for decades, further research on modelling of shear bands in sandy ground is needed.

References

A.E.Dabeet, 2008. *A Practical Model for Load-Unload-Reload Cycles on Sand*. The University of British Columbia.

Addenbrooke, T.I., Potts, D.M. & Puzrin, A.M., 1997. The influence of pre-failure soil stiffness on the numerical analysis of tunnel construction. *Géotechnique*, 47(3), pp.693–712.

Alarcon-Guzman, A., Leonards, G. & Chameau, J.L., 1988. Undrained monotonic and cyclic strength of sands. *Journal of Geotechnical Engineering*, 114(10), pp.1089–1109.

Arslan, H. & Sture, S., 2008. Finite element simulation of localization in granular materials by micropolar continuum approach. *Computers and Geotechnics*, 35(4), pp.548–562.

Ata A., 1996. Ground settlements induced by slurry shield tunneling in stratified soils. *North American Tunneling*, 96, pp.43–50.

Atkinson, J., Richardson, D. & Stallebrass, S., 1990. Effect of recent stress history on the stiffness of overconsolidated soil. *Géotechnique*, 40(4), pp.531–540.

Atkinson, J.H., 1993. *An introduction to the mechanics of soils and foundations: through critical state soil mechanics*, Maidenhead: McGraw-Hill Book Company (UK) Ltd.

Atkinson, J.H. & Potts, D.M., 1977. Stability of a shallow circular tunnel in cohesionless soil. *Geotechnique*, 27(2), pp.203–215.

Attewell, P.B., 1978. Ground movements caused by tunnelling in soil. In *Proceedings of the conference of large ground movements and structures t*. Cardiff: Pentech Press, pp. 812–948.

Attewell, P.B. & Woodman, J.P., 1982. Settlement and Its Derivitives Caused By Tunnelling in Soil. *Ground Engineering*, 2(8), pp.13–22.

Attewell, P.B., Yeates, J. & Selby, A.R., 1986. *Soil Movements Induced by Tunnelling and their Effects on Pipelines and Structures*, Blackie and Son Ltd, UK.

Barratt, D.A., O'Reilly, M.P. & Temporal, J., 1994. Long-term measurements of loads on tunnel linings in overconsolidated clay. *Tunnelling*, pp.469–481.

Been, K. & Jefferies, M., 1985. A state parameter for sands. *Géotechnique*, 35(2), pp.99–112.

Been, K. & Jefferies, M., 2004. Dilatancy in very loose sand. *Canadian Geotechnical Journal*, 41(5), pp.972–989.

Been, K. & Jefferies, M., 1986. Discussion on a state parameter for sands. *Geotechnique*, 36(1), pp.123–132.

Been, K., Jefferies, M. & Hachey, J., 1991. The Critical State of sand. *Geotechnique*, 41(3), pp.365–381.

Van der Berg, 1999. *Measurement and prediction of ground movements around three NATM tunnels*. PhD Thesis, University of Surrey.

Bernat, S. & Cambou, B., 1998. Soil-structure Interaction in Shield Tunnelling in Soft Soil. *Computers and Geotechnics*, 22(3), pp.221–242.

Bernat, S., Cambou, B. & Dubois, P., 1999. Assessing a soft soil tunnelling numerical model using field data. *Geotechnique*, 49(4), pp.4427–452.

Bobet, A., 2001. Analytical solutions for shallow tunnels in saturated ground. *Journal of engineering mechanics*, 127(12), pp.1258–1266.

Bolton, M., 1979. A Guide to Soil Mechanics. *Macmillan Press*, 1.

Bolton, M.D., Dasari, G.R. & Britto, A.M., 1994. Putting Small Strain Non-linearity into Modified Cam-Clay Model. In *Proceedings, 8th International Conference on Computer Methods and Advances in Geomechanics, Morgantown, W. Va, USA, May 1994*. pp. 537–542.

Borst, R., Van den Broek, W.L.A.. & Groen, A.., 1996. Two- and three-dimensional numerical modelling of a guided pipe jacking in soft soil. In *Geotechnical aspects of underground construction in soft ground*. London.

Bowers, K.H. & Redgers, J.D., 1996. Discussion: Observations of lining load in a London clay tunnel. In *Int. Stmposium on Geotechnical Aspects of Underground Construction in Soft Ground*. London: Balkema, p. 335.

Brinkgreve, R.B.., Engin, E. & Swolfs, W.., 2013. *PLAXIS Material Models Manual 2013*, Delft: Plaxis bv.

Brinkgreve, R.B.J., Bakker, K.J. & Bonnier, P.G., 2006. The relevance of small-strain soil stiffness in numerical simulation of excavation and tunnelling projects. In *Proceedings of the 6th European Conference on Numerical Methods in Geotechnical Engineering - Numerical Methods in Geotechnical Engineering*. pp. 133–139.

Burland, J., 1989. Ninth Laurits Bjerrum Memorial Lecture:“ Small is beautiful”-the stiffness of soils at small strains. *Canadian Geotechnical Journal*, 26(4), pp.499–516.

Casagrande, A., 1936. Characteristics of cohesionless soils affecting the stability of slopes and earth fills. *Journal of Boston Society of Civil Engineering*, 23, pp.257–276.

Castro, G., 1969. *Liquefaction of sands*. PhD Thesis, Harvard University.

Celestino, T.. & Ruiz, A.P.T., 1998. Shape of settlement troughs due to tunnelling through different types of soft ground. *Felsbau*, 16(2), pp.118–121.

Celestino, T.B., Gomes, R.A.M.P. & Bortolucci, A.A., 2000. Errors in Ground Distortions Due to settlement trough adjustment. *Tunnelling and Underground Space Technology*, 15(1), pp.97–100.

Chambon, P. & Cort é, J., 1994. Shallow tunnels in cohesionless soil: stability of tunnel face. *Journal of Geotechnical Engineering*, 120(7), pp.1148–1165.

Chu, J., 1995. An experimental examination of the critical state and other similar concepts for granular soils. *Canadian Geotechnical Journal*, 32(6), pp.1065–1075.

Clayton, C. & Heymann, G., 2001. Stiffness of geomaterials at very small strains. *Géotechnique*, 51(3), pp.245–255.

Clough, G.W. & Schmidt, B., 1981. Design and performance of excavations and tunnels in soft clay. In E. Brand & R. Branner, eds. *Soft Clay Engineering*. Elsevier Ltd, pp. 567–634.

Clough, G.W., Sweeney, B.P. & Finno, R.J., 1983. Measured soil response to EPB shield tunneling. *Journal of geotechnical engineering*, 109(2), pp.131–149.

Cording, E.J., 1991. Control of ground movements around tunnels in soil. *PanAmerican conference; 9, Soil mechanics and foundation engineering*, pp.2195–2244.

Cording, E.J. & Hansmire, W.H., 1975. Displacements around soft ground tunnels. In *Proceeding of the 5th Panamerican conference on soil mechanics and foundation engineering*. pp. 571–632.

Dafalias, Y. & Herrmann, L., 1982. Bounding surface formulation of soil plasticity. In *Soil Mechanics-Transient and Cyclic Loads*. London, pp. 253–282.

Dafalias, Y.F. & Manzari, M.T., 2004. Simple Plasticity Sand Model Accounting for Fabric Change Effects. *Journal of Engineering Mechanics*, 130(6), pp.622–634.

Darendeli, B.M., 2001. *Development of a new family of normal - sized modulus reduction and material damping curves*. PhD Thesis, University of Texas at Austin.

Dias, D., Kastner, R. & Maghazi, M., 2000. Three-dimensional simulation of slurry shield tunnelling. In Miyazaki & Fujita, eds. *Geotechnical aspects of underground construction in soft ground*. Rotterdam: Balkema, pp. 351–356.

Dimmock, P.S., 2003. *Tunnelling induced ground and building movement on the Jubilee Line Extension*. University of Cambridge.

Dindarloo, S.R. & Siami-Irdemoosa, E., 2015. Maximum surface settlement based classification of shallow tunnels in soft ground. *Tunnelling and Underground Space Technology*, 49, pp.320–327.

Drucker, D.C., Gibson, R.F. & Henkel, D.J., 1957. Soil mechanics and work hardening theories of plasticity. *Transactions of the American Society of Civil Engineers*, 112, pp.338–346.

Erdélyi, A. & Bateman, H., 1954. *Tables of integral transforms*, McGraw-Hill.

Ezzeldine, O.Y., 1999. Estimation of the surface displacement field due to construction of Cairo Metro Line El Khalafawy - St. Therese. *Tunnelling and Underground Space Technology*, 14(3), pp.267–279.

Farias, M.., Júnior, Á.H.. & De Assis, A.., 2004. Displacement control in tunnels excavated by the NATM : 3-D numerical simulations. *Tunnelling and underground space technology*, 19(3), pp.283–293.

Finno, R.J. & Clough, G.W., 1985. Evaluation of soil response to EPB shield tunneling. *Journal of Geotechnical Engineering*, Ill(2), pp.155–173.

Franzius, J.N., Potts, D.M. & Burland, J.B., 2005. The influence of soil anisotropy and K0 on ground surface movements resulting from tunnel excavation. *Géotechnique*, (3), pp.189–199.

Fujita, K., 1981. On the surface of settlements caused by various methods of shield tunnelling. In *The 11th International Conference on Soil Mechanics and Foundation Engineering*. pp. 609–610.

Gao, Y., Wang, Y.H. & Asce, M., 2014. Experimental and DEM Examinations of K0 in Sand under Different Loading Conditions. *Journal of Geotechnical and Geoenvironmental Engineering*, 140(5), p.04014012.

Gens, A. & Potts, D., 1988. Critical state models in computational geomechanics. *Engineering Computations*, 5(3), pp.178–197.

Gonzalez, C. & Sagaseta, C., 2001. Patterns of soil deformations around tunnels. Application to the extension of Madrid Metro. *Computers and Geotechnics*, 28, pp.445–468.

Graham, J. & Houlsby, G.T., 1983. Anisotropic elasticity of a natural clay. *Geotechnique*, 33(2), pp.165–180.

Graham, J., Noonan, M.L. & Lew, K. V., 1983. Yield states and stress–strain relationships in a natural plastic clay. *Canadian Geotechnical Journal*, 20(3), pp.502–516.

Grant, R.J. & Taylor, R.N., 2000. Tunnelling-induced ground movements in clay. *Proceedings of the Institution of Civil Engineers, Geotechnical Engineering*, 143(1), pp.43–55.

Grove, G.L., 1943. Tunnel linings, with special reference to a new form of reinforced concrete lining. *Journal of the Institution of Civil Engineers*, 20(5), pp.29–42.

Guedes de Melo, P.F.M. & Santos Pereira, C., 2000. The role of the soil k0 value in numerical analysis of shallow tunnels. In *Geotechnical Aspects of Underground Construction in Soft Ground*. pp. 379–384.

Gunn, M., 1993. The prediction of surface settlement profiles due to tunnelling. In *Predictive Soil Mechanics. Proceedings of the Worth Memorial Symposium*. London, pp. 304–316.

Hegedus, D.H. & Cowin, S.C., 1976. Bone remodeling II: small strain adaptive elasticity. *Journal of Elasticity*, 6(4), pp.337–352.

Henkel, D.J., 1959. The Relationships Between the Strength, Pore-Water Pressure, and Volume-Change Characteristics of Saturated Clays. *Géotechnique*, 9(3), pp.119–135.

Hong, S.W. & Bae, G.J., 1995. Ground movements associated with subway tunneling in Korea 1; In *Proceedings of Underground Construction in Soft Ground.* AA Balkema, pp. 229–232.

Jacobsz, S.W., 2002a. *The effects of Tunnelling on Piled Foundations*. The University of Cambridge.

Jacobsz, S.W., 2002b. *The effects of Tunnelling on Piled Foundations*. PhD Thesis, The University of Cambridge.

Jacobsz, S.W., Standing, J.R. & Mair, R.J., 2004. Centrifuge modelling of tunnelling near driven piles. *Soils and Foundations*, 44(1), pp.49–56.

Jefferies, M., 1993. Nor-Sand: a simple critical state model for sand. *Geotechnique*, 43(1), pp.91–103.

Jefferies, M., 1997. Plastic work and isotropic softening in unloading. *Géotechnique*, 47(5), pp.1037–1042.

Jefferies, M. & Been, K., 2000. Implications for critical state theory from isotropic compression of sand. *Géotechnique*, 50(4), pp.419–429.

Jefferies, M. & Been, K., 2006. *Soil liquefaction*, Abingdon: Taylor & Francis.

Jefferies, M. & Shuttle, D., 2002. Dilatancy in general Cambridge-type models. *Géotechnique*, 52(9), pp.625–637.

Jefferies, M. & Shuttle, D., 2011. On the operating critical friction ratio in general stress states. *Géotechnique*, 61(8), pp.709–713.

Kasper, T. & Meschke, G., 2004. A 3D finite element simulation model for TBM tunnelling in soft ground. *International Journal for Numerical and Analytical Methods in Geomechanics*, 28(14), pp.1441–1460.

Kirsch, G., 1898. *Die theorie der elastizitat und die bedurfnisse der festigkeitslehre*,

Koelewijn, A.R. & Verruijt, A., 2006. Simplified three-dimensional numerical modelling of shield tunnel advancement. In *Tunnelling. A Decade of Progress. GeoDelft 1995-2005*. pp. 217–222.

Komiya, K., Soga, K. & Akagi, H., 1999. Finite element modelling of excavation and advancement processes of a shield tunnelling machine. *Soils and Foundations*, 39(3), pp.37–52.

Kristensson, O. & Ahadi, A., 2005. Numerical study of localization in soil systems. *Computers and Geotechnics*, 32(8), pp.600–612.

Kung, G.T.-C., Hsiao, E.C.-L. & Juang, C.H., 2007. Evaluation of a simplified small-strain soil model for analysis of excavation-induced movements. *Canadian Geotechnical Journal*, 44(6), pp.726–736.

Kuwano, R. & Jardine, R.J., 2002. On the applicability of cross-anisotropic elasticity to granular materials at very small strains. *Géotechnique*, 52(10), pp.727–749.

Lade, P. V., 1977. Elasto-plastic stress-strain theory for cohesionless soil with curved yield surfaces. *International Journal of Solids and Structures*, 13(11), pp.1019–1035.

Lee, C.J., Chiang, K.H. & Kuo, C.M., 2004. Ground movement and tunnel stability when tunneling in sandy ground. *Journal of the Chinese Institute of Engineers*, 27(7), pp.1021–1032.

Lee, C.J., Wu, B.R. & Chiou, S.Y., 1999. Soil Movements Around a Tunnel in Soft Soils. *Proceddings of the Nitioanl Science Council， Part A Physical Science and Engineering*, 23(2), pp.235–247.

Lee, K.M., Kerry, R. & Lo, K.Y., 1992. Subsidence owing to tunnelling . I . Estimating the gap parameter. *Canadian Geotechnical Journal*, 29(6), pp.929–940.

Lee, K.M. & Rowe, R.K., 1991. An analysis of three-dimensional ground movements: the Thunder Bay tunnel. *Canadian Geotechnical Journal*, 28(1), pp.25–41.

Lee, K.M. & Rowe, R.K., 1990a. Finite element modelling of the three-dimensional ground deformations due to tunnelling in soft cohesive soils: Part 2—results. *Computers and Geotechnics*, 10, pp.111–138.

Lee, K.M. & Rowe, R.K., 1990b. Finite element modelling of the three-dimensional ground deformations due to tunnelling in soft cohesive soils: Part I—Method of analysis. *Computers and Geotechnics*, 10, pp.87–109.

Li, X., 1997. Modeling of dilative shear failure. *Journal of Geotechnical and Geoenvironmental Engineering*, 123(July), pp.609–616.

Li, X. & Dafalias, Y., 2000. Dilatancy for cohesionless soils. *Geotechnique*, 50(4), pp.449–460.

Li, X., Dafalias, Y. & Wang, Z., 1999. State-dependant dilatancy in critical-state constitutive modelling of sand. *Canadian Geotechnical Journal*, 36, pp.599–611.

Li, Y., 2013. *Ground Movements due to excavation in cohesionless soil: Physical and analytical models*. University of Cambridge.

Ling, H.I. & Yang, S., 2006. Unified Sand Model Based on the Critical State and Generalized Plasticity. *Journal of Engineering Mechanics*, 132(12), pp.1380–1391.

Lo, K.. & Rowe, R.K., 1982. prediction of ground subsidence due to tunnelling in clays. In *Research Report GEOT-10-82. Faculty of Engineering Science, University of Western Ontario*. London.

Loganathan, N. & Poulos, H.G., 1998. Analytical prediction for tunneling-induced ground movements in clays. *Journal of Geotechnical and Geoenvironmental Engineering*, (September), pp.846–856.

Mair, R.J., 1979. *Centrifuge modelling of tunnelling construction in soft clay*. PhD thesis, University of Cambridge.

Mair, R.J., 1994. Discussion on Barratt, O'reilly and Temporal (1994) in tunnelling '94. *Transactions of the Institution of Mining and metallurgy*, 103, pp.188–189.

Mair, R.J., 1989. Selection of design parameters for underground construction. In *The 12th International Conference on Soil Mechanics and Foundation Engineering*. Rio de Janeiro, pp. 2891–2893.

Mair, R.J., Gunn, M.J. & O'Reilly, M.P., 1981. Ground movement around shallow tunnels in soft clay. In *Proceedings of the Tenth ICSMFE*. Stockholm, pp. 323–328.

Mair, R.J. & Taylor, R.N., 1997. Theme lecture: Bored tunnelling in the urban environment. In *The 14th International Conference on Soil Mechanics and Foundation Engineering*. pp. 2353–2385.

Mair, R.J., Taylor, R.N. & Bracegirdle, A., 1993. Subsurface settlement profiles above tunnels in clays. *Geotechnique*, (2), pp.315–320.

Mansour, M., 1996. *Three-dimensional numerical modelling of hydroshield tunnelling*. University of Innsbruck.

Manzari, M. & Dafalias, Y., 1997. A critical state two-surface plasticity model for sands. *Geotechnique*, 47(2), pp.255–272.

Marshall, A.M., 2009. *Tunnelling in sand and its effect on pipelines and piles*. University of Cambridge.

Marshall, A.M. et al., 2012. Tunnels in sands: the effect of size, depth and volume loss on greenfield displacements. *Geotechnique*, (5), pp.385–399.

Marshall, A.M. & Mair, R.J., 2009. Centrifuge modelling to investigate soil-structure interaction mechanisms resulting from tunnel construction beneath buried pipelines. *Geotechnical aspects of underground construction in soft ground*, pp.703–707.

Meschke, G., Kropik, C. & Mang, H.A., 1996. Numerical analyses of tunnel linings by means of a viscoplastic material model for shotcrete. *International Journal for Numerical Methods in Engineering*, 39(February), pp.3145–3162.

Moh, Z.C., Ju, D.H. & Hwang, R.N., 1996. Groudn movements around tunnels in soft ground. In *Int. Symposium on Geotechnical Aspects of Underground Construction in Soft Ground*. London, pp. 725–730.

Moraes Jr, A.H., 1999. *Three-dimensional numerical simulation of tunnels excavated with NATM*. University of Brasilia, Brazil.

Mroueh, H. & Shahrour, I., 2002. Three-dimensional finite element analysis of the interaction between tunneling and pile foundations. *International Journal for Numerical and Analytical Methods in Geomechanics*, 26(3), pp.217–230.

Negro, A. & Queiroz, B.I.., 1999. Prediction and performance of soft ground tunnels. In *Geotechnical aspects of underground construction in soft ground*. Tokyo: Balkema, pp. 409–418.

Negro, A., Sozio, L.E. & Ferreira, A.A., 1996. Tunnelling in Sao Paulo, Brazil. In R. J. Mair & R. N. Taylor, eds. *Int. Stmposium on Geotechnical Aspects of Underground Construction in Soft Ground*. London: Balkema, pp. 295–300.

Negussey, D. & Islam, M.S., 1994. Uniqueness of steady state and liquefaction potential. *Canadian Geotechnical Journal*, 31(1), pp.132–139.

New, B.M. & Bowers, K.H., 1994. Ground movement model validation at the Heathrow Express trial tunnel. In *Tunnelling' 94*. London: IMM, pp. 301–329.

Nomoto, T., Mori, H. & Matsumoto, M., 1995. Overview on ground movements during shield tunnelling - a survey on Japanese shield tunnelling. In *Underground Construction in Soft Ground*. Balkema, pp. 567–572.

Nova, R., 1982. A constitutive model for soil under monotonic and cyclic loading. In *Soil Mechanics-Transient and Cyclic Loads*. Wiley, pp. 343–373.

Nova, R. & Wood, D., 1979. A constitutive model for sand in triaxial compression. *International Journal for Numerical and Analytical Methods in Geomech*, 3, pp.255–278.

Nyren, R., 1998. *Field measurements above twin tunnels in London Clay*. PhD Thesis, Imperial College London.

O'Reilly, M.P., 1988. Evaluating and predicting ground settlements caused by tunnelling in london clay. In *The 5th international symposium, Tunnelling 88*. London: The Institution of mining and metallurgy, pp. 231–241.

O'Reilly, M.P. & New, B.M., 1982. Settlement above tunnels in the United Kingdom-their magnitude and prediction. In *Tunnelling 82. Papers presented at the third International Symposium*. Brighton, UK: Institution of Mining and Metallurgy, pp. 173–181.

Ohta, H., Takeuchi, T. & Nishiwaki, Y., 1995. Performance of linings for shield driven tunnels - a survey on Japanese shield tunnelling. In K. Fujita & O. Kusakabe, eds. *Underground Construction in Soft Ground*. Balkema, pp. 367–374.

Onur, I., Tuncan, M. & Tuncan, A., 2014. An Experimental Study for Determining the Shear Modulus of Toyoura Sand. In *Second European Conference on Earthquake Engineering and Seismology*. Istanbul.

Oztoprak, S. & Bolton, M.D., 2012. Stiffness of sands through a laboratory test database. *Géotechnique*, 63(1), pp.54–70.

Panet, M. & Guenot, A., 1982. Power plants ln-situ stresses and stress around underground openings. In *Proceedings of the International Symposium. Tunneling 82,*. Balkema, pp. 197–204.

Peck, R.B., 1969. Deep excavations and tunnelling in soft ground. *Proc. 7th Int. Conf. on SMFE*, pp.226–290.

Pestana-Nascimento, J.M., 1994. *A unified constitutive model for clays and sands*. Massachusetts Institute of Technology.

Pinto, F., 1999. *Analytical methods to interpret ground deformations due to soft ground tunneling*. Massachusetts Institute of Technology.

Pinto, F. & Whittle, A.J., 2000. Comparision of analytical solutions for ground movements caused by shallow tunnelling in soil. *ASCE Journal of Engineering Mechanics*.

Poorooshasb , B, H., Holubec, I. & Sherbourne, A.N., 1966. Yielding and Flow of Sand in Triaxial Compression Part I. *Canadian Geotechnical Journal*, 111(4), pp.179–190.

Potts, D.M., 1976. *Behaviour of Lined and Unlined Tunnels in Sand.* University of Cambridge.

Poulos, S.J., 1981. The Steady State of Deformation. *Journal of the Geotechnical Engineering Division*, 107(5), pp.553–562.

Roscoe, K. & Burland, J., 1968. On the generalised stress-strain behaviour of "wet" clay. In J. Heyman & Leckie FA, eds. *In Engineering Plasticity*. Cambridge: Cambridge University Press, pp. 535–609.

Roscoe, K., Schofield, A. & Thurairajah, A., 1963. Yielding of clays in states wetter than critical. *Geotechnique*, 13.

Roscoe, K.H., Schofield, A.N. & Wroth, C.P., 1958. On the Yielding of Soils. *Géotechnique*, 8(1), pp.22–53.

Rowe, P., 1962. The stress-dilatancy relation for static equilibrium of an assembly of particles in contact. In *Proceedings of the Royal Society of London*. London.

Rowe, R.K. & Kack, G.J., 1983. A theoretical examination of the settlements induced by tunnelling: four case histories. *Canadian Geotechnical Journal*, 20(2), pp.299–314.

Sadrekarimi, J. & Abbasnejad, A., 2010. Arching effect in fine sand due to base yielding. *Canadian Geotechnical Journal*, 374(March), pp.366–374.

Sagaseta, C., 1987. Analysis of undrained soil deformation due to ground loss. *Geotechnique*, 37(3), pp.301–320.

Salgado, R., Bandini, P. & Karim, A., 2000. Shear strength and stiffness of silty sand. *Journal of Geotechnical and Geoenvironmental Engineering*, 126(5), pp.451–462.

Schanz, T., Vermeer, P. & Bonnier, P., 1999. The hardening soil model: formulation and verification. *Beyond 2000 in computaional Geotechnics*, pp.1–16.

Schofield, A. & Wroth, P., 1968. *Critical state soil mechanics*, London: McGrawHill.

Simpson, B., Atkinson, J. & Jovicic, V., 1996. The influence of anisotropy on calculations of ground settlements above tunnels. In R. J. Mair & R. N. Taylor, eds. *In Geotechnical aspects of underground construction in soft ground: proceedings of the international symposium*. London, pp. 591–595.

Sneddon, I.N., 1951. *Fourier transforms*, New York: McGraw Hill.

Swoboda, G., 1979. Finite element analysis of the new Austrian tunnelling method. In *Proceedings of the 3rd International Conference on Numerical Methods in Geomechanics*. Aachen, pp. 581–586.

Taylor, D., 1948. *Fundamentals of Soil Mechanics*, New York: John Wiley.

Taylor, R.N., 1995. Tunnelling in soft ground in the UK. In K. Fujita & O. Kusakabe, eds. *Proceedings of the 1994 International Symposium on Underground Construction in Soft Ground*. Balkema, New Delhi, India, pp. 123–126.

Verdugo, R. & Ishihara, K., 1996. The steady state of sandy soils. *Soils and Foundations*, 36(2), pp.81–91.

Vermeer, P.A., 1982. A five-constant model unifying well-established concepts. *Results of the International Workshop on Constitutive Relations for Soils*, pp.175–197.

Verruijt, A., 1997. A complex variable solution for a deforming tunnel in an elastic half-plane. *International Journal for Numerical and Analytical Methods in Geomechanics*, 21(January 1996), pp.77–89.

Verruijt, A., 1996. *Complex variable solutions of elastic tunneling problems*,

Verruijt, A. & Booker, J.R., 1996. Surface settlements due to deformation of a tunnel in an elastic half plane. *Geotechnique*, 46(4), pp.4–7.

Vorster, T.E.B. et al., 2005. Estimating the effects of tunneling on existing pipelines. *Journal of Geotechnical and Geoenvironmental Engineering*, (November), pp.1399–1410.

Ward, W.H., Marsland, A. & Samuels, S.G., 1965. The development of earth loading and deformation in tunnel lining in London Clay. In *Proceeding of the sixth international conference on soil mechanics and foundation engineering*. Toronto, pp. 432–436.

Ward, W.H. & Pender, M.J., 1981. Tunnelling in soft ground - General Report. In *10th International Conference on Soil Mechanics and Foundation Engineering*. Stockholm, pp. 261–275.

Wongsaroj, J., 2006. *Three-dimensional finite element analysis of short and long-term ground response to open- face tunnelling in stiff clay*. The University of Cambridge.

Wood, A.M.M., 1975. The circular tunnel in elastic ground. *Geotechnique*, 25(1), pp.115–127.

Wood, D.M., 1990. *Soil Behaviour and Critical State Soil Mechanics*, Cambridge: Cambridge University Press.

Wood, D.M. & Belkheir, K., 1994. Strain softening and state parameter for sand modelling. *Géotechnique*, 44(2), pp.335–339.

Yao, Y.P., Sun, D. a. & Luo, T., 2004. A critical state model for sands dependent on stress and density. *International Journal for Numerical and Analytical Methods in Geomechanics*, 28(4), pp.323–337.

Yao, Y.P., Sun, D. a. & Matsuoka, H., 2008. A unified constitutive model for both clay and sand with hardening parameter independent on stress path. *Computers and Geotechnics*, 35(2), pp.210–222.

Yu, H., 1998. CASM: A unified state parameter model for clay and sand. *International Journal for Numerical and Analytical Methods in Geomechanics*, 22(December 1996), pp.621–653.

Zhao, Y., 2008. *In situ soil testing for foundation performance prediction*. University of Cambridge.

Appendix A. Triaxial tests involved in determination of input model parameters

A.1 The critical state locus

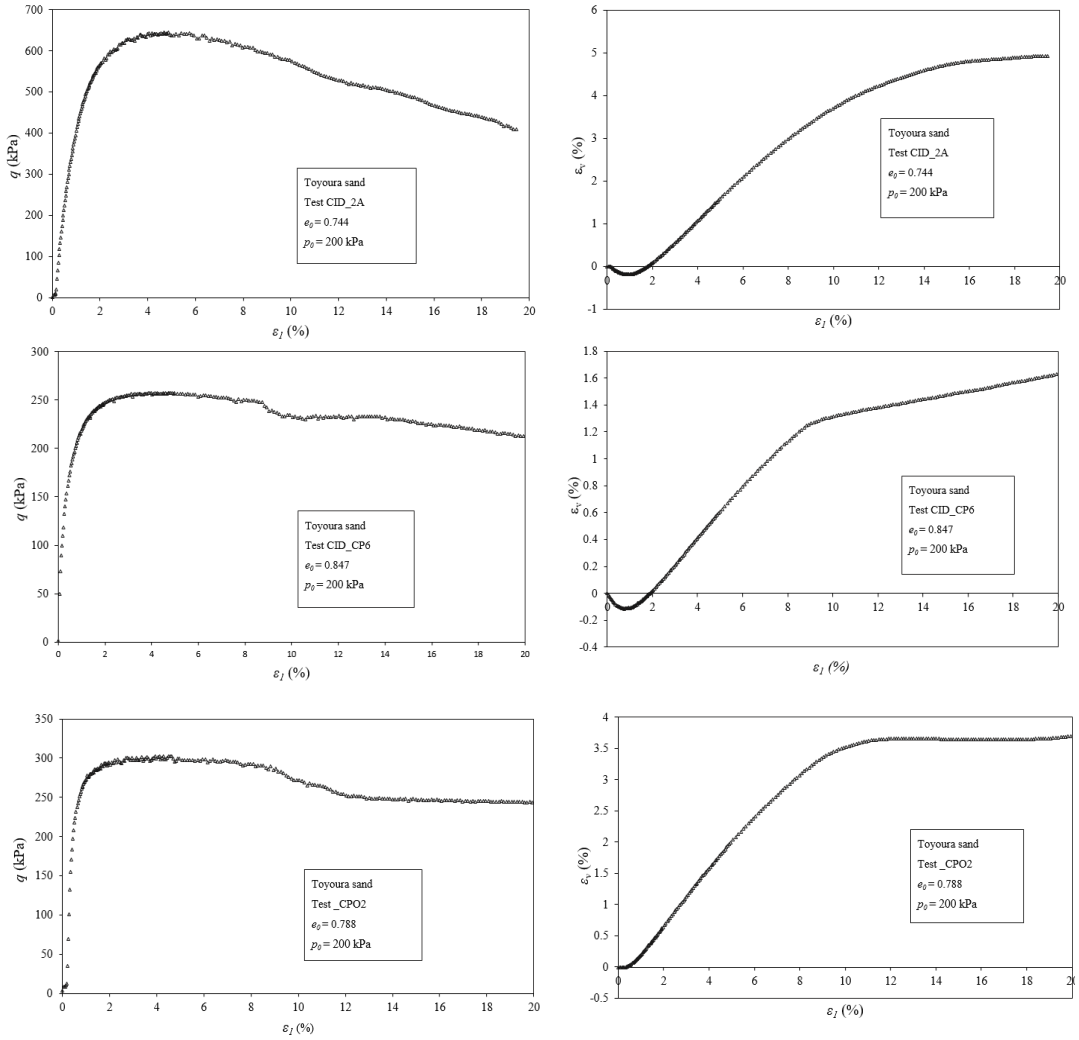

Figure A.1 Drained triaxial compression tests used for deducing the CSL.

The drained and undrained triaxial compression tests data downloaded from the civil engineering consulting company – Golder Associates are plotted in the following figures for the determination of the CSL and input parameter M_{tc}, N and χ_{tc} of the Toyoura sand.

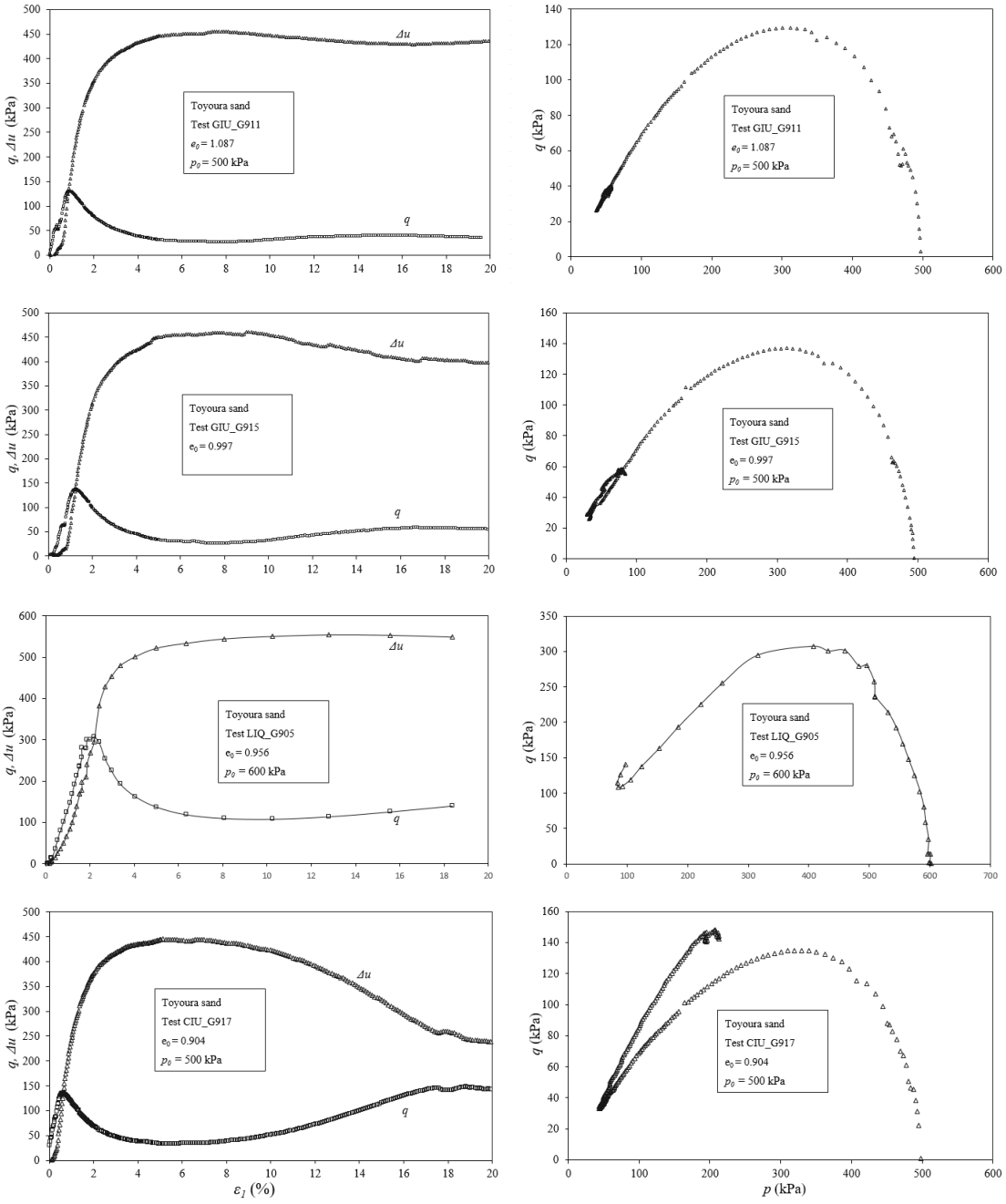

Figure A.2 Undrained triaxial compression tests used for deducing the CSL.

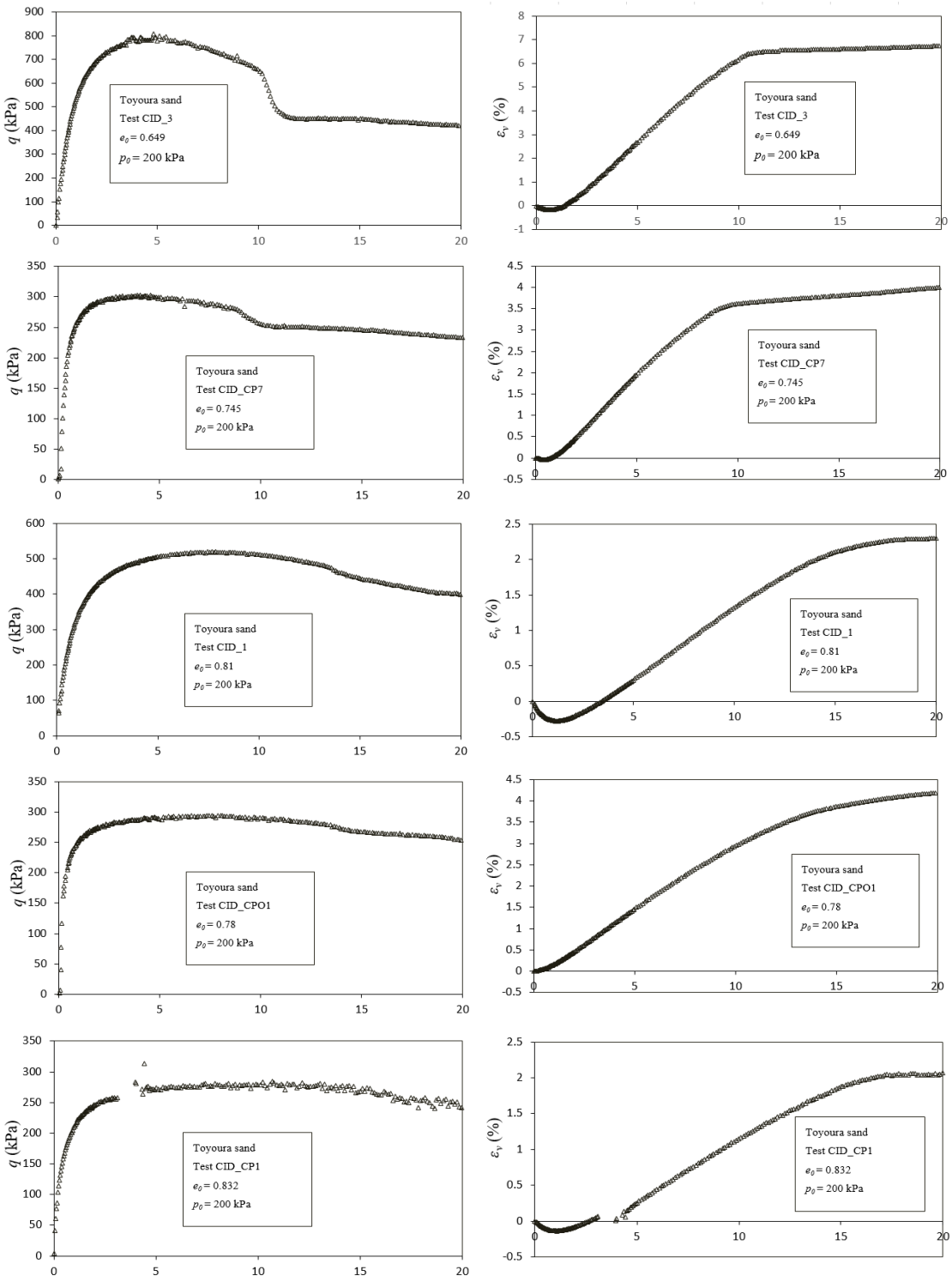

Figure A.3 Drained triaxial compression used for deducing M_{tc} and N.

A.2 M_{tc} and N

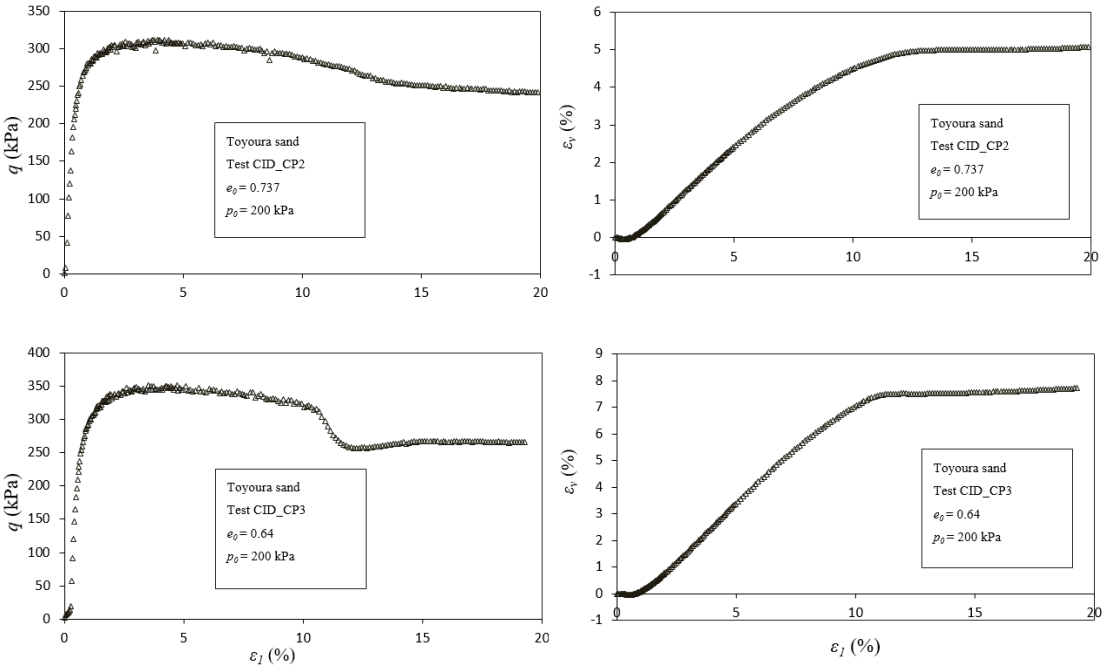

Figure A.4 Drained triaxial compression used for deducing M_{tc} and N.

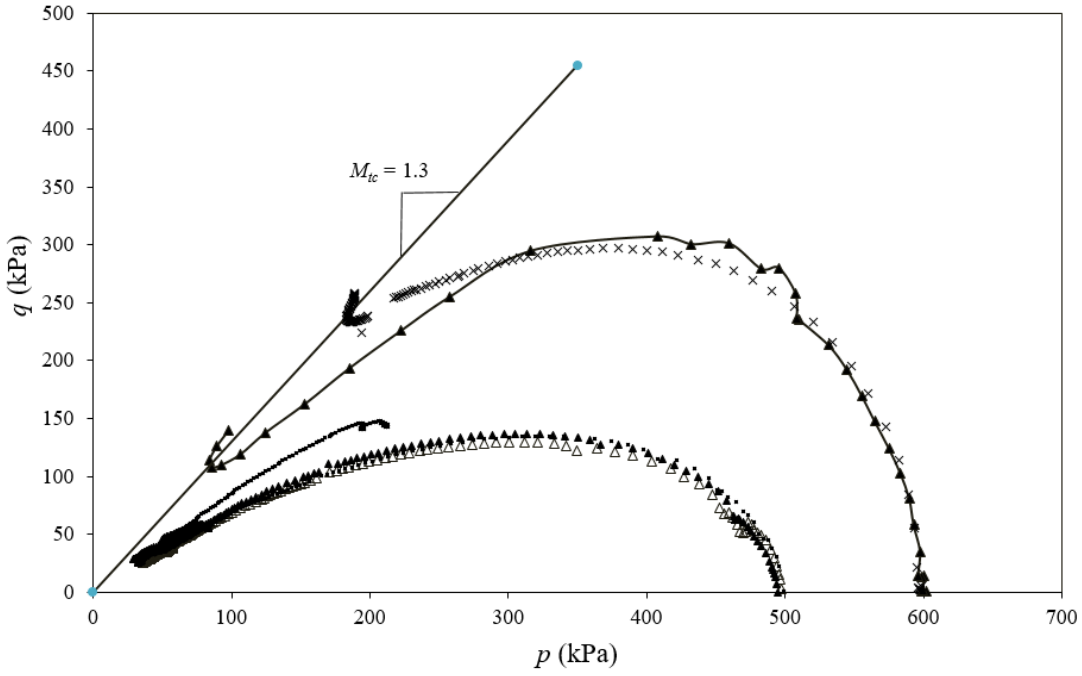

Figure A.5Undrained triaxial compression test used for deducing M_{tc}.

A.3 χ_{tc}

Table A.1 Determination of χ_{tc} using linear and curved CSL.

Tests	D_{min}	ψ_p (liner)	ψ_p(curved)	ε_v	e_0	e	e_c	p_c	lnp_c
CID_2A	-0.324	-0.02542166	-0.00515579	1.3	0.744	0.734328	0.75975	414	6.025866
CID_CP6	-0.11	0.009768611	-0.00528841	0.5	0.837	0.832815	0.823046	200	5.298317
CID_CPO2	-0.46	-0.04844239	-0.06349941	1.7	0.788	0.774604	0.823046	200	5.298317
CID_3	-0.72	-0.1242983	-0.09521716	3.5	0.649	0.626285	0.750583	460	6.131226
CID_CP7	-0.4	-0.08840189	-0.10345891	1.39	0.745	0.734645	0.823046	200	5.298317
CID_CPO1	-0.33	-0.05708639	-0.07214341	1.8	0.78	0.76596	0.823046	200	5.298317
CID_1	-0.13	0.032732564	0.045675748	1.1	0.81	0.80109	0.768357	375	5.926926
CID_CP1	-0.12	-0.00227839	-0.01733541	1.35	0.832	0.820768	0.823046	200	5.298317
CID_CP2	-0.57	-0.10512467	-0.12040348	2.47	0.737	0.718796	0.823921	198	5.288267
CID_CP3	-0.9	-0.20287108	-0.21758794	3.3	0.64	0.61888	0.821751	203	5.313206

Appendix B. Displacements of the FE tunnel periphery

The *x*-*z* direction displacements of the points listed in Figure 5.8 are monitored during numerical modelling. The tunnel volume loss are calculated using AutoCAD according to these 2D movements. As the deformation of the tunnel is theoretically symmetrical, thus, as shown in Figure B.1, the movement from only 9 points on the cylinder are recorded for simplicity. The displacements of each point at corresponding surface contraction levels are listed in the following tables, where $A_0$is the original area of the cylinder, A_1 is the current area after deformation, u_z and u_x are the vertical and horizontal movement respectively.

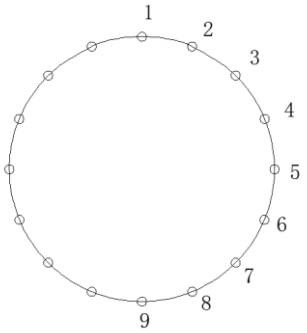

Figure B.1 Nine points used for tunnel volume loss calculation.

Table B.1 Cylinder movement calculated by Hardening Soil.

Points	**0.6% surface contraction**		**1.2% surface contraction**	
	u_z (mm)	u_x (mm)	u_z (mm)	u_x (mm)
1	-0.17490		-0.30209	
2	-0.15028	-0.04656	-0.26411	-0.09411
3	0.07955		0.11927	
4	-0.12794	-0.05549	-0.23099	-0.11846
5	-0.10244	-0.05776	-0.19175	-0.13334
6	0.04629	-0.05840	0.06480	-0.11821
7	0.06399	-0.04545	0.09318	-0.08964
8	-0.48400	-0.06490	-0.11547	-0.14732
9	-0.04641	-0.05800	-0.09386	-0.14785
A_0 (mm^2)	A_1 (mm^2)	$V_{l,t}$ (%)	A_1 (mm^2)	$V_{l,t}$ (%)
2,827.43340	2,812.70130	0.52104	2,797.99880	1.04104

Points	**2.5% surface contraction**		**5.0% surface contraction**	
	u_z (mm)	u_x (mm)	u_z (mm)	u_x (mm)
1	-0.63964		-1.31400	
2	-0.57110	-0.20725	1.19100	-0.39971
3	0.18682		0.26100	
4	-0.51089	-0.26776	-1.07900	-0.51857
5	-0.43821	-0.31280	-0.94300	-0.60830
6	0.07751	-0.26129	0.04100	-0.50639
7	0.13247	-0.19583	0.14900	-0.38212
8	-0.06986	-0.34563	-0.24000	-0.67076
9	-0.23997	-0.36486	-0.56500	-0.71209
A_0 (mm^2)	A_1 (mm^2)	$V_{l,t}$ (%)	A_1 (mm^2)	$V_{l,t}$ (%)
2,827.43340	2,755.42880	2.54664	2,686.81930	4.97321

Table B.3 Cylinder movement calculated by the proposed model with $\psi_0 = 0.1$

Points	**0.0% surface contraction**		**0.4% surface contraction**	
	u_z (mm)	u_x (mm)	u_z (mm)	u_x (mm)
1	-0.31142		-0.47569	
2	-0.22005	-0.00400	-0.35945	-0.03764
3	0.16308		0.21889	
4	-0.16146		-0.28132	-0.01464
5	-0.11302		-0.21231	
6	0.06251	-0.00800	0.08587	-0.04389
7	0.10808	-0.01000	0.14751	-0.05091
8	-0.01809		0.00000	
9		-0.00500	-0.11056	
A_0 (mm^2)	A_1 (mm^2)	$V_{l,t}$ (%)	A_1 (mm^2)	$V_{l,t}$ (%)
2,827.43340	2,812.84200	0.51607	2,800.84600	0.94034

Points	**1.7% surface contraction**		**4.0% surface contraction**	
	u_z (mm)	u_x (mm)	u_z (mm)	u_x (mm)
1	-0.90872		-1.52400	
2	-0.73894	-0.16383	-1.28600	-0.35733
3	0.36601		0.55900	
4	-0.61454	-0.17221	-1.10300	-0.42077
5	-0.49166	-0.15446	-0.90900	-0.44154
6	0.15143	-0.19977	0.22800	-0.43738
7	0.25395	-0.17053	0.38700	-0.35028
8	-0.07259	-0.17428	-0.14000	-0.48333
9	-0.25887	-0.12596	-0.48600	-0.45165
A_0 (mm^2)	A_1 (mm^2)	$V_{l,t}$ (%)	A_1 (mm^2)	$V_{l,t}$ (%)
2,827.43340	2,754.81840	2.56823	2,686.92740	4.96938

Table B.4 Cylinder movement calculated by the proposed model with $\psi_0 = 0$

Points	**0.3% surface contraction**		**1.1% surface contraction**	
	u_z (mm)	u_x (mm)	u_z (mm)	u_x (mm)
1	-0.19846		-0.36837	
2	-0.14669	-0.01722	-0.29499	-0.07476
3	0.12738		0.20686	
4	-0.11132		-0.23900	-0.07904
5	-0.07935		-0.18286	-0.07115
6	0.06413	-0.01959	0.11171	-0.09060
7	0.09327	-0.02292	0.15757	-0.07681
8	0.00773		0.00990	-0.07988
9	-0.02984	0.02903	-0.07577	-0.05857
A_0 (mm^2)	A_1 (mm^2)	$V_{l,t}$ (%)	A_1 (mm^2)	$V_{l,t}$ (%)
2,827.43340	2,813.11450	0.50643	2,794.94780	1.04894

Points	**2.5% surface contraction**		**5.1% surface contraction**	
	u_z (mm)	u_x (mm)	u_z (mm)	u_x (mm)
1	-0.68851		-1.30300	
2	-0.57429	-0.17992	-1.11200	-0.37978
3	0.34134		0.56900	
4	-0.48326	-0.21209	-0.95900	-0.46891
5	-0.38567	-0.22199	-0.78900	-0.52052
6	0.18338	-0.22038	0.28800	-0.46545
7	0.26068	-0.17553	0.42400	-0.36110
8	0.00000	-0.24378	-0.04300	-0.56510
9	-0.17355	-0.22628	-0.38200	-0.56867
A_0 (mm^2)	A_1 (mm^2)	$V_{l,t}$ (%)	A_1 (mm^2)	$V_{l,t}$ (%)
2,827.43340	2,756.25620	2.51738	2,686.15220	4.99680

Table B.5 Cylinder movement calculated by the proposed model with ψ_0 = -0.1

Points	**0.3% surface contraction**		**1.0% surface contraction**	
	u_z (mm)	u_x (mm)	u_z (mm)	u_x (mm)
1	-0.20860		-0.36134	
2	-0.15463	-0.01667	-0.28836	-0.06708
3	0.12507		0.19168	
4	-0.11754	-0.00500	-0.23334	-0.06840
5	-0.08433		-0.17890	-0.05801
6	0.06137	-0.01943	0.10018	-0.08183
7	0.09098	-0.02308	0.14449	-0.07051
8	0.00360	0.00993	0.00225	-0.06657
9	-0.03433	0.03298	-0.07805	-0.04290
A_0 (mm^2)	A_1 (mm^2)	$V_{l,t}$ (%)	A_1 (mm^2)	$V_{l,t}$ (%)
2,827.43340	2,812.55710	0.52614	2,796.06260	1.00952

Points	**2.5% surface contraction**		**5.1% surface contraction**	
	u_z (mm)	u_x (mm)	u_z (mm)	u_x (mm)
1	-0.69304		-1.27400	
2	-0.57856	-0.18033	-1.08400	-0.37985
3	0.33322		0.57800	
4	-0.48788	-0.21292	-0.93300	-0.46979
5	-0.39073	-0.16590	-0.76500	-0.52317
6	0.17719	-0.22188	0.30300	-0.46765
7	0.25371	-0.17632	0.43700	-0.36172
8	-0.00500	-0.24660	-0.02300	-0.57134
9	-0.17897	-0.22919	-0.36100	-0.57604
A_0 (mm^2)	A_1 (mm^2)	$V_{l,t}$ (%)	A_1 (mm^2)	$V_{l,t}$ (%)
2,827.43340	2,757.44030	2.47550	2,686.50450	4.98434

Table B.6 Cylinder movement calculated by the proposed model with ψ_0 = -0.2

Points	**0.3% surface contraction**		**1.0% surface contraction**	
	u_z (mm)	u_x (mm)	u_z (mm)	u_x (mm)
1	-0.18046		-0.31386	
2	-0.14595	-0.02949	-0.26310	-0.15672
3	0.08168		0.13028	
4	-0.11859	-0.02844	-0.22163	-0.08416
5	-0.09159	-0.02160	-0.17764	-0.08460
6	0.04199	-0.03747	0.06749	-0.09198
7	0.06216	-0.03225	0.09969	-0.07343
8	-0.00500	-0.02779	-0.01230	-0.09668
9	-0.04344	-0.01355	-0.08659	-0.08325
A_0 (mm^2)	A_1 (mm^2)	$V_{l,t}$ (%)	A_1 (mm^2)	$V_{l,t}$ (%)
2,827.43340	2,812.41780	0.53107	2,796.08880	1.00859

Points	**2.5% surface contraction**		**5.1% surface contraction**	
	u_z (mm)	u_x (mm)	u_z (mm)	u_x (mm)
1	-0.65576		-1.28300	
2	-0.55975	-0.18631	-1.09500	-0.37726
3	0.25840		0.48900	
4	-0.48332	-0.22915	-0.95100	-0.47162
5	-0.39899	-0.25364	-0.79300	-0.53466
6	0.12839	-0.23046	0.23600	-0.46818
7	0.19322	-0.17817	0.36200	0.35937
8	-0.03323	-0.27869	-0.03700	-0.58609
9	-0.19937	-0.27791	-0.40200	-0.60315
A_0 (mm^2)	A_1 (mm^2)	$V_{l,t}$ (%)	A_1 (mm^2)	$V_{l,t}$ (%)
2,827.43340	2,757.26590	2.48167	2,687.38170	4.95332

Appendix C. Ground response calculated by using the proposed model with ψ_0 = 0.1

C.1 Settlement troughs

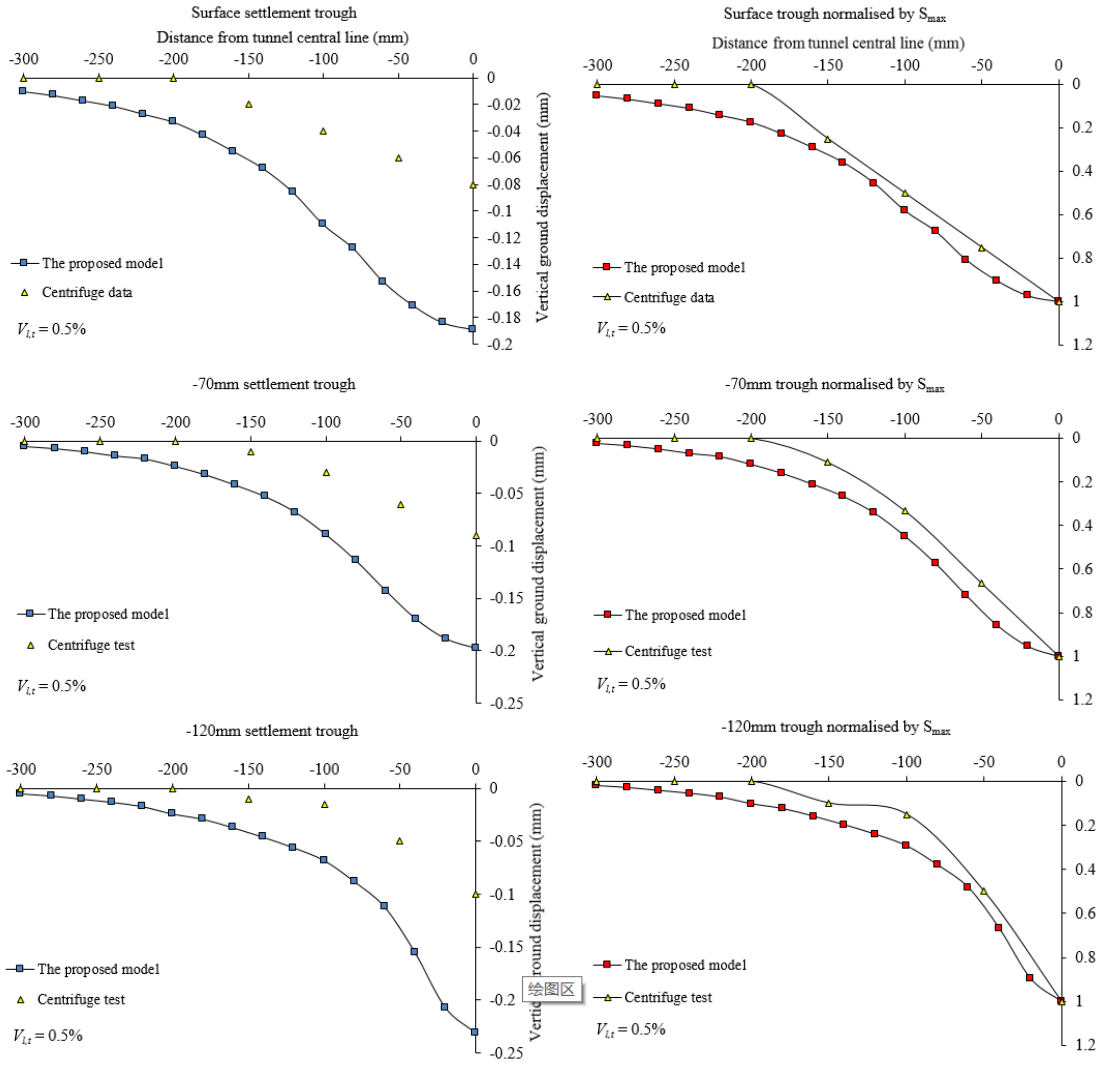

Figure C.2 Settlement troughs with $V_{l,t}$=0.5%.

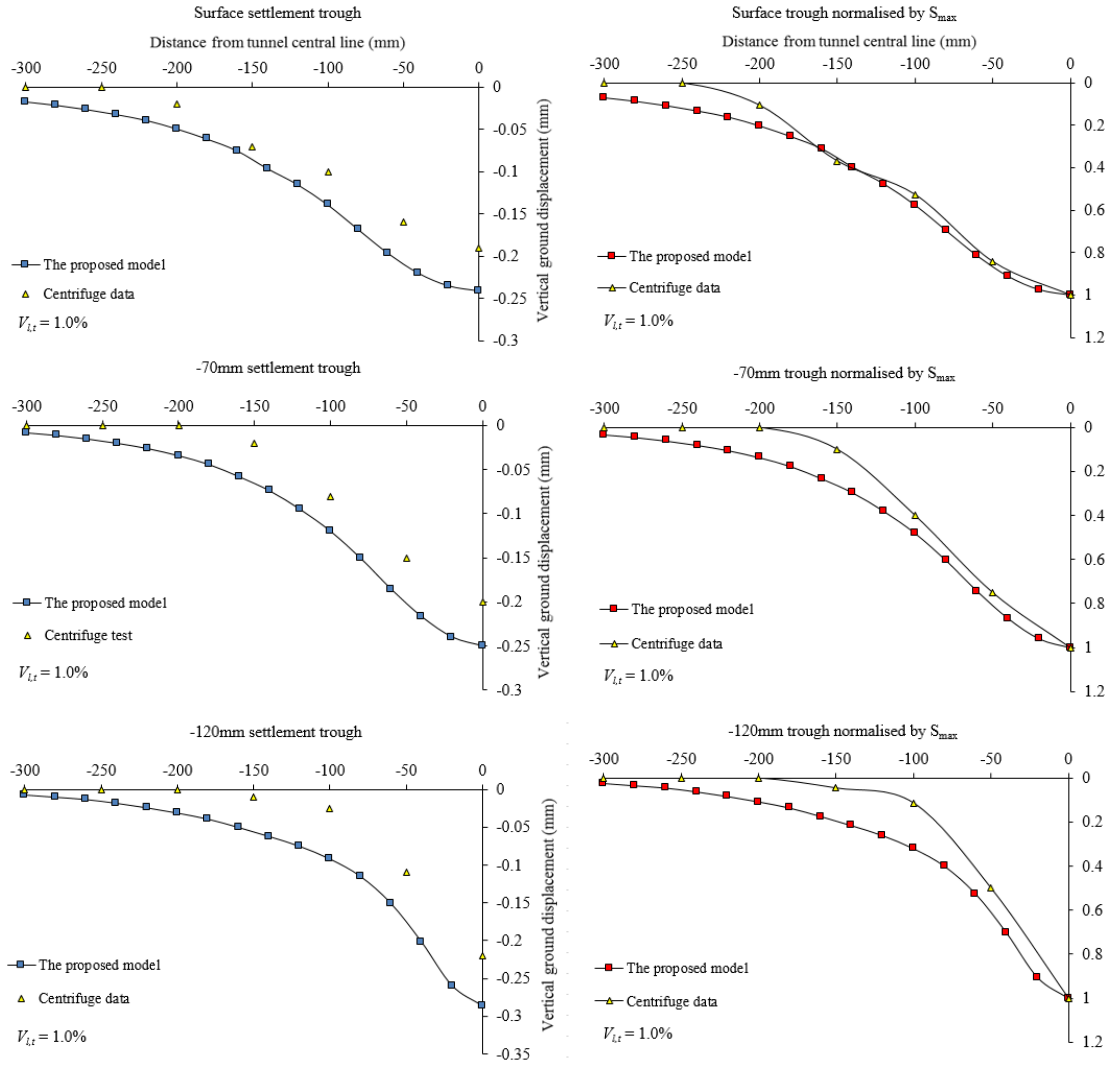

Figure C.3 Settlement troughs with $V_{l,t}$=1.0%.

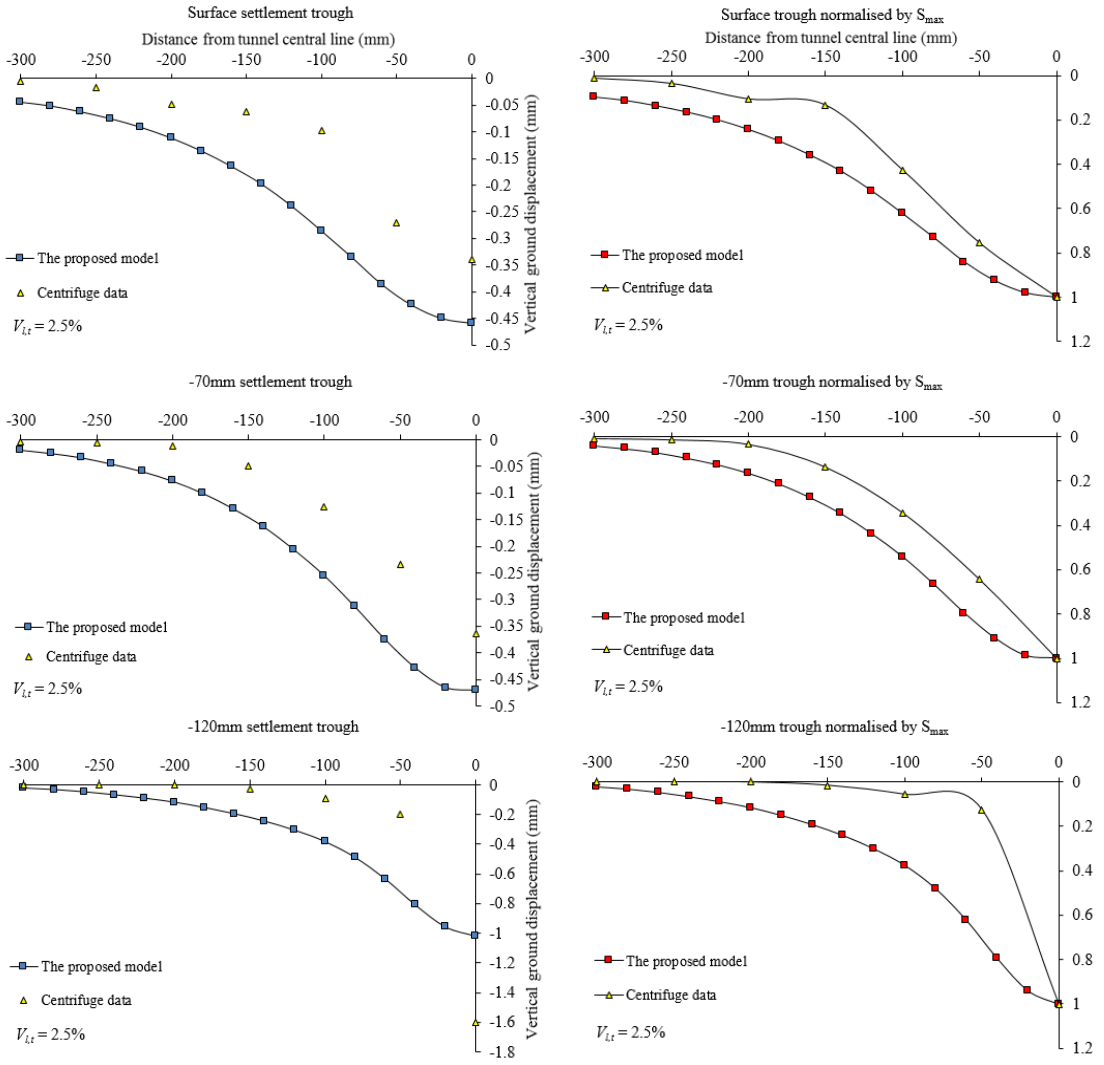

Figure C.4 Settlement troughs with $V_{l,t}$=2.5%.

C.2 Horizontal displacement

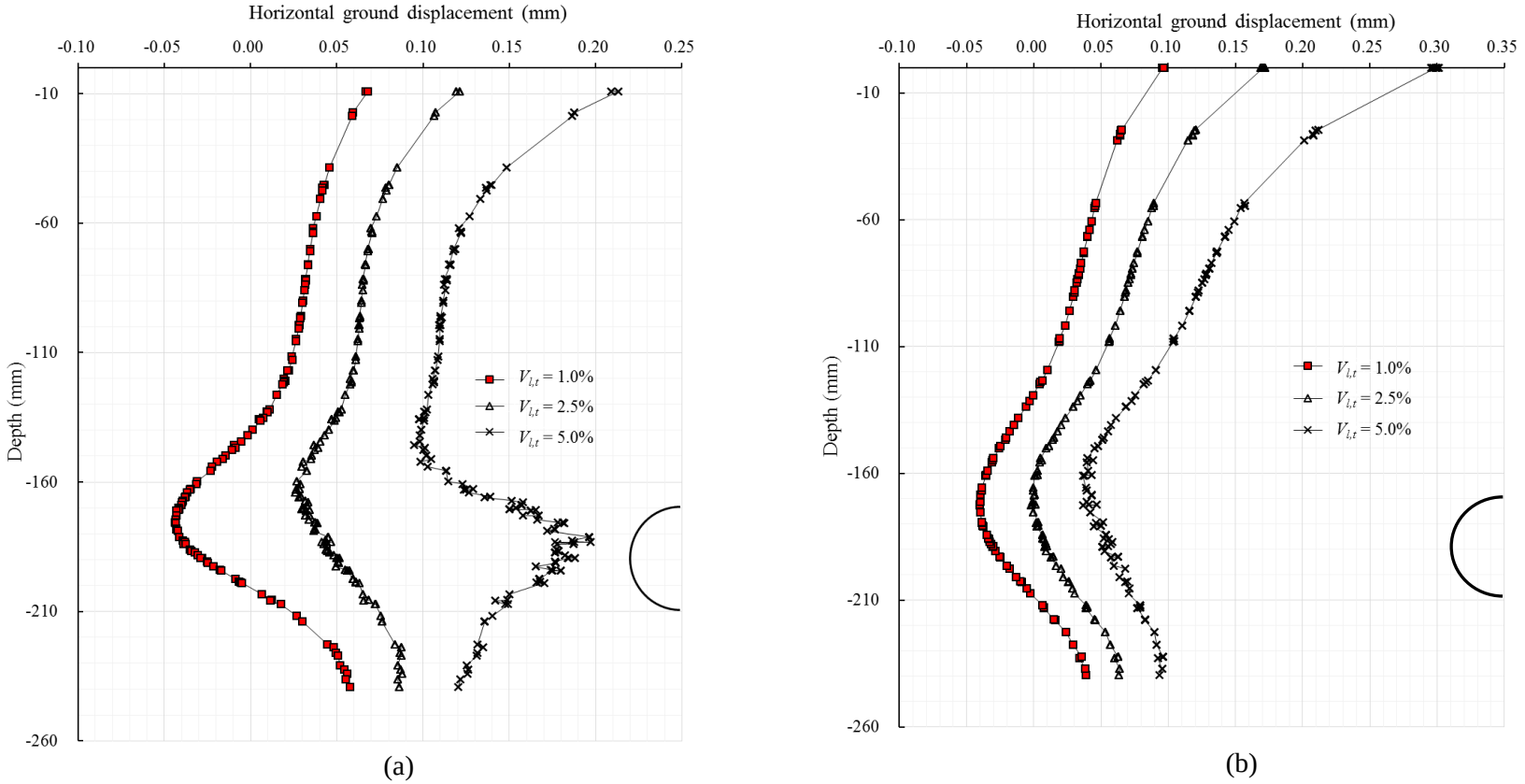

Figure C.6 Horizontal ground displacement (a) 15mm and (b) 30mm away from tunnel periphery.

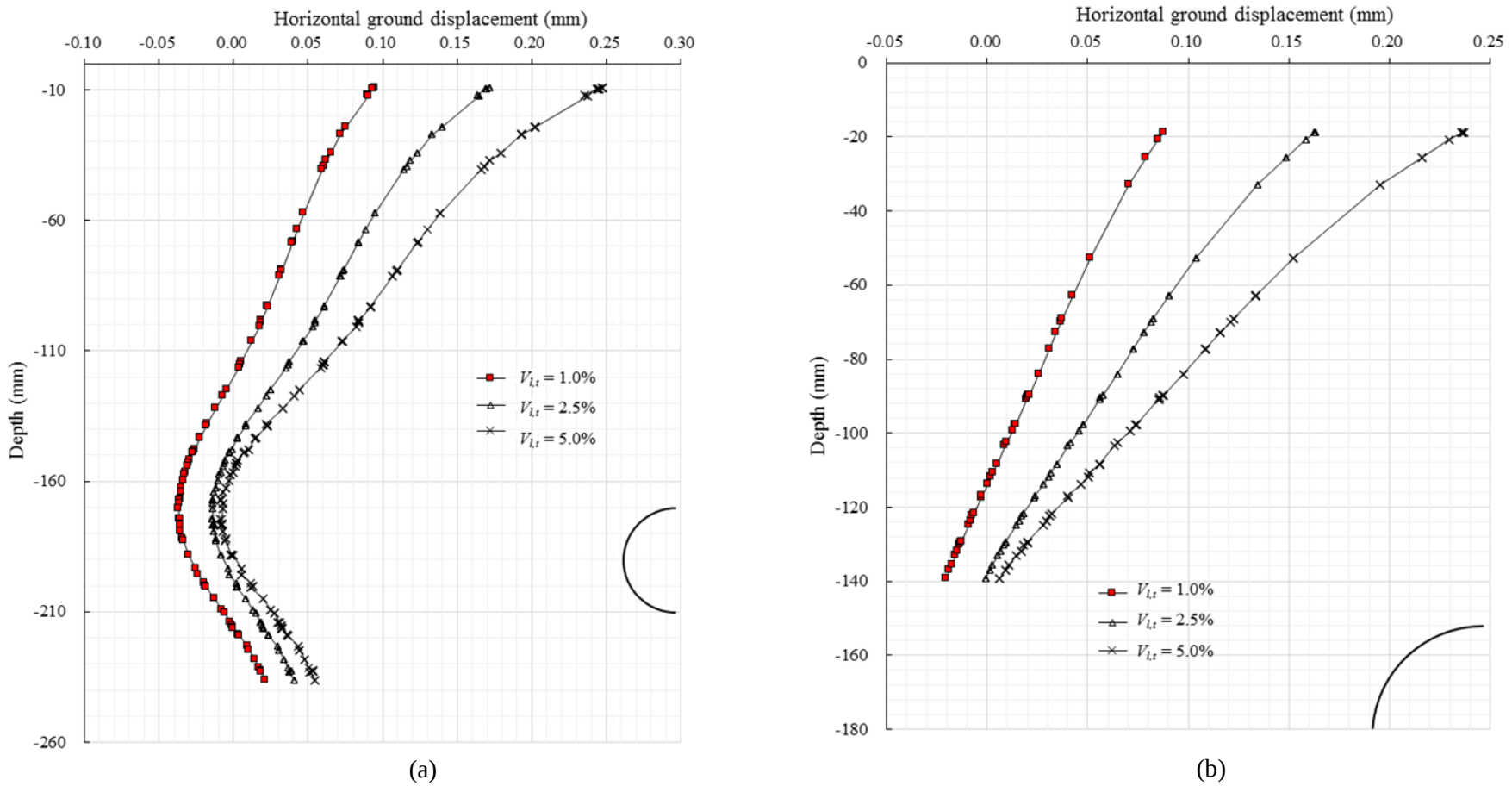

Figure C.7 Horizontal ground displacement (a) 45mm and (b) 60mm away from tunnel periphery.

Appendix D. Effect of K_0

D.1 Effect on horizontal displacement

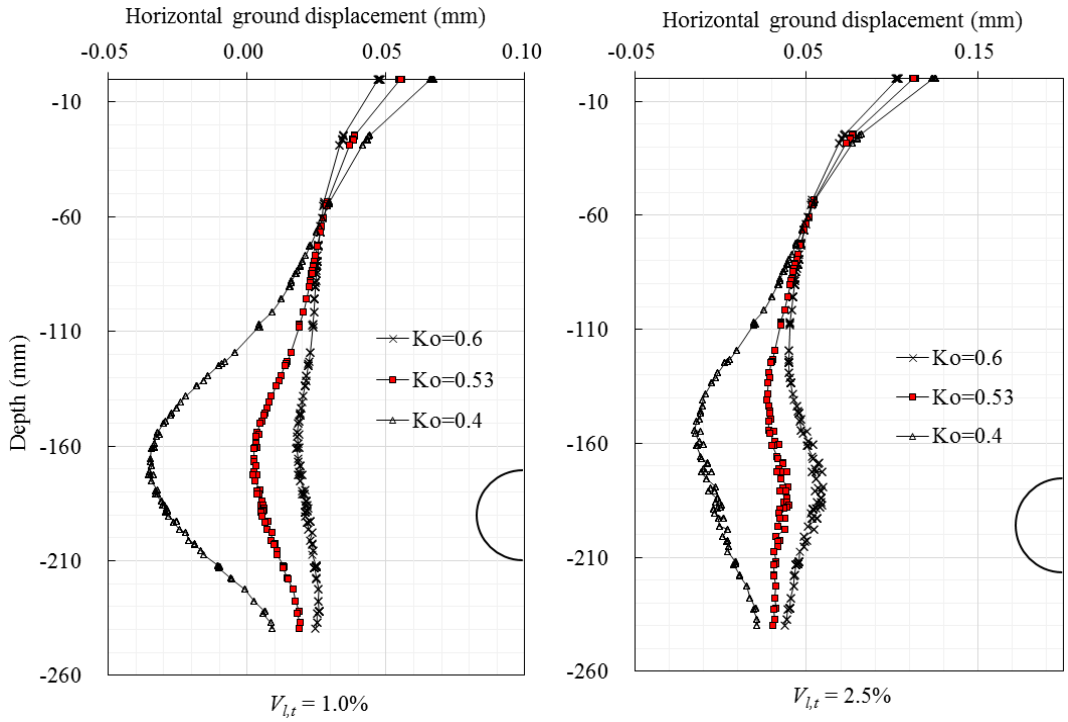

Figure D.1 Effect of K_0 on horizontal ground displacement 30mm from tunnel periphery.

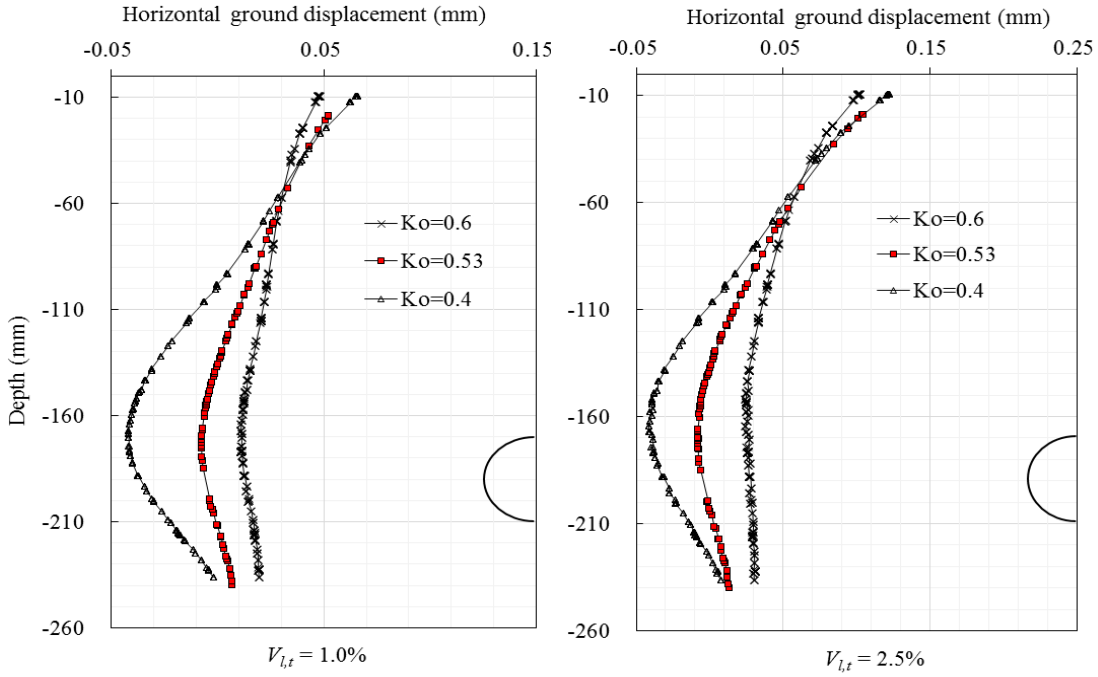

Figure D.2 Effect of K_0 on horizontal ground displacement 45mm from tunnel periphery.

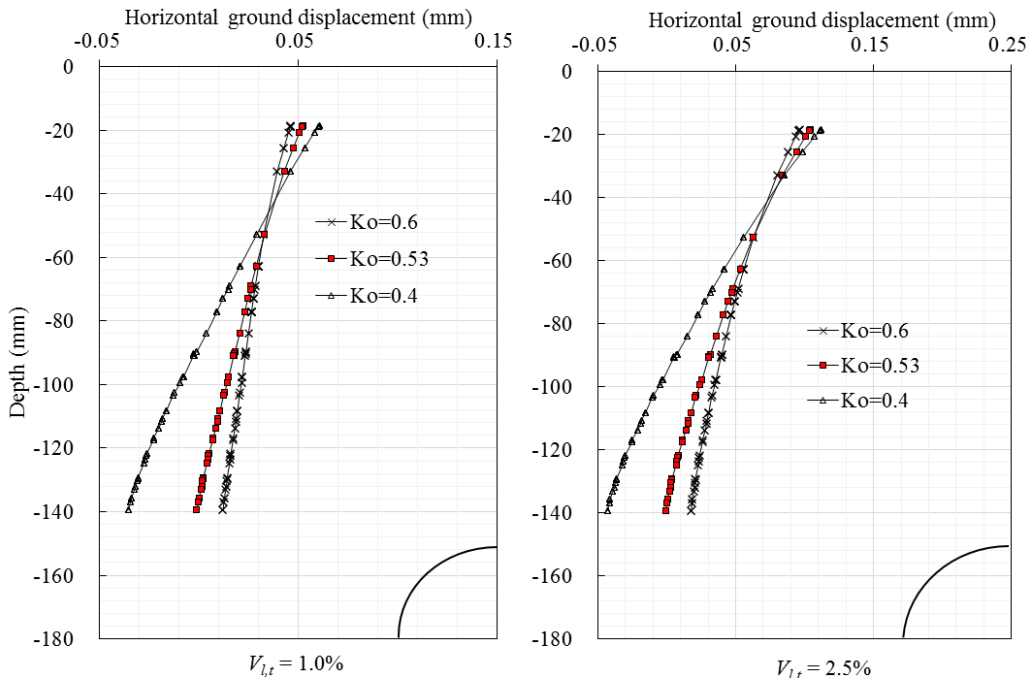

Figure D.3 Effect of K_0 on horizontal ground displacement 60mm from tunnel periphery.

D.2 Effect on stress path

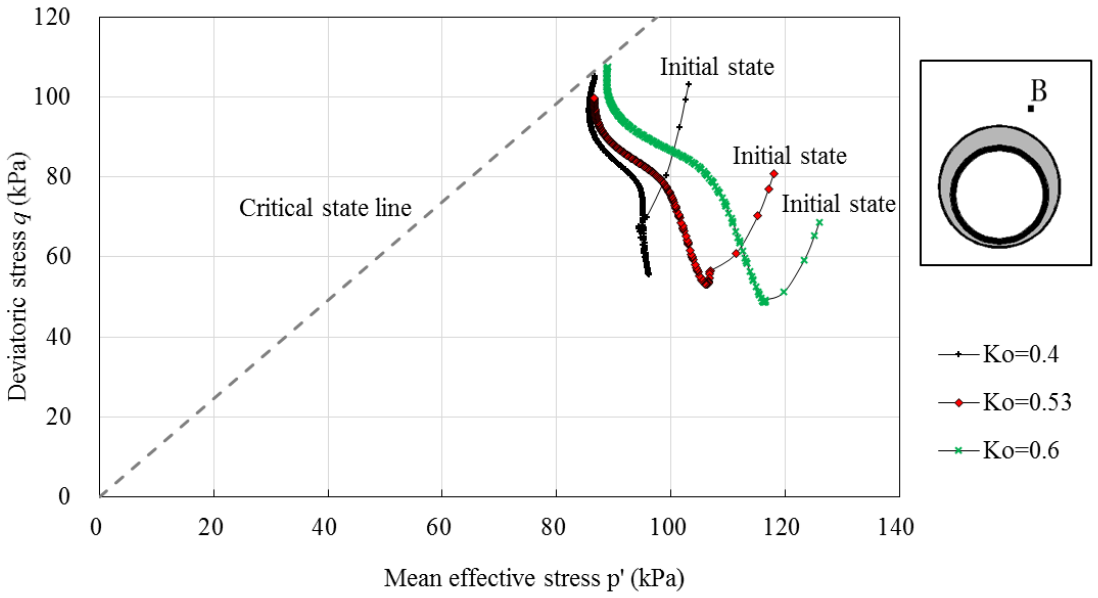

Figure D.4 Effect of K_0 on stress path at point B.

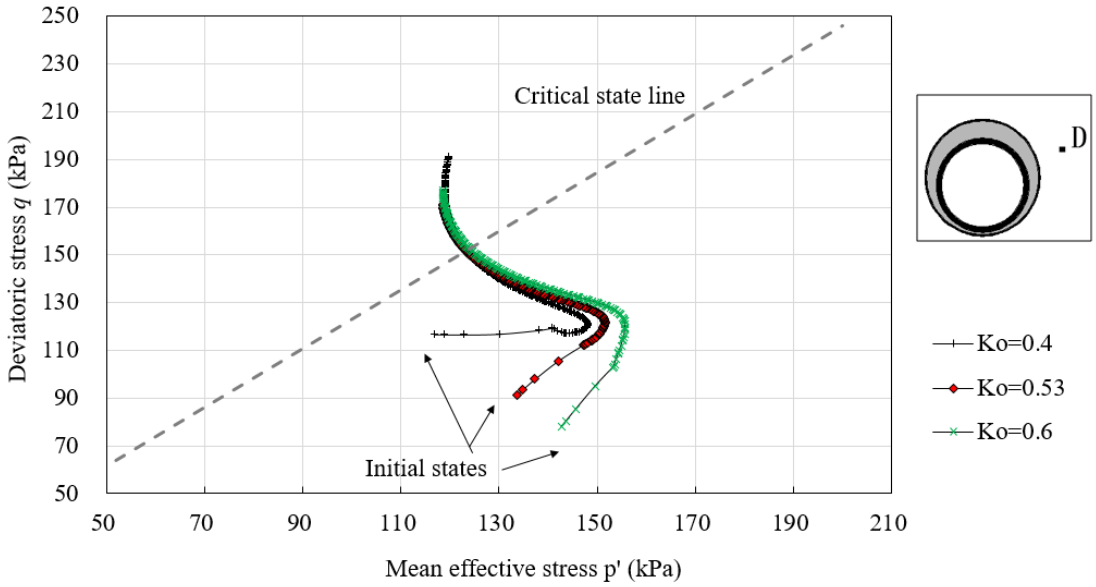

Figure D.5 Effect of K_0 on stress path at point D.

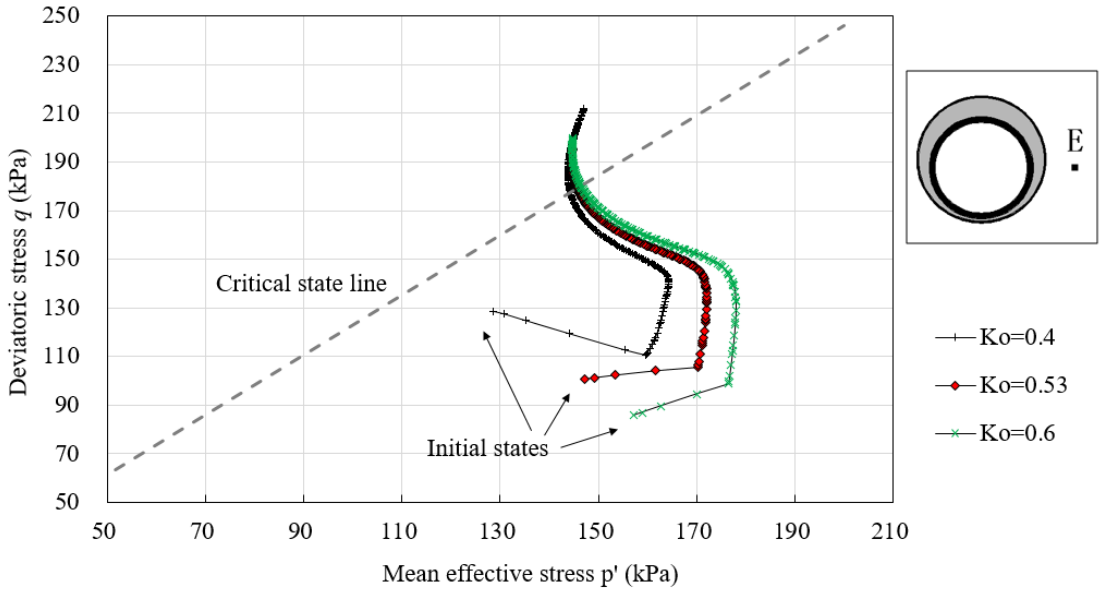

Figure D.6 Effect of K_0 on stress path at point E.

Appendix E. FORTRAN code of the proposed sand model

```
      Subroutine Proposed ( IDTask, iMod, IsUndr,
     *                      iStep, iTer, iEl, Int,
     *                      X, Y, Z,
     *                      Time0, dTime,
     *                      Props, Sig0, Swp0, StVar0,
     *                      dEps, D, BulkW,
     *                      Sig, Swp, StVar, ipl,
     *                      nStat,
     *                      NonSym, iStrsDep, iTimeDep, iTang,
     *                      iAbort )
!
!  Purpose: User supplied soil model (A proposed sand model based on Norsand)
!  By Bowen Yang, The University of Warwick.
!  Last change: 08/2017
!  Depending on IDTask, 1 : Initialize state variables
!                       2 : calculate stresses,
!                       3 : calculate material stiffness matrix
!                       4 : return number of state variables
!                       5 : inquire matrix properties
!                       6 : calculate elastic material stiffness matrix
!                           return switch for non-symmetric D-matrix
!                           stress/time dependent matrix
! Arguments:
!           I/O  Type
!  IDTask    I   I    : see above
!  iMod      I   I    : model number (1..10)
!  IsUndr    I   I    : =1 for undrained, 0 otherwise
!  iStep     I   I    : Global step number
!  iter      I   I    : Global iteration number
!  iel       I   I    : Global element number
!  Int       I   I    : Global integration point number
!  X         I   R    : X-Position of integration point
!  Y         I   R    : Y-Position of integration point
!  Z         I   R    : Z-Position of integration point
!  Time0     I   R    : Time at start of step
!  dTime     I   R    : Time increment
!  Props     I   R()  : List with model parameters
!  Sig0      I   R()  : Stresses at start of step
!  Swp0      I   R    : Excess pore pressure start of step
!  StVar0    I   R()  : State variable at start of step
!  dEps      I   R()  : Strain increment
!  D        I/O  R(,) : Material stiffness matrix
!  BulkW    I/O  R    : Bulkmodulus for water (undrained only)
!  Sig       O   R()  : Resulting stresses
!  Swp       O   R    : Resulting excess pore pressure
!  StVar     O   R()  : Resulting values state variables
!  ipl       O   I    : Plasticity indicator
!  nStat     O   I    : Number of state variables
!  NonSym    O   I    : Non-Symmetric D-matrix ?
!  iStrsDep  O   I    : =1 for stress dependent D-matrix
                                                                      !
```

```
!  iTimeDep 0   I    : =1 for time dependent D-matrix
!  iAbort   0   I    : =1 to force stopping of calculation
!
      Implicit Double Precision (A-H, O-Z)
!
      Dimension Props(*), Sig0(*), StVar0(*), dEps(*), D(6,6),
     *          Sig(*),   StVar(*)
!
!---  Local variables
!
      Dimension dSig(6), xN1(3), xN2(3), xN3(3)

      Double precision deg30R


!
! Expected contents of Props(1..?)
!  1 : G    Shear modulus
!  2 : xNu  Poissons' ratio
!  3 : Alf  Steepness of yield surface in p-q-plane
!  4 : Bet  Steepness of plastic potential function in p-q-plane
!  5 : C    'cohesion' term f = q + Alf*p - C
! 10 : BFac Ratio K/G to calculate Bulk modulus


      If (IDTask .Eq. 1) Then ! Initialize state variables
        ! When there are state variables one could check a maximum
        ! For instance:
        !   StVar(1) contains maximum isotropic stress
        !   StVar(2) contains maximum shear mobilisation
        ! p = -(Sig0(1)+Sig0(2)+Sig0(3))/3
        ! or Call PrnSig(Sig0, ...., P0,Q0)
        !    P = -P0 ! compression positive
        ! ratio = Q0/Max(P,1d0) ! mobilisation degree
        ! StVar0(1) = Max (StVar0(1), p )
        ! StVar0(2) = Max (StVar0(2), ratio )
        Ci   = Props(7) ! Ci
        xNu = Props(9) ! nu

        If (xNu.Gt.0.5d0-1d-6 .Or. xNu.Lt.-1d-6) Then
          Call OK_MessageBox(' Invalid value for "nu" (param 2)')
          iAbort = 1
          Return
        End If
        if (xNu.Lt.0) then
          xNu = 0.0

        end if
        if (xNu.Gt.0.495d0) then
          xNu = 0.495
        end if

        If (iel+int.eq.2) Call WriVec(1,'Props',Props,17)
```

```
      End If  ! IDTask = 1

      If (IDTask .Eq. 2) Then ! Calculate stresses
        Call CopyRVec( StVar0, StVar, nStatV )

        ! undrained condition
        If (IsUndr.Eq.1) Then
          dEpsV = dEps(1) + dEps(2) + dEps(3)
          dSwp  = BulkW * dEpsV
          Swp   = Swp0 + dSwp
        Else
          Swp = Swp0
        End If
!-----------------------------------------------------------------------
!  ***** Get parameters       *****
!-----------------------------------------------------------------------
        Gamma = Props(1)
        xLambda = Props(2)
        xMtc = Props(3)
        HH = Props(4)
        chi = Props(5)
        xNN = Props(6) + 1.d0
        Ci = Props(7)
        Hu = Props(8)
        xNu = Props(9)
        psiini = Props(10)
        Pi_min = Props(11)   !ppi_min
        EpsilonE = Props(12) / 100.d0
        EpsilonR = Props(13) / 100.d0
        DD1 = Props(14)
        DD2 = Props(15)
        RR1 = Props(16)
        RR2 = Props(17)

        chi_im =  chi / (1. - xlambda * chi / xMtc)

cc      Fill elastic matrix
        xK = Stvar0(14)
        Gmax = Stvar0(15)

        If (xK .lt. 1d-6) Then
        Gmax = 10000.d0
        xK = 2.d0 * Gmax *(1.0d0 + xNu) / (3.d0 - 6.d0 * xNu)
        End If
c        p0 = -(Sig0(1)+Sig0(2)+Sig0(3))/3.0d0
c        Gmax = Ci * (p0 / 100.d0) ** 0.5

        P1  = 2.d0* Gmax *(1.d0-xNu)/(1.d0-2.d0*xNu)
        P2  = 2.d0* Gmax *( xNu )/(1.d0-2.d0*xNu)

        Call MZeroR(D,36)
        Do i=1,3
```

```
          Do j=1,3
            D(i,j) = P2
          End Do
          D(i,i) = P1
          D(i+3,i+3) = Gmax
        End Do

        !write E matrix
        If (iEl+Int+iter.Eq.3 .And. iStep.Lt.10) Then
          Call WriMat( -1, 'D66', D, 6, 6, 6 )
        End If

        ! elastic stress increment
        Call MatVec( D, 6, dEps, 6, dSig)

        ! elastic stress + elastic stress increment
        Call AddVec( Sig0, dSig, 1d0, 1d0, 6, Sig )

        ! write Sig array
        Call WriVec( -1, 'Sig', Sig, 6)

        ! determine principal stresses and directions
        iOpt = 1
        Call PrnSig(iOpt, Sig, xN1, xN2, xN3, S1, S2, S3, P, Q) ! p: compression
negative

!-----------------------------------------------------------------------
!  ***** Define strains       *****
!-----------------------------------------------------------------------
        DepsV= Deps(1)+Deps(2)+Deps(3)


        if(Q > 1.e-9) then
        g1 = ( dEps(1) - dEps(2) ) ** 2
        g2 = ( dEps(2) - dEps(3) ) ** 2
        g3 = ( dEps(3) - dEps(1) ) ** 2
        g4 = dEps(4) ** 2 + dEps(5) **  2 + dEps(6) ** 2
        depsG = sqrt ((2./9.) * ( g1 + g2 + g3) + (1./3.)*g4)
        else
            depsG = 0.0
        endif

!-----------------------------------------------------------------------
!  ***** Update state variables       *****
!-----------------------------------------------------------------------
        xMiold = Stvar0(1)
        xLodeold = Stvar0(2)
        etaold = Stvar0(3)
        VoidRatio = Stvar0(4)
        Pimage = Stvar0(5)
        Pimage_Max = Stvar0(6)
        volumechange = Stvar0(7)
        Pfy = Stvar0(8)

                                                                        !
```

```
!-----------------------------------------------------------------------
!  *****  Initialise   *****
!-----------------------------------------------------------------------
!-----------------------------------------------------------------------
!  ***** Get the Initial lode angle   *****
!-----------------------------------------------------------------------
       deg30R = 0.523598
       sq3=sqrt(3.);  ss1=sig0(1)  ;  ss2=sig0(2)
       ss3=sig0(3) ;  ss4=sig0(4);  ss5=sig0(5);  ss6=sig0(6)
       sigm=(ss1+ss2+ss3)/3.   !P
       d2=((ss1-ss2)**2+(ss2-ss3)**2+
     *     (ss3-ss1)**2)/6.+ss4*ss4+ss5*ss5+ss6*ss6
       ds1=ss1-sigm ;  ds2=ss2-sigm  ;  ds3=ss3-sigm
       d3=ds1*ds2*ds3-ds1*ss5*ss5-ds2*ss6*ss6-ds3*ss4*ss4+2.*ss4*ss5*ss6
       dsbar=sq3*sqrt(d2)  !Q

       if(dsbar==0.)then
         theta=0.
       else
         sine=-3.*sq3*d3/(2.*sqrt(d2)**3)
         if(sine>1.)sine=1.  ;  if(sine<-1.)sine=-1. ;theta=asin(sine)/3.
       end if

       if(abs(dsbar).LT.1.e-16) theta = deg30R
       if(theta.GT.deg30R)  theta =  deg30R
       if(theta.LT.-deg30R) theta = -deg30R

       xLode = theta
!-----------------------------------------------------------------------
!  ***** Assign initial state values  *****
!-----------------------------------------------------------------------

        p0 = - (Sig0(1) + Sig0(2) + Sig0(3))    ! compression possitive
        q0 = dsbar
        eta0 = q0 / p0
        etaold = eta0

        psi0 = psiini + volumechange

cc      Calculate Mi
        ! get critical value of M for Inital Lode angle
        xMi0  = xM_psii(xMtc, xNN, Chi, psi0, xLode)
        xMi_tc = xM_psii(xMtc, xNN, Chi, psi0, deg30R)
        xMi_te = xM_psii(xMtc, xNN, Chi, psi0, -deg30R)
        xMiold = xMi0

        Pimage0 = p0 * exp(eta0/xMi0-1.)
cc      limit minimum mean stress to 1 kPa
        if(Pimage0.lt.Pi_min) then
                    Pimage0 = Pi_min
        endif

cc      Initial critical void ratio definition
```

```
        ecrit = Gamma - xLambda * (LOG(p0)-LOG(Pi_min))
        e0 = psi0 + ecrit

        VoidRatio = e0
        Pval = p0
        Qval = q0

        xLodeold = xLode

cc      Initial image state
        Pimage = Pimage0
        PimageOld = Pimage0                                  !Initial P_image
        PiOverP = Pimage0/p0

        PsiImage = psi0 + xLambda * LOG(PiOverP)              !Initial psi image

        PimageOverP_Max = EXP(-chi_im * PsiImage/ xMi_tc )
        Pimage_Max = Pval * PimageOverP_max

        Dp0 = xMi0 * (log(Pval) - log(Pimage))

        Hmod = HH
        Hlode = Hmod * xMi0 / xMi_tc

        XH = Hlode * Pval/PimageOld * (Pimage_Max - PimageOld)
!Initialise

!-----------------------------------------------------------------------
!  ***** Get the current lod angle and stress *****
!-----------------------------------------------------------------------
      deg30R = 0.523598
      sq3=sqrt(3.);  ss1=sig(1)  ;  ss2=sig(2)
      ss3=sig(3) ;  ss4=sig(4);  ss5=sig(5);  ss6=sig(6)
      sigm=(ss1+ss2+ss3)/3.   !P
      d2=((ss1-ss2)**2+(ss2-ss3)**2+
     *     (ss3-ss1)**2)/6.+ss4*ss4+ss5*ss5+ss6*ss6
      ds1=ss1-sigm ;  ds2=ss2-sigm  ;  ds3=ss3-sigm
      d3=ds1*ds2*ds3-ds1*ss5*ss5-ds2*ss6*ss6-ds3*ss4*ss4+2.*ss4*ss5*ss6
      dsbar=sq3*sqrt(d2)   !Q

      if(dsbar==0.)then
        theta=0.
      else
        sine=-3.*sq3*d3/(2.*sqrt(d2)**3)
        if(sine>1.)sine=1.  ;  if(sine<-1.)sine=-1.  ;theta=asin(sine)/3.
      end if

      if(abs(dsbar).LT.1.e-16) theta = deg30R
      if(theta.GT.deg30R)  theta =  deg30R
      if(theta.LT.-deg30R) theta = -deg30R

      xLode = theta
```

```
      Pnew = - ( Sig(1) + Sig(2) + Sig(3) ) / 3          !current guess stress
      Qnew = dsbar

!-----------------------------------------------------------------------
!  ***** Use new stress state to determine the NorSand yield function       *****
!-----------------------------------------------------------------------

!  -- update void ratio with incremental strains to obtain Psi & Psi_im     --

       Void = VoidRatio + (1. + VoidRatio) * depsV       !current void ratio
       volumechange = (1. + VoidRatio) * depsV
       ecrit = Gamma - xLambda * (LOG(Pnew)-LOG(Pi_min))  !current critical void ratio
       Psi_elem = Void - ecrit                                !current state parameter
       Psi_im = psi_elem + xLambda * (LOG(Pimage)-log(Pnew))   !current psi image

!  -- define M_image for yield surface using the new Psi_im & thetaR
        xMi = xM_psii(xMcrit, xNN, Chi_im, Psi_im, xLode)

!  -- define M_image for triaxial compression (theta=30) conditions
       xMitc = xM_psii(xMcrit, xNN, Chi_im, Psi_im, deg30R)

!  -- determine current stresses in the yield surface function
       f = Qnew - Pnew * xMi * ( 1.d0 + log (Pimage) - log (Pnew))

!  -- No yielding yet
       ipl = 0
!-----------------------------------------------------------------------
!  ***** Plastic yielding on f; Output new stress    *****
!-----------------------------------------------------------------------

       If (f .Gt. 1d-6) Then ! plastic stress correction
         !  f = q + Alf * p - c
         !  p = pe - xLam * Bulk * Bet
         !  q = qe - xLam * 3*G
         !  plastic volumetric multiplier ( hardening during loading )

         xK = Stvar0(14)
         Gmax = Stvar0(15)

         If (xK .lt. 1d-6) Then
         Gmax = 10000.d0
         xK = 2.d0 * Gmax *(1.0d0 + xNu) / (3.d0 - 6.d0 * xNu)
         End If

          pt1 = 3.d0 * Gmax * dEpsG
          pt2 = xK * dEpsV * ( xMiold - etaold )
          pt3 = 3.d0 * Gmax
          pt4 = HH*(Pimage_Max/Pimage)*EXP(1.0d0-etaold/xMiold)*Pnew
     *     * xMiold
          pt5 = xK * (xMiold - etaold) ** 2

          xLamv = ( pt1 + pt2 ) / ( pt3 + pt4 + pt5 )
```

```
            !If ( xLamv .Lt. 1d-6 ) Then
            !    xLamv = 1d-6
            !End If

           ! plastic stress correction
           pe = Pnew
           qe = Qnew
           !  p = pe - xLamv * Bulk * Ca
           !  q = qe - xLamv * 3*G * Cb
           Pnew = pe - xLamv * xK * (xMiold - etaold)
           Qnew = qe - xLamv * 3.d0 * Gmax

cc         yield on surface
cc           ipl = 5

           !get back to compression negative for pe
           pe = -pe
           q = qnew
           eta = qnew / pnew

           If (qe.Ne.0) Then
             s1 =  -pnew + q/qe*(s1-pe)
             s2 =  -pnew + q/qe*(s2-pe)
             s3 =  -pnew + q/qe*(s3-pe)
           Else
             s1 =  -pnew
             s2 =  -pnew
             s3 =  -pnew
           End If
           End If !plastic stress correction

         ! as example: update state variables
         ! Pt = -P ! compression positive
         ! ratio = Q/Max(Pt,1d0) ! mobilisation degree
         ! StVar(1) = Max (StVar0(1), pt )
         ! StVar(2) = Max (StVar0(2), ratio )

         ! back to Cartesian stresses; Output sxx, syy, szz, sxy, sxz, syz
         Call CarSig(S1,S2,S3,xN1,xN2,xN3,Sig)

         If (f .Gt. 1d-6 .and. Pimage.gt.Pi_min ) Then
           depsGp = xLamv
           depsVp = xLamv * ( xMiold - etaold )

           Pimage = Pimage + (xH * depsGp)
         End If
         If(Pimage.lt.Pi_min) then              ! set to Pi_min
              Pimage = Pi_min
         End If
!-----------------------------------------------------------------------
!  ***** Plastic yielding on stress cap; Output new stress   *****
!-----------------------------------------------------------------------
```

```
      Pcap = Pimage / PimageOverP_Max
      If ( Pnew .Lt. Pcap ) Then ! Softening

        Pcapold = Pcap
        Psoft = Pnew
cc      Update the first softening stress level P_fy
        Pfy = Max ( Psoft, Pfy )

        ! plastic volumetric multiplier ( softening during unloading )
        Gmax = Gmax0 * (Pnew / pref) ** 0.5

        xNu = Props(9)      ! nu
        HH = Props(4)
        xK = 2.d0 * Gmax *(1.0d0 + xNu) / (3.d0 - 6.d0 * xNu)

        pt1 = 3.d0 *  Gmax * dEpsG
        pt2 = dEpsV * (xK * (xMiold-etaold))/(2.d0*q0-p0)
        pt3 = 3.d0 *  Gmax
        pt4 = Hu / Log( pfy / p0 )
        pt5 = (xK * (xMiold - etaold) ** 2) /
     *         ((2.d0*q0 - xMiold * p0)**2)

        xLamv = ( pt1 - pt2 ) / ( pt3 + pt4 + pt5 )
      !  If ( xLamv .Lt. 0) Then
       !     xLamv = 1d - 6
       ! End If

      ! plastic stress correction
      pe = pnew
      qe = qnew
      !  p = pe - xLamv * Bulk * Ca
      !  q = qe - xLamv * 3*G * Cb
      qnew = qe - xLamv * 3.d0 * Gmax
      pnew = pe - xLamv * xK * (etaold-xMiold) / (2*q0-xMiold * p0)

cc      Softening on stress cap
cc        ipl = 6

      !get back to compression negative for pe
      pe = -pe
      q = qnew
      eta = qnew / pnew

      If (qe.Ne.0) Then
        s1 =  -pnew + q/qe*(s1-pe)
        s2 =  -pnew + q/qe*(s2-pe)
        s3 =  -pnew + q/qe*(s3-pe)
      Else
        s1 =  -pnew
        s2 =  -pnew
        s3 =  -pnew
      End If
```

```
        ! as example: update state variables
        ! Pt = -P ! compression positive
        ! ratio = Q/Max(Pt,1d0) ! mobilisation degree
        ! StVar(1) = Max (StVar0(1), pt )
        ! StVar(2) = Max (StVar0(2), ratio )

        ! back to Cartesian stresses; Output sxx,syy,szz,sxy,sxz,syz
        Call CarSig(S1,S2,S3,xN1,xN2,xN3,Sig)
        End If !plastic stress correction

!-----------------------------------------------------------------------
!  ***** Update the state parameters  *****
!-----------------------------------------------------------------------

        Psi_im0 = PsiImage
        Psi0    = psi

        xLode0 = xLodeold

        xMitc0ld = xM_psii(xMtc, xNN, Chi_im, Psi_im0, deg30R)
        xMi0ld   = xM_psii(xMtc, xNN, Chi_im, Psi_im0, xLode0)

        PimageMax0ld = Pimage_Max
        eta_old = Qval/Pval

        If (Psoft .Lt. Pcapold .and. Pimage.gt.Pi_min ) Then
          depsGp = xLamv
          depsVp = xLamv * (etaold-xMiold) / (2.0d0*q0-xMiold * p0)

        eta_limit = xMi0ld * (1.0 - Chi_im * Psi_im0/xMitc0ld)
        eta_ratio = eta_old/ eta_limit

        Pi_dotSoft = (Pimage_Max - PimageMax0ld) * eta_ratio * Pimage0ld
     *  / PimageMax0ld

        Pimage = Pimage +  Pi_dotSoft
        End If
        If(Pimage.lt.Pi_min) then               ! set to Pi_min
              Pimage = Pi_min
        End If

!  -- Update Lode angle

       sq3=sqrt(3.);  ss1=sig(1)  ;  ss2=sig(2)
       ss3=sig(3) ;  ss4=sig(4);  ss5=sig(5);  ss6=sig(6)
       sigm=(ss1+ss2+ss3)/3.   !P
       d2=((ss1-ss2)**2+(ss2-ss3)**2+
     *     (ss3-ss1)**2)/6.+ss4*ss4+ss5*ss5+ss6*ss6
       ds1=ss1-sigm ;  ds2=ss2-sigm  ;  ds3=ss3-sigm
       d3=ds1*ds2*ds3-ds1*ss5*ss5-ds2*ss6*ss6-ds3*ss4*ss4+2.*ss4*ss5*ss6
       dsbar=sq3*sqrt(d2)  !Q
```

```
        if(dsbar==0.)then
          theta=0.
        else
          sine=-3.*sq3*d3/(2.*sqrt(d2)**3)
          if(sine>1.)sine=1.  ;  if(sine<-1.)sine=-1.  ;theta=asin(sine)/3.
        end if

        if(abs(dsbar).LT.1.e-16) theta = deg30R
        if(theta.GT.deg30R)  theta =  deg30R
        if(theta.LT.-deg30R) theta = -deg30R

        xLode = theta

        Pnew = - ( Sig(1) + Sig(2) + Sig(3) ) / 3          !current guess stress
        Qnew = dsbar

!  -- Update properties with current new stresses

         Pval = Pnew
         Qval = Qnew
         etaold = Qval/Pval

         VoidRatio = VoidRatio + (1. + VoidRatio) * dEpsV
         ecrit = Gamma - xLambda * (LOG(Pval)-LOG(Pi_min))
         psi = VoidRatio - ecrit

          PiOverP = Pimage / Pval
        PsiImage = psi + xLambda * LOG(PiOverP)
        Psi_im = PsiImage

        xMi    = xM_psii(xMtc, xNN, Chi_im, Psi_im, xLode)
        xMi_tc = xM_psii(xMtc, xNN, Chi_im, Psi_im, deg30R)
        xMi_te = xM_psii(xMtc, xNN, Chi_im, Psi_im, -deg30R)
        xMLode = xM_psii(xMtc, xNN, Chi_im, 0.0d0, xLode)           ! value of Mtheta

cc
        PimageOverP_Max = EXP(-chi_im * Psi_im/ xMi_tc )
        Pimage_Max = Pval * PimageOverP_max

        if(Pimage.lt.Pi_min) then              ! set to Pi_min = 1.0 kPa
                     Pimage = Pi_min
        endif
        Dmin = chi_im * PsiImage * xMi/xMi_tc

        Dp = xMi * (LOG(Pval) - LOG(Pimage))

        Hmod = HH
        Hlode = Hmod * xMi / xMi_tc

        XH = Hlode * Pval/Pimage * (Pimage_Max - Pimage)

!************************************
        xMiold = xMi
```

```
        PimageOld = Pimage
        xLodeold = xLode

!-----------------------------------------------------------------------
!  ***** Update the state parameters  *****
!-----------------------------------------------------------------------

        Psi_im0 = PsiImage
        Psi0    = psi

        xLode0 = xLodeold

        xMitcOld = xM_psii(xMtc, xNN, Chi_im, Psi_im0, deg30R)
        xMiOld   = xM_psii(xMtc, xNN, Chi_im, Psi_im0, xLode0)

        PimageMaxOld = Pimage_Max
        eta_old = Qval/Pval

c        If (Psoft .Lt. Pcapold .and. Pimage.gt.Pi_min ) Then
c          depsGp = xLamv
c          depsVp = xLamv * (etaold-xMiold) / (2.0d0*q0-xMiold * p0)

c        eta_limit = xMiOld * (1.0 - Chi_im * Psi_im0/xMitcOld)
c        eta_ratio = eta_old/ eta_limit

c        Pi_dotSoft = (Pimage_Max - PimageMaxOld) * eta_ratio * PimageOld
c     *  / PimageMaxOld

c        Pimage = Pimage +  Pi_dotSoft
c        End If
c        If(Pimage.lt.Pi_min) then             ! set to Pi_min
c             Pimage = Pi_min
c        End If

!  -- Update Lode angle

        sq3=sqrt(3.);  ss1=sig(1)  ;  ss2=sig(2)
        ss3=sig(3) ;  ss4=sig(4);  ss5=sig(5);  ss6=sig(6)
        sigm=(ss1+ss2+ss3)/3.   !P
        d2=((ss1-ss2)**2+(ss2-ss3)**2+
     *      (ss3-ss1)**2)/6.+ss4*ss4+ss5*ss5+ss6*ss6
        ds1=ss1-sigm ;  ds2=ss2-sigm  ;  ds3=ss3-sigm
        d3=ds1*ds2*ds3-ds1*ss5*ss5-ds2*ss6*ss6-ds3*ss4*ss4+2.*ss4*ss5*ss6
        dsbar=sq3*sqrt(d2)   !Q

        if(dsbar==0.)then
          theta=0.
        else
          sine=-3.*sq3*d3/(2.*sqrt(d2)**3)
          if(sine>1.)sine=1.  ;  if(sine<-1.)sine=-1.  ;theta=asin(sine)/3.
        end if

        if(abs(dsbar).LT.1.e-16) theta = deg30R
```

```
        if(theta.GT.deg30R)  theta =  deg30R
        if(theta.LT.-deg30R) theta = -deg30R

        xLode = theta

        Pnew = - ( Sig(1) + Sig(2) + Sig(3) ) / 3         !current stress
        Qnew = dsbar

!  -- Update properties with current new stresses

         Pval = Pnew
         Qval = Qnew
         etaold = Qval/Pval

         VoidRatio = VoidRatio + (1. + VoidRatio) * dEpsV
         ecrit = Gamma - xLambda * (LOG(Pval)-LOG(Pi_min))
         psi = VoidRatio - ecrit

          PiOverP = Pimage / Pval
         PsiImage = psi + xLambda * LOG(PiOverP)
         Psi_im = PsiImage

         xMi    = xM_psii(xMtc, xNN, Chi_im, Psi_im, xLode)
         xMi_tc = xM_psii(xMtc, xNN, Chi_im, Psi_im, deg30R)
         xMi_te = xM_psii(xMtc, xNN, Chi_im, Psi_im, -deg30R)
         xMLode = xM_psii(xMtc, xNN, Chi_im, 0.0d0, xLode)           ! value of Mtheta

cc
         PimageOverP_Max = EXP(-chi_im * Psi_im/ xMi_tc )
         Pimage_Max = Pval * PimageOverP_max

         if(Pimage.lt.Pi_min) then              ! set to Pi_min = 1.0 kPa
                      Pimage = Pi_min
         endif
         Dmin = chi_im * PsiImage * xMi/xMi_tc

         Dp = xMi * (LOG(Pval) - LOG(Pimage))

         Hmod = HH
         Hlode = Hmod * xMi / xMi_tc

         XH = Hlode * Pval/Pimage * (Pimage_Max - Pimage)

!************************************
         xMiold = xMi
         PimageOld = Pimage
         xLodeold = xLode

!-----------------------------------------------------------------------
!  ***** write state variables for next integration step     *****
!-----------------------------------------------------------------------

         Stvar(1) = xMiold
```

```
        Stvar(2) = xLodeold
        Stvar(3) = etaold
        Stvar(4) = VoidRatio
        Stvar(5) = Pimage
        Stvar(6) = Pimage_Max
        Stvar(7) = volumechange
        Stvar(8) = Pfy
        Stvar(16) = xLamv

      End If ! IDTask = 2

      If ( IDTask .Eq. 3 .Or.
     *     IDTask .Eq. 6     ) Then ! Calculate D-Matrix
cc      Get input parameters
        xNu = Props(9)
        Ci = Props(7)
        EpsilonE = Props(12) / 100.d0
        EpsilonR = Props(13) / 100.d0
        DD1 = Props(14)
        DD2 = Props(15)
        RR1 = Props(16)
        RR2 = Props(17)
!-----------------------------------------------------------------------
!  ***** Identify small strain parameters     *****
!-----------------------------------------------------------------------
cc      Define Q old
        deg30R = 0.523598
        sq3=sqrt(3.);  ss1=sig0(1)  ;  ss2=sig0(2)
        ss3=sig0(3) ;  ss4=sig0(4);  ss5=sig0(5);  ss6=sig0(6)
        sigm=(ss1+ss2+ss3)/3.   !P
        d2=((ss1-ss2)**2+(ss2-ss3)**2+
     *     (ss3-ss1)**2)/6.+ss4*ss4+ss5*ss5+ss6*ss6
        ds1=ss1-sigm ;  ds2=ss2-sigm  ;  ds3=ss3-sigm
        d3=ds1*ds2*ds3-ds1*ss5*ss5-ds2*ss6*ss6-ds3*ss4*ss4+2.*ss4*ss5*ss6
        QQ=sq3*sqrt(d2)   !Q0

cc      Define strains

        dEpsV= Deps(1)+Deps(2)+Deps(3)


        if(QQ > 1.e-9) then
        g1 = ( dEps(1) - dEps(2) ) ** 2
        g2 = ( dEps(2) - dEps(3) ) ** 2
        g3 = ( dEps(3) - dEps(1) ) ** 2
        g4 = dEps(4) ** 2 + dEps(5) **  2 + dEps(6) ** 2
        depsG = sqrt ((2./9.) * ( g1 + g2 + g3) + (1./3.)*g4)
        else
            depsG = 0.0
        endif
        dEpsGp = Stvar0(16)

cc      Compute total axial strain
```

```
        dep1 = ( dEpsV - 2.d0 * DepsG ) / 3.d0
        ep1tot = Stvar0(13) + dep1
        Stvar(13) = ep1tot

cc      Get state values
        VoidRatio = 1d-6 + Stvar0(4) + (1. + Stvar0(4)) * dEpsV
        P0 = - ( Sig0(1) + Sig0(2) + Sig0(3) )
        Pnew = - ( Sig(1) + Sig(2) + Sig(3) ) / 3

!-----------------------------------------------------------------------
!  ***** Identify stress reversal point       *****
!-----------------------------------------------------------------------
       dPn = Stvar0(9)
       dPn1 = Pnew - P0
       dQn = Stvar0(10)
       dQn1 = Qnew - Q0

       DirectL = ( dPn1 - dPn ) ** 2 + ( dQn1 - dQn ) ** 2
       DirectR = dPn ** 2 + dPn1 ** 2 + dQn ** 2 + dQn1 ** 2

       If ( DirectL .Ge. DirectR ) Then
           Reversal = 1.
       Else
           Reversal = 0.1d0
       End If

       Stvar(9)  = Pnew - P0
       Stvar(10) = Qnew - Q0
        If ( Reversal .Gt. 0.5 ) Then
          Stvar(11) = P0                    !Stress reversal point
          Stvar(12) = QQ
          Prev = Stvar(11)
          Qrev = Stvar(12)
        Else
          Prev = Stvar0(11)
          Qrev = Stvar0(12)
        End If

        If ( Prev .lt. 1d-6 ) Then    !Make sure Prev larger than zero
          prev = 1d-5
        End If

        etarev = Qrev / Prev          !Stress ratio at reversal point
cc        etarev = 0.1d0

        xib = (Min (Pnew, Prev)) / (Max (Pnew, Prev))

cc      The non-linear elasticity rho
        rr = rr1 * Exp(rr2 * VoidRatio)
        alpha = rr * (xib ** 0.55)
        Ds = DD1 * Exp(DD2 * Log(Pnew/(VoidRatio ** 3)))

        If (depsGp .lt. epsilonE) Then
```

```
          xomega = 1d-6
        Else
          xomega = ((depsGp - epsilonE) / epsilonR) ** 0.88d0
        End If

        Cs = (Ci * (1.d0 + xnu)) / ((1.d0 - 2.d0 * xnu) *
     * ((1 + VoidRatio) ** 4))
        rho = ((1.d0 + xomega ) / Cs) * (sqrt(Pnew / 100.d0)) +
     * Ds * (1.d0 - (xib ** alpha))

        If (rho .lt. 1d-6) Then
            rho = 1d-5
        End if
cc      Pill the elastic matrix
        xK = (1.d0 + VoidRatio) * (Pnew / rho)
        Gmax = xK * 3.d0 * (1.d0 - 2.d0 * xnu) / ( 2 * (1.d0 + xnu) )

        Stvar(14) = xK
        Stvar(15) = Gmax

        F1  = 2.d0* Gmax *(1.d0-xNu)/(1.d0-2.d0*xNu)
        F2  = 2.d0* Gmax *( xNu )/(1.d0-2.d0*xNu)

        Call MZeroR(D,36)
        Do i=1,3
          Do j=1,3
            D(i,j) = F2
          End Do
          D(i,i) = F1
          D(i+3,i+3) = Gmax
        End Do
!        Call WriMat( 1, 'D_Usr', D, 6, 6, 6 )
        BulkW = 0
        If (IsUndr.Eq.1) Then
          ! BulkW = ...
          xNu_U = 0.495d0
          Fac=(1+xNu_U)/(1-2*xNu_U) - (1+xNu)/(1-2*xNu)
          Fac=2D0*G/3D0  * Fac
          BulkW = Fac
        End If
      End If  ! IDTask = 3, 6

      If (IDTask .Eq. 4) Then ! Number of state parameters
        nStatV = 16
      End If  ! IDTask = 4

      If (IDTask .Eq. 5) Then ! matrix type
        NonSym   = 0  ! 1 for non-symmetric D-matrix
        iStrsDep = 1  ! 1 for stress dependent D-matrix
        iTang    = 1  ! 1 for tangent D-matrix
        iTimeDep = 1  ! 1 for time dependent D-matrix
      End If  ! IDTask = 5
```

```
Return
    End ! MyModel

Function xM_psii(xMtc, xNN, Chi_im, Psi_im, xLode)
! take the current triaxial compression Mtc as the reference soil property
! and return the currrent critical stress ratio M (Mi) based on the current
! Lode angle T (in radians) and image state parameter.

! calc the effect of state on Mtc
implicit none
Double precision xMtc, xM_psii, xLode
Double precision xMte, xNN, Chi_im, Psi_im
Double precision xM
Double precision deg30R
Double precision deg45R

      deg30R = 0.523598
      deg45R = 0.785398163

        xMte = xMtc/(1.+xMtc/3.)  ! = Mte (triaxial extension)

        if (xLode.GE.deg30R) then
          xM = xMtc
        elseif (xLode.LE.-deg30R) then
          xM = xMte
        else
          xM = xMtc - (xMtc - xMte) * cos(1.5*xLode + deg45R)
        endif

    xM_psii = xM * (1. - abs(xNN * Chi_im * Psi_im)/xMtc)

End Function xM_psii
```